学位論文

Magnetic study of seafloor hydrothermal systems in various tectonic settings

（多様な地質学的背景を持つ海底熱水系の磁気的研究）

平成２７年１２月博士（理学）申請

東京大学大学院理学系研究科

地球惑星科学専攻

藤井　昌和

Masakazu Fujii

Abstract

An understanding of the seafloor hydrothermal system is essential for discussing the cooling of the oceanic lithosphere, geochemical cycles of many elements, submarine mineral deposits, and specific chemosynthetic ecosystems. Near-seafloor magnetic anomalies can provide vital information such as the location, spatial extent, and mineralization of hydrothermal systems because magnetic minerals are oxidized, transformed, and created during the hydrothermal processes. However, previous magnetic studies are limited on basalt-hosted hydrothermal systems developed in axial areas of mid-ocean ridges (MORs), where hydrothermal fields are typically associated with reduced magnetization. Moreover, there has been limited discussion on the geological controls of hydrothermal systems in volcanic arc, back-arc, and ultramafic-hosted hydrothermal systems. Because seafloor hydrothermal circulation, fluids, and deposits are strongly controlled by tectonic processes, further study in these areas is needed to understand the geological and geophysical frameworks of seafloor hydrothermal systems.

In the present study, therefore, I analyzed near-seafloor magnetic data to discuss the magnetization structures of hydrothermal systems in various tectonic settings of three regions: (i) on- and off-axis hydrothermal fields hosted in andesite in back-arc region of the southern Mariana Trough (SMT), (ii) basalt- to rhyolite-hosted Tarama and Irabu hydrothermal fields (THF and IHF, respectively) in arc and back-arc regions of the Okinawa Trough, and (iii) an ultramafic-hosted hydrothermal field in a non-transform offset massif of the Central Indian Ridge (CIR). In addition, I measured the rock magnetic properties of host rocks from the seafloor near those subjected hydrothermal fields in order to construct an appropriate geologic interpretation of magnetic contrast.

In Chapter 2, I investigate five hydrothermal vent fields of the back-arc spreading region on the SMT. Near-seafloor magnetic data were collected using the *SHINKAI 6500*, a deep-sea human occupied vehicle (HOV). A new three-dimensional (3-D) method is applied to exploit the surrounding bathymetry and varying altitudes of the submersible for estimating the absolute crustal magnetization. The results reveal that magnetic-anomaly-derived absolute magnetizations (MADAMs) show a reasonable correlation with the natural remanent magnetizations (NRMs) of rock samples collected

from the seafloor of the same region. The distribution of MADAM suggests that all five andesite-hosted hydrothermal fields are associated with a lack of magnetization, as is generally observed at basalt-hosted hydrothermal sites of the MORs. The spatial extent of the resulting low magnetization is approximately ten times wider at off-axis sites than that at on-axis sites, possibly reflecting larger accumulations of nonmagnetic sulfides, stockwork zones, and alteration zones at the off-axis sites. Furthermore, I succeeded in distinguishing contiguous low magnetization zones (LMZs) located on the same seafloor volcano, which could not be separated in magnetic anomaly data collected at higher altitudes by an autonomous underwater vehicle (AUV).

In Chapter 3, I show the results of detailed analyses of high-resolution vector magnetic anomalies on arc and back-arc hydrothermal vent fields in the Okinawa Trough, by using the AUV *URASHIMA*. The IHF is developed on the axial area of the back-arc rift and consist of basaltic lavas. The THF is developed between a back-arc rift and arc along with dacite to rhyolite. Active hydrothermal venting was reported in both fields. The obtained magnetizations from both ship-underway and near-seafloor magnetic data are consistent with the values of NRM measured on rock samples. The distribution of crustal magnetization deduced from the magnetic anomaly revealed that both IHF and THF are associated with reduced magnetization. The spatial scale of low magnetization reflecting the extent of the discharge zone is large compared with that found at MORs. Comparisons of detailed bathymetry and magnetization distribution of the Irabu knolls reveal that the magnetization lows are located along the rim of the cauldron structure, indicating that hydrothermal fluids rise from deep areas along the caldera fault. The results show that reduced magnetization related to hydrothermal activity occurs in rhyolite-hosted systems as well as basalt-hosted systems, and that caldera faults are important pathways for forming large discharge zones of hydrothermal systems.

In Chapter 4, I investigate the Yokoniwa hydrothermal field (YHF), an inactive ultramafic-hosted hydrothermal vent field, by using high-resolution vector magnetic anomalies from the HOV *SHINKAI 6500* and the AUV *r2D4*. The YHF is developed at a non-transform offset massif of the CIR. Dead chimneys are widely observed around the YHF along with a very weak venting of low-temperature fluids. This indicates that the hydrothermal activity of the YHF is almost finished. The distribution of crustal magnetization from the magnetic anomaly revealed that the YHF is associated with

enhanced magnetization, which also occurs at the ultramafic-hosted Rainbow and Ashadze-1 hydrothermal sites of the Mid-Atlantic Ridge (MAR). The results of rock magnetic analysis on the seafloor rock samples including basalt, dolerite, gabbro, serpentinized peridotite, and hydrothermal sulfide show that only highly serpentinized peridotite carries high magnetic susceptibility and NRM intensity that can explain the high magnetization of the YHF. These observations reflect abundant and strongly magnetized magnetite grains within the highly serpentinized peridotite.

In Chapter 5, I discuss three topics on the basis of these near-seafloor magnetic anomaly surveys and rock magnetic analyses with previous studies: (i) the magnetic signature of volcanic lava-hosted hydrothermal systems, (ii) magnetic mineral formation at ultramafic-hosted hydrothermal systems, and (iii) the locations and spatial scales of seafloor hydrothermal systems. I draw the following conclusions about the general magnetic characteristics reflecting the hydrothermal alteration and evolution of hydrothermal systems.

1. Volcanic lava-hosted hydrothermal fields in various tectonic settings, including volcanic arcs and back-arc regions as well as MORs, are generally characterized by reduced magnetization, reflecting primarily the alteration of titanomagnetite within volcanic rocks, with accumulation of nonmagnetic hydrothermal deposits as a secondary source. This signature is generally common even if the type of basement rock differs from basalt to rhyolite.
2. Ultramafic-hosted hydrothermal systems developed in non-transform offset massifs of slow-spreading ridges are characterized by enhanced magnetization. I propose the following three-stage model for magnetic mineral formation in ultramafic-hosted hydrothermal fields: During the initial stage of an ultramafic-hosted hydrothermal system, magnetite forms with serpentine and H_2 through hydrothermal alteration of peridotites, and pyrrhotite mineralization occurs under reductive conditions. Once the serpentinization reaction has progressed, the amount of magnetite creation increases dramatically, strengthening the magnetization. Pyrrhotite creation continues as long as the H_2 content of the hydrothermal fluids continues to create a reducing environment in this developing stage. Hot and reduced hydrothermal fluids maintain the stability of magnetite and pyrrhotite with no low-temperature oxidation. Finally, once the reaction of the ultramafic rock ceases, H_2 is no longer formed in

the system. The conditions then become oxidative, which allows pyrrhotite to be converted into nonmagnetic iron sulfide or oxide, reducing considerably their magnetization considerably.

3. The hydrothermal process involves complex interplay between the dynamics of heat supply and the evolution of crustal permeability to allow seawater to access the source. As a result, the locations and spatial scales of hydrothermal systems are controlled by the tectonic background of each vent field. Off-axis hydrothermal vent sites in seafloor spreading regions are larger than on-axis sites, reflecting the longevity of the hydrothermal activity. On-axis sites located in neo-volcanic zones are likely controlled by dike intrusions over decadal timescales, whereas off-axis sites are controlled by off-axis magmatic activity over thousands of years. Hydrothermal fields related to volcanic arc and back-arc volcanism with summit calderas have horizontal spatial scales equal to or larger than detachment-controlled large hydrothermal fields at slow-spreading ridges. It is implied that the permeability structure and style of hydrothermal circulation may play important roles in the formation of larger demagnetized hydrothermal fluid pathways in caldera-controlled systems.

A major finding is that the presence of hydrothermal sulfides and the oxidation, transformation, and creation of magnetic minerals produce specific magnetic signatures at hydrothermal vent sites in various tectonic settings. These signatures can be used to detect and characterize both active and inactive hydrothermal sites. Near-seafloor magnetic survey using underwater vehicles such as HOVs or AUVs can therefore be an important component of deep-sea exploration of seafloor hydrothermal systems.

Contents

1. Introduction

1-1. Significance of Understanding Seafloor Hydrothermal Systems..... 9

1-2. Previous Studies..... 12

1-2-1. Seafloor hydrothermal systems 12

1-2-2. Magnetic mineralogy of hydrothermal systems 17

1-2-3. Magnetic anomalies associated with hydrothermal systems..... 20

1-3. Goal of This Study..... 25

2. On- and Off-axis Hydrothermal Fields in Back-arc Region of Southern Mariana Trough

2-1. Geological Background..... 44

2-2. Data and Methods 45

2-2-1. Data acquisition..... 45

2-2-2. Initial processing 46

2-2-3. Forward modeling..... 47

2-2-4. Estimation of absolute magnetization 49

2-3. Results 50

2-3-1. MADAM and seafloor geology 50

2-3-2. Evaluation of MADAM by comparison with rock NRM 52

2-3-3. Comparison of MADAM with AUV equivalent magnetization..... 53

2-4. Discussion..... 55

2-4-1. Processes causing the weak magnetization zones..... 55

2-4-2. Duration of hydrothermal activity and size of magnetic low..... 55

2-5. Chapter Conclusions..... 58

3. Basalt- to Rhyolite-hosted Tarama and Irabu Hydrothermal Fields in Arc and Back-arc Regions of Okinawa Trough

3-1. Geological Background 70
3-2. Data and Methods 71
3-2-1. Data acquisition 71
3-2-2. Imaging the magnetic anomaly: ship-underway 72
3-2-3. Imaging the magnetic anomaly: AUV 72
3-2-4. Rock magnetic properties and petrological observation 74
3-3. Results 75
3-3-1. Magnetization from ship-underway mapping 75
3-3-2. Magnetization from AUV mapping 76
3-3-3. Rock magnetic properties and petrography 76
3-4. Discussion 78
3-4-1. Magnetization intensity reflecting host rock difference 78
3-4-2. Strongly magnetized Irabu knolls 80
3-4-3. Processes causing weak magnetization zones 82
3-5. Chapter Conclusions 85

4. Ultramafic-hosted Yokoniwa Hydrothermal Field in Non-transform Offset Massif of Central Indian Ridge
4-1. Geological Background 100
4-2. Data and Methods 101
4-2-1. Imaging the magnetic anomaly: AUV 101
4-2-2. Imaging the magnetic anomaly: HOV 102
4-2-3. Rock magnetic properties measurements 105
4-2-4. Grain density and petrology on serpentinized peridotites 106
4-3. Results 107
4-3-1. Magnetization from AUV data 107
4-3-2. Magnetization from HOV data 107
4-3-3. Magnetic properties of rock samples 109
4-3-4. Serpentinization degree and petrography 110
4-4. Discussion 112
4-4-1. Basaltic volcanism on western slope of Yokoniwa Rise 112
4-4-2. Evolution of magnetite during serpentinization 114
4-4-3. Processes causing strong magnetization zones 116

4-5. Chapter Conclusions 119

5. Discussion

5-1. Magnetic Signature of Volcanic Lava-hosted Hydrothermal Systems 137

5-2. Magnetic Evolution at Ultramafic-hosted Hydrothermal Systems 140

5-3. Location and Spatial Scale of Seafloor Hydrothermal Systems 144

6. Conclusions

Acknowledgements

Bibliography

Chapter 1

Introduction

1-1. Significance of Understanding Seafloor Hydrothermal Systems

Hydrothermal alteration occurring in the oceanic lithosphere affects the physical, chemical, and biological processes of the Earth system. These hydrothermal systems are strongly related to the cooling of the oceanic lithosphere through vent fluids ranging from >300°C (black smokers) to <50°C, and are responsible for ~20% of the Earth's total heat loss (11 TW) [e.g., *Stein and Stein*, 1992, 1994]. Moreover, they contribute to substantial element exchange between seawater and the oceanic lithosphere with water fluxes of $\sim 3.5 \times 10^{12}$ kg/yr for black smokers, and $\sim 6.4 \times 10^{14}$ kg/yr for low-temperature venting [e.g., *Elderfield and Schultz*, 1996]. Precipitation of sulfide minerals from hydrothermal fluids at or below the seafloor is preserved as volcanogenic massive sulfide deposits in a wide range of ancient and modern geological settings [*Barrie and Hannington*, 1999]. Recycling of hydrothermally altered oceanic crust into mantle likely produces some of mantle's chemical heterogeneity [e.g., *Hofman*, 1988]. Moreover, the delivery of mantle-derived materials to seawater through hydrothermal systems has profound effects on seawater chemistry [e.g., *Wheat and Mottl*, 2000]. Chemical energy offered by hydrothermal vents creates a unique habitat for diverse biological communities [e.g., *Jannasch and Mottl*, 1985]. Further, recent studies have indicated the significance of hydrothermal systems on other planets. Active hydrothermal vents are believed to exist on Jupiter's moon Europa [e.g., *Lowell and DuBose*, 2005] and on Saturn's moon Enceladus [e.g., *Hsu et al*., 2015] and ancient hydrothermal vents have been speculated to exist on Mars [e.g., *Newsom*, 1980].

It is important to understand the geophysical and geological backgrounds of seafloor hydrothermal systems because the spatial scale, duration time, and hydrothermal fluid chemistry are controlled by differences in the host rock, heat source, and fluid pathways. The location and spatial extent of hydrothermal activity are often difficult to constrain by field observations. However, studies on near-seafloor magnetic anomalies can provide vital information on the subsurface structure because the oxidation, transformation, and production of magnetic minerals during hydrothermal processes cause distinct changes in the magnetization of the seafloor.

The extent of the hydrothermal alteration zone or the up-flow zone can be evaluated by the areal extent of the low magnetization zone in the crust, which results from the oxidation and transformation of the magnetic minerals. In the last few decades, numerous near-seafloor magnetic studies conducted on basalt-hosted hydrothermal systems of mid-ocean ridges (MORs) revealed that they are typically associated with reduced magnetization [e.g., *Tivey et al*., 1993; *Tivey and Johnson*, 2002; *Zhu et al*., 2010; *Tivey and Dyment*, 2010]. Hydrothermal vents exist in other tectonic settings such as volcanic arcs and back-arc spreading centers; however, their geophysical characteristics are presently poorly constrained, and their magnetic structures have not been effectively studied thus far. The chemical compositions of arc–back-arc hydrothermal fluids exhibit tremendous diversity relative to the basalt–rhyolite host rock with strong contributions from magmatic volatiles [*Ishibashi and Urabe*, 1995]. Further study is needed to understand the magnetic signatures of arc–back-arc hydrothermal systems hosted in more felsic, or siliceous, host rock compositions, such as andesite, dacite, and rhyolite, as well as basalt. Volcanic arc and back-arc hydrothermal systems have attracted much attention, owing mainly to the possibility of their use of submarine resources. Massive sulfides formed by hydrothermal activity in the arc–back-arc context are significantly more enriched in valuable metals such as Ag, Au, Cu, Pb, and Zn than those in other MORs [*Rona*, 2008].

Although the magnetic response of MOR hydrothermal systems hosted in volcanic rock is relatively well known, particularly in basalt, the magnetic response of ultramafic-hosted hydrothermal systems remains poorly documented. Recent studies of near-seafloor magnetics have reported high magnetization zones in the active ultramafic-hosted Rainbow and Ashadze-1 hydrothermal fields [*Nakase*, 2002; *Tivey and Dyment*, 2010; *Szitkar et al*., 2014b]. These magnetic highs are considered to reflect

the presence of mineralized stockwork, in which several chemical processes such as serpentinization and sulfide mineralization create and preserve strongly magnetized minerals. In the most often investigated ultramafic-hosted Rainbow hydrothermal field on the Mid-Atlantic Ridge (MAR), the magnetization estimated from magnetic anomaly mapping reaches ~30 A/m; however, the magnetization of sulfide-impregnated serpentinized peridotites collected in the same region is too small to explain the intensity of the magnetic anomaly [*Szitkar et al*., 2014b]. Magnetic mapping studies combined with investigation of the magnetic properties of host rocks are needed to determine the geological characteristics of the formation of high magnetization zones. Exposures of ultramafic rocks are extensively distributed within slow-spreading environments, where alteration processes significantly influence the submarine ecosystem and result in high concentrations of metals [e.g. *Fouquet et al*., 2010; *Kelley et al*., 2005; *Nakamura and Takai*, 2014]. Therefore, investigation of the magnetic signatures in these ultramafic-hosted hydrothermal systems is also important for detecting active and inactive hydrothermal sites and their mineralization states.

Diverse hydrothermal vent systems have been reported on more than 600 fields in various tectonic settings, such as MORs, volcanic arcs, back-arc spreading regions, and hot spots [e.g., *Hannington et al*., 2011]. These hydrothermal systems are generally developed at water depths of a few thousand meters, and the extent on the seafloor is usually a few hundred meters or less. To detect such relatively small geophysical and geological features, high-resolution near-seafloor surveys are required rather than those at the sea-surface. Near-seafloor surveys have become more tractable with deep-tow systems, dynamically positioned ships, and recent development of autonomous underwater vehicles, which allow detailed mapping of the seafloor on a scale relevant to the hydrothermal activity. By understanding present-day hydrothermal systems, we can explore buried deposits preserved off-axis to determine the past-history of hydrothermal activity and to assess the seafloor resources.

1-2. Previous Studies

1-2-1. Seafloor hydrothermal systems

During the early age of the development of seafloor spreading theory, *Bostrom et al*. [1969] reported that sediments from active MORs have very low Al and Ti contents and high Fe and Mn contents. They suggested that such ridges should be affected by volcanic emanations containing Fe and Mn that subsequently mix with ocean bottom waters. Moreover, the measured conductive heat flow in ocean basins younger than ~60 Ma has been reported to be less than the value predicted by the conductive plate cooling model [e.g., *Bullard et al*., 1956; *Lister*, 1970]. On the basis of these observations, *Lister* [1972] suggested that hydrothermal circulation is the dominant heat transfer process at ridge crests.

One of the first reports of an active hydrothermal field was the Trans-Atlantic Geotraverse (TAG) site on the MAR, which was based on extensive dredge samples of thick hydrothermal Mn encrustations overlying and cementing talus deposits [*Scott et al*., 1974]. However, active hydrothermal fluid venting was visually confirmed more than a decade afterward [*Rona et al*., 1986]. In 1977, the first vents, low-temperature structures <17°C hosting animal communities, were discovered near the Galápagos Rift seafloor [*Corliss et al*., 1979]. High-temperature vents at 300°C were first discovered on the East Pacific Rise (EPR) in 1979 (Fig. 1-1) [*Spiess et al*., 1980]. Such a temperature is below the boiling point of seawater at ambient pressure. These high-temperature vents are referred to as black smokers because the metal sulfide precipitation colors the hot fluids black. In 2000, a completely different type of hydrothermal system known as the Lost City was discovered on the MAR [*Kelley et al*., 2001]. Unlike black smoker vents, the chimneys at the Lost City are composed of $CaCO_3$ with maximum height of 60 m. During the past 40 years, the discovery rate of vent sites has increased dramatically in response to improved detection techniques and finding strategies. Currently, more than 600 hydrothermal vent fields have been documented in various tectonic settings such as MORs, hot spots, volcanic arcs, and back-arc basins (Fig. 1-2) [e.g., *Hannington et al*., 2011].

The newly formed oceanic lithosphere is extensively fissured and faulted, providing pathways for seawater penetration of the crust. Circulation of seawater generally occurs at depths of 1–2 km and may occur >8 km below the seafloor based on

seismicity [e.g. *Wolfe et al*., 1995; *Carbotte et al*., 2012] and axial magma chamber depth [e.g., *Sinton and Detrick*, 1992; *Singh et al*., 2006]. Water can be heated by hot rocks at depth, producing a highly chemically reactive fluid that undergoes a significant exchange of elements with the host rocks (Fig. 1-3) [*Humphris and McCollom*, 1998]. In the down-welling zone, low-temperature oxidation and alkali fractions dominate, and extensive replacement of pillow basalts and sheet flows occurs by minerals such as iron oxyhydroxides, zeolites, and clays, all of which are common at temperatures below about 100°C [e.g., *Gillis and Robinson*, 1988, 1990]. Alkalis such as K, Rb, and Cs are fixed within the replaced minerals. Uptake of these elements is balanced within the rocks by losses of Mg, Si, S, and, in some cases, Ca [e.g., *Gillis and Robinson*, 1990; *Alt*, 1995]. As fluids penetrate deeper into the crustal section, elements such as Cu, Zn, Fe, Pb, and S, as well as silica, are leached out from rocks at temperatures of 350–550°C [e.g., *Seyfried et al*., 1988; *Von Damm*, 1995], and are incorporated into the hydrothermal fluid. At temperatures higher than 150°C, uptake of Mg is accompanied by losses of alkalis such as K, Rb, and Li from the basaltic material [e.g., *Seyfried*, 1987; *Gillis and Robinson*, 1990; *Alt*, 1995]; moreover, sulfate is removed from seawater during the precipitation of anhydrite [e.g., *Barker et al*., 2010]. Elements such as Na, Mg, and Ca are added to the rock to form greenschist facies mineral assemblages that include minerals such as chlorite amphiboles, and Na-rich plagioclase at temperatures of 300–450°C. The heated fluid is sufficiently buoyant for returning to the seafloor and emerging in hydrothermal vents. Such vents may be concentrated into narrow jets or can be broadly distributed as diffuse emanations. The base of the reaction zone, where hydrothermal fluids reach their highest temperatures, is considered to be either near the sheeted dike–gabbro interface or within the underlying gabbroic rocks. The altered rock in this high-temperature zone contains amphibolite facies mineral assemblages that include amphibole and plagioclase. When fluids reach the seafloor at temperatures of 350–400°C or more, they are reduced, acidic at pH values of 2–6 and highly enriched in Li, K, Rb, Cs, Cu, Fe, and silica with respect to the seawater [e.g., *Von Damm*, 1995]. The debouching fluids actually range from just above ambient temperature (~2°C) to >400°C and have a wide range of chemical properties. They may be acidic or alkaline with salinities higher or lower than seawater, and they carry a wide and variable range of dissolved minerals that may precipitate onto the sea floor. The dissolved elements may include Ca, Fe, Mn, Zn, Ni, Cu, and Au, and the range of gases

includes H_2, He, CO_2, and CH_4. They may produce large, potentially economically important mineral deposits and can influence the chemistry of seawater. The dramatic changes in ambient temperature and chemistry near the seafloor cause precipitation of minerals such as anhydrite, barite, pyrite, chalcopyrite, and sphalerite [e.g., *Hannington et al*., 1995]. In many hydrothermal deposits, anhydrite and fine sulfide particles form the initial chimney structures. Anhydrite precipitates with sulfide from seawater at temperatures of 150°C, and during seawater mixing with hydrothermal fluid. High-temperature sulfide minerals precipitate to form the chimney structure, allowing the inner fluid to become insulated from the surrounding seawater. At temperatures above 250°C, chalcopyrite begins to form.

The most common type of hydrothermal vent in MORs is high temperature, basalt-hosted vents characterized by black smokers. This is the only type reported thus far on fast-spreading ridges, although it is also found less frequently on slow- and ultraslow-spreading ridges [e.g., *Baker and German*, 2004]. The diversity of hydrothermal vent fields among MORs can be understood by comparing three distinctly different types of deposits hosted in basalt, including those found on fast-spreading ridges such as the EPR, intermediate-spreading ridges such as the Endeavour Segment of the Juan de Fuca Ridge (JFR), and slow-spreading ridges such as the TAG active hydrothermal mound on the MAR (Fig. 1-4) [*Tivey*, 2007]. First, hydrothermal fields on the fast-spreading EPR occur in areas ranging from a few square meters to several hundreds of meters with ~2 m structures forming mounds that stand <15 m high. This type is relatively short-lived, lasting a few years or decades (Fig. 1-4a) [e.g., *Haymon and Kastner*, 1981; *Kadko et al*., 1985]. At the second type of the Main Endeavour Field on the JFR, the hydrothermal vents and the style of venting differ significantly from those on the EPR. Hydrothermal vents with chimneys rise nearly vertically from the seafloor to heights greater than 10 or 20 m (Fig. 1-4b) [*Delaney et al*., 1992]. The third type of hydrothermal field on slow-spreading ridges is considerably larger and endures for long periods, at least intermittently for 100 ka [e.g., *Lalou et al*., 1995; *Humphris and Cann*, 2000]. Basalt-hosted hydrothermal systems on slow-spreading ridges are generally associated with neo-volcanic zones within axial valleys. Examples of this type include the Snake Pit [*Karson and Brown*, 1988], the Lucky Strike [*Fouquet et al*., 1995], the 4°48′S area on the MAR [*Koschinsky et al*., 2008], the 49°39′E area of the Southwest Indian Ridge (SWIR) [*Zhu et al*., 2010], Loki's Castle on the Mohns

Ridge [*Pedersen et al*., 2010], and the Beebe vent field on the Mid Cayman Spreading Center [*Connelly et al*., 2012]. These fields are associated with neo-volcanic zones and contain high-temperature black smokers together with low-temperature diffuse venting. Conversely, the TAG site [*Rona et al*., 1986] is a good example of a hydrothermal field that is not directly associated with a neo-volcanic zone. Although its vent fluids are similar to those at neo-volcanic sites, the TAG is situated at the edge of a median valley. The hydrothermal system tends to be much larger and longer-lived than the equivalent systems at fast-spreading ridges (Fig. 1-4c).

Another type of hydrothermal vent system is that hosted in ultramafic rocks. This type has been discovered only on slow- and ultraslow-spreading ridges, where sub-seafloor peridotite outcrops are relatively common or where seawater can readily access peridotite through major faults. Several vent fields such as the Rainbow [*German et al*., 1996], Nibelungen [*Melchert et al*., 2008], and Ashadze [*Cherkashov et al*., 2008] occur in non-transform offsets where the mafic crust is thin or patchy and large-scale normal faulting or detachment faults is common [e.g., *deMartin et al*., 2007; *Escartin et al*., 2008]. The Rainbow site has high-temperature vents with black smokers that emit low-pH fluids moderately enriched in Si, Cu, and Zn [*Andreani et al*., 2014], which is consistent with reactions involving basalt or gabbro in addition to peridotite. The Rainbow site is considerably long-lived, at least intermittently for more than 20 ka [e.g., *Kuznetsov et al.,* 2006]. The Lost City appears to be hosted purely by ultramafic rocks. The vent site is located on 1.5 Ma crust 15 km from the axis of the MAR, and on top of the detachment footwall associated with the oceanic core complex of the Atlantis Massif [*Kelley et al*., 2001]. The Lost City is characterized by low-temperature fluid and carbonate precipitation and is significantly larger and longer-lived than most basalt-hosted fields [*Fruh-Green et al*., 2003; *Ludwig et al*., 2011]. An ultramafic-hosted site, Shinkai Seep Field (SSF), has also been found in a fore-arc setting in the Mariana Trench, although no evidence of active fluid venting has been noted [*Ohara et al*., 2012]. Vent fields of these ultramafic-hosted hydrothermal systems show high concentrations of H_2 and CH_4. This suggests the influence of a peridotite body because olivine and pyroxene in ultramafic rocks are hydrated to produce serpentine with the release of H_2 [e.g., *Schroeder et al*., 2002].

McCaig et al. [2007] presented a model that explains fault-controlled hydrothermal systems in terms of the development stage of detachment faults (Fig. 1-5). In their

model, hydrothermal circulation around detachment faults evolves from basalt-hosted site (TAG type), to footwall ultramafic-hosted site (Rainbow type) and then to low-temperature ultramafic-hosted site (Lost City type). Hot gabbroic plutonic rocks are intruded into the detachment footwall beneath neo-volcanic zones. Seawater penetrates into the deep crust to mine heat from gabbroic plutons and is discharged through the permeable fault zones and overlying basalts without sufficient interaction with the peridotite body. This process is similar to that of the style of the TAG site (Fig. 1-5A). If the hydrothermal fluid reaches a shallower, cooler gabbroic body that had been displaced from the neo-volcanic zone by structural movement on the detachment fault, the hydrothermal fluids can interact with both the gabbro and ultramafic body of the footwall before discharging in the axial valley wall with mixed properties. Such a process occurs at the Rainbow site (Fig. 1-5B). Off-axis, low-temperature circulation can occur completely within the ultramafic footwall, driven mainly by residual magmatic heat. This process describes that occurring at the Lost City site (Fig. 1-5C).

Seafloor hydrothermal vent fields are also widely distributed along volcanic arcs and back-arc basins. Hydrothermal vent deposits have been reported at intra-oceanic, back-arc basin spreading centers of the Mariana Trough and Lau and North Fiji Basins, in marginal back-arc basins of the Okinawa Trough, at submerged island-arc volcanoes of the Izu–Bonin, Mariana, and Tonga–Kermadec arcs, and in areas with more complex tectonic histories of the Manus Basin where arc volcanism and back-arc rifting occur in old arc crust [e.g., *Hannington et al*., 2005]. These deposits display both similarities and differences compared with that found on MORs and are as large [e.g., *Iizasa et al*., 1999; *de Ronde et al*., 2005]. The diversity observed in hydrothermal deposit compositions in back-arc basins, rifted arcs, and island-arc volcanoes can be attributed to many factors including the composition of the host rock such as basalt, andesite, dacite, and rhyolite; the contributions of magmatic volatiles; and the depth and structure of the substrate. The compositions of more felsic, or siliceous, host rock such as andesite, dacite, and rhyolite reflect the addition of H_2O and other volatiles from subducted sediments and hydrated oceanic crust in addition to partial melting in the mantle wedge [*Hannington et al*., 2005]. The chemical compositions of hydrothermal fluids exhibit tremendous diversity relative to the host rock with strong contributions from magmatic volatiles [*Ishibashi and Urabe*, 1995]. Low-pH fluids suggest the addition of magmatic volatiles such as SO_2 [*Ishibashi and Urabe*, 1995; *Hannington et*

al., 2005]. In a volcanic arc setting, hydrothermal vents are located on conical volcanoes, sometimes occurring within the summit caldera, and often emerge in water depths <1000 m. These shallow depths enable the boiling of fluids to enhance metal enrichment [*Hannington et al*., 2005]. The contents of economic metals such as Ag, Au, Ba, Cu, Pb, Sb, and Zn in massive sulfides formed by hydrothermal activity in the arc–back-arc context are generally higher than those on other MORs [*Rona*, 2008]. For example, the volcanogenic massive sulfide deposit in the Myojin Knoll of the Izu-Bonin submarine caldera, known as the Sunrise deposit, is notably rich in Au and Ag and has been interpreted as the modern analog of Kuroko-type polymetallic sulfide deposits [*Iizasa et al*., 1999]. Deposits hosted in an andesite body at the Vai Lili field on the Valu Fa Ridge of the Lau Basin are rich in barite, sphalerite, tennantite, and galena relative to the MOR deposits [*Fouquet et al*., 1993]. At the Brothers volcano in the Kermadec arc, active black smokers and massive sulfide deposits are present on the caldera wall and emit sulfur-rich very low-pH vent fluids [*de Ronde et al*., 2005]. At the PACMANUS vent area on Pual Ridge in the Manus Basin, sulfide deposits are enriched in Au, Ag, Pb, As, Sb, and Ba relative to the MOR deposits [*Moss and Scott*, 2001].

Volcanic arc and back-arc volcanisms in shallower depth can create pyroclastic rock that is very porous with much greater permeability than volcanic lavas erupted in deeper water [e.g., *Fiske et al*., 2001]. Seawater entrainment can be enhanced as the permeability increases, resulting in subsurface deposition of sulfide minerals and anhydrite, generation of more acidic fluid, and subsequent metal remobilization causing further metal enrichment. Further studies of the fluids, deposits, and geological backgrounds in volcanic arc and back-arc settings are needed to obtain better constraints for the development. In such processes, host rock composition and structure and magmatic volatile contribution play important roles, particularly in determining the composition of vent fluids and deposits.

1-2-2. Magnetic mineralogy of hydrothermal systems

Hydrothermal processes can oxidize, transform, and create magnetic minerals, which can change the crustal magnetization. The modification of three minerals generally occurs in hydrothermal systems through the (i) alteration of titanomagnetite within volcanic rock, (ii) creation of magnetite through serpentinization and

hydrothermal mineralization, and (iii) creation of pyrrhotite through sulfide mineralization under reductive conditions.

Oxides of Fe and Ti are the Earth's most important magnetic minerals and occur in three series; (i) stoichiometric titanomagnetites with spinel structures with solid solutions between end-member magnetite ($Fe^{2+}Fe_2^{3+}O_4$) and ulvöspinel ($Fe_2^{2+}Ti^{4+}O_4$); (ii) nonstoichiometric (oxidized) titanomagnetites or titanomaghemites, in which some Fe^{2+} ions migrate to the surface to be converted to Fe^{3+}, leaving ordered vacancies in the spinel lattice; and (iii) titanohematites, or hemoilmenites, with rhombohedral structures with solid solutions between hematite ($\alpha Fe_2^{3+}O_3$) and ilmenite ($Fe^{2+}Ti^{4+}O3$).

The magnetization of young oceanic crust arises primarily from the extrusive basaltic lavas that form the uppermost section of the seafloor. This magnetization is primarily a thermal remanent magnetization (TRM) carried by titanomagnetite grains. Titanomagnetites are altered into less-magnetic minerals such as titanomaghemite, titanohematite, and pyrite by contact with the pervasive circulation of hot and acidic hydrothermal fluid beneath the hydrothermal sites. Early studies of rock magnetic properties of basalt in terrestrial lava outcrops [*Ade-Hall et al*., 1971], the ocean floor [*Irving*, 1970; *Watkins and Johnson*, 1971], ocean crustal drilling sites [*Ade-Hall et al*., 1973], and laboratory experiments [*Johnson and Merrill*, 1972, 1973] have demonstrated that magnetization is significantly affected by low-temperature oxidation (maghemitization), in which the initial titanomagnetite is altered to titanomaghemite. This alteration process is considered to be relatively regional and broad in scale [e.g., *Johnson and Atwater*, 1977]. With more extreme alteration, titanomagnetite pseudomorphs change into titanohematite grains [*Ade-Hall et al*., 1971]. Clues for understanding the behavior of magnetic minerals relative to hydrothermal activity were obtained from a massive sulfide body in the Troodos Ophiolite complex in Cyprus. This investigation was based on the results of magnetic survey showing a strong low-magnetic field over a stockwork zone hosted within in a basaltic sequence [*Johnson et al*., 1982]. Rock magnetic studies have revealed that titanomagnetite in the basaltic rock had been replaced by nonmagnetic sulfide minerals and that the basalt itself had been altered to a clay, silica, and chlorite assemblage within the stockwork up-flow zone [*Johnson et al*., 1982; *Hall*, 1992].

Not all types of hydrothermal activity result in reduced magnetization and magnetic mineral destruction including oxidation and transformation. In some environments,

hydrothermal activity can result in magnetite formation. The process of serpentinization can produce significant magnetite deposition. Moreover, clear evidence has been presented that magnetite formation can occur through the normal seafloor alteration of peridotite [*Bina and Henry*, 1986; *Toft et al*., 1990; *Nazarova*, 1994; *Dyment et al*, 1997; *Oufi et al*., 2002] and in the place where vigorous hydrothermal systems that are located in serpentinized peridotite bodies [*Klein et al*., 2013b; *Szitkar et al*., 2014b]. Recent laboratory experiments designed to react the San Carlos olivine, $(Mg_{0.91}, Fe_{0.09})_2SiO_4$, with 250–350°C water at 50 MPa demonstrated a linear relationship between the magnetite production and the reaction progress of the serpentinization [*Malvoisin et al*., 2012]. Multiple studies of natural serpentinized peridotites recovered during an Ocean Drilling Program (ODP) using isotopic, magnetic, and thermodynamic constraints revealed that samples with abundant magnetite contained Fe-poor brucite and were formed through serpentinization at temperatures of 200–300°C [*Klein et al*., 2013b]. Investigations of abyssal peridotites recently exposed on the seafloor can provide important constraints for the serpentinization mechanism through comparisons with samples from xenoliths [e.g., *Ferré et al*., 2013] and onland oceanic core complexes [e.g., *Maffione et al*., 2014] because they are expected to have preserved the primary state of geological history without experiencing weathering, low-temperature oxidation, and tectonic metamorphism. Previous work by *Oufi et al*. [2002] investigated the magnetic properties of variably abyssal serpentinized peridotites obtained from seven deep-sea drilling sites, but the serpentinization degree of their samples was limited to 40%–100%. In this range, the compiled data showed that the magnetic susceptibility increased with the progression of serpentinization. In addition, some highly serpentinized peridotites having high natural remanent magnetization (NRM) showed large regional differences, which created difficulties in understanding the nonlinear changes of magnetic properties in the serpentinization reaction. Data with a wide range of serpentinization degrees from the same location are needed for further understanding of magnetite formation and magnetic susceptibility of serpentinized peridotite.

Magnetite is equally common as a primary and secondary minerals in sedimentary and metamorphic rocks and can form as part of a hydrothermally mineralization process. An example is the sediment-hosted Bent Hill hydrothermal system in the Middle Valley on the northeastern JFR, which was confirmed by drilling [e.g., *Korner*, 1994].

Pyrrhotite ($Fe_{1-x}S$) is a common magnetic mineral resulting from hydrothermal activity. The magnetic behavior of this iron sulfide mineral varies according to its crystal structure and composition. Pyrrhotite is a stable form of iron sulfide for the oxygen fugacity fO_2 < FMQ (fayalite ($FeSiO_4$) ↔ magnetite + quartz), whereas paramagnetic pyrite (FeS_2) is dominant under more oxidizing conditions [*Lorand et al*., 2005]. Monoclinic pyrrhotite (Fe_7S_8) is weakly magnetic (ferromagnetic) with a Curie temperature of 325°C; however, the magnetic properties weaken with greater S content, as the iron sulfide becomes more pyritic in composition. Hexagonal pyrrhotite (Fe_9S_{10}) is nonmagnetic (antiferromagnetic) at room temperature, although it has a restricted ferrimagnetic range due to thermally activated vacancy ordering above its λ-transition temperature of ~200°C until its Curie temperature at 265°C. Some hydrothermal vents containing pyrrhotite have been reported in the axial valley of the Endeavour Segment at 47°57′N [*Tivey and Delaney*, 1986], the Bent Hill massive sulfide (BHMS) over the Middle Valley [*Korner*, 1994] of the JFR, and the Rainbow hydrothermal field of the MAR [*Marques et al*., 2006].

1-2-3. Magnetic anomalies associated with hydrothermal systems

The location and spatial extent of hydrothermal activity are difficult to constrain by field observations; however, studies on near-seafloor magnetic anomalies can highlight these features because magnetic minerals are oxidized, transformed, and created through the hydrothermal processes. Deep-sea, high-resolution magnetic measurement techniques have been developed to detect weak and short-wavelength magnetic anomalies and to reveal the high-resolution magnetization distribution and relevant processes. Such techniques use either deep-towed magnetometers [e.g., *Sayanagi et al*., 1994; *Sager et al*., 1998; *Gee et al*., 2000; *Pouliquen et al*., 2001; *Tivey et al*., 2003; *Yamamoto et al*., 2005; *Tivey et al*., 2006; *Granot et al*., 2012; *Caratori-Tontini et al*., 2014] or deep-sea vehicles such as autonomous underwater vehicles (AUVs) [e.g., *Tivey et al*., 1998; *Zhu et al*., 2010; *Caratori-Tontini et al*., 2012a, 2012b; *Honsho et al*., 2013], remotely operated vehicles (ROVs) [e.g., *Dyment et al*., 2005; *Szitkar et al*., 2014a, 2014b], or human-occupied vehicles (HOVs) [e.g., *Tivey et al*., 1993; *Fujiwara and Fujimoto,* 1998; *Honsho et al*., 2009; *Sato et al*., 2009]. The results of previous near-seafloor magnetic surveys on seafloor hydrothermal fields

in various tectonic settings are summarized in Table 1-1.

High-resolution magnetic field mapping has revealed discrete zones of demagnetized crust associated with hydrothermal vent deposits hosted in basaltic seafloor, which represents patterns of subsurface up-flow of the hydrothermal fluid. The first observation showing the reduction of magnetization at a hydrothermal site was acquired over the TAG basalt-hosted hydrothermal site of the MAR by using a three-component fluxgate magnetometer fixed to the frame of the HOV *Alvin* (Fig. 1-6) [*Tivey et al*., 1993]. The authors of that study continued the observed magnetic anomaly upward to a datum plane at a depth of 3600 m (~20 m above the highest point of the mound), and they inverted the data to equivalent magnetization. The relative magnetization low was located directly beneath a sulfide mound area ~200 m in diameter with an abrupt contrast to higher magnetization at the edge of the mound, indicating a tightly constrained source. The amplitude of the magnetization low was approximately 12 A/m relative to the mean magnetization of the surrounding area. In addition, similar reduced magnetization associated with hydrothermal deposits has been observed in other hydrothermal fields of MORs including the 4°48′S fields [*Tivey and Dyment*, 2010] and the inactive site Krasnov [*Szitkar et al*., 2014a] of the MAR, the Main Endeavour Field of the JFR [*Tivey and Johnson*, 2002; *Tivey et al*., 2014], and a site on the SWIR [*Zhu et al*., 2010]. The near-bottom *Autonomous Benthic Explorer* (*ABE*) collected magnetic data over the 4°48′S area, where several active black smoker fields including the Comfortless Cove, Turtle Pits, and Red Lion are located within the axial rift on very fresh volcanic lava, and the zones of discrete reduced magnetization associated with the Red Lion and Comfortless Cove vent areas were clarified (Fig. 1-7) [*Tivey and Dyment*, 2010; *German et al*., 2008]. Because the Turtle Pits hydrothermal site also lies on the edge of a large zone of reduced magnetization ~200 m diameter, a wider area of alteration was believed to be buried under recently erupted lava flows. In the Main Endeavour Field of the JFR, *Tivey and Johnson* [2002] found discrete magnetization lows associated with each cluster of vents separated from each other by only 200 m, implying highly focused zones of hydrothermal alteration or hydrothermal deposits (Fig. 1-8). Relatively intense magnetization lows at <3 A/m compared with that in the surrounding area with diameters of ~100 m were centered directly beneath the vent clusters, which implies a near-vertical, narrow, pipe-like source region was located directly beneath the surface expression of the vent edifices. Magnetization lows were

also associated with both inactive and extinct vent zones, suggesting that the alteration of magnetic minerals rather than temporary thermal demagnetization is the primary process responsible for the reduced magnetization. In the ultraslow-spreading SWIR, *Zhu et al*. [2010] reported near-seafloor magnetic data collected during the AUV *ABE* survey at multiple elevations, and revealed a well-defined low crustal magnetization zone near a local topographic high (Fig. 1-9). This active hydrothermal vent field is the first to be observed on the SWIR and was located within and adjacent to the reduced magnetization zone at the local topographic high. This implies that the magnetic low may be the result of hydrothermal alteration of magnetic minerals. The maximum reduction in the crustal magnetization was 3 A/m.

Reduced magnetization associated with hydrothermal vent fields have also been found in hydrothermal systems along volcanic arcs and back-arc basins. Although the chemical compositions of arc–back-arc hydrothermal fluids exhibited tremendous diversity relative to the basalt–rhyolite host rock species with strong contributions from magmatic volatiles [*Ishibashi and Urabe*, 1995], the magnetic signature of the arc–back-arc hydrothermal fields was similar to that of MORs. The few studies performed on the magnetic signatures of specific arc–back-arc vent fields include the Hakurei Field within a caldera of the Izu–Ogasawara arc–back-arc volcano (Bayonnaise knoll) [*Honsho et al*., 2013], the Brothers Field within a caldera of the Kermadec intraoceanic arc volcano (Brothers volcano) [*Caratori-Tontini* et al, 2012], and the hydrothermal site on the Aeolian Palinuro arc [*Caratori-Tontini* et al., 2014]. The near-seafloor magnetic study for the Bayonnaise knoll was conducted by using the AUV *URASHIMA* at a general altitude of 80 m (Fig. 1-10) [*Honsho et al*., 2013]. That study reported the distribution of a low magnetization zone extending across an area of ~500 m × ~300 m associated with the Hakurei hydrothermal deposit, which contains active and inactive sulfide chimneys over an area of ~500 m × ~700 m within the summit caldera ~3 km in diameter. The amplitude of the magnetization low was approximately 0.5 A/m relative to the surrounding area. The correlation between the elongated direction of the magnetization low and the caldera wall strike strongly suggests that the up-flow zone was restricted by the caldera fault structure. At the Brothers volcano of the Tonga–Kermadec arc, a near-seafloor magnetic study using the AUVs *ABE* and *Sentry* at an altitude of ~50 m revealed two hydrothermal fields marked by reduced magnetization (Fig. 1-11) [*Caratori-Tontini et al*., 2012]. The amplitude of that magnetization low was

approximately 3–4 A/m relative to the surrounding area. In the hydrothermal field of the NW caldera wall, the very low magnetization extending across an area of 1 km × 0.5 km is consistent with the area of focused venting that includes black smoker chimneys and numerous dead spires. The hydrothermal site on the dacitic volcanic cone with lower temperature venting and apparent magmatic degassing is also consistent with the reduced magnetization zone, although its amplitude and spatial scale were less than those at the NW caldera wall site.

Weakened magnetic anomalies are interpreted as locally altered up-flow zones formed through hydrothermal activity because hydrothermal alteration processes oxidize and transform Fe–Ti oxide minerals such as titanomagnetite, which preserves magnetic remanence in oceanic extrusive rocks [*Irving*, 1970; *Ade-Hall et al*., 1971; *Watkins and Johnson*, 1971; *Rona*, 1978; *Johnson et al*., 1982; *Wooldridge et al*., 1990; *Pariso and Johnson*, 1991; *Hall*, 1992]. Similar magnetic lows have been confirmed in the ancient analogs of seafloor hydrothermal systems found in ophiolites, where zones of demagnetized crust are associated with the mineralized stockwork of ore bodies [*Hall*, 1992; *Richards et al*., 1989; *Walls and Hall*, 1998]. Furthermore, studies on volcanic geothermal areas in New Zealand have shown that hydrothermal alteration of magnetic minerals rather than thermal demagnetization is the most important mechanism for reduced magnetic anomalies [*Hochstein and Soengkono*, 1997]. In the seafloor realm, reduced magnetization zones have been observed in both active and extinct vent areas, suggesting that differences in the thermal environment do not significantly affect magnetic anomalies [*Tivey and Johnson*, 2002; *Szitkar et al*., 2014a]. Another explanation for reduced magnetic anomalies is the progressive accumulation of thick nonmagnetic hydrothermal deposits that cover the underlying magnetized layer and result in an apparent magnetic low owing to the increased distance between the measurement point and the underlying magnetized basalt [*Szitkar et al*., 2014a; *Szitkar and Dyment*, 2015].

In addition to the magnetic low at the basalt-hosted systems, it has been shown that hydrothermal activity led to enhanced crustal magnetization in the BHMS deposits, which are located on a sediment-covered axial valley of the JFR [*Tivey*, 1994; *Gee et al*., 2001]. In a deep-tow magnetic survey conducted at altitudes of 50–100 m, and a strong magnetization of 5 A/m assuming a uniformly magnetized body was reported (Fig. 1-12) [*Gee et al*., 2001]. This magnetic high was interpreted as the upper portion of a

sulfide mound with significantly higher induced magnetization of 10% magnetite + pyrrhotite. *Korner* [1994] showed that the ratio of saturation remanence to saturation magnetization of a drilled hydrothermal deposit was 0.01–0.15, suggesting that the magnetite within the sulfide mound occurred primarily as coarse, multi-domain grains.

Magnetization highs associated with hydrothermal vent fields have also been found in ultramafic-hosted active hydrothermal fields of the MAR [*Tivey and Dyment*, 2010; *Szitkar et al*., 2014b]. Previous studies on near-seafloor magnetics have reported high magnetization zones in the active ultramafic-hosted hydrothermal fields where high-temperature venting occurs; these include the Rainbow site with relatively higher magnetization intensity of ~30 A/m (Fig. 1-13) and the Ashadze-1 site with relatively higher magnetization intensity of ~4 A/m (Fig. 1-14) [*Tivey and Dyment*, 2010; *Szitkar et al*., 2014b]. These magnetic highs are considered to reflect the presence of mineralized stockwork, in which several chemical processes such as serpentinization and sulfide mineralization create and preserve strongly magnetized magnetite [*Szitkar et al*., 2014b]. At the Rainbow hydrothermal site, the estimated magnetization determined by magnetic anomaly mapping reached to ~30 A/m; however, the magnetization of sulfide-impregnated serpentinized peridotites collected in the same region was too small to explain the intensity of the magnetic anomaly [*Szitkar et al*., 2014b].

Enhanced magnetic anomalies in ultramafic-hosted hydrothermal sites are interpreted as magnetized bodies with large quantities of magnetic minerals, mostly magnetite and pyrrhotite, created by high-temperature hydrothermal alteration [*Tivey*, 1994; *Gee et al*., 2001; *Tivey and Dyment*, 2010; *Szitkar et al*., 2014b]. However, despite some high-resolution studies on magnetization around hydrothermal fields as previously mentioned, magnetic mapping studies combined with rock magnetic studies are limited. Therefore, the origin of magnetic anomalies such as the type of magnetic mineral, its amount, and whether magnetization was induced or remanent remain unclear. Exposures of ultramafic rocks are extensively distributed within slow-spreading environments [e.g., *Dick*, 1989; *Cannat*, 1993; *Cannat et al*., 1995; *Michael et al*., 2003], where alteration processes significantly influence the submarine ecosystem and result in high concentrations of metals [e.g. *Fouquet et al*., 2010; *Kelley et al*., 2005; *Takai et al*., 2006; *Nakamura and Takai*, 2014]. Therefore, detailed investigation of these ultramafic-hosted hydrothermal systems is important for understanding active and inactive hydrothermal sites and their mineralization states.

1-3. Goal of This Study

In this study, I determine the magnetic signatures of seafloor hydrothermal systems in various tectonic settings by utilizing both mapping of magnetic anomalies and rock magnetic properties.

On the basis of near-seafloor magnetic anomaly surveys and rock magnetic analyses presented in chapters 2, 3, and 4 and the results of previous research, I discuss the overall magnetic response of hydrothermal systems in various tectonic settings to reveal following parameters: (i) the magnetic signature of volcanic lava-hosted hydrothermal systems, (ii) the magnetic mineral formation at ultramafic-hosted hydrothermal systems, and (iii) the locations and spatial scales of seafloor hydrothermal systems. In terms of (i), I newly reveal magnetic signatures of hydrothermal systems in a back-arc spreading region, back-arc rift, and a rhyolite-hosted volcanic arc, which are described in Chapter 2 for the southern Mariana Trough (SMT) and Chapter 3 for the Okinawa Trough. To clarify (ii), particularly the origin of magnetization highs, I provide new field data of an inactive ultramafic-hosted hydrothermal site of the Central Indian Ridge (CIR), based on comprehensive magnetic data including both magnetic anomalies and rock magnetic properties described in Chapter 4. In addition, I investigate the relationship between the magnetic properties and serpentinization process. For (iii), I newly discuss the relationship between the spatial scale and duration time of hydrothermal fields based on my original results in a back-arc spreading region (Chapter 2), back-arc rift calderas (Chapter 3), and an ultramafic exposure (Chapter 4) and previous research of fast-spreading ridges, slow-spreading ridges controlled by detachment faults, volcanic arc and back-arc rift calderas, and ultramafic exposures.

In Chapter 2, I present detailed analyses of the near-seafloor, high-resolution vector magnetic data acquired by the HOV *SHINKAI 6500* both on and off the SMT back-arc spreading region, where five hydrothermal vent fields are located. I use the vector magnetic anomaly along the HOV tracks to estimate the absolute magnetization intensity of the shallow sub-seafloor by applying an improved 3-D version of the analysis method based on forward modeling proposed by *Honsho et al*. [2009] for 2-D structures. To evaluate estimated magnetic-anomaly-derived absolute magnetization (MADAM), I compare values of MADAM with both the equivalent magnetization computed by using AUV data and the NRM measured on rock samples. I clarify the

spatial extent and magnetic signature associated with the hydrothermal vent fields by using detailed seafloor geological features, which are analyzed by using video and photographs acquired during the *SHINKAI 6500* dives. Moreover, I discuss the relationship between the obtained magnetization distribution and the tectonic background of on- and off-axis hydrothermal systems.

In Chapter 3, I present multiple analyses of ship-underway and near-seafloor magnetic data and rock magnetic properties of collected samples from the Tarama and Irabu knolls in the Okinawa Trough. I perform near-seafloor vector magnetic measurements at an altitude of ~100 m by using the AUV *URASHIMA* during the R/V *Yokosuka* cruise YK14-16 in 2014. The Irabu knolls are located on the axial area of a back-arc rift and consist of basaltic lavas. The Tarama Knoll is located between a back-arc and an arc along with rhyolite. I use magnetic anomalies along the AUV tracks to estimate the equivalent magnetization intensity by applying the inversion technique using the Akaike Bayesian information criterion (ABIC) [*Honsho et al*., 2012]. I inspect the effects of host rock variation by comparing the estimated magnetizations from both ship-underway and near-seafloor magnetic anomalies with the NRM measured on rock samples. In addition, I clarify the relationship between the magnetization distribution and confirmed hydrothermal vent fields. Finally, I discuss the spatial extent of the hydrothermal vent fields in addition to the magnetic contrast of these fields compared with that of surrounding fresh lava flows. This information is determined from detailed seafloor topographic features derived from high-resolution multibeam bathymetry data acquired by using the AUV *URASHIMA*.

In Chapter 4, I explore the ultramafic-hosted Yokoniwa Hydrothermal Field (YHF), located on the CIR. The YHF is primarily an extinct hydrothermal system; therefore, it represents a unique target for investigating the differences in magnetic signatures between active and inactive hydrothermal systems hosted within ultramafic rocks. I investigate the magnetization distribution from magnetic anomalies obtained by the AUV *r2D4* and the HOV *SHINKAI 6500*, and I analyze the magnetic properties of rock samples collected near the YHF including basalt, dolerite, gabbro, serpentinized peridotite, and hydrothermal sulfide. On the basis of these multiple analyses, I discuss the magnetic signature of the inactive ultramafic-hosted YHF, the evolution of magnetite grains during serpentinization, and the process causing the strong magnetization at the YHF.

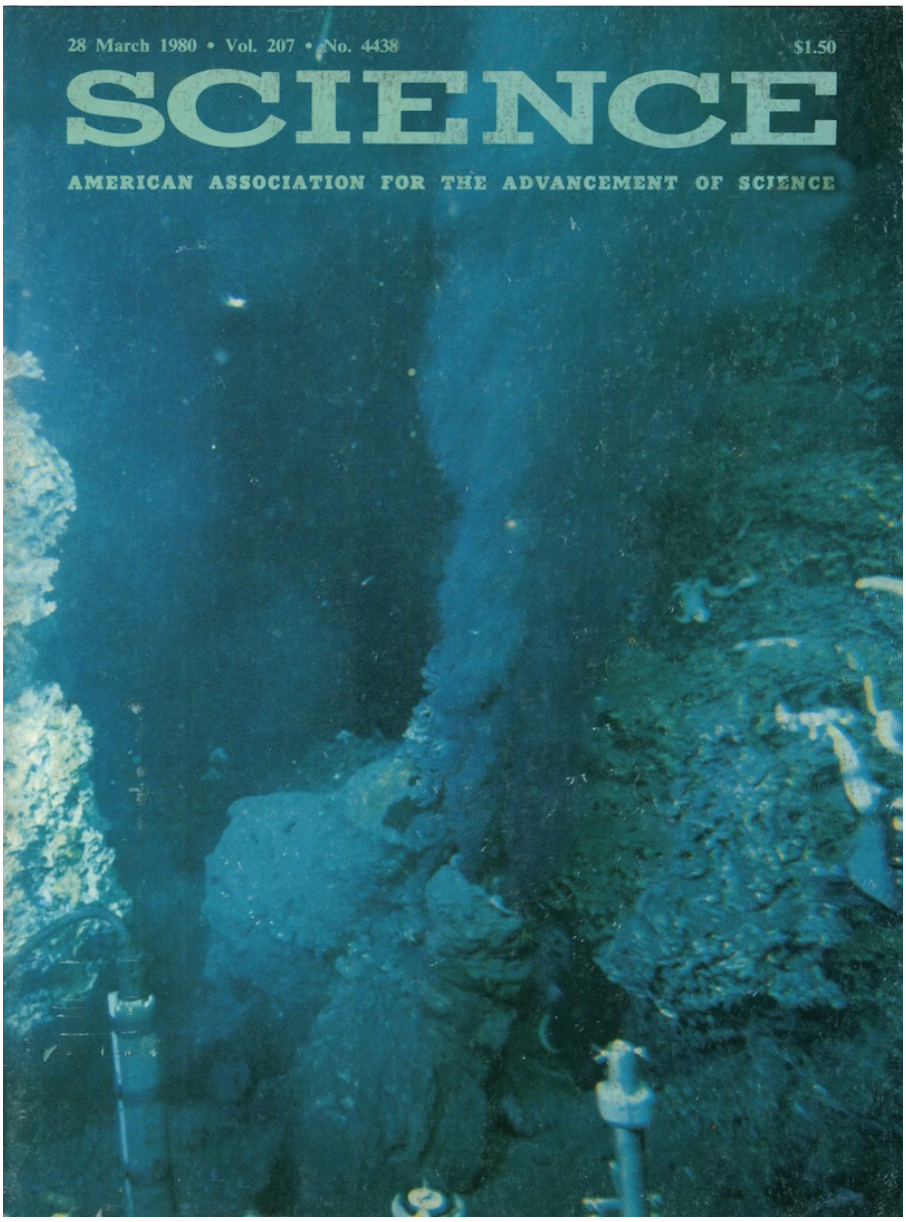

Figure 1-1. First published image of black smoker venting [*Spiess et al.*, 1980].

First published image of black smoker venting captured by the submersible *Alvin* during the RISE cruise on the East Pacific Rise in 1979.

Image courtesy of *Spiess et al*. [1980].

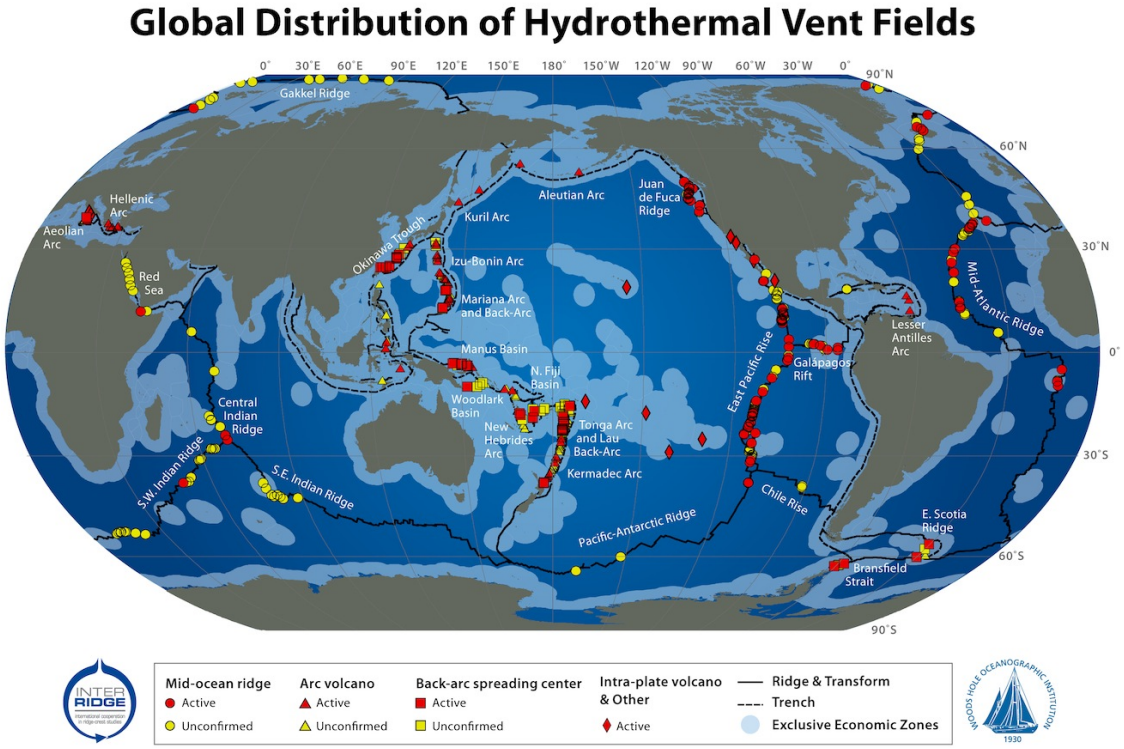

Figure 1-2. Global distribution of hydrothermal vent fields.

The data are from InterRidge Vents Database, Version 2.0, released on March 5, 2010. The static map is credited to S. Beaulieu, K. Joyce, and S.A. Soule, Woods Hole Oceanographic Institution (*WHOI*) [2010]. The plate boundary shape was determined by data sources of the University of Texas PLATES Project.
(http://vents-data.interridge.org/maps)

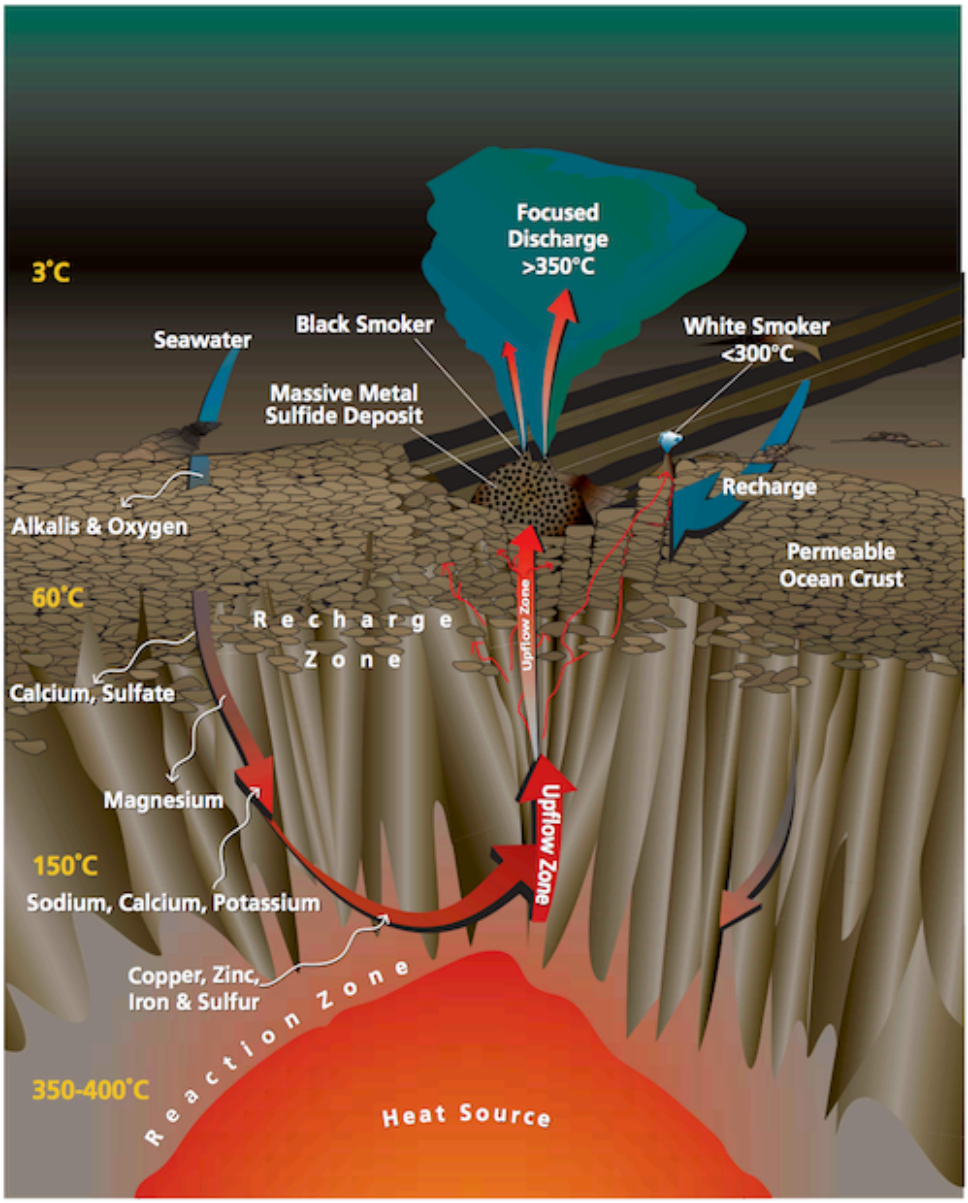

Figure 1-3. Schematic diagram showing downwelling of seawater and progressive heating with changes in the resultant hydrothermal fluid compositions, properties, and temperature [*Humphris and McCollom*, 1998].

The interaction with basaltic host rocks causes fluids to lose all Mg, O_2, and sulfate. At their deepest penetration, the resultant fluids are enriched in metals and magmatic gases, and become extremely hot at temperatures >400°C. The fluids are also buoyant, causing them to rise toward the seafloor through narrow, pipe-like conduits. The mixing of hydrothermal fluids with seawater causes metal precipitation, forming black smoker edifices. Figure courtesy of *Humphris and McCollom* [1998]

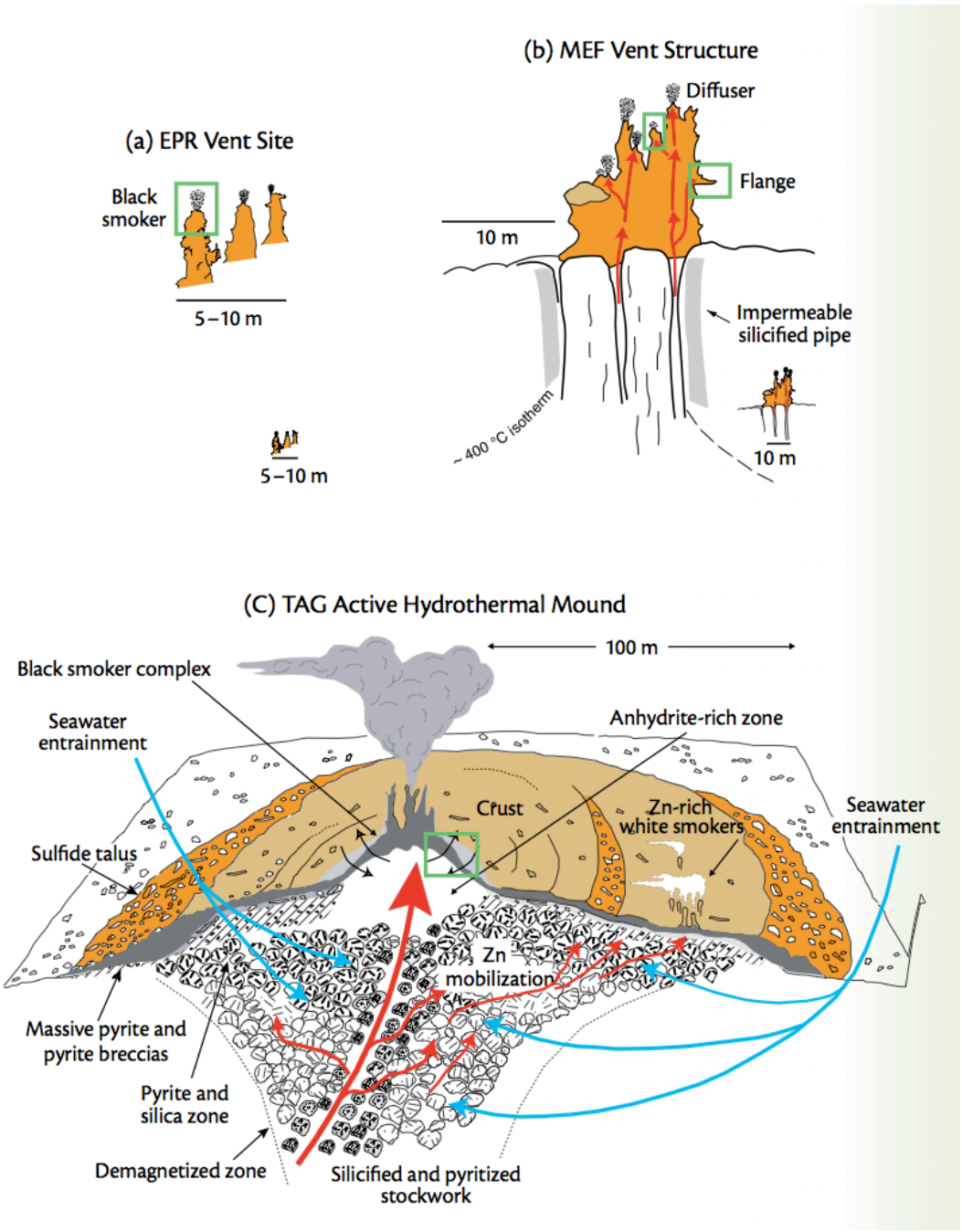

Figure 1-4. Schematic diagram showing differences in vent structure size, morphology, and influencing processes in different tectonic and geologic settings [*Tivey*, 2007].

(a) East Pacific Rise (EPR) hydrothermal vent fields showing tall spires topped by black smoker chimneys. The total accumulation at each vent site is low likely owing to the passage of hot fluids through the structure into the plume above coupled with frequent eruptions, which can bury the deposits.

(continued)

(b) The Main Endeavour Field (MEF) of the Juan de Fuca Ridge (JFR). The MEF includes ~15 structures and covers an area of ~400 m × 200 m. It has been proposed that the steep-sided structures are underlain by pipe-like stockworks sealed by intense silicification of the alteration pipes, preventing entrainment of seawater. The presence of higher-pH fluids provides an explanation for the silicification. (c) The Trans-Atlantic Geotraverse (TAG) active hydrothermal mound. Vigorous venting through the black smoker combined with significant entrainment of seawater into and beneath the mound triggers the deposition of pyrite, chalcopyrite and anhydrite; the generation of fluid with lower pH; and the remobilization of Zn and other trace metals, which are then deposited at the outer edges and on the upper surface of the mound. The very large size compared with structures from the EPR and MEF is the result of efficient mineral deposition owing to seawater entrainment combined with the recurrence of hydrothermal activity at this same location over a period of several tens of thousands of years. Figure courtesy of *Tivey* [2007].

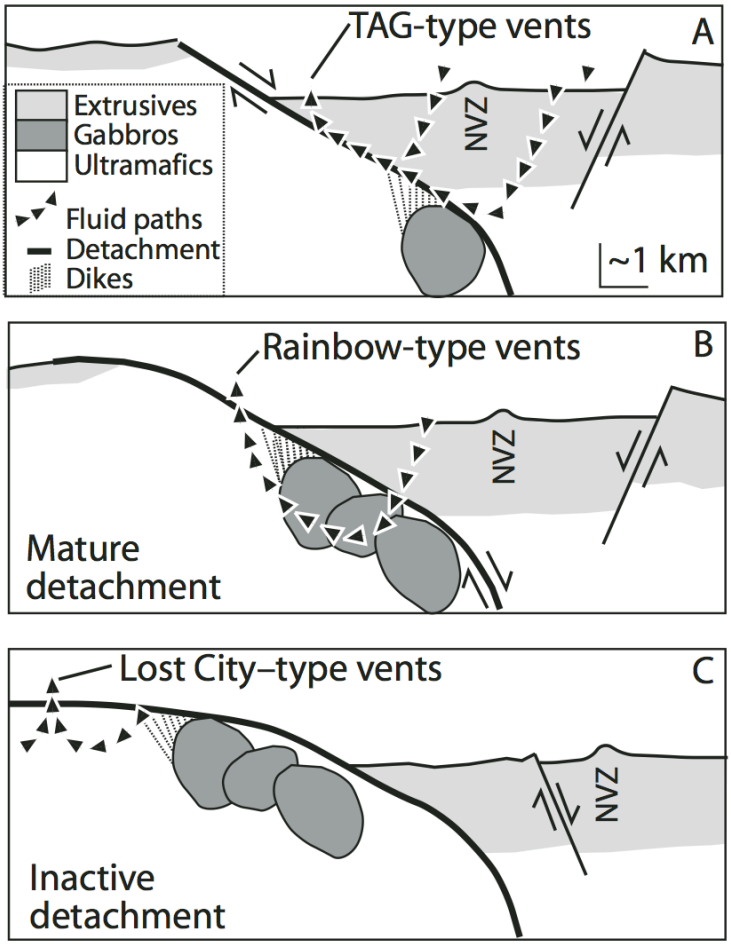

Figure 1-5. Model for fluid circulation and types of hydrothermal venting in and around detachment faults [*McCaig et al*., 2007].

(A) Early intense circulation at high temperatures is driven by gabbroic intrusions into the variably serpentinized ultramafic footwall. The flow follows detachment owing to deformation-enhanced permeability. Trans-Atlantic Geotraverse (TAG)-type vents arise if final discharge passes through highly permeable basaltic lavas at shallow depths in the hanging wall. (B) As early-formed gabbros move away from neo-volcanic zone, the flow moves down into the cooling foot-wall, resulting in the observed isotopic alteration in gabbro and intense talc–tremolite alteration in serpentinized peridotite. Discharge through the exposed ultramafic-rich footwall gives rise to vent fluids similar in composition to those of the Rainbow-type vents. (C) Far from the ridge axis, low-temperature circulation in the serpentinite leads to Lost City–type venting once the footwall peridotite has cooled by exposure on the seafloor. Figure courtesy of *McCaig et al*. [2007].

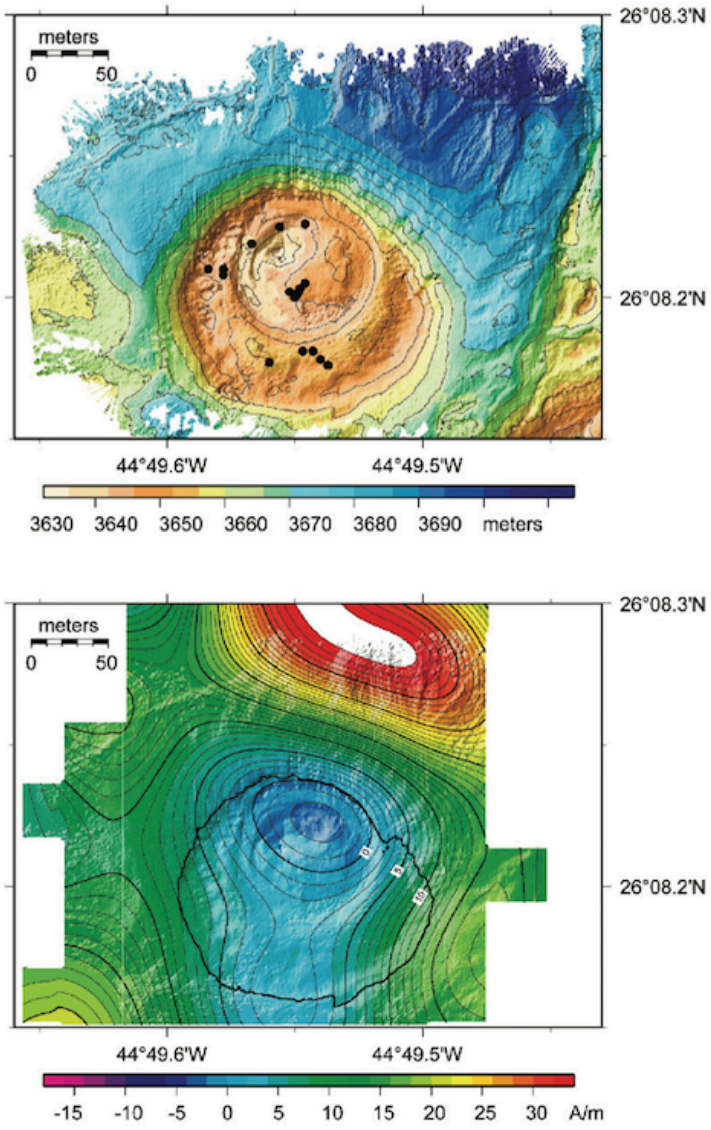

Figure 1-6. Detailed bathymetry and magnetization distribution over the Trans-Atlantic Geotraverse (TAG) hydrothermal mound on the Mid-Atlantic Ridge (MAR) [*Tivey and Dyment*, 2010].

(Top) High-resolution multibeam bathymetry of the TAG mound obtained by ROV *Jason* [*Roman and Singh*, 2007]. The contour interval is 5 m. (Bottom) High-resolution crustal magnetization from near-seafloor magnetic data collected by submersible *Alvin* over the TAG mound at an altitude of ~20 m showing reduced magnetization directly over the mound [*Tivey et al.*, 1993]. The contour interval is 1 A/m. The bold line is the 3645 m isobath delineating the mound extent. Figure courtesy of *Tivey and Dyment* [2010].

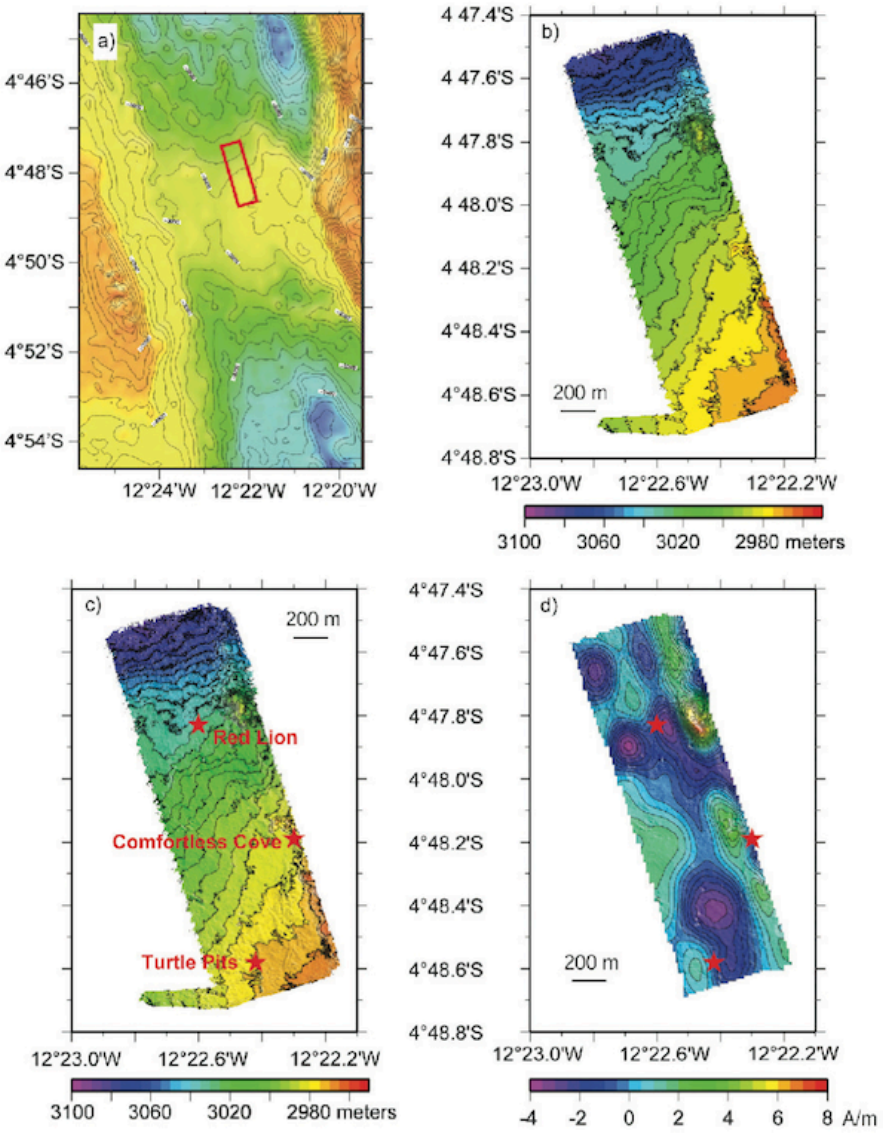

Figure 1-7. Detailed bathymetry and magnetization distribution over the hydrothermal sites of the 4°48′S region on the Mid-Atlantic Ridge (MAR) [*Tivey and Dyment*, 2010].

(a) Regional ship-based multibeam echo sounder bathymetry [*German et al*., 2008]. (b) High-resolution near-bottom multibeam bathymetry data from the *Autonomous Benthic Explorer* (*ABE*) multibeam. (c) High-resolution bathymetry with the locations and names of active vent sites represented by red stars. (d) Relative crustal magnetization showing zones of reduced magnetization associated with the active vent sites shown by red stars in (c). The data were collected along track lines spaced ~50 m apart at an altitude of ~50 m. Figure courtesy of *Tivey and Dyment* [2010].

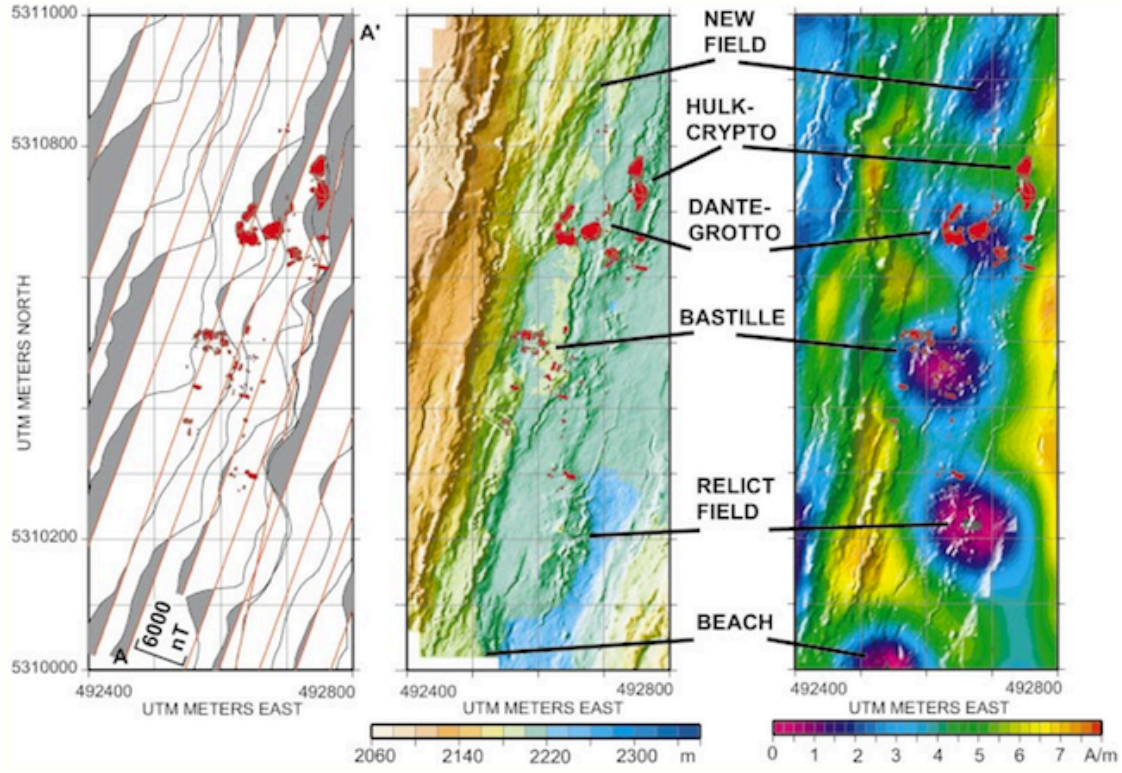

Figure 1-8. Detailed bathymetry and magnetization distribution over the hydrothermal sites of the 4°48′S region on the Mid-Atlantic Ridge (MAR) [*Tivey and Johnson*, 2002].

(Left) Observed magnetic anomalies along the ROV *Jason* track lines shown in red lines. Red areas are published locations of the Main Endeavour Field sulfide chimney edifices. (Middle) High-resolution near-bottom multibeam bathymetry. (Right) Crustal magnetizations showing correlation of circular magnetization lows with active and inactive vent areas. Data were collected along track lines spaced ~40 m apart at altitude of ~20 m. Figure courtesy of *Tivey and Johnson* [2002].

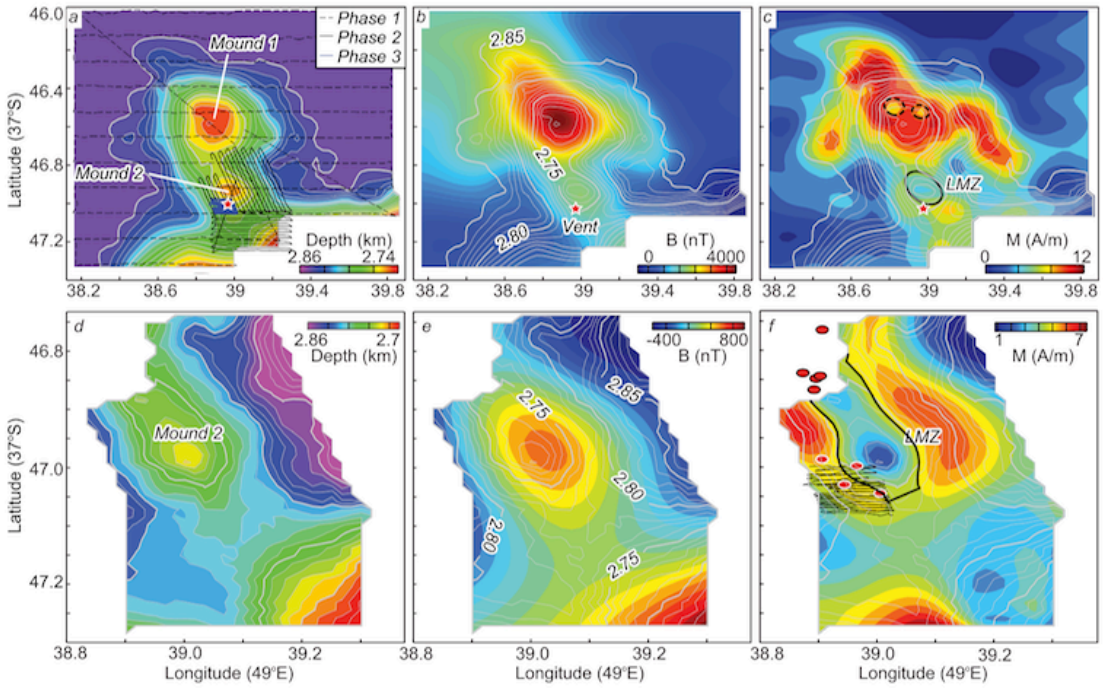

Figure 1-9. Detailed bathymetry and magnetization distribution over the hydrothermal sites of Southwestern Indian Ridge (SWIR) [*Zhu et al.*, 2010].

(a) Bathymetry collected during the *Autonomous Benthic Explorer* (*ABE*) Phase-1 survey. Gray contours delineate the seafloor depth with 10 m intervals. The track lines of *ABE* surveys Phase-1 (flying at a constant depth of 2625 m), Phase-2 (50 m above the seafloor with a track spacing of 30 m), and Phase-3 (5 m above the seafloor with a track spacing of 10 m) are shown by black dashed, black solid, and blue dashed lines, respectively. (b) Near-seafloor magnetic anomalies collected during the *ABE* Phase-1 survey. (c) Crustal magnetization from data collected during the *ABE* Phase-1 survey. The two sub-circular local topographic highs are labeled as Mound 1 and Mound 2. The red star indicates the location of the high-temperature hydrothermal vent field. The ellipses indicate three low magnetization zones (LMZs). (d) Bathymetry collected during the *ABE* Phase-2 and Phase-3 surveys. (e) Near-seafloor magnetic anomalies collected during the *ABE* Phase-2 and Phase-3 surveys. (f) Crustal magnetization from data collected during the *ABE* Phase-2 and Phase-3 surveys. The black ellipse indicates the area of the LMZ. Black solid lines show the track lines of the *ABE* Phase-3 survey, during which time the bottom photographs were obtained. Red dots represent the locations of active hydrothermal vents. Figure courtesy of *Zhu et al.* [2010].

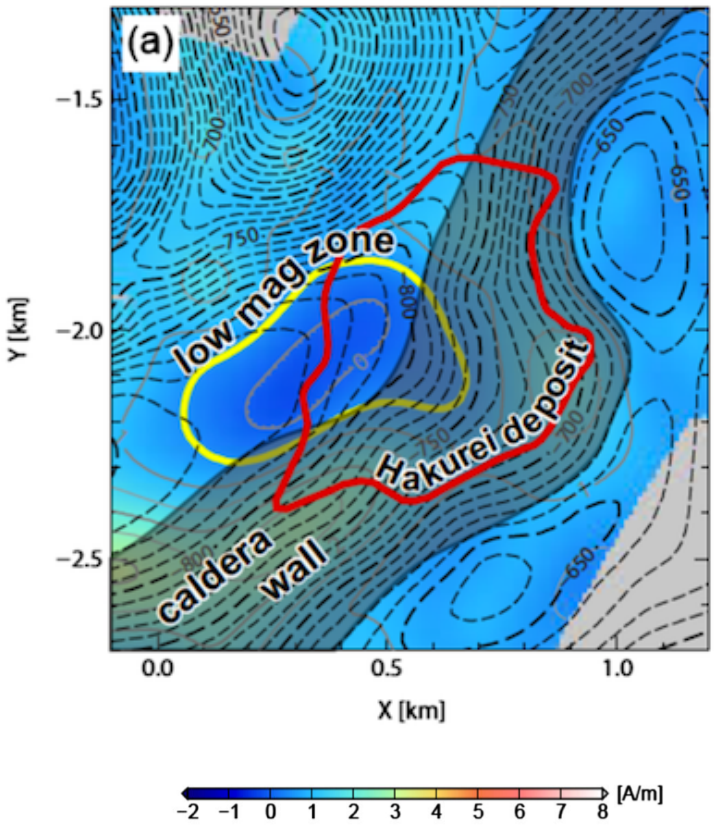

Figure 1-10. Detailed bathymetry and magnetization distribution over the Hakurei hydrothermal sites of Izu–Ogasawara arc–back-arc volcano [*Honsho et al*., 2013]. The magnetization map is shown by the color scale. The low magnetization zone (LMZ) is represented by an area of magnetization intensity lower than 0.5 A/m. The topographic contours (dashed lines) have an interval of 10 m. The data were collected along track lines at an altitude of ~80 m. The configuration of the Hakurei deposit is outlined by the red line [*Iizasa et al*., 2004]. The LMZ and the caldera wall fault are represented by a yellow line and by the shading, respectively. Figure courtesy of *Honsho et al.* [2013].

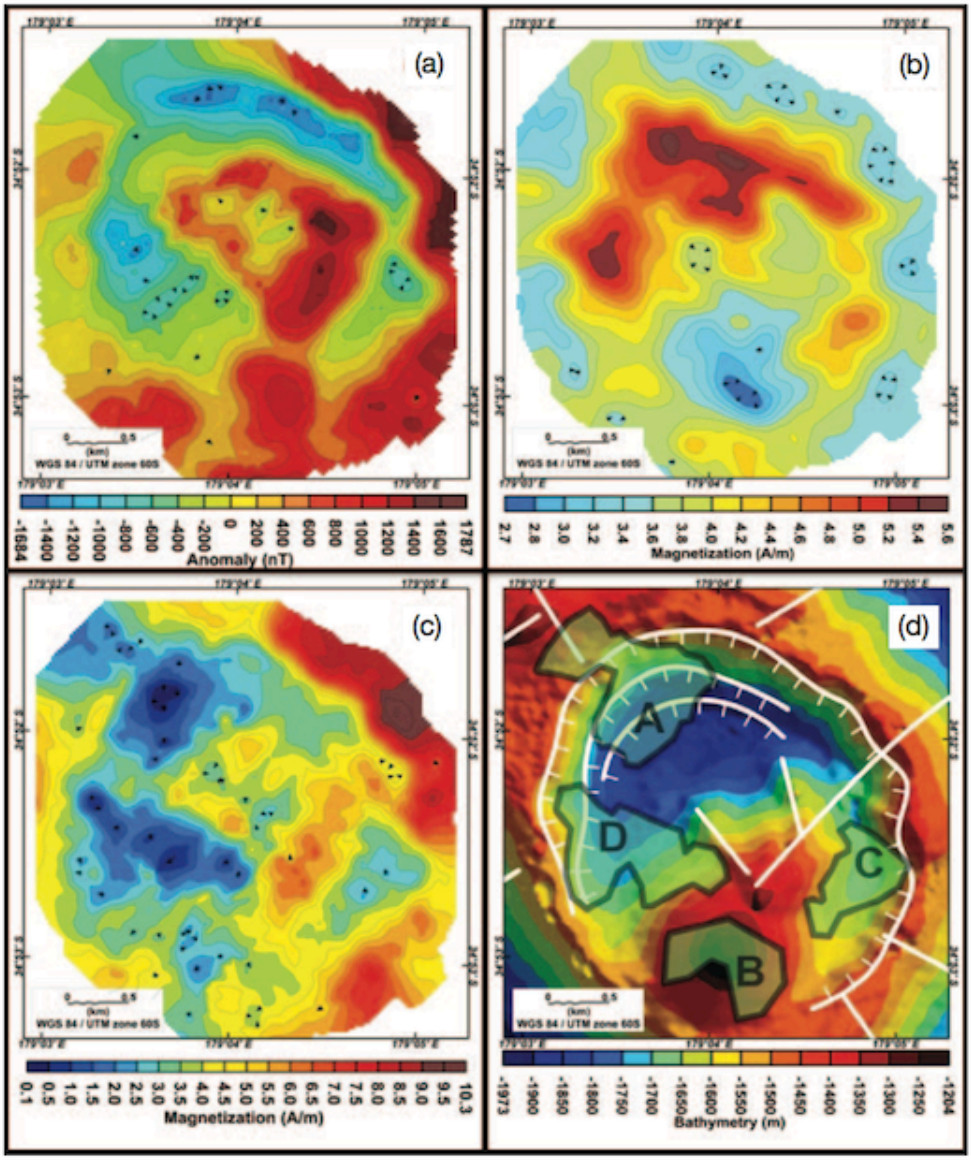

Figure 1-11. Detailed bathymetry and magnetization distribution over the hydrothermal sites of the Brothers volcano on the Tonga–Kermadec arc [*Caratori-Tontini et al*., 2012].

(a) Nears-seafloor magnetic anomaly map from data collected by the AUVs *Autonomous Benthic Explorer* (*ABE)* and *Sentry* at an altitude of ~50 m. (b) Annihilator map. (c) Crustal magnetization distribution from inversion of magnetic data determined after adding the annihilator. (d) Bathymetric map with the main faults, lineaments, and hydrothermal fields of the NW caldera wall site (A) and Brothers caldera at the cone site (B). Figure courtesy of *Caratori-Tontini et al*. [2012].

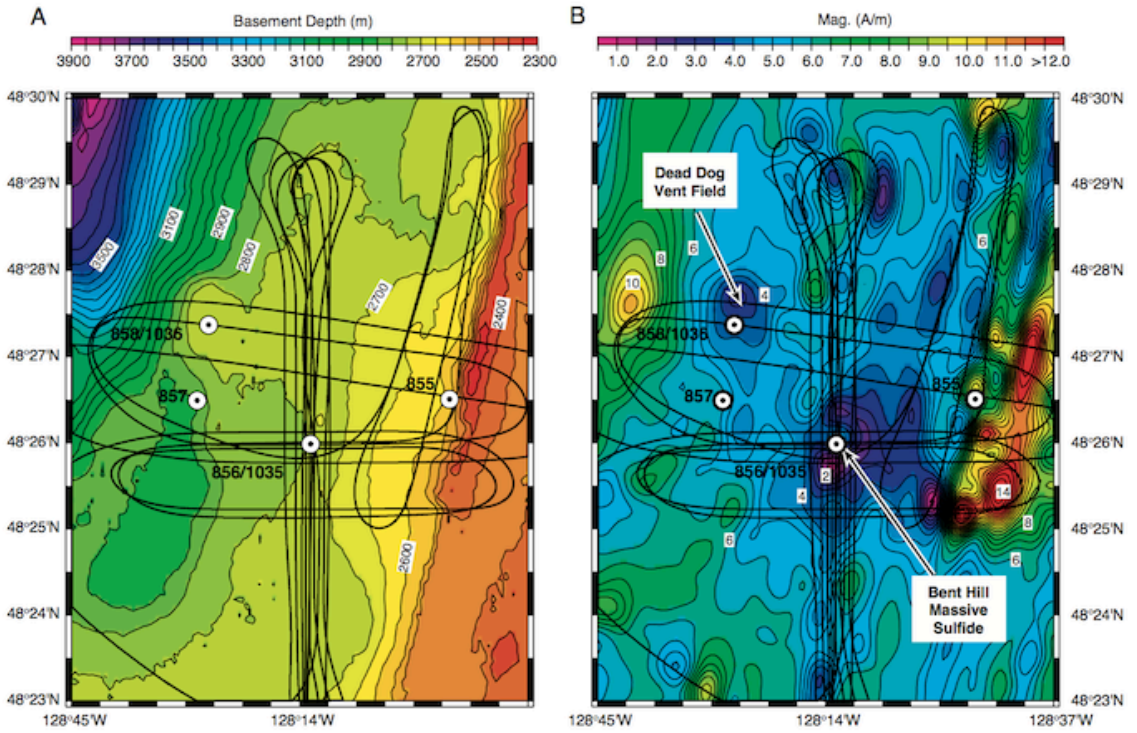

Figure 1-12. Detailed bathymetry and magnetization distribution over the Bent Hill Massive Sulfide of the Middle Valley on the Juan de Fuca Ridge (JFR) [*Gee et al*., 2001].

(a) Contour map of sediment-basement interface used for magnetic inversion. (b) Crustal magnetization distribution. Sufficient magnetic annihilator has been added to the solution to make the magnetizations positive. Locations of Ocean Drilling Program (ODP) drill sites (circles) and near bottom survey tracks are shown for reference. Figure courtesy of *Gee et al*. [2001].

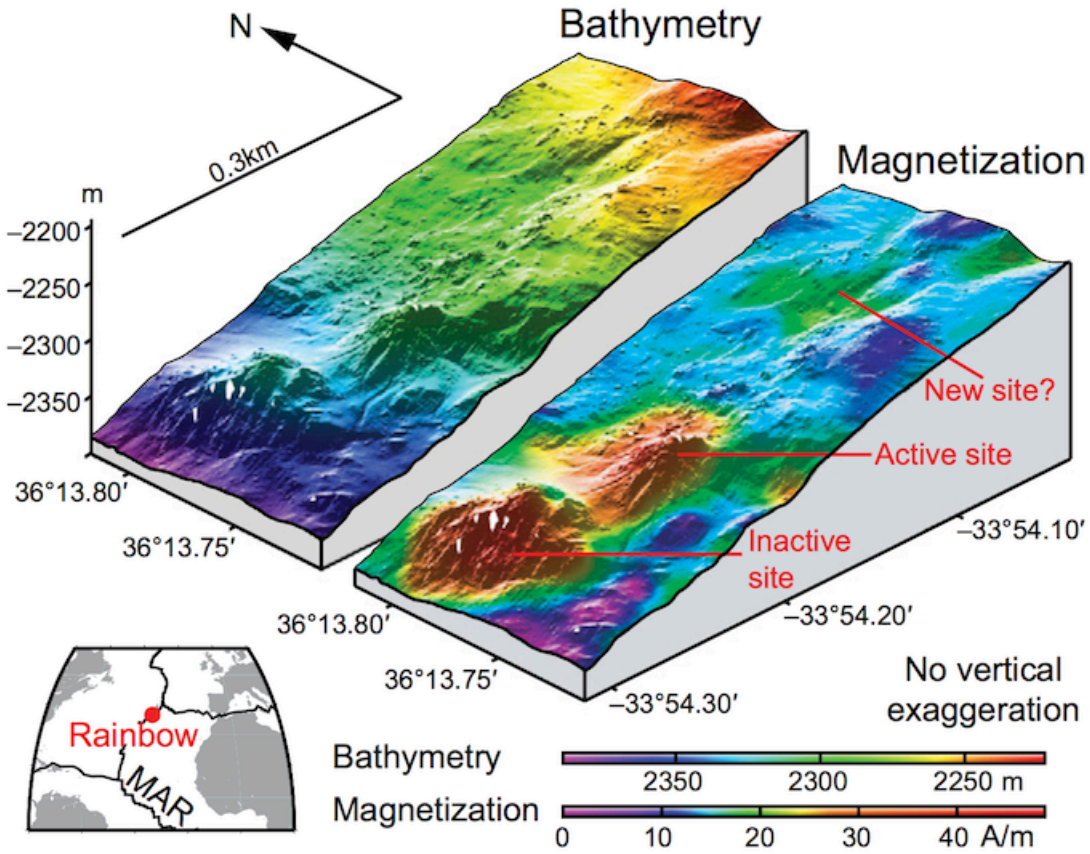

Figure 1-13. Detailed bathymetry and magnetization distribution over the ultramafic-hosted hydrothermal site Rainbow of the Mid-Atlantic Ridge (MAR) [*Szitkar et al*., 2014b].

(Left) High-resolution near-seafloor multibeam bathymetry in three-dimensional (3-D) view. The westernmost hydrothermal mound is cut by a fault on its western flank, resulting in stockwork mineralization outcrops and hydrothermal debris in the talus. (Right) Crustal magnetization draped on bathymetry in 3-D view. The strong positive magnetization contrast is associated with the two active hydrothermal mounds. The data were collected by the ROV *Victor* along track lines spaced ~10 m apart at an altitude of ~10 m. Figure courtesy of *Szitkar et al*. [2014b].

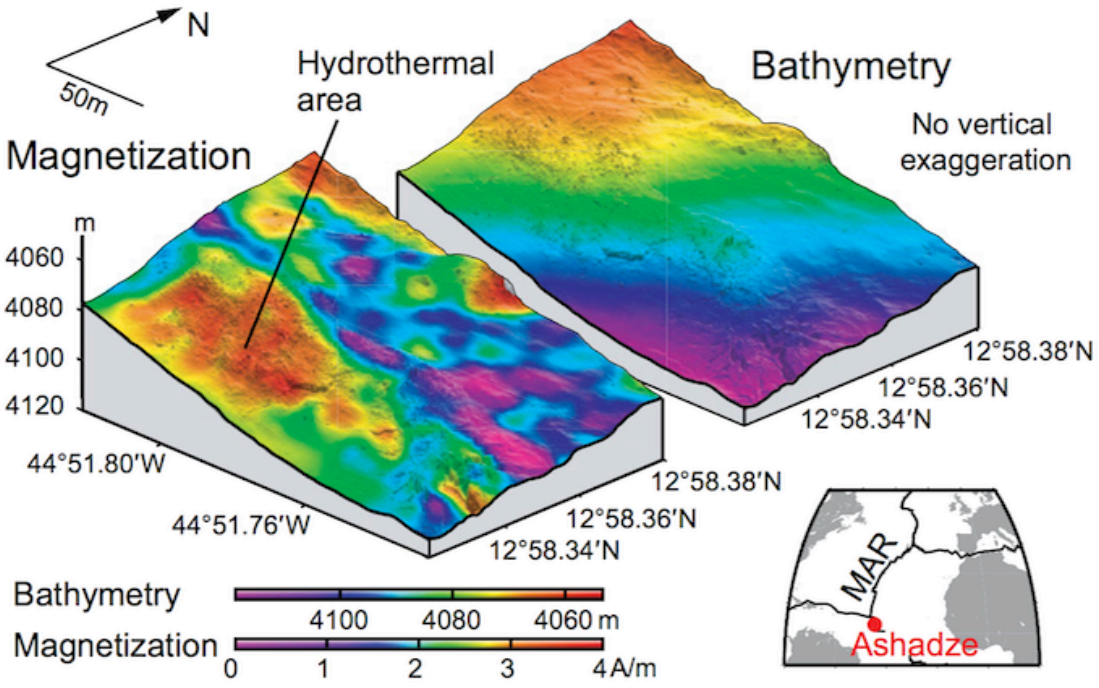

Figure 1-14. Detailed bathymetry and magnetization distribution over the ultramafic-hosted hydrothermal site Ashadze-1 of the Mid-Atlantic Ridge (MAR) [*Szitkar et al.*, 2014b].

(Right) High-resolution near-seafloor multibeam bathymetry in three-dimensional (3-D) view. (Left) Crustal magnetization draped on bathymetry in 3-D view. The strong positive magnetization contrast is associated with the active hydrothermal site. The data were collected by the ROV *Victor* along track lines spaced ~10 m apart at an altitude of ~10 m. Figure courtesy of *Szitkar et al*. [2014b].

Table 1-1. Summary of previous near-seafloor magnetic surveys in various tectonic setting.

Vent field	Active (A) Inactive (I)	Region	Tectonic setting	Terrain	Magnetization contrast	Reference
TAG	A	Mid-Atlantic Ride	Mid-ocean ridge	Basaltic	- 12 A/m	1, 2, 3
Krasnov	I	Mid-Atlantic Ride	Mid-ocean ridge	Basaltic	- 12 A/m	4
4°48′S area	A	Mid-Atlantic Ride	Mid-ocean ridge	Basaltic	- 3–4 A/m	2
Rainbow	A	Mid-Atlantic Ride	Mid-ocean ridge	Ultramafic	+ >30 A/m	2, 5, 6
Ashadze	A	Mid-Atlantic Ride	Mid-ocean ridge	Ultramafic	+ 4A/m	6
Main Endeavour	A	Juan de Fuca Ridge	Mid-ocean ridge	Basaltic	- 3 A/m	7, 8
Bent Hill Massive Sulfide	I	Juan de Fuca Ridge	Mid-ocean ridge	Sedimeted-basaltic	+ 5 A/m	9
Nameless	A	Southwest Indian Ridge	Mid-ocean ridge	Basaltic	- 3 A/m	10
Hakurei	A	Izu-Ogasawara arc	Back-arc rift	Andesitic to dacitic	- <1 A/m	11
Brothers	A	Kemdec arc	Arc volcano	Dacitic	- 3–4 A/m	12
Palinuro	A	Aeolian arc	Arc volcano	Basaltic	- <2 A/m	13, 14

1: *Tivey et al*., 1993, 2: *Tivey and Dyment*, 2010, 3: *Szitkar and Dyment*, 2014, 4: *Szitkar et al*., 2014a, 5: *Nakase*, 2002, 6: *Sztikar et al*., 2014b, 7: *Tivey and Johnson*, 2002, 8: *Tivey et al*., 2014, 9: *Gee et al*., 2001, 10: *Zhu et al*., 2010, 11: *Honsho et al*., 2013, 12: *Caratori-Tontini et al*., 2012, 13; *Caratori-Tontini et al*., 2014, 14; *Szitkar et al*., 2015.

Chapter 2

On- and Off-axis Hydrothermal Fields in Back-arc Region of Southern Mariana Trough

In this chapter, I present a detailed analysis of the high-resolution vector magnetic data acquired by the HOV *SHINKAI 6500* on five hydrothermal vent fields in the back-arc spreading axis (Snail and Yamanaka sites), off-axis foot (Archean site), and off-axis volcano (Pika and Urashima sites) areas of the southern Mariana Trough (SMT). A new 3-D forward scheme was applied to exploit the surrounding bathymetry and varying altitudes of the submersible for estimating the absolute crustal magnetization. The results reveal that magnetic-anomaly-derived absolute magnetizations (MADAMs) show reasonable correlation with the natural remanent magnetizations (NRMs) of the rock samples collected from the seafloor of same region. The distribution of MADAM suggests that all five andesite-hosted hydrothermal fields are associated with reduction of magnetization, as is generally observed at basalt-hosted hydrothermal sites. Furthermore, both the Pika and Urashima sites were found to have their own distinct low magnetization zones, which could not be distinguished in the magnetic anomaly data collected at higher altitudes by the AUV. The spatial extent of the resulting low magnetization is approximately ten times wider at off-axis sites than that at on-axis sites, possibly reflecting larger accumulations of nonmagnetic sulfides, stockwork zones, and alteration zones at the off-axis sites.

2-1. Geological Background

The southern Mariana Trough (SMT) is located along the convergent margin between the Pacific and Philippine Sea plates [e.g., *Stern et al*., 2003] (Fig. 2-1a). The subduction of the Pacific plate beneath the Philippine Sea plate began in early Eocene (~50 Ma) [e.g., *Seno and Maruyama*, 1984]. From ~30 Ma to ~20 Ma, the proto-Mariana arc rifted, forming the Parece Vela back-arc basin [*Okino et al*., 1999]. Seafloor extension has focused on the eastern side of the Philippine Sea plate for the last 6 Ma, resulting in the development of the Mariana Trough [*Hussong and Uyeda*, 1982]. Seafloor spreading started in the central part of the trough, which was followed by propagation to both the northern and southern areas [*Martinez et al*., 2000; *Yamazaki et al*., 2003], forming a crescent-shaped basin ~200-km wide at its central point. The spreading axis is now located on the eastern side of the basin, indicating highly asymmetric spreading [*Deschamps and Fujiwara*, 2003; *Asada et al*., 2007].

In the southernmost part of the SMT, the general trend of the arc-trench system changes from N–S to E–W. South of 14°N, seafloor spreading began 3 Ma, with a half rate of 33 km/Myr for the west side and 13 km/Myr for the east side [*Seama et al*., 2015]. The seafloor morphology of axial high features is characteristic of fast and/or strongly magmatic spreading context. The distance between the spreading axis and the active Mariana arc volcanic front is ~20 km, suggesting a complex magmatic environment influenced by back-arc and arc-type magmas [*Martinez et al*., 2000]. Analyses of sea-surface gravity data have revealed a thick crust (5800–6800 m on average) in the SMT, which is in agreement with vigorous magmatic activity with sheet-like mantle upwelling under the spreading axis [*Kitada et al*., 2006].

Five active hydrothermal vent fields have been discovered in the SMT between 12°55’N and 12°57’N (Fig. 2-1b) [*Wheat et al*., 2003; *Ishibashi et al*., 2004; *Urabe et al*., 2004; *Kakegawa et al*., 2008; *Nakamura et al*., 2013]. These fields are aligned perpendicularly to, and within ~5 km from, the spreading axis. The Snail and Yamanaka sites are located on the axial area, where undeformed volcanic structures have been reported based on high-resolution bathymetric surveys, which have been interpreted as the current neo-volcanic zone (NVZ) [*Yoshikawa et al*., 2012]. At the Snail site that displays both active and dead chimneys, and is surrounded by fresh pillow basalt, the maximum temperature of venting fluid was 248°C at the time of discovery in May 2003

[*Wheat et al*., 2003]. The Yamanaka site is located on a volcanic edifice 1.2 km southwest of the Snail site. It consists of white smokers, dead sulfide chimneys, and altered pillow lavas [*Kakegawa et al*., 2008].

The Archean site is located at the eastern foot of the axial high, where active black smokers have been observed on the top of a 50-m-high mound made of pyrite, chalcopyrite, and sphalerite [*Urabe et al*., 2004]. The highest recorded fluid temperatures were 213°C in 2004 and 341°C in 2005 [*Ishibashi et al*., 2004, YK05-09 cruise report].

The Pika and Urashima sites lie on a 400-m-high off-axis seamount ~5 km from the spreading axis. The Pika site is located on the top of a seamount and consists of black smokers, white smokers, dead chimneys, and sulfide mounds. The Urashima site was discovered in 2010 at the northern foot of the seamount 500 m from the Pika site and it comprises large black smokers (>10 m) and dead chimneys [*Nakamura et al*., 2013]. The highest recorded fluid temperatures at the Pika and Urashima sites are 330°C and 280°C, respectively [*Urabe et al*., 2004, *Nakamura et al*., 2013].

2-2. Data and Methods

2-2-1. Data acquisition

Near-seafloor exploration surveys were conducted around the five hydrothermal vent fields of the SMT using the HOV *SHINKAI 6500* of the Japan Agency for Marine-Earth Science and Technology (JAMSTEC) during two scientific cruises of the *R/V Yokosuka*. Five dives were conducted during the YK10-10 cruise in August 2010 and other nine dives during the YK10-11 cruise in September 2010. Four dives (#1218, #1220, #1227, and #1228) were devoted to the axial area, including the Snail and Yamanaka sites, five dives (#1216, #1217, #1221, #1223, and #1224) to the off-axis area around the Archean site, and five dives (#1214, #1219, #1222, #1225, and #1226) to the off-axis seamount on which the Pika and Urashima sites are located. All fourteen dives were navigated by acoustic ranging using the super-short baseline positioning system. Magnetic data were generally collected at altitude lower than 15 m, but occasionally, at altitudes of several tens of meters.

A three-component fluxgate magnetometer, developed by the Atmosphere and Ocean Research Institute of the University of Tokyo, was rigidly fixed to the front side

of *SHINKAI 6500*. Both vector magnetic data and the attitude of the submersible (heading, pitch, and roll) from a gyrocompass and a motion sensor (OCTANS, IXBLUE Inc.) were collected at a 10-Hz sampling rate. The accuracy of the magnetometer is 0.4 nT.

The surface geology along the dive tracks was constrained by examining video and still camera records for each dive. In some limited areas, no visual observation of the surface geology was obtained because of the higher altitude of the submersible. I classified the geological features into five categories: (i) fresh lava, (ii) fractured lava, (iii) sediment-covered lava, (iv) debris and breccia, (v) and hydrothermal material. The hydrothermal areas were characterized by sulfide deposits, chimneys, pluming hot water, white bacteria mats, and biological habitats.

2-2-2. Initial processing

Because the magnetometer was mounted on the submersible, magnetic data were strongly affected by the magnetization of the vehicle. The observed magnetic field vector ($\vec{H}_{obs}$) is expressed as the sum of induced ($\mathbf{AR}\vec{F}$) and permanent ($\vec{H}$) magnetic fields of the vehicle and the ambient geomagnetic field ($\vec{F}$) as following [*Isezaki*, 1986];

$$\begin{aligned}\vec{H}_{obs} &= \mathbf{R}\vec{F} + \mathbf{AR}\vec{F} + \vec{H}_p \\ &= (\mathbf{A} + \mathbf{E})\mathbf{R}\vec{F} + \vec{H}_p\end{aligned}$$

where,

$$\mathbf{R} \equiv \mathbf{r}(\theta_2)\mathbf{p}(\theta_3)\mathbf{h}(\theta_1)$$

$$\equiv \begin{pmatrix} 1 & 0 & 0 \\ 0 & \cos(\theta_2) & \sin(\theta_2) \\ 0 & -\sin(\theta_2) & \cos(\theta_2) \end{pmatrix} \begin{pmatrix} \cos(\theta_3) & 0 & -\sin(\theta_3) \\ 0 & 1 & 0 \\ \sin(\theta_3) & 0 & \cos(\theta_3) \end{pmatrix} \begin{pmatrix} \cos(\theta_1) & \sin(\theta_1) & 0 \\ -\sin(\theta_1) & \cos(\theta_1) & 0 \\ 0 & 0 & 1 \end{pmatrix}.$$

I used data collected during 360° rotations performed spontaneously by the submersible during its descent to estimate both the induced magnetization vector of the vehicle, expressed by the magnetic susceptibility tensor **A** (nine coefficients) and remanent magnetization vector $\vec{H}_p$ (three coefficients) of the vehicle using a dumped least square method developed by *Honsho et al*. [2009]. Parts of the data obtained at depths

shallower than 500 m below sea surface or deeper than 500 m above the seafloor were not used in order to avoid the magnetic effects of the ship and the seafloor. The coefficients were estimated individually for each dive. For example, I obtained the following coefficients of dive#1223 using a dumping factor of 7,

$$\mathbf{A} = \begin{pmatrix} 0.03618 & 0.03499 & 0.00155 \\ -0.03769 & 0.01583 & 0.00051 \\ -0.06182 & 0.00616 & 0.00021 \end{pmatrix},\ \vec{\mathrm{H}}_{\mathrm{p}} = \begin{pmatrix} -274 \\ -1928 \\ 441 \end{pmatrix} \text{ and } \sigma = \begin{pmatrix} 47 \\ 47 \\ 34 \end{pmatrix}.$$

The quantity σ is model error of observation equation. Based on these coefficients, the attitude of the submersible, and the regional geomagnetic field (approximated by the International Geomagnetic Reference Field, IGRF [*IAGA Working Group V-MOD*, 2010]), I computed the magnetic effects of the submersible during the survey and removed them from the data. The correction was performed for each dive and the resulting vector magnetic field was rotated to the geographical coordinates, giving the model error σ in the ranges 47–200, 47–175, and 29–68 nT in the northern, eastern, and downward components, respectively.

The subsequent three-dimensional analysis required both the position of the magnetometer and the seafloor topography. The super-short baseline position was smoothed and resampled at intervals of 1 sec using a Gaussian function filter after removing outliers. The altitude data were collected every 1 sec with 1-m resolution and the distance between the altimeter and magnetic sensor was taken into account to obtain the geometry of the experiment. The seafloor topography was extracted from the 2-m-interval grid built from data collected by the AUV *Urashima* using a 400-kHz multibeam echo sounder (SeaBat 7125 AUV, Reson Inc., Denmark) during the YK09-09 cruise [*Yoshikawa et al.*, 2012]. Additional sea-surface bathymetric data (50-m-interval grid) were compiled for areas not surveyed by the AUV *Urashima*.

2-2-3. Forward modeling

The three components of the synthetic magnetic anomaly along the dive tracks, at the same locations as the observed data, were simulated assuming uniform magnetization of the seafloor, with direction parallel to the geocentric axial dipole field (inclination: 24°, declination: 0°) and intensity of 1 A/m (Fig. 2-2). There was not much difference between the results based on assumption of magnetization direction parallel to the geocentric axial dipole and the IGRF (inclination: 11°, declination: 1°). A

half-infinite magnetic source was considered, the upper boundary of which was constrained by the bathymetry. The magnetic source was modeled by a collection of half-infinite rectangular prisms with lateral dimensions of 2 m. Magnetic anomalies at each calculation point were obtained by applying the algorithm of *Bhattacharyya* [1964], which provides the magnetic anomaly produced by uniformly magnetized prisms, via the summing up of the contributions of all prisms located within 100 m from the point. Each prism is oriented parallel to the northern, eastern, and downward axes, and has magnetization **M** (M_N, M_E, M_Z). Dimensions are given by $n2 \leqq n' \leqq n1$, $e1 \leqq e' \leqq e2$, and $z_1 \leqq z \leqq \infty$. If the anomaly due to the prism is observed in a regional field directed parallel to **F** (F_N, F_E, F_Z), the three components of anomalous field (northern: ΔN, eastern: ΔE, downward: ΔZ) at the origin is given by

$$\Delta N = C_m F_N \left[-M_N \arctan\left(\frac{n'e'}{n'^2 + rz_1 + {z_1}^2}\right) - M_E \log(r + z_1) + \frac{M_Z}{2} \log\left(\frac{r - e'}{r + e'}\right) \right] \Bigg|_{n1}^{n2} \Bigg|_{e1}^{e2}$$

$$\Delta E = C_m F_E \left[-M_N \log(r + z_1) - M_E \arctan\left(\frac{n'e'}{r^2 + rz_1 - x'^2}\right) + \frac{M_Z}{2} \log\left(\frac{r - n'}{r + n'}\right) \right] \Bigg|_{n1}^{n2} \Bigg|_{e1}^{e2}$$

$$\Delta Z = C_m F_Z \left[-\frac{M_N}{2} \log\left(\frac{r - e'}{r + e'}\right) + \frac{M_E}{2} \log\left(\frac{r - n'}{r + n'}\right) + M_Z \arctan\left(\frac{n'e'}{rz_1}\right) \right] \Bigg|_{n1}^{n2} \Bigg|_{e1}^{e2}$$

where

$$r = n'^2 + e'^2 + {z_1}^2,$$

and C_m is magnetic permeability of free space in SI unit. This equation provide magnetic anomaly of a prism with top at z_1 and bottom at infinity [*Bhattacharyya,* 1964]. If magnetic anomaly is calculated twice, once for $z_1 = z_t$ and $M = M_0$, and once for $z_1 = z_b$ and $M = -M_0$, then according to superposition principle, the sum of the two

calculations provide the magnetic field of a prism with magnetization M_0, top at z_t and bottom at z_b.

Figure 2-3 shows synthetic total magnetic anomaly profiles computed for magnetic source layers of various thicknesses. Although I adopted a half-infinite source, these models show that the synthetic magnetic anomalies at altitudes lower than 40 m are not significantly affected by magnetic sources deeper than 200 m.

Figure 2-4 shows a comparison between observed and synthetic magnetic anomalies along dive #1227. The three components of the synthetic anomaly show similarities with those of the observed anomaly, except for the scale that reflects the low (1 A/m) intensity of magnetization assumed for the modeling.

2-2-4. Estimation of absolute magnetization

The ratio of the observed magnetic anomaly to the synthetic anomaly, computed with unit magnetization intensity, represents an estimate of the absolute magnetization intensity of the shallow sub-seafloor. In order to estimate this ratio quantitatively, I used the linear transfer function technique in the frequency domain [*Honsho et al*., 2009]. This approach has been originally used in gravity studies to estimate a ratio of gravity to elevation as a function of wave number [*McKenzie and Bowin*, 1976; *Watts*, 1978].

Both observed and synthetic anomalies were resampled at every 1-m interval along the dive tracks. The magnetization was estimated for each 128-m-wide sliding window shifted by steps of 16 m along the tracks. The coherency, ratio of the observed to synthetic anomalies together with its error, and polarity (given by the phase difference between the two signals) were obtained over wavelengths between 16 and 128 m. This procedure was applied to each component of the anomaly. I retained estimations with a coherency greater than 0.3 on at least two components for further interpretation. The ratios of observed to synthetic northern and downward components were finally averaged and adopted as best estimate of absolute magnetization intensity of the shallow sub-seafloor. This was done for two reasons: (ii) the eastern component is nearly perpendicular to the IGRF direction in the survey area, i.e. it is more susceptible to correction errors mainly affected by heading error, resulting in a lower S/N ratio; and (ii) the absolute magnetization computed from this component tends to be extremely large, because the synthetic magnetic anomaly is small due to the assumption that the

magnetization direction is parallel to the axial dipole field. The magnetization polarity was regarded as normal for phases between -90° and 90° and reversed for phases between 90° and 270°.

2-3. Results

2-3-1. MADAM and seafloor geology

The four dives in the axial area including the Snail and Yamanaka sites provided 312 reliable estimates of magnetic-anomaly-derived absolute magnetization (MADAM) ranging from 1–116 A/m (Fig. 2-5a). The 55 estimates among them shows coherency higher than 0.5 in both northern and downward components. Thirty-two percent of the data indicate high magnetization stronger than 30 A/m, whereas 19% are associated with magnetizations weaker than 10 A/m. Extremely high intensities (>70 A/m) are observed in the NVZ, north of the Snail site, south of the Yamanaka site, and in the central volcanic mound (12°56’52”N, 143°36’57”E). Relatively low intensities (<10 A/m) are observed around the Snail site and in an area ~200–500 m from the NVZ, where many faults trending NNE–SSW to NE–SW extend parallel to the NVZ.

The video records in this area show fresh lavas, fractured lavas, and hydrothermal material. Sulfide deposits, biological communities, and chimneys were observed near the Snail site (Figs. 2-5b and 2-5c), and fresh pillow lavas seen around the Snail hydrothermal area (Figs. 2-5b and 2-5d). At the Yamanaka site, sea anemones are growing within the weak fluid venting (Figs. 2-5b and 2-5e) on top of fresh pillow lavas (Figs. 2-5b and 2-5e): lavas on the western slope of the axial high are fractured and appear to be older (Figs. 2-5b and 2-5g).

The five dives in the off-axis area including the Archean site provided 204 reliable estimates of MADAM ranging from 0.4–29 A/m (Fig. 2-6a). The 22 estimates among them shows coherency higher than 0.5 in both northern and downward components. More than 85% show intensities weaker than 10 A/m. At the top of the mound, the magnetization is generally weaker than 3 A/m, whereas stronger magnetizations (>10 A/m) are found outside the mound.

In this off-axis area, video records show debris and breccia, sediment-covered lavas, and hydrothermal material. Active and dead chimneys and sulfide deposits were observed at the top of the mound (Figs. 2-6b and 2-6c), and debris and breccia

distributed widely on the slopes of the mound (Figs. 2-6b and 2-6d). The relatively flat seafloor around the mound was covered mostly by pillow lavas with sediment (Figs. 2-6b and 2-6e).

The five dives in the area of the off-axis seamount including the Pika and Urashima sites provided 250 estimates of MADAM ranging from 0.6–61 A/m (Fig. 2-7a). The 28 estimates among them shows coherency higher than 0.5 in both northern and downward components. Sixty-six percent indicate magnetization weaker than 10 A/m, and 12% stronger than 20 A/m. The magnetization is weak (<5 A/m) on the top of the seamount where the Pika site is situated. Relatively high magnetization (<17 A/m) is indicated on the northern slope of the seamount between the Pika and Urashima sites. At the northern foot of the seamount, low magnetization values (<5 A/m) are concentrated around the Urashima site. This low magnetization concentration is surrounded by an area of high magnetization larger than 10 A/m, including several very high magnetization points (~60 A/m) near the northeastern edge of the survey area. The magnetization is also very high (~54 A/m) on the southwestern side of the seamount where small conical mounds are observed.

The video records show fresh lavas, sediment-covered lavas, debris and breccia, and hydrothermal material in the area of the off-axis seamounts. Sulfide sediments and both active and dead chimneys were seen near the Pika site (Figs. 2-7b and 2-7c). Dead chimneys were scattered within a few 100 m of the top of the seamount. Sediment-covered lavas were distributed just south of the Pika site (Figs. 2-7b and 2-7d), and Active chimneys, many dead chimneys, and sulfide deposits were observed at the Urashima site (Figs. 2-7b and 2-7e). Sediment-covered lavas were distributed widely outside the hydrothermal areas (Figs. 2-7b and 2-7f), and debris and breccia observed on the slope between the Pika and Urashima sites (Figs. 2-7b, 2-7g, and 2-7h). An extensive area of fresh pillow lavas was discovered on the southwestern side of the seamount (Figs. 2-7b, 2-7i, and 2-7j).

The five investigated hydrothermal fields in the SMT (Fig. 2-1b) are clearly associated with a low MADAM: essentially, the three off-axis sites appear almost non magnetic. Only the Yamanaka site is not associated with a clear zone of weak magnetization, but the estimated MADAM values are relatively lower (27–46 A/m) than those of the nearby volcanic mound (~116 A/m) (Figs. 2-5a and 2-5b).

While the hydrothermal areas are characterized by weak magnetization, the areas

covered by lavas often display strong magnetization (with one exception, discussed below). Extremely high magnetizations are associated with fresh pillow lavas along the NVZ, outside the Snail and Yamanaka sites (Figs. 2-5a and 2-5b) and on the southwestern part of the off-axis seamount (Figs. 2-7a and 2-7b). The areas of fractured lavas in the axial zone also exhibit relatively strong magnetization (>10 A/m) (Figs. 2-5a and 2-5b). In addition, the MADAM values in the area of sediment-covered lavas near the Archean mound and Urashima are relatively high (>10 A/m) (Figs. 2-6a and 2-6b, and 2-7a and 2-7b). A notable exception is the western topographic high in the spreading center (12°56'52"N, 143°36'57"E), which is surrounded by an area of low magnetization (Figs. 2-5a and 2-5b). In this area, fractured lavas are widespread (Fig. 2-5b) and numerous regional normal faults resulting from tectonic deformation are observed [*Yoshikawa et al*., 2012]. Thus, it would be expected that many fissures enable seawater to permeate the lavas and sub-seafloor crust, promoting low-temperature alteration of the volcanic layer, and therefore reducing crustal magnetization.

2-3-2. Evaluation of MADAM by comparison with rock NRM

Several methods have been developed to invert magnetic anomalies into equivalent magnetization [e.g., *Parker and Huestis*, 1974]. Because of the intrinsic non-uniqueness of the potential field problem, an infinite number of solutions exist: an annihilator, i.e. a distribution of magnetization that produces no anomaly in the geometry of the experiment, can be determined and added in any amount to a given solution to produce an infinity of other solutions. On the other hand, my forward scheme provides estimates of absolute magnetization of the shallow sub-seafloor (MADAM), which can be directly compared with the magnetization borne by rock samples, i.e., the natural remanent magnetization (NRM) of lavas. The thickness of effective source is generally up to 30 m for my experiment design, in which data were mostly acquired at an altitude of ~10 m (Fig. 2-3). NRM measurements were reported by *Mochizuki et al*. [2012] on samples from the study area: 19 volcanic rocks collected during nine *SHINKAI* 6500 dives in various places and seven seafloor cores obtained using benthic multi-cores. One-inch specimens were drilled from the rock and core samples in the laboratory. NRMs of the specimens were measured using a spinner magnetometer (Natsuhara Giken) at Kumamoto University. NRM measurements were performed on specimens of 11

samples from the axial area, 7 samples from the off-axis area, and 8 samples from the off-axis seamount area. For the sake of comparison, we averaged 2 to 39 MADAM values around each rock sampling location within a 50-m radius (100-m radius for five sampling locations), and the averages were compared with the NRM values (Fig. 2-8). It can be seen that the MADAM determinations are generally consistent with the NRM values.

It is observed that NRM of rock samples tend to be larger for higher values (>10 A/m) than MADAM and smaller for lower values. The former signature is explained by the grain-size distribution of lava flows. The NRM measured on rock samples reflects the magnetization of lava flows, whereas MADAM characterizes the sources located within the shallow sub-seafloor. Due to the quick cooling, magnetic grain size is smaller in lava outcrops than in the sub-seafloor, and its NRM is stronger [e.g. *Marshal and Cox* 1971; *Kent and Gee*, 1996], suggesting high values of NRM on samples collected from the lava surface. The latter signature might be affected by the degree of low-temperature oxidation of titanomagnetite. A wide range of magnetization intensity is observed for the results of both MADAM and NRM of the rocks samples, from just a few to several tens of A/m. This is primarily due to low-temperature oxidation, which causes an exponential reduction of NRM of lava flows with age [e.g. *Irving*, 1970; *Johnson and Atwater*, 1977; *Gee and Kent*, 1994; *Zhou et al*., 2001]. This process must be faster on the surface than in the interior of the lavas, resulting in weaker NRM than MADAM of the rock samples when both values are low (<10 A/m).

The maximum value of MADAM in the axial area is extremely high compared to the values from previous study of magnetic anomaly [*Honsho et al*., 2009] and rock samples [e.g. *Gee and Kent*, 1994; *Zhou et al*., 2001]. However, I adopted all MADAM estimations, up to 116 A/m for interpretation, based on following two reasons, (i) the reliability of MADAM estimations is confirmed by comparison with rock NRM values collected at very close places as mentioned above (Fig. 2-8), and (ii) rock NRM values in the axial area are also extremely high (>100 A/m in 1 site and 70–90 A/m in 4 sites). Moreover, 12 specimens of rock samples show NRM values higher than 100 A/m.

2-3-3. Comparison of MADAM with AUV equivalent magnetization

A distribution of equivalent magnetization (EM) was computed using magnetic

anomaly data collected by the AUV Urashima in 2009 during YK09-08 [*Nogi et al*., 2011]. The EM was estimated by a spectral inversion method [*Parker and Huestis*, 1974; *Macdonald et al*., 1980] using the vertical component of the anomaly, assuming a thickness of 250 m for the magnetized layer and a magnetization direction parallel to the axial dipole field [*Nogi et al*., 2011; *Nakamura et al*., 2013]. Because the AUV survey was conducted at an altitude of ~100 m above the seafloor, the EM from the AUV data likely reflects the wider and deeper crustal structures than the MADAM estimates from my HOV study. The MADAM distribution is generally consistent with the large-scale structures depicted by the EM in all the surveyed areas (Fig. 2-9).

In the axial area, both the EM and MADAM values are highest along the NVZ, especially in the central volcanic mound (12°56’52”N, 143°36’57”E), and on the southern volcanic edifice where fresh lavas are observed (Fig. 2-9a). A zone of high EM is aligned NE–SW, consistent with the distribution of high MADAM on crossing dive tracks, suggesting recent lava flows. Far from the NVZ, both MADAM and EM are lower, especially near the western topographic high in the fault zone (Fig. 2-9a). Next to the Snail site, relatively low values of both EM and MADAM align along a NNE–SSW trend.

While the lowest values of both EM and MADAM are recognized on the top of the Archean mound, higher values are consistently distributed around the mound (Fig. 2-9b). In particular, the highest values of both EM and MADAM are located on the western and southwestern sides of the mound, suggesting that younger lava flows erupted on the surrounding older and rugged seafloor [*Yoshikawa et al*., 2012].

In the off-axis seamount area, high values of EM are located on its northeastern and western flanks, consistent with the MADAM distribution (Fig. 2-9c). In contrast, low values of both MADAM and EM are located on the Pika and Urashima sites. Moreover, according to the EM map, these sites appear located within a continuous low-magnetization zone, whereas they can be distinguished as two separate lows on the MADAM results. This observation confirms that near-seafloor magnetic measurements using HOVs help to characterize small-scale features that would remain undetected with AUV surveys.

2-4. Discussion

2-4-1. Processes causing the weak magnetization zones

All five back-arc hydrothermal sites investigated in the SMT are clearly associated with low crustal magnetization (Figs. 2-5, 2-6, and 2-7). The followings could be a cause for magnetization reduction: (i) thermal demagnetization, where hot fluid heats the surrounding lava above the Curie temperature of its magnetic minerals [*Wooldridge et al*., 1992]; (ii) hydrothermal alteration, in which volcanogenic magnetic minerals, such as titanomagnetite, are replaced by non-magnetic minerals within the up-flow zone [*Johnson et al*., 1982; Hall, 1992]; and/or (iii) the presence of non-magnetic hydrothermal deposits [*Szitkar et al*., 2014a]. In the off-axis area, inactive hydrothermal areas also exhibit reduced magnetizations (Figs. 2-6 and 2-7), confirming that the alteration of the magnetic minerals and/or the presence of non-magnetic hydrothermal deposits rather than thermal demagnetization are the major processes leading to the reduced magnetization. The narrow zones of low magnetization are centered on vent areas, moreover low magnetization zones are confirmed in both HOV (~10 m altitude) and AUV (~100 m altitude) results, indicating the presence of low magnetization source at depths from near-seafloor to hundreds of meters. The modeling study of the magnetization zone in the TAG hydrothermal site proposed a pipe-like source body with a radius of 100 m [*Tivey et al*., 1993; *Tivey and Dyment*, 2010; *Szitkar and Dyment*, 2015]. The horizontal extent of this narrow pipe-like body is comparable to my investigated sites and also to the stockwork zones found in volcanogenic massive sulfide deposits such as the Cyprus ophiolite [e.g. *Johnson et al*., 1982]. These observations potentially suggest that the zones of reduced or null magnetization of hydrothermal sites in SMT are either up-flow zones of hydrothermal fluid beneath separate vent systems in the uppermost crust, or accumulations of sulfide deposits associated with each vent system.

2-4-2. Duration of hydrothermal activity and size of magnetic low

In the SMT, I observe that the spatial extent of the low magnetization zone differs depending on the on- or off-axis location of the sites (Fig. 2-10). Low magnetization zones at the on-axis sites of Snail and Yamanaka are ~30 m in diameter, whereas they are ~120 m at the off-axis sites of Archean, Pika, and Urashima. This difference is

probably a consequence of a longer duration of hydrothermal activity.

Both the Snail and Yamanaka sites are located in the NVZ. Gravity data suggest a relatively thick crust (~6.8 km) in the 12.7–13.5°N segment, i.e., a stronger magmatic activity with sheet-like mantle upwelling [*Kitada et al*., 2006]. Moreover, a seismic refraction study reveals that the upwelling zone is characterized by low seismic velocity 1.5 km below the seafloor, beneath the axial area in this region [*Sato et al*., 2015b]. A magma chamber was detected 15 km northeast along the spreading axis at ~3-km depth during a reflection seismic study [*Becker et al*., 2010]. Therefore, the heat source for the Snail and Yamanaka hydrothermal activity is probably episodic dike intrusion at the spreading axis, similar to the fast-spreading East Pacific Rise hydrothermal systems, where vent site activity might be controlled by dike intrusion over decadal timescales [e.g., *German and Lin*, 2004]. This type of heat supply sustains hydrothermal circulations in an episodic manner, and the hydrothermal areas tend to be small in the axial area.

On the other hand, the Archean site is located 2 km from the NVZ, and although there is no direct information regarding the heat source for this site, the existence of a large hydrothermal mound indicates a stronger hydrothermal flux or a longer duration of hydrothermal circulation. Radiometric dating showed that the maximum age of the sulfide deposits from the Archean site is at least ~3500 years [*Takamasa et al*., 2013; *Ishibashi et al*., 2015], substantiating the presence of long-lived hydrothermal activity.

Both the Pika and Urashima sites find their heat source in the off-axis volcanism forming the seamount on which they are located. The off-axis eruption is confirmed by the observation of fresh lavas with high magnetization in this study (Figs. 2-7a, 2-7b, 2-7i, and 2-7j), and the high seismic velocity structure [*Sato et al*., 2015b]. The off-axis volcano covers an area of more than several tens of square kilometers with a maximum height of ~400 m. This off-axis volcanism is probably a long-lived heat source during the formation and cooling of the seamount. *Sato et al*. [2015b] showed that the seismicity around the off-axis volcano was very low during the observation period of three months, suggesting that volcanism might have ceased. Sulfide chimneys and debris/breccia collected from these sites also indicates an age of up to ~9000 years [*Ishibashi et al*., 2015]. The growth of the Pika and Urashima hydrothermal sites might therefore be in their late stage.

The hydrothermal alteration zones and hydrothermal deposit zones grow with age

and hydrothermal activity, which in turn is controlled by the heat source, i.e., the magmatic activity. Long-lived and giant hydrothermal sites have been reported in slow and ultraslow-spreading environments, e.g., the TAG field, controlled by tectonic faults associated with a low-angle detachment fault [e.g., *Tivey and Dyment*, 2010], or the large field discovered at 49°39'E on the Southwest Indian Ridge [*Zhu et al*., 2010]. In contrast, the hydrothermal systems in the SMT are not associated with large fault systems cutting across the deeper crust and uppermost mantle, as suggested by the bathymetry and the very low seismicity [*Sato et al*., 2015b]. The five studied hydrothermal fields investigated are primarily controlled by magmatic activity.

2-5. Chapter Conclusions

I applied a method based on the comparison of near-seafloor three-component magnetic anomaly data with the 3-D forward modeling approach in the spectral domain to estimate the absolute crustal magnetization of the shallow sub-seafloor near five hydrothermal sites of the SMT. The analysis of these MADAMs led to the following conclusions:

1. The five hydrothermal vent fields of the back-arc spreading region in the SMT are characterized by low-intensity magnetization generally lower than 5 A/m in the off-axis area. The hydrothermal alteration of magnetic minerals present in the extrusive lavas and/or the deposits of non-magnetic hydrothermal material are responsible for the reduced magnetization in these zones.
2. The MADAM estimates are generally consistent with the NRM values of rock samples from the seafloor of the same region, although the NRM values tend to be larger than the MADAM estimates for higher values and smaller for lower values. The former difference might reflect variations in magnetic grain size, in which fast cooling results in a smaller grain size; therefore, stronger NRM is observed for the outcropping rock samples with respect to the bulk MADAM estimates. The latter difference might reflect the difference in degree of low-temperature oxidation. Indeed, the low-temperature oxidation of the outcropping rock is higher than that of the sub-seafloor; therefore, the NRM values could be weaker than the MADAM values.
3. The distribution of MADAM estimates is generally consistent with equivalent magnetizations deduced from AUV surveys, although the resolution of the former is higher than the latter. For example, the individual magnetic signatures of the Pika and Urashima sites could be detected only by using high-resolution near-seafloor measurements undertaken by the HOV.
4. The off-axis hydrothermal vent sites are larger than the on-axis sites, reflecting the longevity of the hydrothermal activity. The Snail and Yamanaka sites, both located in the axial area, are likely controlled by dike intrusions over decadal timescales, whereas the Archean, Pika, and Urashima sites are likely controlled by off-axis magmatic activity over thousands of years.

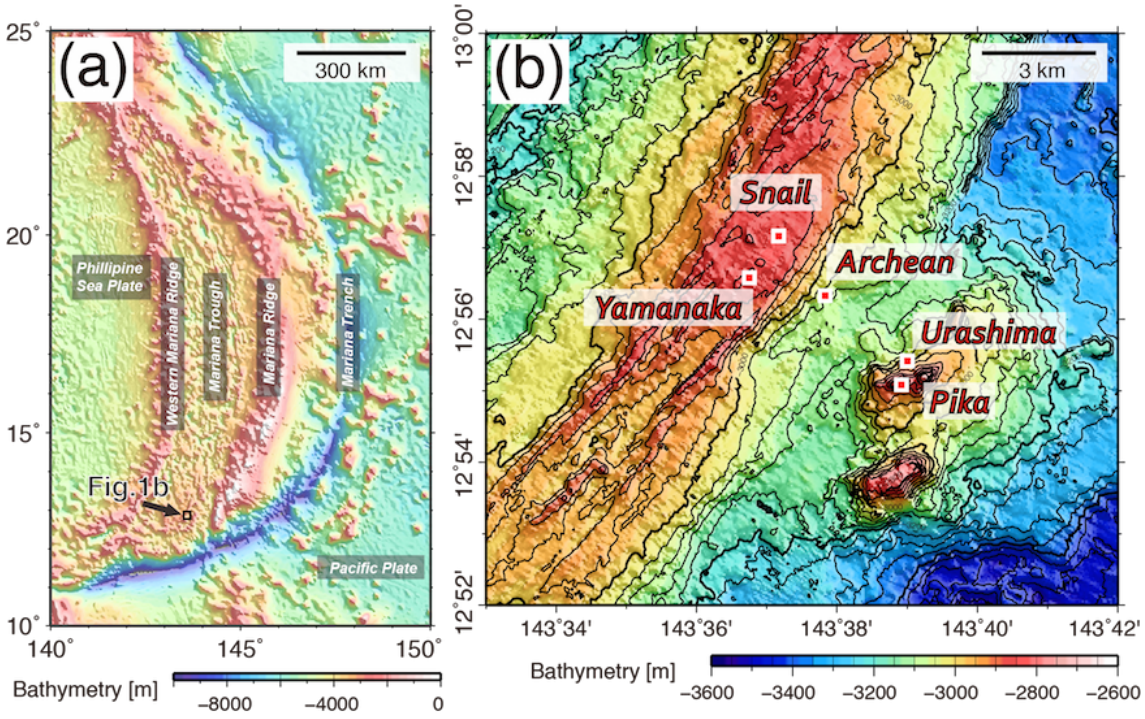

Figure 2-1. Seafloor bathymetry and locations of studied hydrothermal fields.

(a) Seafloor bathymetry of the Mariana Trough. Contour interval is 1 km. Bathymetry map is based on grid data from ETOPO1 [*Amante and Eakins*, 2009]. (b) Detailed seafloor bathymetry of the southern Mariana Trough. Red squares indicate locations of hydrothermal vents fields. Contour interval is 40 m. Bathymetry is made using 0.025-nmi-interval grid data from *Seama et al*. [2015].

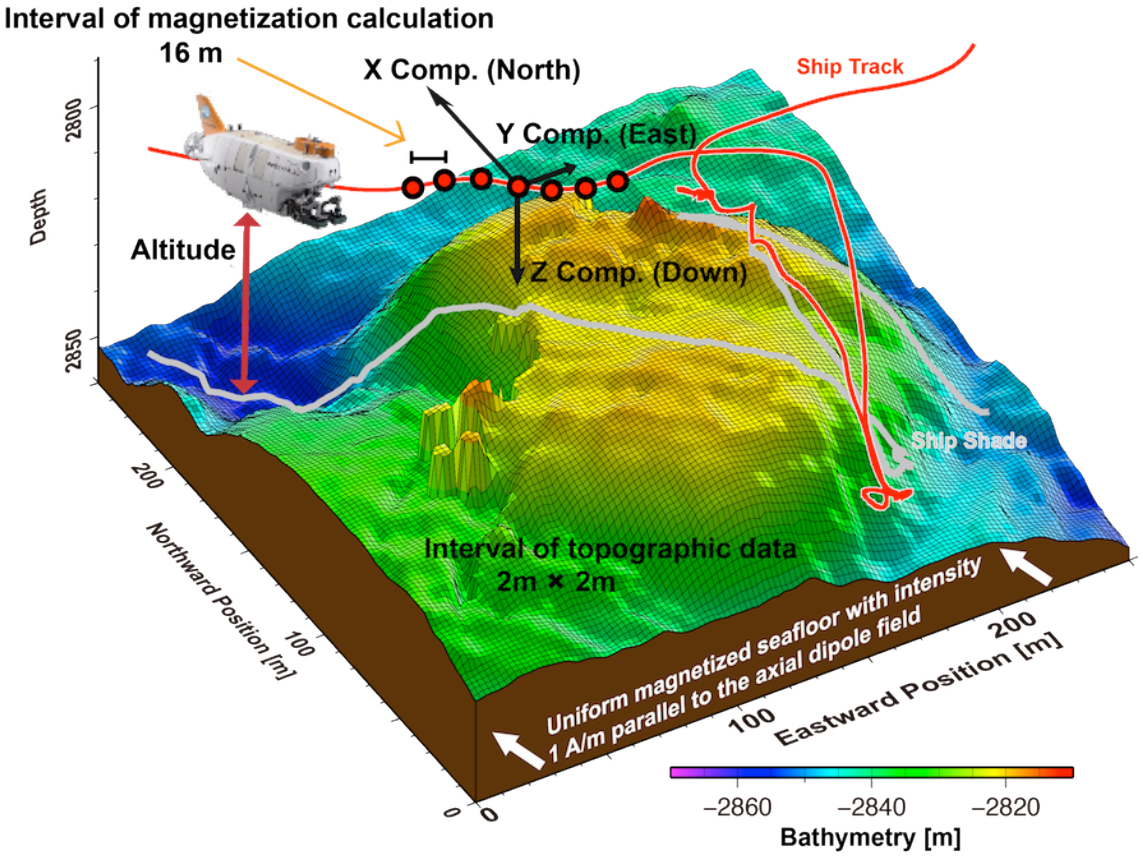

Figure 2-2. Schematic diagram of the method deriving the absolute magnetization. Colored grid: bathymetry collected by AUV; red line: submersible track; white line: submersible path projected on the seafloor. See text for details.

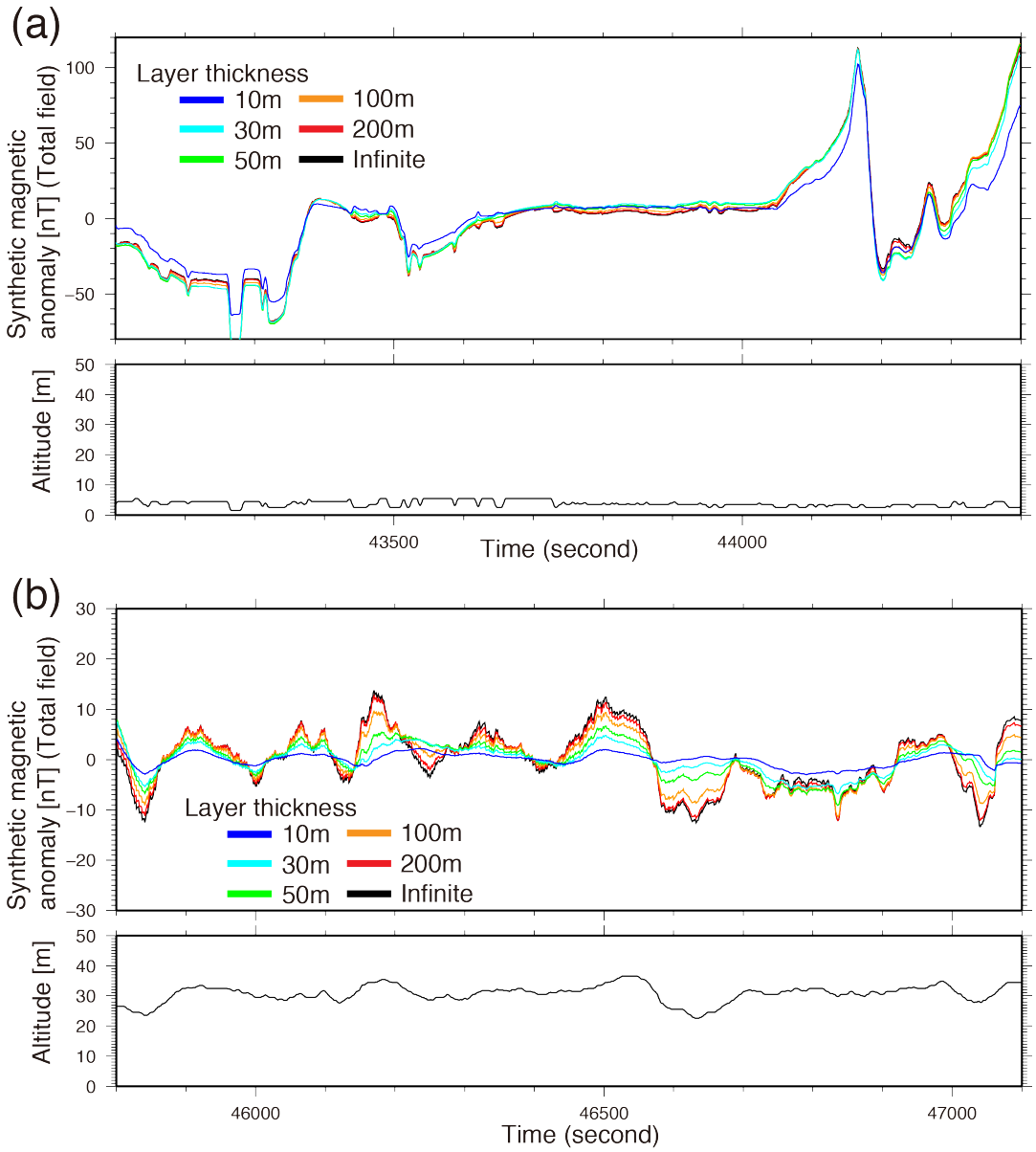

Figure 2-3. Synthetic magnetic anomalies assuming various thickness of layer source.

Synthetic total magnetic anomaly calculated by 3D forward modeling along the track of dive 6K#1227 using bathymetric data collected by AUV, for dive altitudes of (a) <10 m and (b) 20–40 m, assuming different magnetic source layer thicknesses: 10 m (blue line), 30 m (light blue line), 50 m (green line), 100 m (orange line), 200 m (red line), and infinite (black line).

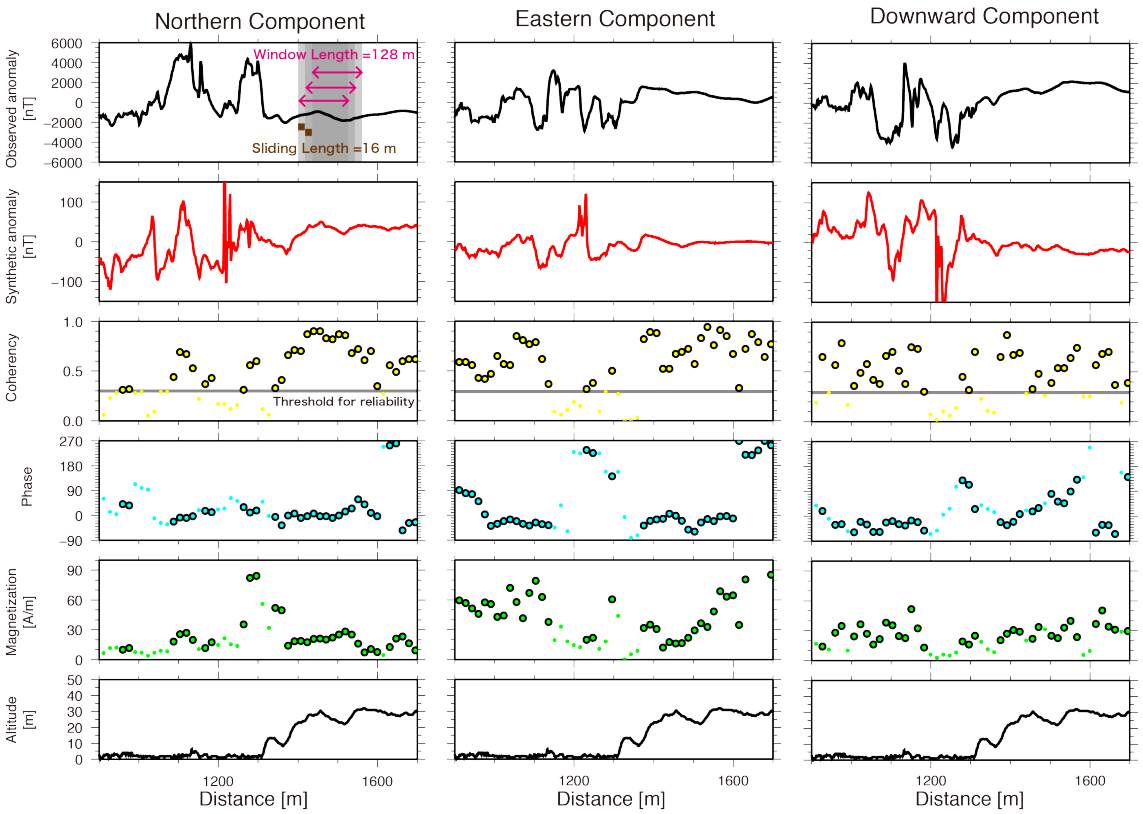

Figure 2-4. Example of absolute magnetization estimations.

Analysis of the northern (left), eastern (center), and downward (right) components of the magnetic anomaly. From top to bottom, observed (black line) and synthetic (red line) magnetic anomaly intensity, coherency (yellow circles), phase (blue circles), magnetization (green circles), and vehicle altitude (black line). Circles with black solid rims are those considered reliable (coherency >0.3 on at least two components).

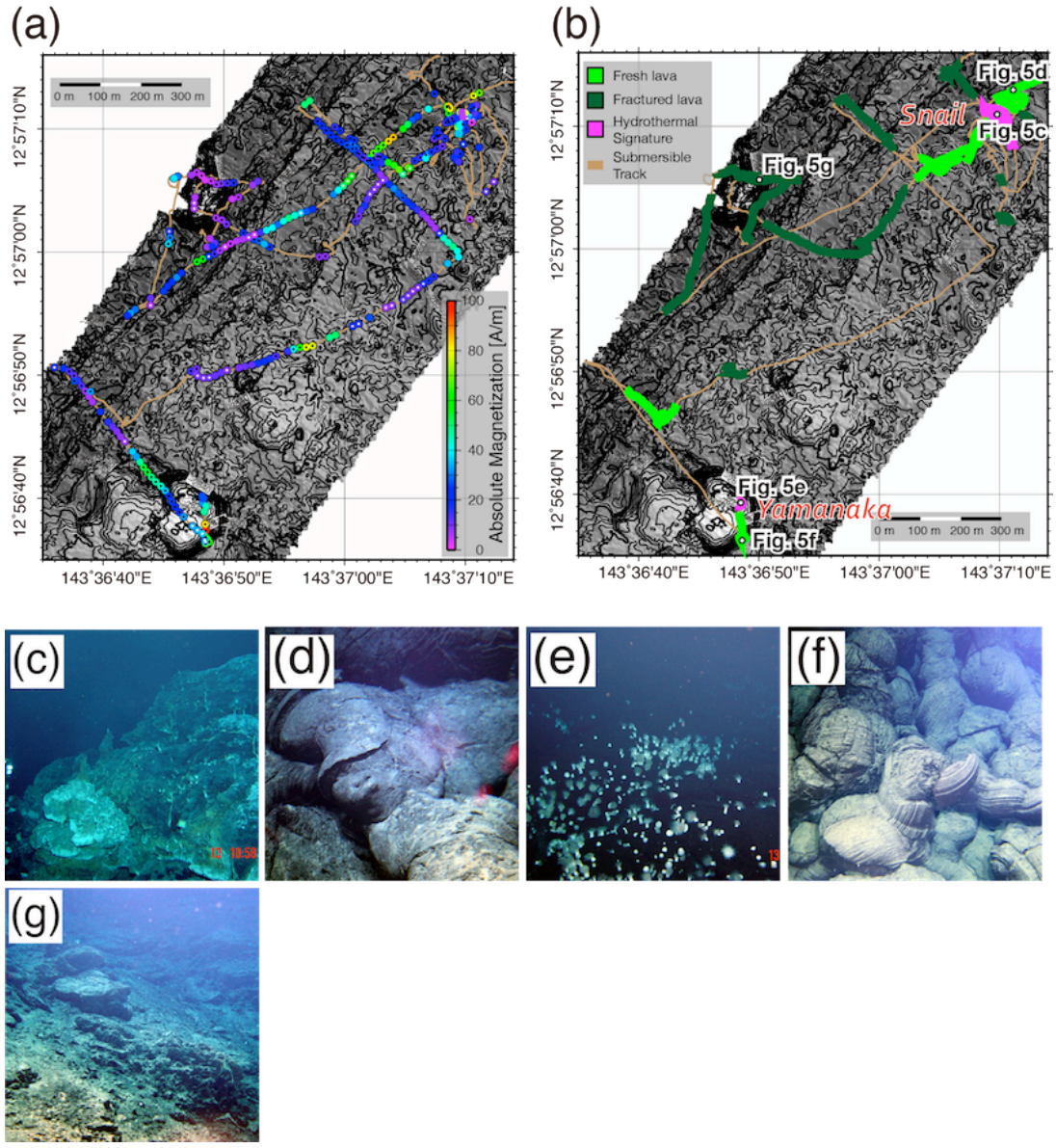

Figure 2-5. Results from the axial area including the Snail and Yamanaka sites.

(a) Distribution of magnetic-anomaly-derived absolute magnetization (MADAM). Magnetization intensity is shown by the rainbow colors of the outer circles and polarity shown by the black and white colors of the inner circles. Black and white circles mean normal and reverse polarity, respectively. Background: contoured and shaded bathymetry. (b) Geological observation along dive tracks. Photographs of (c) hydrothermal site Snail, (d) fresh pillow lava around the Snail site, (e) hydrothermal site Yamanaka, (f) fresh pillow lava near the Yamanaka site, (g) fractured lavas west of the neo-volcanic zones.

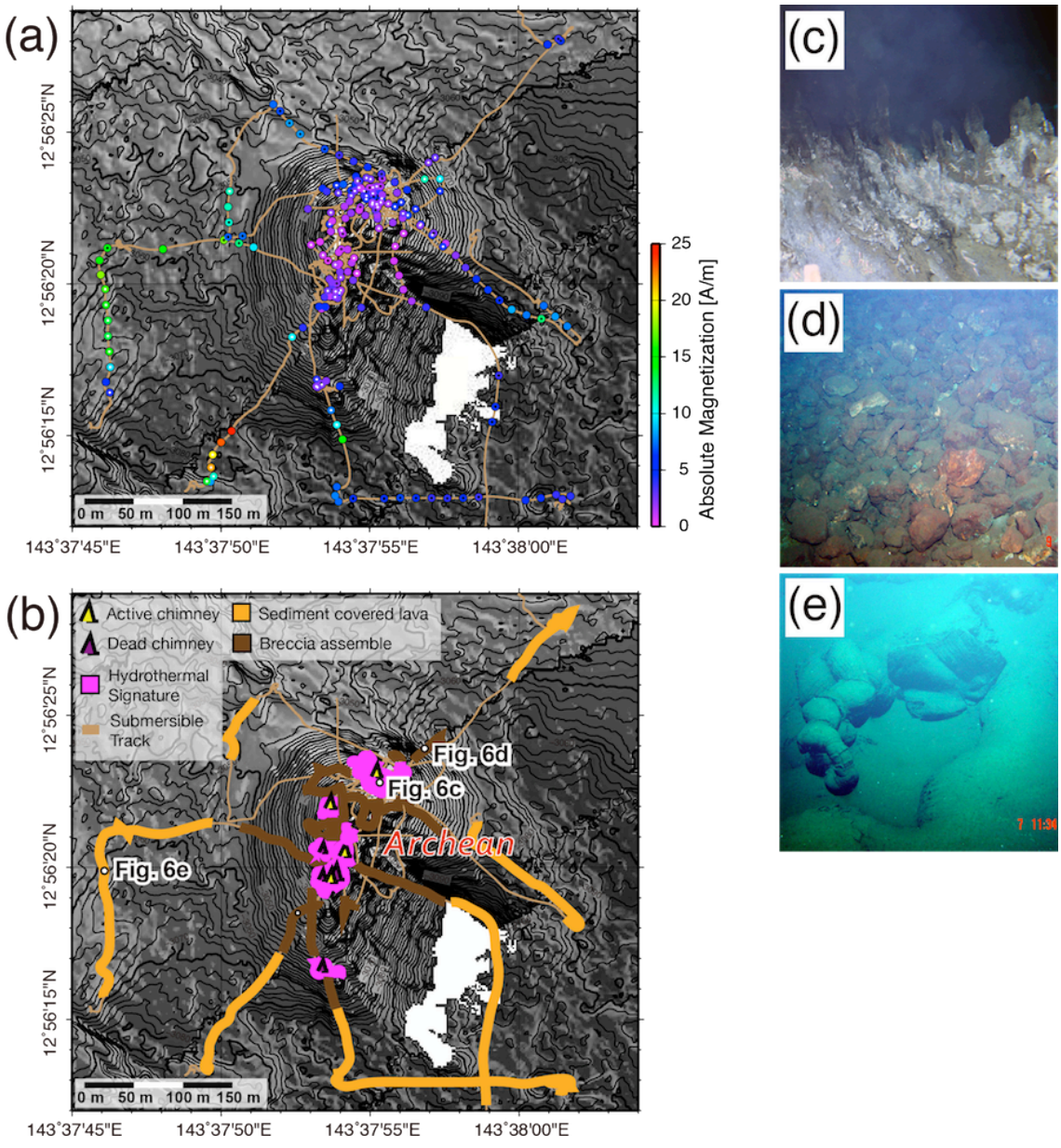

Figure 2-6. Results from the off-axis area including the Archean sites.

(a) Distribution of magnetic-anomaly-derived absolute magnetization (MADAM). Intensity is shown by the rainbow colors of the outer circles and polarity shown by the black and white colors of the inner circles. Black and white circles mean normal and reverse polarity, respectively. Background: contoured and shaded bathymetry. (b) Geological observations along dive tracks. Photographs of (c) hydrothermal site Archean, (d) debris and breccia around the Archean site, (e) sediment-covered lavas around the Archean site.

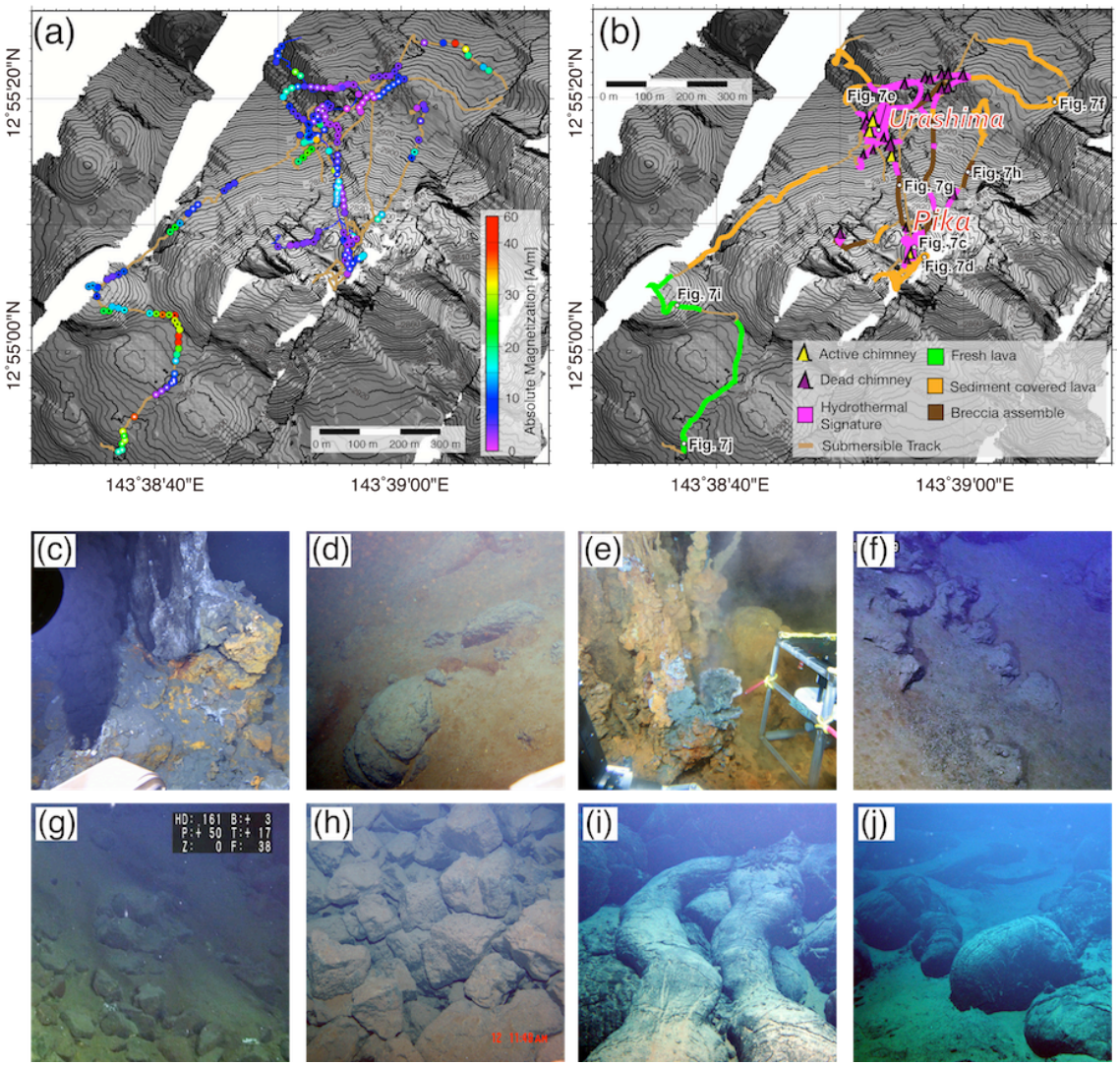

Figure 2-7. Results from the axial area including the Pika and Urashima sites.

(a) Distribution of magnetic-anomaly-derived absolute magnetization (MADAM). Intensity is shown by the rainbow colors of the outer circles and polarity shown by the black and white colors of the inner circles. Black and white circles mean normal and reverse polarity, respectively. Background: contoured and shaded bathymetry. (b) Geological observations along dive tracks. Photographs of (c) hydrothermal site Pika, (d) sediment-covered lavas near the Pika site, (e) hydrothermal site Urashima, (f) sediment-covered lavas around the Urashima site, (g) and (h) debris and breccia between the Pika and Urashima sites, (i) and (j) fresh pillow lava on the southwestern slope of the off-axis seamount.

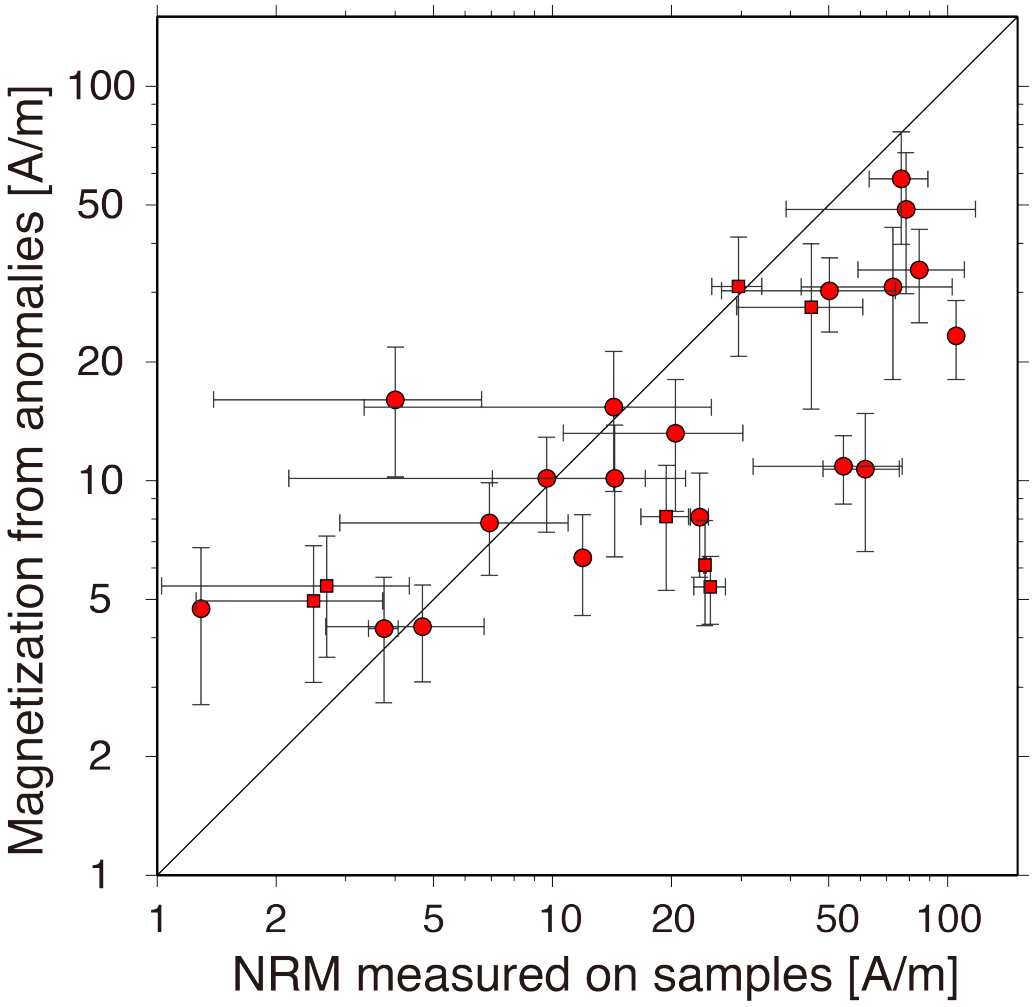

Figure 2-8. Comparison between MADAM and NRM measured on rock samples. Magnetic-anomaly-derived absolute magnetization, MADAM. NRM, natural remanent magnetization. Circles and squares show NRM dataset from samples collected by submersible and seafloor coring [*Mochizuki et al*., 2012], respectively. Error bars of x- and y-axes show standard deviations of NRM values and MADAM estimates for each point, respectively.

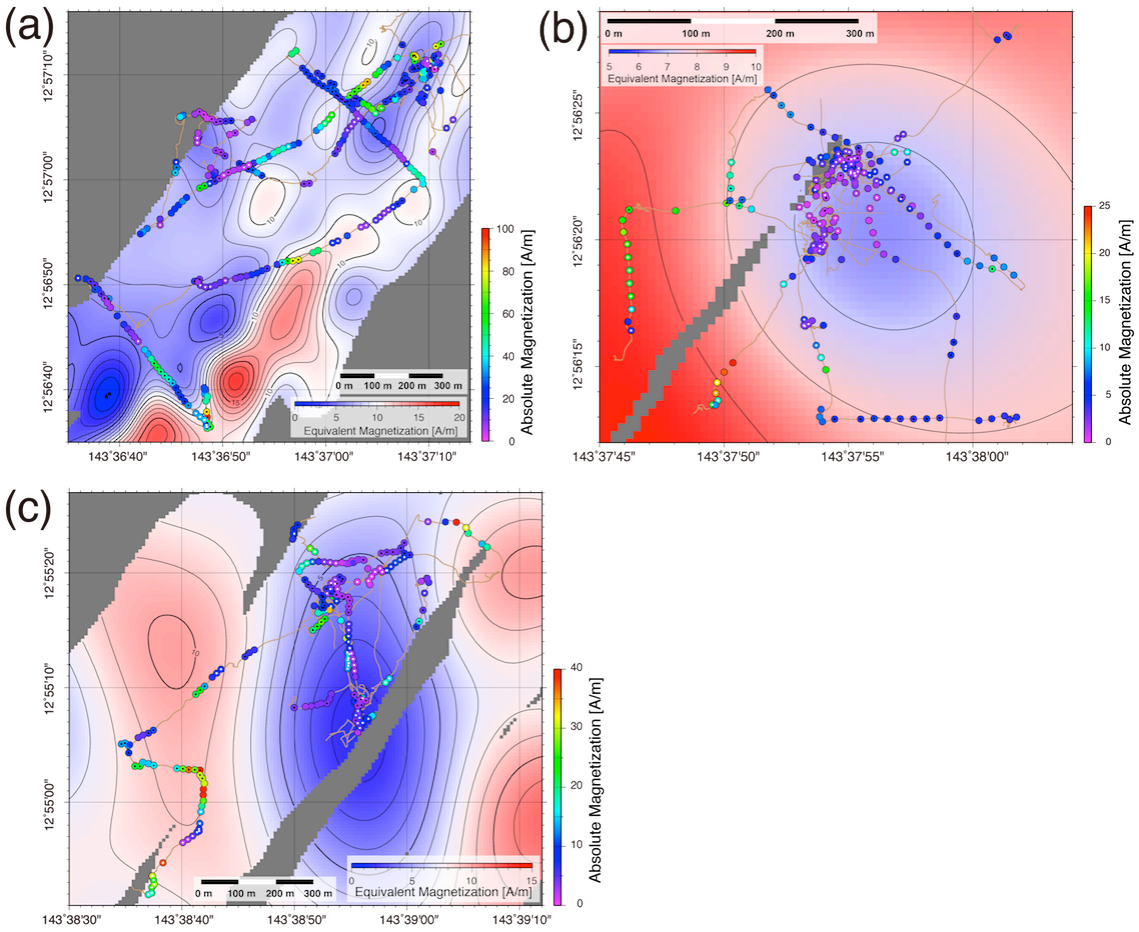

Figure 2-9. Comparison between MADAM from HOV and EM from AUV. Magnetic-anomaly-derived absolute magnetization, MADAM. Human occupied vehicle, HOV. Equivalent magnetization, EM. Autonomous underwater vehicle, AUV. The EM data is based on *Nogi et al*. [2011]. MADAM plots are those shown in Figs. 5–7. (a) On-axis area, including the Snail and Yamanaka sites; (b) off-axis area at the foot of the axial high, including the Archean site; (c) off-axis seamount area, including the Pika and Urashima sites.

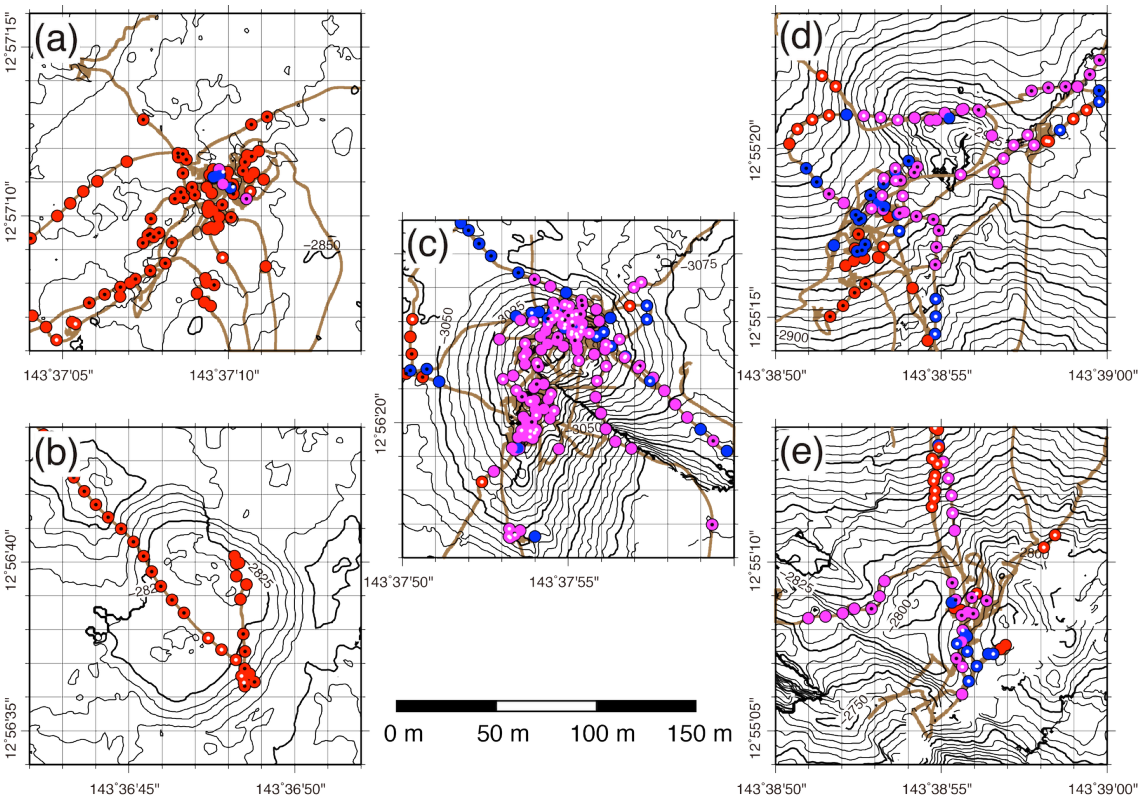

Figure 2-10. Spatial scale of low magnetization zones.

Distribution of magnetic-anomaly-derived absolute magnetization around five hydrothermal fields of the Southern Mariana Trough, represented at the same scale: Sites Snail (a), Yamanaka (b), Archean (c), Urashima (d), and Pika (e). Red circles denote magnetization intensity >10 A/m, blue circles 5–10 A/m, and purple circles <5 A/m. Brown lines show submersible dive tracks. Isobaths of the background are plotted for every 10 m (thin lines) and 50 m (thick lines).

Chapter 3

Basalt- to Rhyolite-hosted Tarama and Irabu Hydrothermal Fields in Arc and Back-arc Regions of Okinawa Trough

In this chapter, I present a detailed analysis of the high-resolution vector magnetic anomalies performed on arc and back-arc hydrothermal vent fields in the Okinawa Trough by using the AUV *URASHIMA*. The Irabu hydrothermal fields (IHFs) are developed on the axial area of back-arc rift and consist of basaltic lavas. The Tarama hydrothermal field (THF) is developed between back-arc rift and arc along with dacite to rhyolite. Active hydrothermal venting was reported in both the IHF and THF. The distribution of crustal magnetization deduced from the magnetic anomaly revealed that both the IHF and THF are associated with reduced magnetization, as widely observed at lava-hosted hydrothermal fields of mid-ocean ridges (MORs). The spatial scale of low magnetization reflecting the extent of discharge zone is large compared with that found at MORs. Comparisons with detailed bathymetry and magnetization distribution of the Irabu knolls reveal that the magnetization lows are located along the rim of the cauldron structure, indicating that hydrothermal fluids rise along the caldera fault from the deep regions. These results demonstrate that reduced magnetization related to hydrothermal activity occurs in rhyolite-hosted systems as well as basalt-hosted systems, and that the caldera fault is an important pathway in the formation of large discharge zones of hydrothermal systems.

3-1. Geological Background

The Okinawa Trough is a back-arc basin located behind the Ryukyu arc-trench system along the eastern margin of the Eurasian continent with length of >1200 km (Fig. 3-1). It is characterized by active rifting structures and magmatism along the depression and is believed to represent a transition from a rifting stage to initial spreading [e.g., *Sibuet et al*., 1987]. Global positioning system (GPS)-derived velocity field data indicate a spreading rate of ~50 mm/year at the direction of 175° in the southern Ryukyu Islands (~123.6°E) [*Nishimura et al*., 2004]. Seismic exploration has revealed a minimum crustal thickness of 8 km and low velocity gradient interpreted as oceanic crust at the southernmost part [*Klingelhoefer et al*., 2009], implying that the Okinawa Trough is still in the nascent stage of back-arc basin formation. Recent volcanic activity at the axial part of the southern Okinawa Trough has formed minor ridges and knolls composed of bimodal assemblages of young basaltic–rhyolitic volcanic rocks [*Shinjo et al*., 1999].

The Tarama Knoll is located approximately 40 km west of the Irabu knolls near the arc volcanoes (25°06′N, 124°32′E; Figs. 3-1, 3-2, and 3-3a). Another topographic high, the Tarama Hill, is located southwest from the Tarama Knoll (Fig. 3-3A). The Tarama Knoll is a conical knoll with height of ~500 m and diameter of ~4 km. The surrounding seafloor of the Tarama Knoll has been sedimented, resulting in smooth, flat appearance compared with the surrounding seafloor. A rock sample from the lava flows collected during the previous *Natsushima* cruise NT10-06-leg2 is composed of dacite [T. Nozaki, personal communication]. Pyroclastic pumices have also been observed. Low-temperature fluid venting and associated brown-colored sediment have been reported at the top of the knoll [NT09-10-leg2 cruise report; NT10-06-leg2 cruise report; NT11-18 cruise report].

The Irabu knolls are located at the axial segment boundary of the back-arc rift zone in the southern Okinawa Trough (25°14′N, 124°53′E; Figs. 3-1, 3-2, and 3-3B), and consist of three knolls known as the Irabu-West, Irabu-South, and Irabu-East. The direction of the back-arc axis changes at the Irabu knolls from 85° at the west side to 65° at the east side. The Irabu-West is a conical volcanic knoll with a relative height of ~450 m and diameter of ~2 km. The Irabu-East extends N–S with length of ~3 km and a relative height of ~350 m and involves two caldera-like depression structures at the

north and south sides. Several ENE–WSW-trending faults cut the surrounding basement of the knolls, implying that it has been subjected to tectonic deformation associated with the back-arc rifting (Fig. 3-3B). Faulting and deformation signatures were not observed in the Irabu knolls; therefore, the basement should be affected by the overprint of recent back-arc volcanism forming the Irabu knolls. The rock samples from lava flows collected in previous *Yokosuka* cruises YK11-20 and KY14-02 are composed of basalt–andesite [T. Nozaki, personal communication]. Active hydrothermal vents have been confirmed at the top the Irabu-West [NT11-17 cruise report; NT11-20 cruise summary; NT13-25 cruise report], and along the northern rim of the southern caldera on the Irabu-East [YK12-05 cruise report; NT13-25 cruise report], where dead chimneys are also distributed. Within the northern caldera on the Irabu-East, water discoloration was reported twice during submersible *SHINKAI 6500* dives 1301 and 1302 [YK12-05 cruise report].

3-2. Data and Methods

3-2-1. Data acquisition

The ship-underway and near-seafloor geophysical observations on the Irabu and Tarama knolls were performed during the cruise YK14-16 of R/V *Yokosuka* in August 2014.

The underway geophysical mapping covers an area including the Irabu and Tarama knolls and the graben structure of the back-arc rifting (Fig. 3-2). Densely gridded survey with 1 mile spacing was conducted on the Irabu and Tarama knolls. The data of seafloor bathymetry and total magnetic field were successfully measured at general ship speeds of 12 knots by using a 12 kHz multibeam echo sounding system (EM122, Kongsberg) and a ship-towed proton precession magnetometer with sampling rate of 20 s (Type STC 10, Kawasaki Geological Engineering Co., Ltd.), respectively.

Four dive surveys were conducted using the AUV *URASHIMA* at a general altitude of 100 m, with two dives devoted to each site (Fig. 3-2). The AUV collected bathymetric and vector magnetic field data by using a 400 kHz multibeam echo sounding system (SeaBat 7125 AUV, Teledyne Reson) and three-axis fluxgate-type magnetometers (TIERRA TECHNICA Ltd.; National Institute of Polar Research), respectively. Calibration spins of the vehicle, known as a figure-8 loop, were performed

with pitch variation of −29° to 31° to correct the effect of vehicle magnetization. The diameter of the vehicle rotation was 100 m. Attitude data including heading, pitch, and roll were collected independently by using an optical gyroscope with a sampling rate of 10 Hz. All dives were navigated by both acoustic ranging using a super-short baseline positioning system (SSBL) and an inertial navigation system (INS).

3-2-2. Imaging the magnetic anomaly: ship-underway

The total magnetic anomalies were calculated after subtracting the International Geomagnetic Reference Field (IGRF) from the observed total magnetic field by the shipboard proton magnetometer. The 0.5-mile-grided anomalies were calculated by using the gridding algorithm for adjustable tension continuous curvature surface, known as "surface" in the Generic Mapping Tool software.

Crustal magnetization was then calculated to remove skewness and to correct the effects of bathymetry by using the 3-D Fourier inversion method of *Parker and Huestis* [1974] and *Macdonald et al*. [1980]. The direction of seafloor magnetization was considered to be the same as the IGRF, and a magnetized layer thickness of 1000 m was assumed. The upper surface of the magnetized layer was assumed to be the same as the seafloor. Taylor expansion up to the ninth order was conducted; ten iterations provided sufficient convergence of the solution. A band-pass filter, cosine tapered at short wavelengths of 1–1.5 km and at long wavelengths of 10–12 km, was applied to each iteration for stabilizing the solution. The appropriate annihilator was added to the inversion solution to make the resultant magnetization positive, assuming that the thermal remanent magnetization was preserved on the seafloor volcanoes in the study area within the Brunhes normal chron.

3-2-3. Imaging the magnetic anomaly: AUV

The calibration of vehicle magnetization was performed following the method of *Isezaki* [1986] and by using data obtained during the figure-8 loops. Magnetic data were merged with attitude data after considering a proper time shift between them. The ambient geomagnetic field vector was estimated from the IGRF [*IAGA Working Group V-MOD*, 2010]. After the vehicle calibration and the subtraction of the IGRF value, three components of the magnetic anomalies were obtained.

The magnetization intensity distributions were calculated by using the Akaike Bayesian Information Criterion (ABIC) inversion method developed by *Honsho et al*. [2012]. The observation equation of the total-field anomaly produced by the magnetization distribution can be expressed by a probability density function of data **d** for given model parameters **a** as

$$p(\mathbf{a};\ \sigma^2, \alpha^2, |\mathbf{d}) = c(2\pi\sigma^2)^{-\frac{N+P}{2}}(\alpha^2)^{\frac{P}{2}}||\mathbf{E}||^{\frac{1}{2}}||\Lambda_P||^{\frac{1}{2}} \exp\left[-\frac{1}{2\sigma^2}s(\mathbf{a})\right]$$

where,

$$s(\mathbf{a}) = (\mathbf{d} - \mathbf{Ha})^T\mathbf{E}^{-1}(\mathbf{d} - \mathbf{Ha}) + \alpha^2\mathbf{a}^T\mathbf{Ga}$$

and **d** is an N dimensional data vector, **a** is an M ($\equiv K \times L$) dimensional model parameter vector, **H** is an $N \times M$ dimensional coefficient matrix, **G** is an $M \times M$ dimensional matrix, P is the rank of the matrix **G**, $||\Lambda_P||$ represents the absolute value of the product of nonzero eigenvalues of G, c is a normalizing factor, and $||\mathbf{E}||$ denotes the absolute value of the determinant of **E**. Once the values of hyperparameters α^2 and σ^2 are fixed, the maximization of the posterior probability density function is achieved by minimizing $s(\mathbf{a})$. The solution is given as

$$\mathbf{a}^* = (\mathbf{H}^T\mathbf{E}^{-1}\mathbf{H} + \boldsymbol{\alpha}^2\mathbf{G})^{-1}\mathbf{H}^T\mathbf{E}^{-1}\mathbf{d}$$

and the covariance of $\mathbf{a}^*$ is

$$\mathbf{C} = \boldsymbol{\sigma}^2(\mathbf{H}^T\mathbf{E}^{-1}\mathbf{H} + \boldsymbol{\alpha}^2\mathbf{G})^{-1}.$$

The hyperparameters α^2 and σ^2 determine the relative importance of the information from data and the prior constraint ABIC, which is based on the entropy maximization principle, provides us a measure by which the values of the hyperparameters can be determined. Based on the necessary conditions for the maximum of marginal likelihood function (α^2, σ^2), we obtain

$$\boldsymbol{\sigma}^2 = s(\mathbf{a}^*)/(N + P - M).$$

Then, the ABIC as a function of α^2 is defined by

$$\mathrm{ABIC}(\alpha^2) = (N + P - M)\log s(\mathbf{a}^*) - P\log\alpha^2 + \log||\mathbf{H}^T\mathbf{E}^{-1}\mathbf{H} + \boldsymbol{\alpha}^2\mathbf{G}|| + C$$

where C is a constant term independent of α^2. Finding the value of α^2 which minimizes the ABIC can be undertaken numerically. Once we obtain the best estimate of α^2, the model parameter vector **a** and its covariance matrix **C** are given by previously mentioned equations. This approach is a space domain inversion method; therefore, the solution does not suffer from smoothing owing to high-cut filtering or error caused by data reduction on a flat surface, which can occur in other inversion

methods [e.g., *Parker and Huestis*, 1974]. During this procedure, the magnetic data were merged with positioning and depth data. The seafloor bathymetric data utilized in the analysis were obtained by up-sampling of a 20 m grid based on ship-underway multibeam echo-sounding. The magnetization direction was assumed to be parallel to the IGRF with 36.7° inclination and −4.4° declination in the Irabu knolls (25.208°N, 124.950°E), and 36.5° inclination and −4.4° declination in the Tarama Knoll (25.100°N, 124.533°E). For the magnetized source geometry, uniform 1000 m thick layers and magnetization direction parallel to the IGRF were considered.

3-2-4. Rock magnetic properties and petrological observation

Volcanic rock samples were collected from the seafloor surface by using the ROV *Hyper Dolphin*. On the Tarama Knoll, they were collected during dive 1109 in the R/V *Natsushima* NT10-06-leg2 cruise. On the Irabu knolls, they were collected during dives 1330 and 1332 in the *Natsushima* NT11-20 cruise and dive 1624 in the R/V *Kaiyou* KY14-02 cruise (Fig. 3-2). Measurements of the rock magnetic properties and petrological observations were performed on one rhyolite sample from the Tarama Knoll and on fourteen samples of basalt to andesite from the Irabu knolls. Four cubic subsamples (~2 cm each) and several chips were cut from each sample. The cubic subsamples were used for measurements of NRM and magnetic susceptibility. The chip subsamples were used for measurements of high-temperature magnetization and magnetic hysteresis parameters. The chip subsamples of representative rocks from the Irabu knolls were used for first-order reversal curve (FORC) measurements.

The NRM and magnetic susceptibility were measured on all cubic subsamples by using a spinner magnetometer (DSPIN, Natsuhara Giken) at the Atmosphere and Ocean Research Institute (AORI), University of Tokyo, and a magnetic susceptibility meter (Kappabridge KLY-3, AGICO) at the Center for Advanced Marine Core Research (CMCR), Kochi University, respectively. High-temperature magnetic analyses were performed on the chip subsamples. The temperature dependence of the saturation magnetization (Ms) above room temperature was measured by using a magnetic balance (MNB-89, Natsuhara Giken) at the CMCR. The samples were heated from 50°C to 700°C and were cooled back to 50°C in a vacuum (~1 Pa) at a rate of 12°C/min. The inducing magnetic field was 0.5 T. The Ms was measured on the chips by using a

vibrating sample magnetometer (VSM; MicroMag 3900, Princeton Measurements Corp.) at the CMCR. During the Ms measurement procedure, the magnetic hysteresis parameters were also measured to estimate the ferromagnetic grain-size distributions in the rock samples based on the Day plot [e.g., *Day et al*., 1977]. This device displays the remanence ratio (saturation remanent magnetization to saturation magnetization) against the coercivity ratio (remanent coercivity to coercivity). The FORC measurements were conducted by using an alternating gradient magnetometer (AGM; MicroMag 2900, Princeton Measurements Corp.) at the CMCR. The FORC diagrams provide information on the distribution of coercivity (Hc) for a magnetic grain assemblage [e.g., *Roberts et al*., 2000]. The field spacing was set to 2.25 mT, and a total of 100 FORCs were measured with Hc values of 0–120 mT and local interaction field (Hu) values of −40 mT to 40 mT. A smoothing factor of 2 was used [*Roberts et al*., 2000] and the irregularFORC software [*Zhao et al*., 2015] was used for data processing.

Mineralogical and textual analyses for representative samples from the Irabu knolls were conducted on a thin section by using reflected light microscopy, field emission scanning electron microscopy (SU 8200, Hitachi High-Technologies), and energy dispersive spectrometry (FlatQUID XFlash, Bruker AXS).

3-3. Results

3-3-1. Magnetization from ship-underway mapping

The amplitude variation of the magnetic anomaly observed from the surface ship was up to 460 nT at the Tarama Knoll and 760 nT at the Irabu knolls (Fig. 3-4B). The distribution of crustal magnetization was estimated by using a 3-D inversion technique to remove skewness and to correct for the effects of bathymetry (Fig. 3-4C). The resultant magnetization intensity with the addition of the appropriate annihilator varies up to 18 A/m (Fig. 3-4D). The magnetization intensity distribution showed a maximum magnetization of ~18 A/m at the Irabu knolls centered on the Irabu-East. High magnetization areas were also observed at the ridges within the axial graben and in small knolls to the west of the Irabu knolls. In the Tarama area, the highest magnetization of 6 A/m corresponds to the Tarama Hill. The magnetization intensity at the Tarama Knoll showed a maximum of 3 A/m, which is considerably lower than that observed in the Irabu area.

3-3-2. Magnetization from AUV mapping

The high-resolution magnetization intensity distribution in the Tarama and Irabu knolls was estimated from three components of magnetic anomalies obtained by AUV *URASHIMA* using the ABIC inversion analysis technique.

The two dives in the Tarama Knoll revealed varying magnetization intensity up to 4 A/m (Fig. 3-5). The magnetization intensity distribution showed low magnetization of less than 2 A/m generally at the top of the knoll and in the southeastern part. Magnetization intensity higher than 3 A/m was observed at the southwestern part of the knoll. The resultant magnetization distribution showed some lineaments parallel to the survey tracks, which was caused by wide intervals on survey lines resulting in unstable solutions despite the low amplitude of the magnetic anomaly.

The two dives in the Irabu knolls revealed varying magnetization intensity up to ~60 A/m (Fig. 3-6). The magnetization distribution showed variations of magnetization intensity generally with short wavelengths of ~100 m. A comparison with detailed bathymetry from the AUV data is shown in Figures 3-6E−R; the locations are summarized in Figure 3-6D. The magnetization intensity distribution showed that high magnetization zones >35 A/m that correspond to the area with the topographic highs (Figs. 3-6E−N). The highest magnetization zones were located at the southwestern top of the north caldera wall at the Irabu-East where the volcanic lava sample was collected (Fig. 3-6D) and its western foot (Fig. 3-6C). In contrast, reduced magnetization zones <15 A/m were observed at the top of the Irabu-West (Fig. 3-6N), the NW rim of the south caldera in the Irabu-East (Fig. 3-6M), and the NE rim of the north caldera in the Irabu-East (Fig. 3-6L). One specific feature is that high magnetization >40 A/m was observed at the SE rim of the north caldera in the Irabu-East (Fig. 3-6E).

3-3-3. Rock magnetic properties and petrography

All of the basalt–rhyolite lavas show a relatively broad range of magnetic susceptibility and NRM values (Figs. 3-7A and 3-7B; Table 3-1). The magnetic susceptibility of lava samples is 0.0004–0.0048 SI and is a proxy for the concentration and representative grain size of ferromagnetic minerals. The NRM intensity varied at 3.1–214.4 A/m, suggesting the abundance of single domain (SD) and pseudo single domain (PSD) sized grains in a specimen. This variation could have also been

controlled by the strength of the Earth's magnetic field at the time the magnetization was acquisition, geochemistry (e.g., Fe and Ti content), or the degree of alteration with age. The NRM values of basalt to basaltic andesite were significantly larger than those of andesite to rhyolite (Fig. 3-7C). The Koenigsberger ratio (Q: NRM/induced magnetization) varied at 61–6209 (Table 3-1), where the ambient magnetic field was assumed to be 40000 nT. All lava samples showed Q values significantly higher than 1 (Fig. 3-7A); therefore, the specimen's remanent magnetization contributed dominantly to the magnetic anomalies. Three lava samples from the Irabu knolls (HPD#1330G01, HPD#1330G02, and HPD#1330G06) show quite low Q values at ~120, in which the magnetic susceptibility and NRM intensities are >0.025 SI and <10 A/m, respectively. The sample from the Tarama Knoll (HPD#1109R01) shows a Q value of 84 with magnetic susceptibility of 0.11 SI and NRM of 3.1 A/m.

In the lava samples, the remanence ratio (Mr/Ms), which is the saturation remanent magnetization against the saturation magnetization, and the coercivity ratio (Hcr/Hc), which is the remanent coercivity against the coercivity, varied at 0.10–0.57 and 1.15–4.45, respectively (Fig. 3-7D; Table 3-2). The hysteresis properties were distributed within the SD to the multi-domain (MD) region of the Day plot [*Day et al*., 1977; Fig. 3-7D]. Lavas with low NRM intensities tended to show low remanence ratios and high coercivity ratios, indicating an abundance of MD grains.

Thermomagnetic analyses showed single Curie temperatures of 280–490°C (Figs. 3-7E and 3-7F; Table 3-2). The warming and cooling curves were almost identical in all measured samples (Figs. 3-7E and 3-7F). These observations indicate that main magnetic carrier was stoichiometric titanomagnetite, and that the alteration during heating was small. Low-temperature oxidation (maghemitization) was not indicated for all measured samples. The variations of these Curie temperatures among the samples indicate titanomagnetite with various degrees of Ti substitution [*Hunt et al*., 1995]. *Hunt et al*. [1995] indicate the compositional dependence of the Curie temperature (T_C) for titanomagnetite with Ti content (x) and showed the following best-fit equation: $T_C = 575 - 552.7\,x - 213.3\,x^2$. The end-members are magnetite ($x = 0$) and ulvöspinel ($x = 1$). On the basis of this equation and the measured Curie temperatures, we estimated the Ti contents (x) of the rock samples to be 0.15–0.45 for titanomagnetite ($Fe_{3-x}Ti_xO_4$; Table 3-2). The estimated Ti contents were applied to determine the saturation magnetization based on the empirical equations showing linear relationship between the saturation

magnetization (J_S) and Ti content as follow: Js = 92 × (1 − 1.23 *x*) [*Hunt et al*., 1995]. The ratio of the measured saturation magnetization of the rock samples against the estimated saturation magnetization of the titanomagnetite grains reflects the titanomagnetite amount. The calculated titanomagnetite amounts of all lava samples were 0.2–3.2 wt.% (Table 3-2).

The thin section images from reflected light microscopy are shown in Figure 3-8. Samples with higher titanomagnetite amounts contained larger titanomagnetite grain sizes, which were observed as shiny white grains. The FORC distributions for the HPD#1330G02 sample showed contours diverging toward the Hu axis with low coercivity (Hc) at the peak of <20 mT (Fig. 3-8), which is suggestive of the dominance of MD grains [*Roberts et al*., 2000]. In contrast, dull surfaces were observed on the thin section of the HPD#1330G05, which shows FORC distributions near Hc = 0 and Hu = 0, indicating the presence of super-paramagnetic (SP) grains (Fig. 3-8). Sample HPD#1330G03, which had the highest NRM, contained smaller amounts of titanomagnetite with higher coercivities and closed contours in FORC distributions (Fig. 3-8), which is suggestive of a larger contribution of SD grains. This sample contains titanomagnetite grains of several tens to hundreds of nanometers in size and dendritic titanomagnetite grains (Fig. 3-9).

3-4. Discussion

3-4-1. Magnetization intensity reflecting host rock difference

The results of both ship-underway and AUV magnetic imaging showed that the regional magnetization intensity is significantly larger in the Irabu knolls than that in the Tarama Knoll (Figs. 3-4, 3-5, and 3-6). This magnetic contrast likely reflects the host rock differences, particularly in the amount of titanomagnetite serving as the main NRM carrier within the volcanic rocks. The rock magnetic measurements showed that all lava samples from the Irabu knolls have NRM intensity of 7–214 A/m, which is significantly higher than that in the samples from the Tarama Knoll (3 A/m). Because the silica content in rhyolite is generally larger than that in basaltic rocks, the amounts of magnetite and NRM are decreased. The quantitative explanation for the NRM variation has been regarded to be difficult because the NRM intensities of volcanic rocks may vary in relation to several factors such as the geomagnetic field strength at the timing of

remanence acquisition [e.g., *Ravilly* et al., 2001]; the amount of magnetic minerals, mainly titanomagnetite; grain chemistry, particularly the Ti content of titanomagnetite [e.g., *Dunlop and Ozdemir*, 2007]; magnetic domain state (equivalent to grain size) of the magnetic minerals [e.g., *Marshall and Cox*, 1971; *Ryall and Ade-Hall*, 1975; *Gee and Kent*, 1997]; and the degree of low-temperature oxidation [*Gee and Kent*, 1994]. My new rock magnetic data of all collected samples presents the host rock difference of NRM under consideration of these factors.

Thermomagnetic analysis revealed that all collected lava samples contain titanomagnetite as the magnetic carrier and have not been affected by low-temperature oxidation (maghemitization). Because maghemitization begins almost immediately after extrusion and considerably decreases the NRM [e.g., *Gee and Kent*, 1994], all collected lava samples should be fresh. Therefore, the acquisition timing of the thermal remanent magnetization for all samples is considered to be almost the same, and the effect of geomagnetic field strength as well as the degree of low-temperature oxidation can be ignored for following discussion.

The Curie temperature and hysteresis parameters such as Hcr/Hc and Mr/Ms are useful in determining the Ti content of titanomagnetite ($Fe_{3-x}Ti_xO_4$) and the magnetic domain state, respectively. The lava sample from the Tarama Knoll (HPD#1109R01) is rhyolite with a Curie temperature of 490°C, equivalent to x = 0.15, and hysteresis parameters of Hcr/Hc = 2.42 and Mr/Ms = 0.16, which is regarded as the magnetic domain state of the PSD (Table 3-1 and 3-2). One sample from the Irabu knolls (HPD#1330G02) shows similar a Curie temperature of 480°C, equivalent to x = 0.16, and magnetic hysteresis parameters of Hcr/Hc = 2.64 and Mr/Ms = 0.10. The comparison of HPD#1109R01 (rhyolite) with HPD#1330G02 (basaltic andesite) enables evaluation of the relationship between the NRM and the titanomagnetite amount considering the magnetic domain state, the Ti content, and the degree of low-temperature oxidation.

The titanomagnetite amount of HPD#1109R01, at 0.9 wt.%, is about one-third that of HPD#1330G02, at 3.1 wt.%. This result is consistent with the bulk rock geochemistry showing that the Fe content of HPD#1109R01 as Fe_2O_3 at 3.2% is about one-third that of HPD#1330G02, at 11.2% [T. Nozaki, personal communization]. The NRM intensity of HPD#1109R01, at 3.1 A/m, is also about one-third that of HPD#1330G02, at 9.4 A/m. These results indicate that the lower NRM intensity of

rhyolite from the Tarama Knoll was caused mainly by a smaller titanomagnetite content owing to low Fe diluted by the silica content.

3-4-2. Strongly magnetized Irabu knolls

The ship-underway-derived magnetization distribution showed that an intensity of up to 18 A/m in the Irabu knolls. This value is large compared with the magnetization intensities of MORs, which are typically several A/m or less even on younger seafloors [e.g., *Dyment et al*., 2015]. Moreover, the magnetization intensity from the AUV, which reflects a shallower part of the sub-seafloor, is up to 60 A/m. This amplitude is also significantly larger than estimated magnetization variation from near-seafloor magnetic anomalies of other hydrothermal sites [e.g., *Tivey and Dyment*, 2010]. This extremely high crustal magnetization in the Irabu knolls is likely caused by fresh basaltic extrusives containing numerous SD grains with low Ti content.

The rock magnetic analysis of the fourteen collected volcanic rocks collected from the Irabu knolls showed large variation of NRM intensity ranging from 7 A/m to 214 A/m. The NRM of >200 A/m is the largest reported NRM value of volcanic rocks collected from the seafloor, including MOR and back-arc basin basalts [e.g., *Gee and Kent*, 2007; Chapter 2]. As previously mentioned, all samples have not been affected by low-temperature oxidation (maghemitization). Because the bulk element composition of Fe is almost the same among all samples [T. Nozaki, personal communication], the potential of erupted magma for the crystallization of titanomagnetite is not much different. Therefore, the titanomagnetite amount, magnetic domain state, and Ti content of titanomagnetite are important for NRM variation among samples from the Irabu knolls.

The sample with the highest NRM intensity, HPD#1330G03, shows a magnetic domain state of complete SD and a titanomagnetite amount of 0.8 wt.% (Table 3-1; Figs. 3-7D and 3-8). The other four samples with a magnetic domain state of complete SD, HPD#1330G07, HPD#1330G08, HPD#1332G05, and HPD#1624G01, also show relatively high NRM intensities of 38–116 A/m and similar titanomagnetite contents of 0.7–1.1 wt.% (Table 3-1; Fig. 3-7D). In contrast, three samples with magnetic domain states of PSD and MD (HPD#1330G01, HPD#1330G02, and HPD#1330G06) show small NRM intensities of 7–10 A/m but larger titanomagnetite amounts of 2.5–3.2 wt.%

(Table 3-1; Figs. 3-7D and 3-8). These results indicate that the contribution of SD grains rather than abundant MD grains is important for acquisition of strong remanent magnetization.

Low NRM intensity of 8 A/m was also observed for sample HPD#1330G05, in which the contributions of SP grains were shown by the FORC measurement (Fig. 3-8). The values of Mr/Ms and Hcr/Hc show SD–SP mixing trends in the Day plot (Fig. 3-7D). The titanomagnetite amount of this sample, at 0.2 wt.%, is small compared with that in other samples with SD and MD grains, suggesting that crystal growth of titanomagnetite is insufficient due to the rapid cooling rate or reduction of pressure. The other two samples, HPD#1332G02 and HPD#1332G04, with low titanomagnetite amount of 0.2 wt.% and low NRM were likely affected by SP contribution. These results indicate that rapid crystal growth inhibits the creation of titanomagnetite and enables the formation of SP rather than SD grains. Because the NRM values are higher in SD grains than those in both MD and SP grains, proper crystal growth rate in the formation of SD grains is important for the acquisition of high NRM values. The growth rate of SD grains is faster than MD crystallization and slower than SP crystallization.

All of the rocks from the Irabu knolls show a Ti content (x) of 0.15–0.45 for titanomagnetite ($Fe_{3-x}Ti_xO_4$), which is generally smaller than that of primary oxide in MOR basalts (MORBs), i.e. $Fe_{2.4}Ti_{0.6}O_4$, which is known as TM60 because it contains 60 mol.% Ti. The actual compositions in MORBs range from TM50 to TM70 [*Dunlop and Ozdemir*, 2007]. Although titanomagnetite has the same inverse spinel structure as magnetite, the Curie temperature generally shows a linear decrease with an increase in the Ti content because the exchange interaction is weakened. The replacement of Fe in octahedral sites by nonmagnetic Ti^{4+} causes a decrease in spontaneous magnetization as x increases. Therefore, the magnetization in the host rock of the Irabu knolls is potentially high magnetization owing to low-Ti titanomagnetite grains. *Hunt et al.* [1995] reported an empirical relationship, showing that saturation magnetization (Js) decreases linearly with an increase in Ti content (x) for titanomagnetite ($Fe_{3-x}Ti_xO_4$) as follows: $Js = 92 \times (1 - 1.23\ x)$. Although the value of saturation magnetization for MORBs such as TM60 ($x = 0.6$) is 24 A/m, the values for samples from the Irabu knolls (x = 0.15–0.45) are significantly larger, ranging from 41 A/m to 74 A/m. The bulk element composition of Ti regarded as TiO_2 for samples from the Irabu knolls, at 0.5–

0.8% [T. Nozaki, personal communication], is also small compared with that from MORBs. For the latter, 2010 samples show Ti contents of 1.5% with 1σ of 0.4% [W*hite and Klein*, 2014]. These observations indicate that the Irabu knolls consist of volcanic extrusives generated from low-Ti magma resulting higher NRM.

In summary, the high magnetization of the Irabu knolls reflects the non-oxidized (fresh) volcanic layer containing abundant SD grains of titanomagnetite with low Ti content. The large amplitude of magnetization derived from AUV's magnetic anomaly, at ~60 A/m, is sensitive for the uppermost crust a few hundred meters below the seafloor, which reflects the contribution of abundant SD titanomagnetite grains that cooled near the seafloor. The volcanic rock samples collected from the seafloor surface have not been oxidized. The smaller amplitude of the ship-underway-derived magnetization, at~18 A/m, is attributed to the effects of the oxidized extrusive layer that erupted previously and large contributions of MD titanomagnetite grains within owing gradual cooling in deep.

3-4-3. Processes causing weak magnetization zones

The magnetization distribution from near-seafloor magnetic anomalies at an altitude of ~100 m shows that the reduced magnetization zones are clearly associated with active hydrothermal vent fields in both the Tarama and Irabu fields. The following factors are possible causes of the magnetization reduction: (i) hydrothermal alteration, in which volcanogenic magnetic minerals such as titanomagnetite are replaced by non-magnetic minerals within the up-flow zone [e.g., *Johnson et al*., 1982; *Hall*, 1992]; and/or (ii) the presence of non-magnetic hydrothermal deposits [*Szitkar et al*., 2014a]. Previous studies have revealed that the alteration of magnetic minerals rather than thermal demagnetization is the major cause of the reduced magnetization [*Hochstein and Soengkono*, 1997; *Tivey and Johnson*, 2002]. Moreover, the lavas in the Tarama and Irabu knolls have Curie temperatures of 280–490°C, which are significantly higher than those of MORBs such as ~170°C for TM60. This suggests a small thermal effect for near-seafloor magnetic anomalies, reflecting a shallow sub-seafloor layer.

Low magnetization zones were observed at the southern caldera of the Irabu-East (Fig. 3-5P) and at the NW caldera rim. This reduced magnetization is generally elongated NE–SW parallel to the local strike of the caldera and also extends into the

caldera wall. In this area, active hydrothermal vents with chimney structures and dead chimneys have been observed in previous ROV surveys (Fig. 3-5P) that extended horizontally at least 100 m (Fig. 3-5P). The extent of the hydrothermal deposit corresponds to the area with low magnetization <12 A/m at most. The correspondence of a magnetic low with hydrothermal activity indicates that the reduced magnetization zones are associated with hydrothermal processes. Because magnetic anomalies from AUV data at an altitude of ~100 m are sensitive for the shallow crust a few hundred meters below the seafloor, the low magnetization zones reflect the source at depths from near-seafloor to hundreds of meters. The magnetic low likely reflects the discharge zones of the hydrothermal fluid, where hydrothermal alteration occurs and hydrothermally deposits accumulate. The area with magnetization intensity <12 A/m extends across an area of ~200 m × ~300 m, suggesting that crustal alteration or hydrothermal deposition occurs at the same scale. This low magnetization zone associated with hydrothermal activity in the southern caldera of the Irabu-East is large compared with the lateral scale of hydrothermal alteration found at MORs [e.g., *Tivey and Dyment*, 2010; *Tivey and Johnson*, 2002]. The lowest peak of the magnetization intensity was positioned at the foot of the caldera wall (Fig. 3-5P), which implies that the up-flow zone is somewhat restricted by the caldera fault structure.

An additional low magnetization zone observed at the western slope of the Irabu-West (Fig. 3-5Q) is generally elongated E–W parallel to the local strike of the rift faulting. The area with magnetization intensity <12 A/m extends across an area of ~250 m × ~300 m. In this area, active hydrothermal vents with chimney structures and dead chimneys have been observed at the top of Irabu-West in previous ROV surveys (Fig. 3-5Q). Reduced magnetization zones may reflect hydrothermal alteration or hydrothermal deposit accumulation. The lowest peak of the magnetization intensity was positioned 200 m SW of the confirmed hydrothermal activity (Fig. 3-5Q). The low magnetization zone elongation occurs in the eastern side parallel to the direction of regional rift faults. These observations imply that the western slope of the Irabu-West is generally altered due to hydrothermal activity controlled by regional rift faulting. Moreover, another low magnetization peak <8 A/m was identified at the eastern side of the Irabu-West. A high magnetization zone >20 A/m bridges the two reduced magnetization zones on the western and eastern slopes of the Irabu-West. Because the volcanic rocks of basalt to andesite were collected near this high magnetization zone

(Fig. 3-5Q), new lava flows with high magnetization likely overprinted the crust and separated the large reduced magnetization zones as two magnetic lows. Thermomagnetic analysis of these collected rocks shows that low-temperature oxidation did not occur, suggesting that these samples are newly erupted and have not been exposed in the seafloor even for a short time. This interpretation imply that the reduced magnetization zones formed prior to recent volcanic eruption across an area of ~600 m × ~250 m and are generally elongated E–W direction approximately parallel to the local strike of the rift faulting.

The low magnetization zone of <12 A/m was also observed at the northern caldera of the Irabu-East (Fig. 3-5R). This magnetic low is located at the NE caldera rim. Therefore it is expected that an additional hydrothermal field exists at this caldera boundary fault. Although no geological observations were conducted in this region, the correspondence of the magnetic low with the caldera structure is similar to the southern caldera of Irabu-East, where active hydrothermal activity was confirmed. The previous submersible surveys discovered seawater discoloration 200 m from low magnetic zones twice [YK12-05 cruise report]. These observations suggest that an unconfirmed hydrothermal vent field has likely developed at the NE rim of the northern caldera in the Irabu-East.

3-5. Chapter Conclusions

Near-seafloor magnetic fields were obtained by using the AUV *URASHIMA* near the active hydrothermal fields of the Tarama and Irabu knolls, the Okinawa Trough. The volcanic rocks collected from both knolls were used for rock magnetic measurements and petrological observations. The integrated analysis of the magnetic anomaly and rock magnetic properties led to the following conclusions:

1. The hydrothermal vent fields of the arc region of the Tarama Knoll and the back-arc rift of the Irabu knolls in the Okinawa Trough are characterized by reduced magnetization. The hydrothermal alteration of magnetic minerals present in the extrusive lavas and the deposits of non-magnetic hydrothermal material are responsible for the reduced magnetization in these zones.
2. The regional magnetic anomalies of the Irabu and Tarama knolls reflect differences in the host rocks. The NRM intensity of the basaltic rocks from the Irabu knolls is approximately three times that of the rhyolite from the Tarama Knoll. A comparison of both samples with a similar magnetic domain state revealed that the high NRM intensity of basaltic rocks was caused by larger titanomagnetite content. As a result, these basaltic rocks produced strong magnetic anomalies near the Irabu knolls.
3. The basaltic rocks from the Irabu knolls show high NRM intensity ranging from 7 A/m to 214 A/m. The sample with 214 A/m NRM shows the highest NRM value in volcanic rock collected from the seafloor worldwide. This extremely strong NRM was caused by less oxidation, abundant SD titanomagnetite grains formed under proper crystal growth rates, and low Ti content for titanomagnetite. These strongly magnetized basaltic host rocks produced large variations of magnetic anomalies in the Irabu knoll, resulting in a clear magnetic contrast between hydrothermal discharge zones and their surroundings areas.
4. The reduced magnetization zones related to hydrothermal activity of the Irabu knolls are located at the rim of the caldera in an elongated direction parallel to the local strike of the caldera, and extend into the caldera wall. These observations suggest that the hydrothermal fluids ascended through the caldera fault and caused accumulation of hydrothermal deposits and the occurrence of hydrothermally altered zones in both the caldera floor rim and wall.

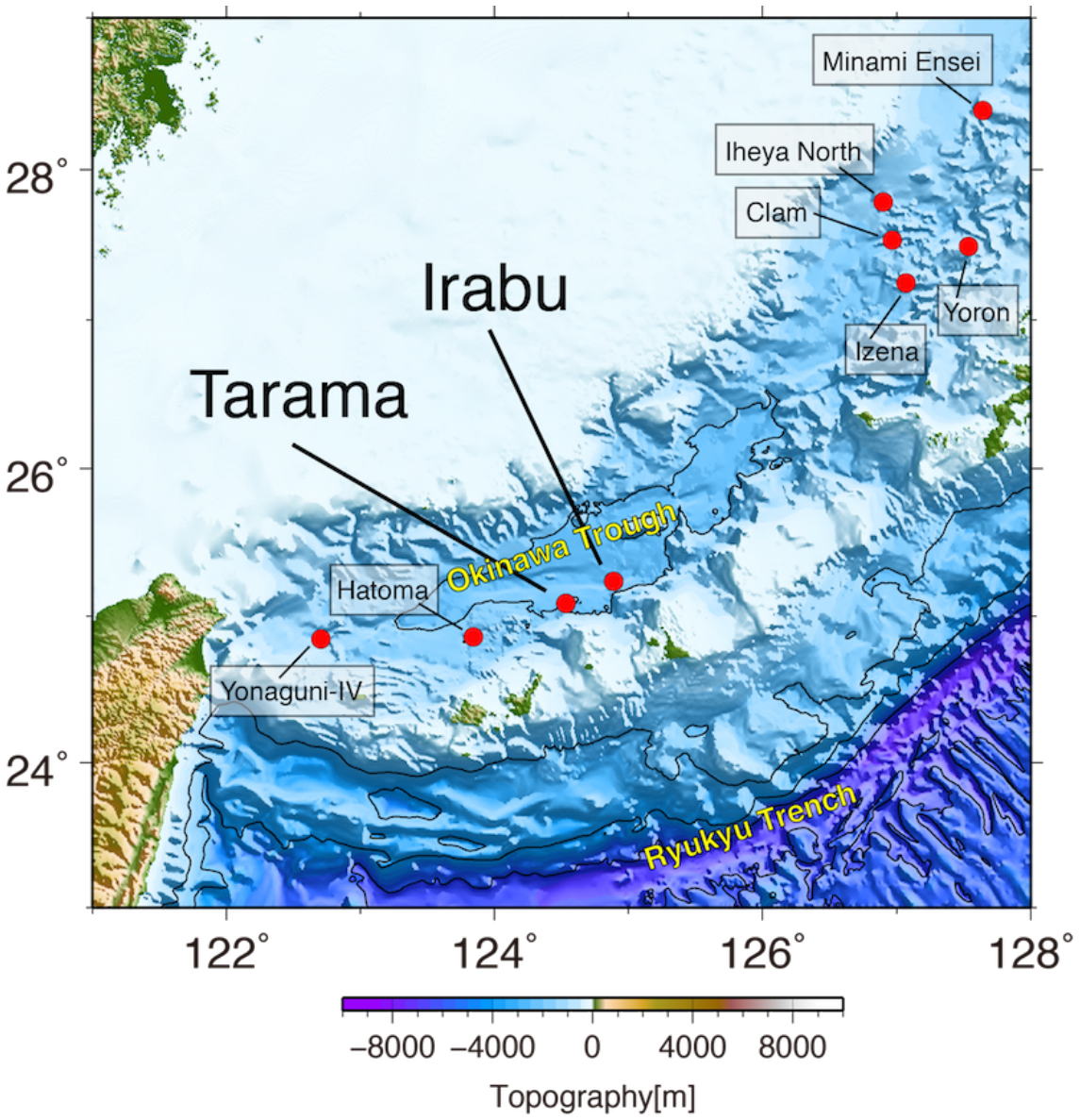

Figure 3-1. Locations of the Tarama and Irabu knolls in the southern Okinawa Trough.

Seafloor bathymetric map indicating the seafloor hydrothermal fields of the Okinawa Trough by red circles.

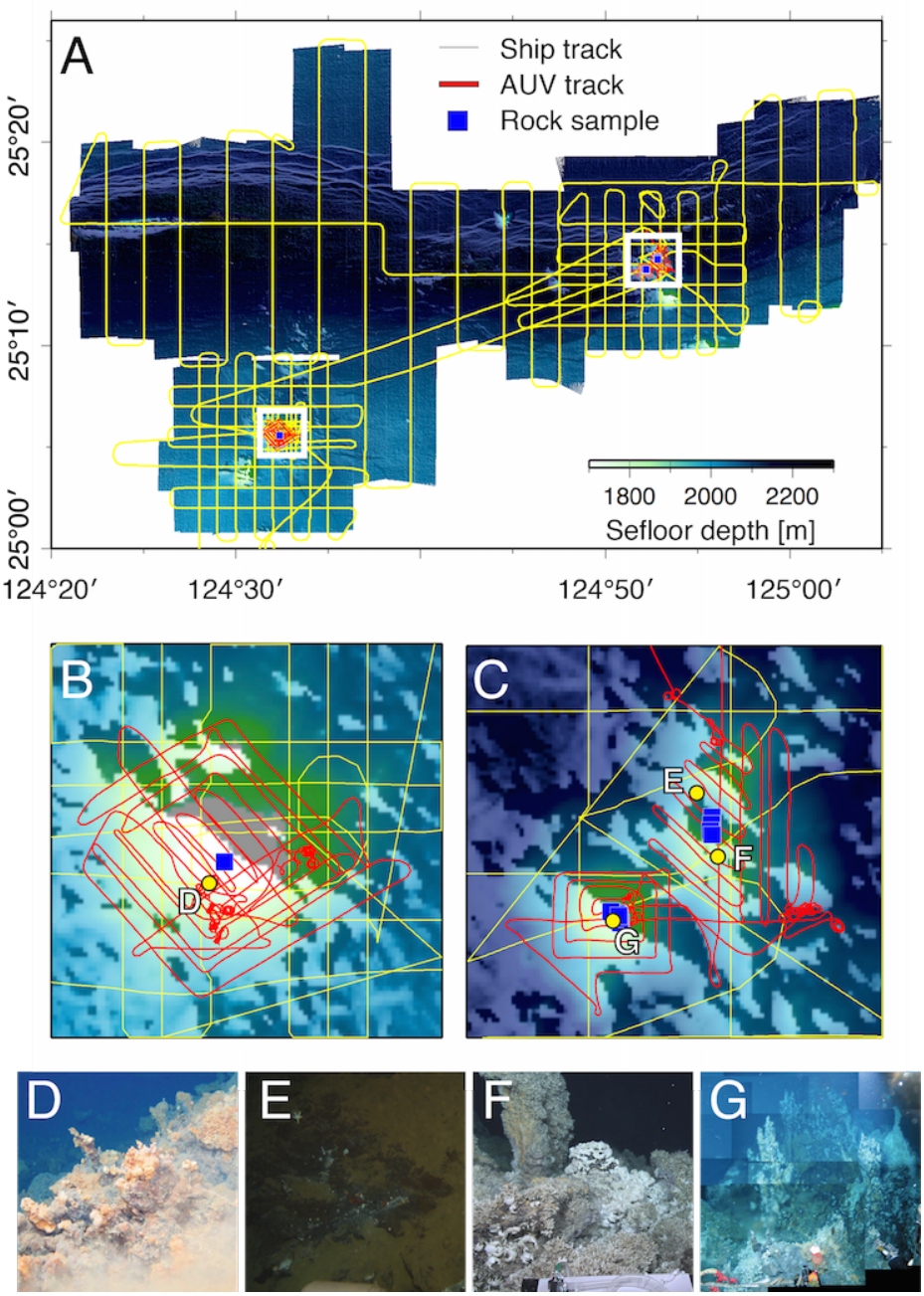

Figure 3-2. Survey tracks and lava sample locations.

The ship-underway (yellow lines) and autonomous underwater vehicle (AUV; red lines) survey tracks obtained during the *Yokosuka* YK14-16 cruise and locations of collected rock sample (blue squares). (A) Regional map of the area. (B), (C) Magnified areas near the Tarama Knoll and the Irabu knolls, respectively. (D) Hydrothermal site on the Tarama Knoll [*Yamanaka et al.*, 2015]. (E) Hydrothermal biota of bivalves and crustaceans. (F) Hydrothermal site on the Irabu-East. (G) Hydrothermal site on the Irabu-West [NT13-25 cruise report].

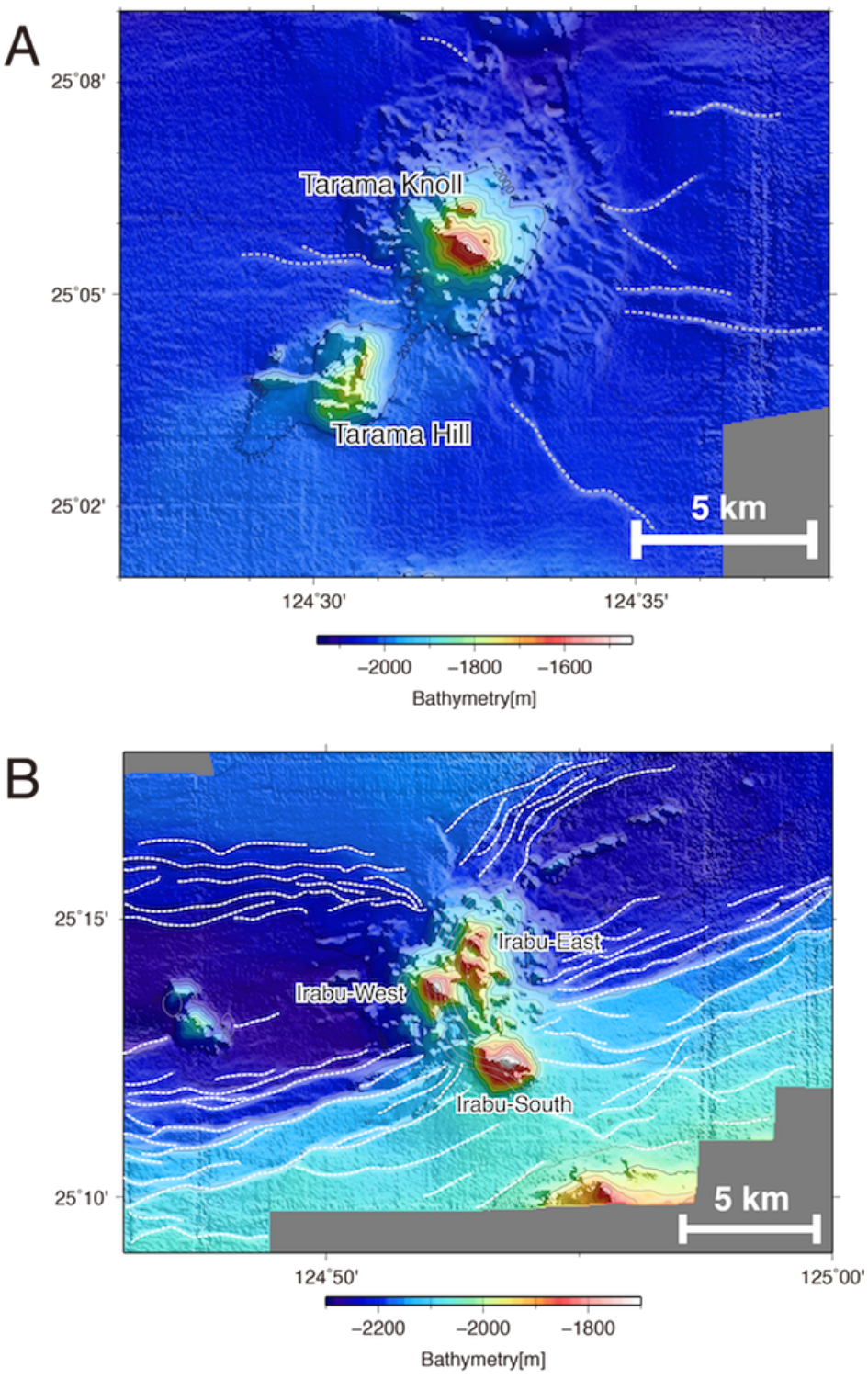

Figure 3-3. Seafloor bathymetry of the Tarama and Irabu knolls.

Seafloor bathymetric map showing (A) the Tarama Knoll and (B) the Irabu knolls. The Tarama Hill is located SW of the Tarama Knoll. The Irabu knolls consist of Irabu-West, Irabu-East, and Irabu-South. The white dashed lines show the interpreted topographic lineaments.

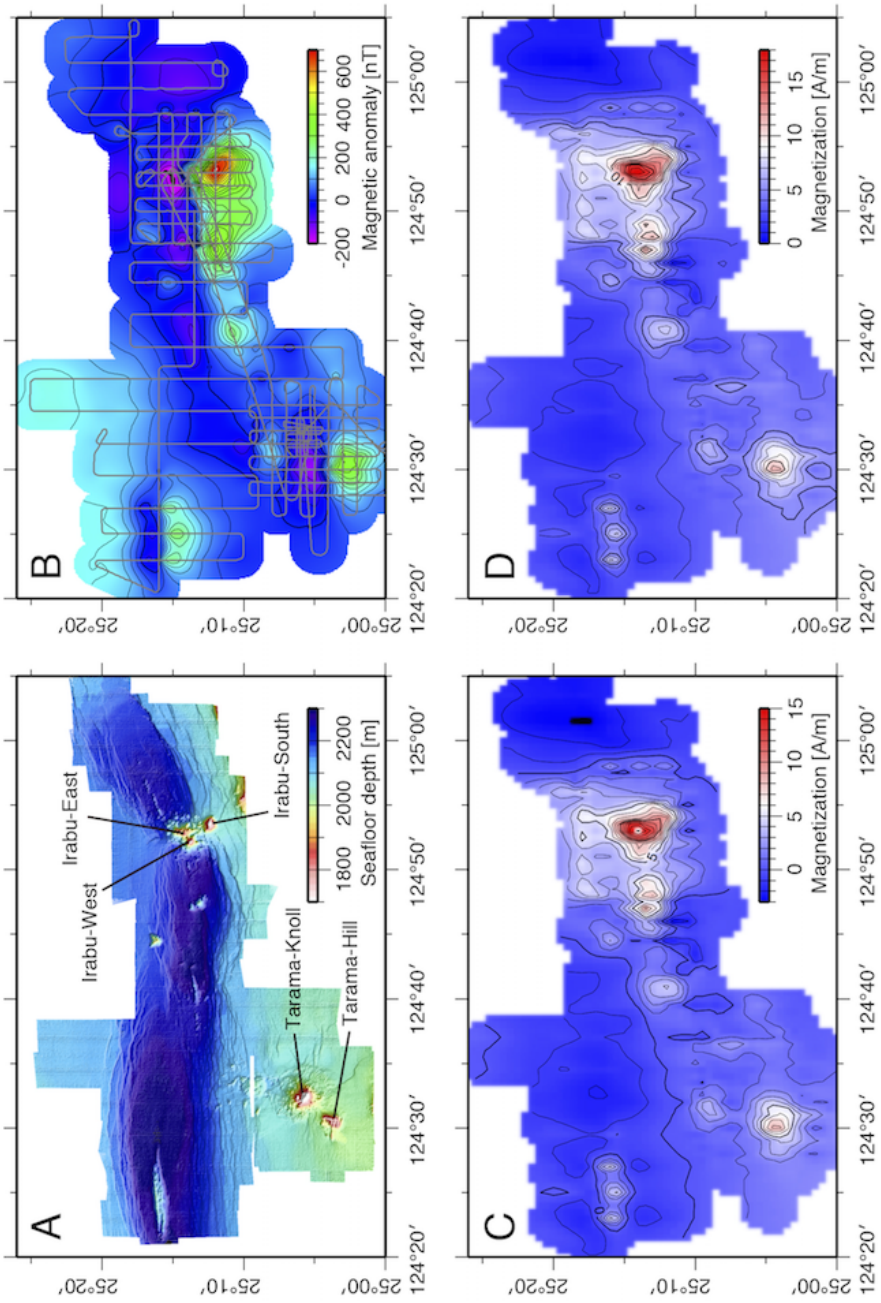

Figure 3-4. Seafloor bathymetry, magnetic anomalies and magnetization from ship-underway mapping.

(A) Seafloor bathymetric map and (B) magnetic anomaly map with a contour interval of 50 nT. The survey tracks are shown in gray lines. (C) Crustal magnetization calculated from magnetic anomaly amplitudes with a contours interval of 1 A/m. (D). Crustal magnetization after the addition of the annihilator calculated from magnetic anomaly amplitudes. The contours are at 1 A/m intervals.

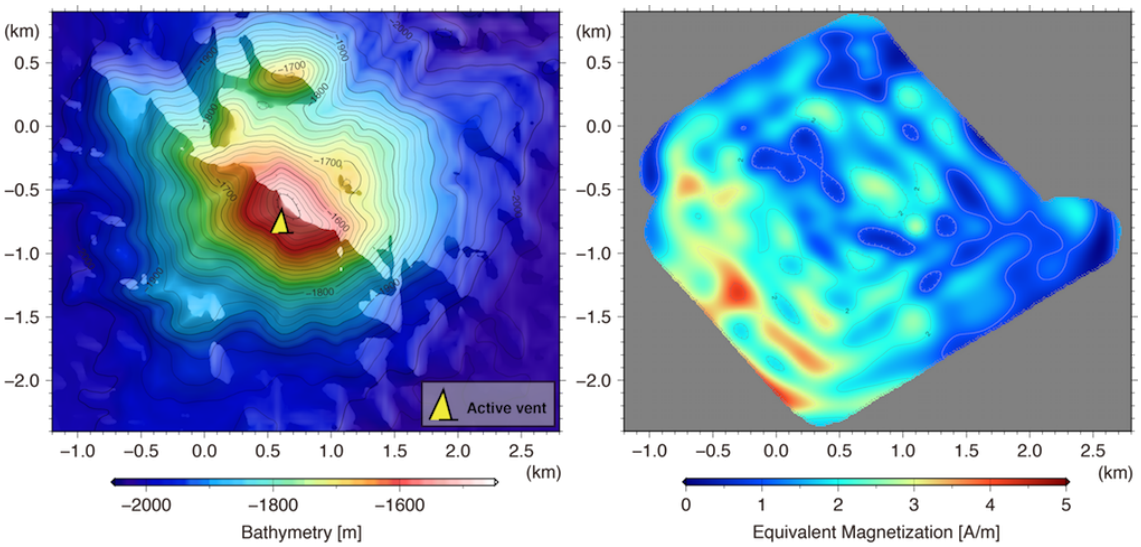

Figure 3-5. Magnetization distributions and seafloor bathymetry of Tarama Knoll. (Left) Seafloor bathymetric map with contours at 100 m intervals. The active hydrothermal vent confirmed in a previous cruise is shown by the yellow cone. (Right) Crustal magnetization calculated from magnetic anomaly amplitudes collected along autonomous underwater vehicle (AUV) tracks at an altitude of ~100 m. The contours are at 1 A/m intervals.

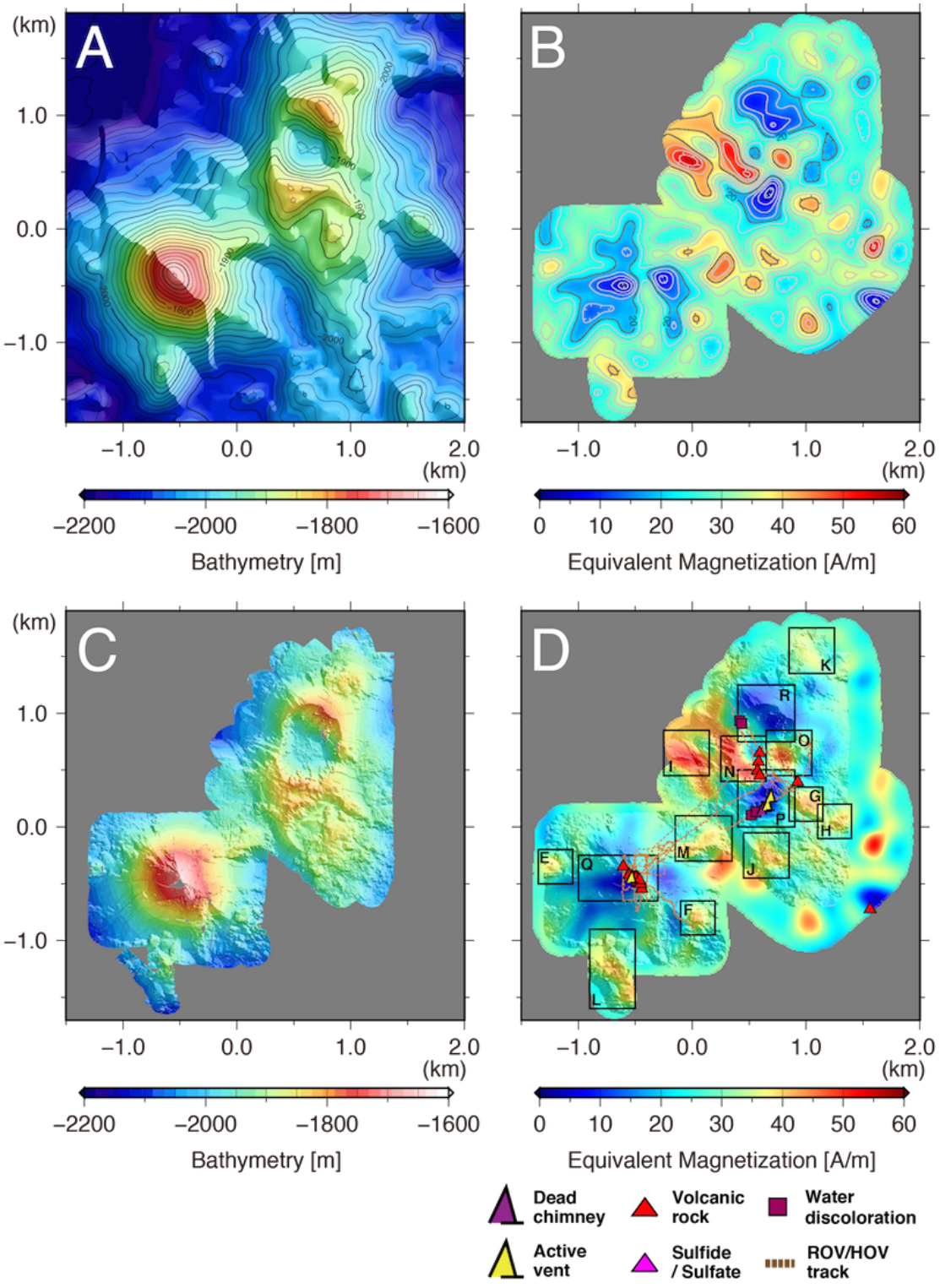
A
B
C
D
(km)
1.0
0.0
−1.0
−1.0
0.0
1.0
2.0
(km)
−2200
−2000
−1800
−1600
Bathymetry [m]
0
10
20
30
40
50
60
Equivalent Magnetization [A/m]
K
R
O
I
N
A
G
P
H
M
J
E
Q
F
L
Dead chimney
Volcanic rock
Water discoloration
Active vent
Sulfide / Sulfate
ROV/HOV track

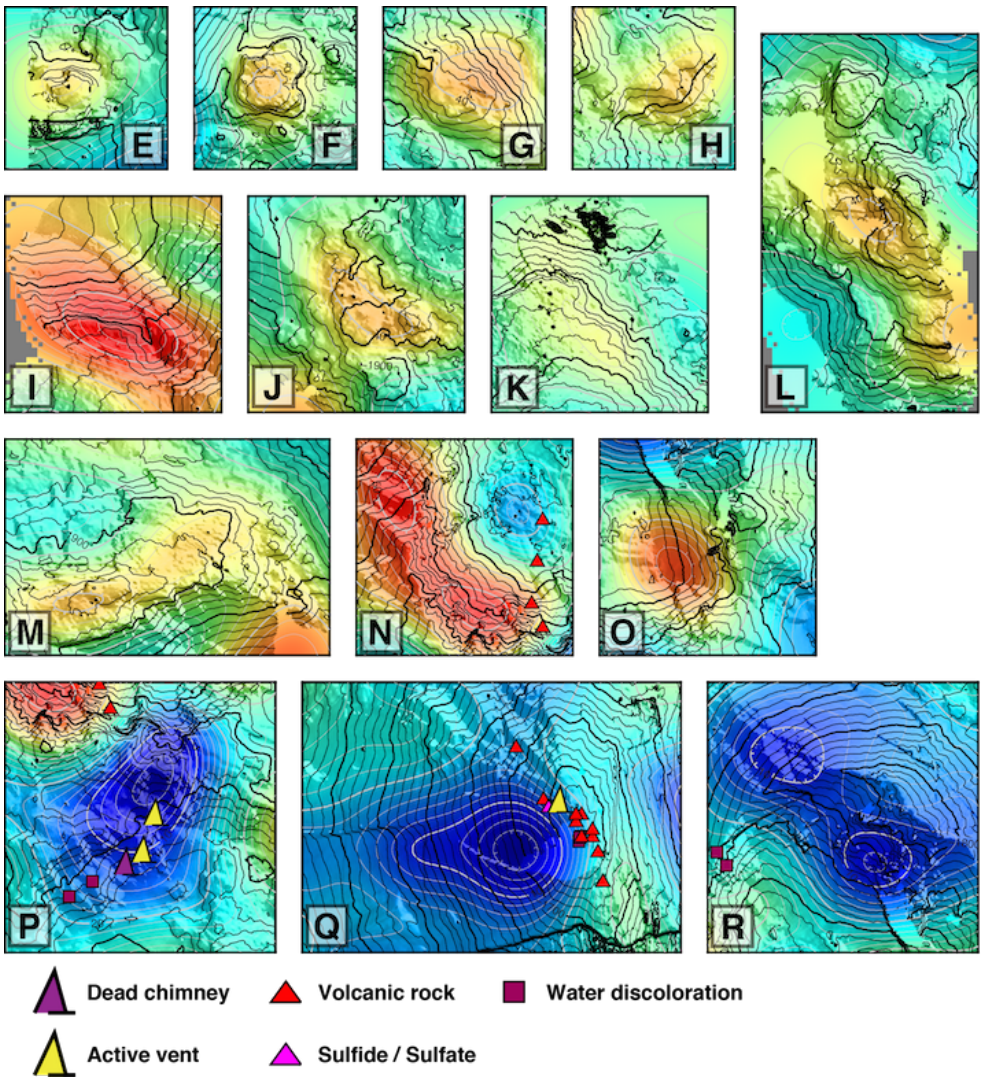

Figure 3-6. Magnetization distributions and seafloor bathymetry of Irabu knolls.
(A) Seafloor bathymetry from ship-underway data of the Tarama Knoll with contours at 20 m intervals. (B) Crustal magnetization calculated from magnetic anomaly amplitudes collected along autonomous underwater vehicle (AUV) tracks at an altitude of ~100 m. The contours are at 1 A/m intervals. (C) High-resolution seafloor bathymetry from AUV data. (D) Crustal magnetization with high-resolution bathymetric shading. Dead chimneys (purple cones), active hydrothermal vents (yellow cones), water discoloration (purple square), volcanic rocks (red triangles), and sulfide and sulfate (purple triangle) reported in previous remotely operated vehicle (ROV) surveys (grey broken lines). Magnified maps in (E)–(R) show crustal magnetization. The symbols comparing with high-resolution seafloor bathymetry are the same as those in (D). Bathymetric contours (black) are at 10 m intervals. Magnetization contours (white) are at 2 A/m intervals.

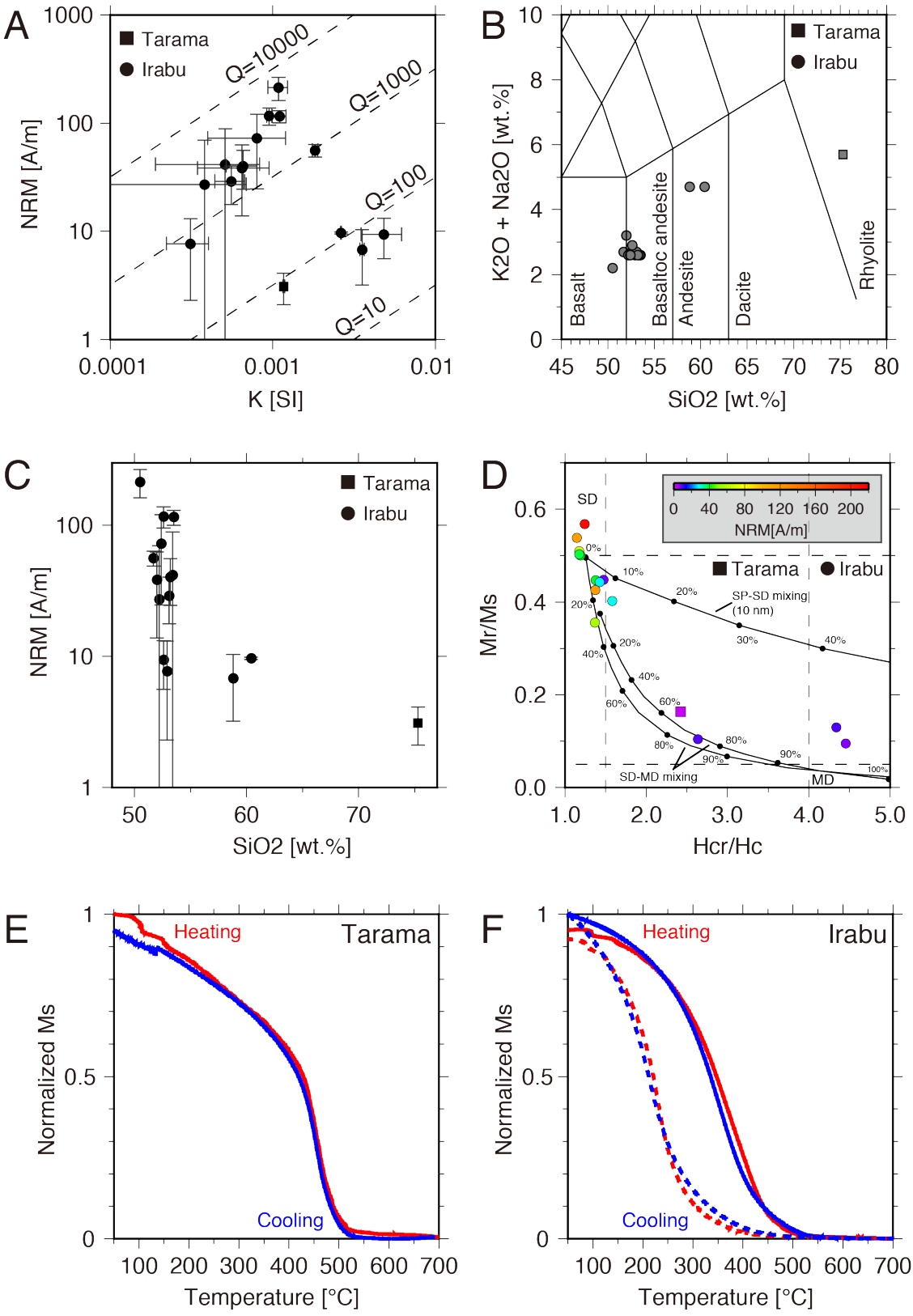

Figure 3-7. Rock magnetic properties of collected lava samples.

Characteristics of rock samples from the Tarama and Irabu knolls.

(continued)

(A) Magnetic susceptibility (K) versus natural remanent magnetization (NRM), illustrating the Koenigsberger ratio (NRM/induced magnetization). (B) Silica versus total alkali, illustrating the type of volcanic rock [T. Nozaki, personal communication]. (C) Silica versus NRM. (D) Day plot [*Day et al*., 1977] showing NRM intensity. The solid lines show theoretical mixing curves of SD–MD and SP–SD for magnetite [*Dunlop*, 2002]. SD, single-domain; MD, multi-domain; SP, super-paramagnetic. (E) Warming (red) and cooling (blue) thermomagnetic curves from 50°C to 700°C for sample HPD#1109R01 from the Tarama Knoll. (F) Warming (red) and cooling (blue) thermomagnetic curves from 50°C to 700°C for samples HPD#1330G03 (solid line) and HPD#1330G06 (broken line) from the Irabu knolls.

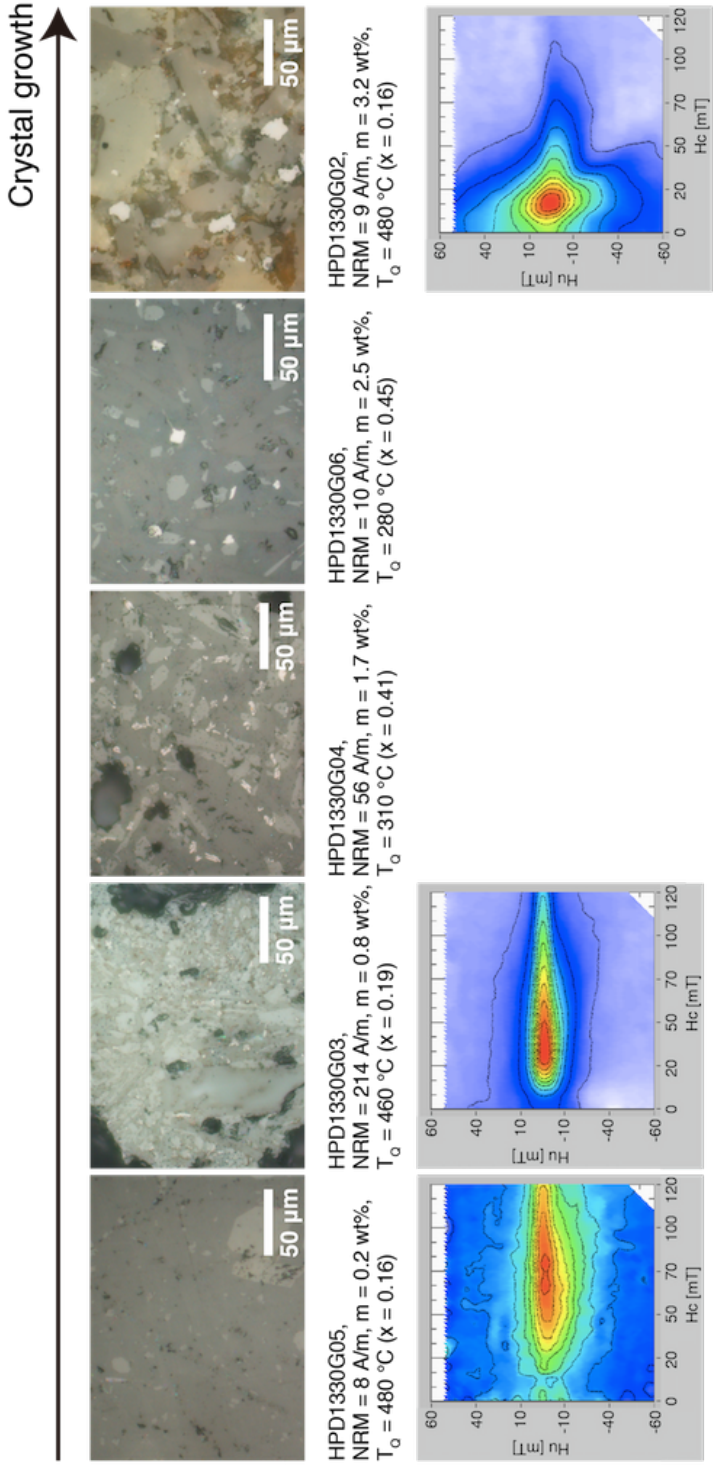

Figure 3-8. Petrography and first-order reversal curve (FORC) diagrams of lavas from the Irabu knolls.

Reflection images (top), and first-order reversal curve (FORC) diagrams of representative samples from the Irabu knolls, illustrating the relationship between the petrographical, grain size, and magnetic domain state.

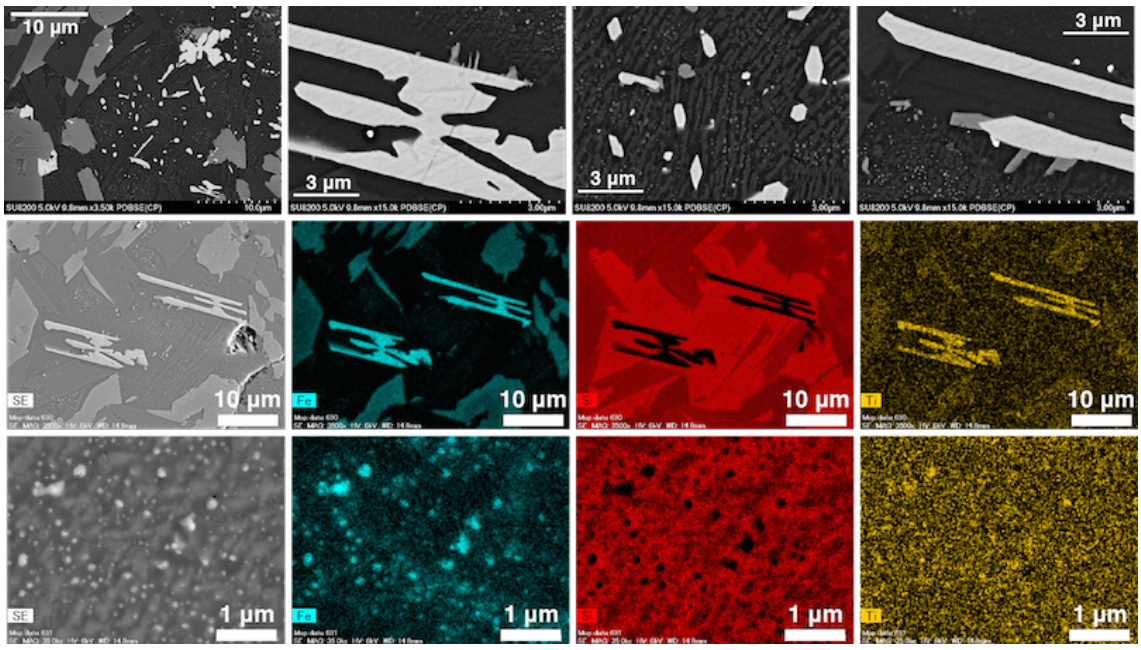

Figure 3-9. Backscattered electron (BSE) images and composition mapping of the basaltic lava sample with the highest magnetization (HPD#1330G03) from the Irabu knolls.

Table 3-1. Rock magnetic properties including natural remanent magnetization (NRM) and magnetic susceptibility of lava samples from the Tarama and Irabu knolls.

Sample name	Location	Rock type	Latitude (°N)	Longitude (°E)	Depth (m)	SiO_2 (%)	K_2O+Na_2O (%)	Fe_2O_3 (%)	TiO_2 (%)	Density (kg/m^3)	σ_{DEN} (kg/m^3)	NRM (A/m)	σ_{NRM} (A/m)	K (SI)	σ_K (SI)	Q
HPD#1109R01	Tarama	RL	25.0930	124.5394	1536	75.3	5.7	3.2	0.2	2.61	0.04	3.1	1.0	0.0012	0.00002	84
HPD#1330G01	Irabu	AN	25.2392	124.8809	1974	58.8	4.7	9.8	0.8	2.62	0.06	6.8	3.6	0.0035	0.00010	61
HPD#1330G02	Irabu	BA	25.2385	124.8808	1971	52.6	2.7	11.2	0.7	2.94	0.04	9.4	3.8	0.0048	0.00135	61
HPD#1330G03	Irabu	BS	25.2378	124.8807	1918	50.5	2.2	10.9	0.6	2.97	0.03	214.4	52.0	0.0011	0.00015	6209
HPD#1330G04	Irabu	BS	25.2374	124.8809	1880	51.7	2.7	10.1	0.7	2.88	0.02	56.3	7.5	0.0018	0.00007	972
HPD#1330G05	Irabu	BA	25.2290	124.8704	1660	52.9	2.6	10.3	0.6	2.77	0.03	7.7	5.4	0.0003	0.00009	779
HPD#1330G06	Irabu	AN	25.2290	124.8704	1660	60.4	4.7	10.1	0.8	2.39	0.01	9.7	0.2	0.0026	0.00002	116
HPD#1330G07	Irabu	BA	25.2292	124.8701	1646	53.5	2.6	10.4	0.6	2.85	0.01	115.6	15.0	0.0011	0.00011	3297
HPD#1330G08	Irabu	BA	25.2293	124.8702	1650	53.4	2.6	10.5	0.6	2.82	0.03	41.7	47.4	0.0005	0.00032	2572
HPD#1332G02	Irabu	BA	25.2284	124.8706	1682	53.1	2.7	10.1	0.6	2.84	0.01	29.0	11.3	0.0006	0.00012	1644
HPD#1332G03	Irabu	BA	25.2290	124.8702	1647	53.2	2.6	10.1	0.6	2.82	0.02	40.3	15.7	0.0007	0.00014	1923
HPD#1332G04	Irabu	BA	25.2293	124.8701	1647	52.2	2.6	10.0	0.6	2.82	0.04	27.2	42.7	0.0004	0.00031	2245
HPD#1332G05	Irabu	BA	25.2295	124.8695	1632	52.4	2.6	10.2	0.6	2.83	0.04	72.6	47.9	0.0008	0.00040	2852
HPD#1624R01	Irabu	BA	25.2288	124.8705	1675	52.0	3.2	10.7	0.5	2.84	0.04	38.4	24.5	0.0006	0.00030	1866
HPD#1624R02	Irabu	BA	25.2291	124.8704	1661	52.6	2.9	10.4	0.6	2.86	0.03	117.1	21.5	0.0010	0.00004	3868

Abbrevations are RL, rhyolite; AN, andesite; BA, basaltic andesite; BS, basalt; σ_{DEN}, standard deviation of density; NRM, natural remanent magnetization; σ_{NRM}, standard deviation of natural remanent magnetization; K, magnetic susceptibility; σ_K, standard deviation of magnetic susceptibility; Q, Koenigsberger ratio.

Table 3-2. Detailed rock magnetic properties of lava samples from the Tarama and Irabu knolls.

Sample name	MDF (mT)	T_C (°C)	*x*	Ms-grain (Am2/kg)	Hcr/Hc	Mr/Ms	Magnetic domain state	Ms (Am^2/kg)	Titanomagnetite (wt%)	Hc (mT)
HPD#1109R01	-	490	0.15	76	2.42	0.16	SD + MD	0.7	0.9	21.2
HPD#1330G01	100	280	0.45	41	4.45	0.10	MD + SD + SP	1.3	3.2	5.9
HPD#1330G02	37	480	0.16	74	2.64	0.10	MD + SD	2.4	3.2	10.8
HPD#1330G03	83	460	0.19	70	1.24	0.57	SD	0.6	0.8	59.3
HPD#1330G04	39	310	0.41	45	1.37	0.36	SD + MD	0.8	1.7	14.2
HPD#1330G05	128	480	0.16	74	1.48	0.45	SD + SP	0.2	0.2	63.3
HPD#1330G06	84	280	0.45	41	4.34	0.13	MD + SD + SP	1.0	2.5	8.0
HPD#1330G07	48	390	0.30	58	1.15	0.54	SD	0.6	1.0	31.2
HPD#1330G08	58	430	0.24	65	1.19	0.50	SD	0.6	0.9	38.2
HPD#1332G02	73	460	0.19	70	1.58	0.40	SD + SP	0.2	0.2	59.4
HPD#1332G03	71	470	0.18	72	1.38	0.45	SD + SP	0.2	0.3	57.4
HPD#1332G04	62	480	0.16	74	1.43	0.44	SD + SP	0.2	0.2	65.6
HPD#1332G05	40	390	0.30	58	1.17	0.51	SD	0.7	1.1	29.8
HPD#1624R01	53	430	0.24	65	1.17	0.50	SD	0.5	0.7	28.4
HPD#1624R02	43	480	0.16	74	1.37	0.43	SD + MD	0.3	0.5	42.1

Abbrevations are MDF, median destructive field; T_C, Curie temperuture; *x*, Ti conten; Ms-grain, saturation magnetization of titanomagnetite with Ti contetn *x;* Hcr, remanent coercivity; Hc, coercivity; Mr, saturation remanent magnetization; Ms, saturation magnetization.

Chapter 4

Ultramafic-hosted Yokoniwa Hydrothermal Field in Non-transform Offset Massif of Central Indian Ridge

In this chapter, I present a detailed analysis of the high-resolution vector magnetic measurements performed on the Yokoniwa Hydrothermal Field (YHF), an inactive ultramafic-hosted hydrothermal vent field, by using the data of the HOV *SHINKAI 6500* and the AUV *r2D4*. The YHF is developed at a non-transform offset massif of the Central Indian Ridge (CIR). Dead chimneys have been widely observed near the YHF along with a very weak venting of low-temperature fluids, indicating that the hydrothermal activity of the YHF is almost finished. The distribution of crustal magnetization from the magnetic anomaly reveals that the YHF is associated with enhanced magnetization. The results of rock magnetic analysis on seafloor rock samples including basalt, dolerite, gabbro, serpentinized peridotite, and hydrothermal sulfide show that only highly serpentinized peridotite carries high magnetic susceptibility and the natural remanent magnetization (NRM) intensity that can explain the high magnetization of the YHF. These observations reflect abundant and strongly magnetized magnetite grains within the highly serpentinized peridotite. The present analysis reveals the origin of the magnetic high and the development of subsurface chemical processes in ultramafic-hosted hydrothermal systems. Furthermore, these results highlight the use of near-seafloor magnetic field measurements as a powerful tool for detecting and characterizing ultramafic-hosted hydrothermal systems.

4-1. Geological Background

The YHF (Fig. 4-1) is located in the southernmost part of the CIR near the Rodriguez triple junction. The tectonic development of the area has been reported by past studies [*Briais*, 1995; *Honsho et al*., 1996; *Mendel et al*., 2000; *Okino et al*, 2015; *Sato et al*., 2009]. The CIR is a slow–intermediate-rate spreading ridge system with a well-developed axial valley, which is segmented by many fracture zones and non-transform discontinuities (NTDs). The full spreading rate in the southernmost segment, CIR-segment1 (CIR-S1), is approximately 47 mm/yr [MORVEL: *DeMets et al*., 2010]. The CIR-S1 is a 20-km segment with a deep axial valley, where undeformed volcanic cones and flat-topped volcanic knolls are distributed within the neo-volcanic zone. Since the segment length shortens in the farther off-axis, it is considered that CIR-S1 was newly created during the evolution of the triple junction [*Munschy and Schlich*, 1988; *Honsho et al*., 1996; *Mendel et al*., 2000].

There is a 26-km long lateral offset, i.e. NTD, between CIR-S1 and S2. Along the trace of this NTD, the ridge-parallel abyssal hill pattern is strewn with several domed highs composed of ultramafic rocks. In the northwest off-axis area of this NTD, a corrugated domed high, together with an exposure of highly deformed serpentinized peridotite and a high residual mantle Bouguer anomaly, have been recognized as an oceanic core complex (OCC), named the 25°S OCC, which is exposed along a detachment fault [*Mitchell et al*., 1998; *Morishita et al*., 2009; *Sato et al*., 2009]. Another OCC (the Uraniwa Hills) has been identified 15 km east of the ridge axis, where troctolites, olivine gabbros, and dunite have been sampled [*Kumagai et al*., 2008; *Morishita et al*., 2009; *Nakamura et al*, 2009]. A unique domed high with exposures of serpentinized peridotite, known as the Phoenix knoll, has been confirmed within the southern end of the axial valley of CIR-S2 [*Morishita et al*., 2015; *Okino et al*., 2015]. Between the two nodal basins at the northern end of CIR-S1 and the southern end of CIR-S2, a shallow domed-like massif has developed with height of 1700 m above the rift valley floor. This massif, the Yokoniwa Rise, is recognized as a non-transform offset (NTO) massif [*Okino et al*., 2015]. Previous sea-surface magnetic surveys identified the Brunhes/Matuyama boundary along the eastern off-axis of CIR-S1 and S2 [*Honsho et al*., 1999; *Sato et al*., 2009; *Okino et al*., 2015], suggesting that the Yokoniwa Rise formed in the Brunhes normal chron (~0.78Ma).

Two hydrothermal fields are located within CIR-S1. The Kairei Hydrothermal Field (KHF) was identified in 2000, near the top of the ridge-parallel volcanic knoll (the Hakuho Knoll), on the eastern flank of CIR-S1. The Hakuho Knoll is entirely composed of pillow and sheet lavas. The KHF is characterized by the high H_2 content of venting fluids and associated chemosynthetic ecosystems [*Gamo et al*., 2001; *Takai et al*., 2004], which are considered to reflect the interaction of seawater with troctolites beneath the Uraniwa Hills and/or serpentinization processes along a detachment fault beneath [*Nakamura et al*., 2009; *Okino et al*., 2015].

The YHF was identified in 2009, and is located on top of the Yokoniwa Rise. Hydrothermal sulfides and small dead chimneys (< 1 m) have been observed (Fig. 4-2-v), along with weak venting of low-temperature fluids (< 5°C) and a small biological community (< 1 m^2) (Fig. 4-2-iv). Submersible surveys have revealed that the serpentinized peridotite is exposed extensively on the eastern slope of the Yokoniwa Rise (25°15'–17'S and 70°04'–05'E), while small quantities of gabbro, dolerite, and basalt have been identified in a few outcrops (Fig. 4-2) [*Okino et al*., 2015; *Sato et al*., 2015a]. Basalts outcrops on the western slopes of the Yokoniwa Rise (Fig. 4-2) are partly covered by sediments.

4-2. Data and Methods

4-2-1. Imaging the magnetic anomaly: AUV

A high-resolution magnetic survey of the YHF region was performed using the AUV *r2D4* during a cruise of the R/V *Hakuho-maru* (KH10-6) in November 2010. The AUV collected magnetic field data along four N–S track lines within an area of ~7 by ~2 km and at an altitude of 30–200 m (mean = 80 m; Fig. 4-2). A three-axis fluxgate type magnetometer with a sampling rate of 8 Hz was attached to the AUV. A calibration spin of the vehicle, known as a figure-8 loop, was performed in order to correct for the effect of vehicle magnetization, which was performed using the calibration technique of *Isezaki* [1986]. Attitude data (heading, pitch, and roll) were collected independently using an optical gyroscope (IXEA PHINS IMU) with a sampling rate of 2 Hz. Magnetic data were merged with attitude data after considering a time shift of 3.75 s between them. The ambient geomagnetic field vector was estimated from the International Geomagnetic Reference Field (IGRF) [*IAGA Working Group V-MOD*, 2010]. After the

vector summation of three components and the subtraction of the IGRF value, the total magnetic anomalies were obtained.

Magnetization intensity distributions were calculated using the Akaike's Bayesian Information Criterion (ABIC) inversion method developed by *Honsho et al*. [2012]. This approach is a space domain inversion method; therefore, the solution does not suffer from smoothing due to high-cut filtering or error caused by reducing data onto a flat surface, as can occur in other inversion methods [e.g., *Parker and Huestis*, 1974]. During this procedure, the magnetic data were merged with positioning and altitude data from a Doppler velocity log (WHN-300, Teledyne RD Instruments). Seafloor bathymetric data utilized in the analysis were obtained by up-sampling of a 20-m grid based on surface multibeam echo-sounding. The magnetization direction was assumed to be parallel to the IGRF at 25˚16'S, 70˚04'E (inclination: −60° and declination: −23°). For the magnetized source geometry, four cases were considered: constant 100 m and 500 m thick layers, a half-infinite body, and a layer with a flat lower boundary at a maximum water depth of +200 m.

4-2-2. Imaging the magnetic anomaly: HOV

Near-seafloor magnetic surveys around the YHF were performed using the HOV *SHINKAI 6500* during two scientific cruises of the R/V *Yokosuka*. Two dives (6K#1170 and 6K#1176) were conducted during the YK09-13-leg2 cruise in August 2009 and another dive (6K#1331) was completed during the YK13-03 cruise of March 2013 (Fig. 4-2). The HOV *SHINKAI 6500* covered 7.3 km in distance and provided magnetic data for both the western and eastern slopes of the Yokoniwa Rise, at between 3500 and 2400 m depth. A three-axis fluxgate type magnetometer was rigidly fixed to the front side of the *SHINKAI 6500*. Both vector magnetic data and the attitude of the submersible (heading, pitch, and roll) were collected at a sampling rate of 10 Hz. Attitude data were collected using a gyrocompass and an OCTANS motion sensor (IXBLUE Inc., United States). The calibration of vehicle magnetization was performed following the method of *Isezaki* [1986] and using data obtained during the helical loops performed spontaneously at depth of 500 m beneath the sea surface and 500 m above the seafloor. To obtain an optimal solution, a time shift of 0.4 s was added to attitude data. All dives were navigated by acoustic ranging using the super-short baseline

positioning system. The distance between the altimeter and the magnetic sensor were taken into account in order to obtain the geometry of the experiment. To estimate magnetization intensity distributions, two analytical methods were applied to all data: the forward modeling technique combined with frequency analysis [*Honsho et al*., 2009; *Talwani and Heirtzler*, 1964] for short-wavelength variations in the magnetic anomaly, and the inversion technique in frequency domain [*Honsho et al*., 2009, *Parker and Huestis*, 1974] for long-wavelength anomalies. To conduct these two-dimensional analyses, the dive tracks of 6K#1170 and 1331 were projected onto a straight line, with the track of 6K#1176 divided into two straight lines because its course changed significantly.

Based on short-wavelength variations in the magnetic anomaly, the absolute magnetization was estimated from the ratio of the observed magnetic anomaly to the synthetic anomaly computed for a 1 A/m magnetization intensity representing the unit magnetization intensity of the seafloor. The position and strike of magnetic boundaries, which can be obtained using vector data of the geomagnetic anomaly [*Seama et al*., 1993, *Korenaga*, 1995], were not considered in this analytical procedure. The horizontal (x) and vertical (z) components of the synthetic anomaly were calculated using the forward technique of a two-dimensional polygonal body [*Talwani and Heirtzler*, 1964], and were obtained every 1 m along each dive paths by summation of anomalies from the upper boundary of the magnetized layer, which was constrained by the topographic surface. The anomalous field (survey direction: ΔX, downward: ΔZ, total: ΔT) due to two-dimensionally infinite rectangular block is given by

$$\Delta X = \sum_{l=1}^{N} \hat{F}_x B_{lx}$$

$$\Delta Z = \sum_{l=1}^{N} \hat{F}_z B_{lz}$$

$$\Delta T = \sum_{l=1}^{N} \left(\hat{F}_x B_{lx} + \hat{F}_z B_{lz} \right)$$

where,

$$B_x = -2C_m (\mathbf{M} \cdot \hat{\mathbf{n}}) \left[\hat{\mathbf{s}}_\mathbf{x} \log \frac{r_2}{r_1} - \hat{\mathbf{s}}_\mathbf{z} (\theta_1 - \theta_2) \right]$$

$$B_z = -2C_m (\mathbf{M} \cdot \hat{\mathbf{n}}) \left[\hat{\mathbf{s}}_\mathbf{z} \log \frac{r_2}{r_1} - \hat{\mathbf{s}}_\mathbf{x} (\theta_1 - \theta_2) \right]$$

and C_m is magnetic permeability of free space in SI unit, r1 and r2 are distanced between observation point and each ends of the rectangular block, θ_1 and θ_2 are angle between observation point and each ends of the rectangular bloc, **M** is magnetization direction vector, $\hat{\mathbf{s}}_\mathbf{x}$ and $\hat{\mathbf{s}}_\mathbf{z}$ are unit vector parallel to both ends of block, $\hat{\mathbf{n}}$ is unit vector perpendicular to both ends of block, and F_x and F_z are ambient field parallel to the infinite rectangular block and downward direction. Seafloor topography was defined by the depth and altitude of the vehicle at the same interval. The magnetized layer was assumed to be uniformly magnetized with a half-infinite thickness and a magnetization direction parallel to IGRF. For short-wavelength anomaly variations, the contribution of magnetic sources shallower than 50 m was significant and synthetic anomalies were not affected by the differences in assumed layer thickness when the thickness was more than 100 m (Fig. 4-3). Before comparison between the observed and synthetic anomaly, a band-pass filter of between 20 and 300 m was applied in order to remove both long-wavelength variations and spiky noise. The ratio of the observed magnetic anomaly to the synthetic anomaly ratio, representing absolute magnetization, was calculated by the technique improved by *Honsho et al*., [2009], based on a linear transfer function in the Fourier domain used to acquire quantitative solutions. Absolute magnetization was estimated at 16 m intervals along the track using a 128 m wide sliding window (segment). Spectrums were then averaged over wavelengths between 32 and 128 m in order to obtain a ratio of observed to synthetic anomalies, together with error, coherency, and phase. These calculations were applied to all sets of segments for the x and z components, providing individual results. The averaged values between the x and z ratio of observed to synthetic anomalies were adopted as best estimate of absolute magnetization intensity. Estimations with a coherency greater than 0.5 in both

components were retained for further interpretation. The magnetization polarity was regarded as normal for phases between −90° and 90° and reversed for phases between 90° and 270°.

While the short-wavelength variation of a magnetic anomaly provides the magnetic structure of the uppermost sub-seafloor, long-wavelength variation gives information on the magnetic layer over a greater depth range. I applied the magnetic inversion technique improved by *Honsho et al*. [2009] in order to take full advantage of the varying altitude of the vehicle above the seafloor. First, magnetic anomaly was inverted to magnetization distribution in substitute geometry, using the method of *Parker and Huestis* [1974], as defined by a level observation plane and pseudo topography (vehicle altitude), the same as equivalent geometry proposed by *Hussenoeder et al*. [1995]. In the next step, the synthetic magnetic anomaly was calculated in real geometry using this inversion solution and the forward technique of *Talwani and Heirtzler* [1964]. Since the difference between the observed and calculated synthetic magnetic anomaly was obtained, this differential anomaly was inverted to magnetization using the substitute geometry. Finally, the differential magnetization solution was added to the last magnetization obtained in first step. In order to correct the error due to switching geometry, these procedures were repeated until the inversion solution of magnetization converged. A high-cut filter, cosine tapered curves of 1.0 at a wavelength of 300 m and 0.0 at a wavelength of 250 m, was used for the inversion calculation. In forward modeling with real geometry, an upper boundary of the magnetized layer was defined by depth and altitude. A uniform magnetized layer with 500 m thickness, and a direction of magnetization parallel to the IGRF was assumed. The annihilator was also solved by the same procedure.

4-2-3. Rock magnetic properties measurements

Rock magnetic property measurements were performed on collected rock samples, including; 5 sulfides, 11 basalts, 4 dolerites, 2 gabbros, and 30 serpentinized peridotites. Samples were mostly collected on the seafloor around the YHF during the submersible *SHINKAI 6500* dives of 6K#1170, 6K#1176, and 6K#1331 with the exception of 5 serpentinized peridotite samples, which were obtained by a dredge haul of KH10-6-DR11 conducted during the KH10-6 cruise (Fig. 4-2).

Rock samples were divided into four cubic subsamples (2-cm cubic) and several chips (~500 mg). For two, small serpentinized peridotites, just two cubed materials were prepared. Cubic sub-samples were used for measurements of natural remanent magnetization (NRM), and magnetic susceptibility. Chips were used for measurements of low- and high-temperature magnetic experiments.

The NRM intensity and magnetic susceptibility measurements were conducted on all cubed materials using a spinner magnetometer (DSPIN, Natsuhara Giken) at the Atmosphere and Ocean Research Institute (AORI), University of Tokyo, and a magnetic susceptibility meter (Kappabridge KLY-3, AGICO) at the Center for Advanced Marine Core Research (CMCR), Kochi University, respectively. Thermomagnetic analyses were performed on chips of representative rock samples. For low-temperature measurements, an isothermal remanent magnetization (IRM) was imparted to the samples using a field of 3 T at 6 K after cooling in a zero field, which was followed by measurement of the IRM during warming up to 300 K using a magnetic property measurement system (MPMS-XL5, Quantum Design Inc.) at the CMCR. The temperature dependence of saturation magnetization above room temperature was measured using a magnetic balance (MNB-89, Natsuhara Giken) at the CMCR. Samples were heated from 50 to 700°C and cooled back to 30°C in a vacuum (~1 Pa) at a rate of 12°C/min. The inducing magnetic field was 0.5 T.

4-2-4. Grain density and petrology on serpentinized peridotites

The serpentinized peridotites from the Yokoniwa Rise were represented by Clinopyroxene-bearing harzburgites to lherzolites. Microstructures were examined on polished thin sections, and back-scattered electron (BSE) images were acquired using a transmitted and reflected light microscopy, a scanning electron microscopy (SEM; SU3500, Hitachi High-Technologies), and a field emission SEM (SU 8200, Hitachi High-Technologies).

In order to confirm reaction states of serpentinized peridotites, bulk grain density (d) was measured on all cubic subsamples of serpentinized peridotites using a high precision microbalance with a resolution of 0.01 mg and a gas-pycnometer (AccuPycTM 1330 Pycnometer) at the Atmosphere and Ocean Research Institute (AORI), University of Tokyo.

Saturation magnetization (Ms) was measured on several chip materials (N = 4−12) for each serpentinized peridotite using a vibrating sample magnetometer (VSM; MicroMag 3900, Princeton Measurements Corp.) at the CMCR. During the Ms measurement procedure, the magnetic hysteresis parameters were also measured to estimate the ferromagnetic grain-size distributions in the rock samples based on the Day plot [e.g., *Day et al*., 1977]. This device displays the remanence ratio (saturation remanent magnetization to saturation magnetization) against the coercivity ratio (remanent coercivity to coercivity). The measurements of first-order reversal curves (FORCs) were conducted on the chip sample by using an alternating gradient magnetometer (AGM; MicroMag 2900, Princeton Measurements Corp.) at the CMCR. The FORC diagrams provide information on the distribution of coercivity (Hc) for a magnetic grain assemblage [e.g., *Roberts et al*., 2000]. The field spacing was set to 2.25 mT, and a total of 100 FORCs were measured with Hc values of 0–120 mT, and local interaction field (Hu) values of −40 mT to 40 mT. A smoothing factor of 2 was used [*Roberts et al*., 2000] and the irregularFORC software [*Zhao et al*., 2015] was used for data processing.

4-3. Results

4-3-1. Magnetization from AUV data

The distribution of equivalent magnetization (EM) was estimated from the total magnetic anomaly obtained by AUV *r2D4* using the ABIC inversion analysis technique of *Honsho et al*. [2012]. The basic equations of inversion method are shown in Chapter 3. The results along the track line are shown in Figure 4-4. High amplitude magnetization (−5 to 28 A/m) was estimated when a 100 m-thick magnetic layer was assumed. Magnetization intensities showed smaller variation: −2 to 11 A/m in a 100 m-thick magnetic layer model, −2 to 10 A/m in a half-infinite body model, and −2 to 8 A/m in a flat lower boundary model. Regardless of the magnetic layer model employed, significant positive magnetization (~30 A/m using 100 m-thick layer model and ~10 A/m using the other thickness layer models) was located on the YHF.

4-3-2. Magnetization from HOV data

Absolute magnetization distribution was estimated from the short-wavelength

magnetic anomaly obtained by HOV *SHINKAI 6500* using forward modeling and frequency analysis techniques [*Honsho et al*. 2009; *Talwani and Heirtzler*, 1964]. The results for all 4 lines were plotted together with the bathymetric signature in shown in Figure 4-5. The estimated values of absolute magnetization with high coherency (> 0.5) ranged from 0.4–16.7 A/m (Fig. 4-5B). The absolute magnetization values of lines 1, 2, 3, and 4 were 2.4–16.7, 1.0–6.9, 0.4–4.6, and 1.4−2.4 A/m, respectively. Strong magnetization higher than 7 A/m was observed only for line 1 on the western slope of the Yokoniwa Rise, where basalt and hydrothermal sulfide samples were collected. The absolute magnetization values were up to 8 A/m around the YHF. Approximately 50% of the reliable estimates within every segment were acquired along line 1, and almost all estimates with high coherency along line 1 showed a positive phase (−90 to 90°; Fig. 4-5B), representing the acquisition of remanence during the normal (positive) magnetic chron. In contrast, on the eastern slope, where serpentinized peridotite dominates, low absolute magnetization values less than 7 A/m were observed (Figs. 4-5C, 4-5D, and 4-5E), although gabbro and dolerite were also collected at this location. For lines 2, 3, and 4 on the eastern slope, reliable estimates with high coherency represented less than 20 % for which the phase distribution was complicated (Figs. 4-5C, 4-5D, and 4-5E), possibly due to the low signal-to-noise ratio caused by the weakly magnetized crust, or reflecting a disturbance in the magnetization direction resulting from faulting, and/or block rotation or due to geometry error caused by the sedimentation.

Equivalent magnetization (EM) distribution was estimated from the long-wavelength magnetic anomaly obtained by HOV *SHINKAI 6500* using an inversion method in equivalent geometry [*Honsho et al*., 2009; *Parker and Huestis*, 1974]. The results along all 4 lines were plotted together with the bathymetric signature and collected rock species in Figure 4-6. Along line 1, relatively high EM intensity was recognized in the western region (x = 100–700 m) where basalts were observed (Fig. 4-6B). The EM value increased from −5 A/m at the minimum point (x = 1000 m) to 2 A/m at the eastern end, where the YHF is located (Fig. 4-6B). For line 2, the maximum EM value of 4 A/m was observed in the easternmost part at 3500 m deep. The EM intensity decreased to −3 A/m near the area of x = 1600−1900 m at a depth of 2900−3000 m, and increased to 0−1 A/m at 2600 m depth (Fig. 4-6C). The largest variation in EM, up to 10 A/m, was observed in line 3 (Fig. 4-6D), with the lowest value at the eastern end of the slope at a depth of 3050 m, and increasing to the west.

High EM values were observed in the area of x = 1100−1700 m. For line 4, the EM showed a high value (~3 A/m) near the YHF (x = 0), which was larger than that of the southern area (Fig. 4-6E).

4-3-3. Magnetic properties of rock samples

The measured NRM intensity (A/m) and magnetic susceptibility (SI) were 0.02–0.09 (mean: 0.05) and 0.0008–0.0016 (mean: 0.0010), respectively, in sulfide, 0.01–6.33 (mean: 1.48) and 0.0007–0.0110 (mean: 0.0025) in basalt, 0.05–0.44 (mean: 0.18) and 0.0017–0.0143 (mean: 0.0063) in dolerite, 0.85–1.78 (mean: 1.31) and 0.0061–0.0268 (mean: 0.0165) in gabbro, and 0.20–8.35 (mean: 2.17) and 0.0016–0.0867 (mean: 0.0347) in serpentinized peridotite (Table 4-1, Fig. 4-7A). Koenigsberger ratio values (Q: NRM/induced magnetization) were 0.7–2.7 (mean: 1.3) in sulfide, 0.3–74.1 (mean: 37.1) in basalt, 0.2–3.6 (mean: 1.5) in dolerite, 0.9–8.1 (mean: 4.5) in gabbro, and 0.4–5.1 (mean: 1.9) in serpentinized peridotite (Table 4-1, Fig. 4-7A). Induced magnetization was calculated for a magnetic field of 45000 nT.

Basalt samples are divided into two groups of low and high Q values, possibly reflecting the degree of low-temperature oxidation and grain size distribution of ferromagnetic minerals (mostly titanomagnetite). A similar signature is also observed in dolerites. Sulfide samples have weak magnetic signatures with low magnetic susceptibility and NRM intensity. Serpentinized peridotites carried strong NRM and had high magnetic susceptibility. In more than 80% of serpentinized peridotites, magnetization primarily originates from remanence rather than from induced magnetization (Q > 1). Magnetization for each rock sample was estimated using the sum of NRM with induced magnetization (Fig. 4-7B). It was assumed that the NRM vectors were parallel to the current geomagnetic field vector; therefore magnetization values represent the maximum estimation for in-situ magnetization contributing to the magnetic anomaly. This assumption is reasonable because the rocks appeared to have acquired the NRM (thermoremanent magnetization and chemical remanent magnetization) during the Brunhes normal polarity epoch when the Yokoniwa Rise evolved. However, there is no available data showing the direction of their NRM. The serpentinized peridotites exhibit the strongest magnetization among the tested samples, although there is a large variation in the magnetization values. High- and

low-temperature experiments showed a Curie temperature of ~580°C and a rapid transition between 90 and 120 K, which were interpreted as the Verwey transition [e.g., *Ozdemir et al*., 1993], suggesting that the magnetic carrier in serpentinized peridotite is magnetite. The details of magnetic properties of serpentinized peridotites are shown in chapter 4-3-4.

Measurements of four cubic subsamples for each serpentinized peridotite indicate that the NRM and susceptibility do not vary significantly within each sample. The averaged values of the relative standard deviations for the NRM intensity and magnetic susceptibility are 26% and 22%, respectively. The majority (>75%) of samples had less than 30% of relative standard deviations for the NRM intensity and magnetic susceptibility (Fig. 4-8). These values can be treated as a homogeneity index at a 2-cm scale.

4-3-4. Serpentinization degree and petrography

Most samples of serpentinized peridotites displayed macroscopic foliation, which was characterized by variable amounts of dynamic recrystallization processes of olivine grains (Fig. 4-9). Some samples with light brown color had experienced weathering processes. Peridotites with low serpentinization degrees were characterized by sparse veins developed within or around olivine grains. Submicron-sized magnetite-bearing veins were evolved and scattered with increasing serpentinization degrees.

The serpentinization degree was estimated from bulk grain density. The density values of olivine and pyroxene are 3.37 and 3.28 g/cm^3, respectively, whereas the density of serpentine is 2.55 g/cm^3, thus indicating a decrease in density after serpentinization (Tables 4-1 and 4-2). *Miller and Christensen* [1997] analyzed ophiolitic and abyssal serpentinized peridotites, and proposed the following empirical equation between the density (d) and serpentinization degree (S): $S = (3.3 - d)/0.785$. Magnetite has a large density of 5.2 g/cm^3 and biases the degree of serpentinization. I adopted the improved equation proposed by *Oufi et al*. [2002] who took the magnetite volume fraction (m) into account as follows: $S = (3.3 - [(d - 5.2 * m)/(1 - m)]/0.785$. The magnetite volume fraction of each sample was estimated from saturation magnetization by assuming that magnetite is the only mineral contributing to saturation magnetization in samples (Ms of pure magnetite is 92 Am2/kg). Observed Ms values were

0.1−5.0 Am2/kg (average 2.1 Am2/kg), which were equivalent to a magnetite amount of 0.1−5.5 wt% (average 2.3 wt%; Table 4-2, Fig. 4-10A).

Grain density values ranged from 2.63 to 3.17 g/cm^3 (average 2.80 g/cm^3; Tables 4-1 and 4-2, Fig. 4-10A). The relative standard deviation (RSD) for the density of each serpentinized peridotite was less than 1% in general (Fig. 4-8), thus indicating that density varies little within each rock sample.

The investigated 30 serpentinized peridotite samples showed large variation in the degree of serpentinization (Tables 4-1 and 4-2), i.e., 17−100%, where the majority of samples had high degrees of serpentinization (S >70%), six samples had moderate degrees of serpentinization (S= 40−70%), and six samples had low degrees of serpentinization (S <40%). The magnetite amount, NRM intensity and magnetic susceptibility of serpentinized peridotite increases with the increase of serpentinization degrees (Figs. 4-10B, 4-10C, and 4-10D).

The remanence ratio of samples varied between 0.08 and 0.37, and the values were distributed within the pseudo-single-domain (PSD) region of the Day plot (Fig. 4-11). Highly serpentinized samples tended to show low coercivity ratios compared to slightly serpentinized samples.

Thermomagnetic analyses showed a single high Curie temperature of ~580°C as mentioned in chapter 4-3-3 (Fig. 4-9). The warming and cooling curves are almost identical, thus indicating that low-temperature oxidation (maghemitization) did not occur. The low-temperature measurements showed a rapid decrease of magnetization between 90−120 K, which is indicative of the Verwey transition for magnetite [e.g., *Özdemir et al*., 1993] (Fig. 4-9). These results indicate that magnetite carried the magnetization. One noteworthy feature was that the characteristic linear change of magnetization in the high-temperature thermomagnetic curve was observed in the peridotite with <20% serpentinization and low magnetite amounts (0.1 wt%) (6K1170-R25). This signature was possibly affected by Ti substitution in primary magnetite and/or small grains.

Peridotites with high degrees of serpentinization exhibited magnetite grain aggregates within the veins, which had a complex growth structure with dendritic or capillary crystallization. Magnetite creation occurred in veins within olivine grains, not within pyroxene grains. While magnetite occurred as an assemblage of needle-like grains (<1 μm long) in the highly serpentinized peridotites, it was developed along the

primary mineral rim or cracks with the size of several micrometers (Fig. 4-12). The FORC distributions for the samples with lower serpentinization degree (<60%) showed contours diverging toward the Hu axis and coercivity (Hc) was low, i.e., ~10 mT or lower at the peak, which is suggestive of the dominance of multi-domain (MD) grains. In contrast, FORC distributions for the samples with higher serpentinization degree (>60%) had higher coercivities and closed contours, which is suggestive of a larger contribution from single-domain (SD) grains. Slightly serpentinized samples showed FORC distributions near $Hc = 0$ and $Hu = 0$, thus indicating the presence of super-paramagnetic (SP) grains. The completely serpentinized samples showed higher coercivities and interacting fields, thus indicating the presence of anisotropic grains and concentration of SD grains, respectively. This signature is consistent with the microstructures on polished thin sections that showed an assemblage of needle-like grains.

In summary, the variation of magnetization (under the 45000 nT field) in serpentinized peridotites is considered as a function of serpentinization degree (Fig. 4-13). The magnetization values increases nonlinearly as progress of serpentinization. The maximum value of magnetization is up to 11 A/m for a sample with a serpentinization degree of 96%, which is caused by magnetite concentration as a result of serpentinization progress.

4-4. Discussion

4-4-1. Basaltic volcanism on western slope of Yokoniwa Rise

Magnetization polarities from the HOV magnetic anomaly were entirely positive on the lava-dominant area of the western slope. These results are consistent with previous sea-surface magnetic studies, which identified the Brunhes/Matuyama boundary along the eastern off-axis of CIR-S1 and suggests that the Yokoniwa Rise formed in the Brunhes normal chron [*Honsho et al*., 1999; *Sato et al*., 2009; *Okino et al*., 2015]. On the basis of these results, I consider that these basaltic lavas erupted and acquired thermal remanent magnetization during the Brunhes normal epoch.

The absolute magnetization from the HOV magnetic data, using a short wavelength signal, showed the highest magnetization (~16 A/m) for areas in which basaltic pillow lavas are distributed (Fig. 4-5B). However, this signature was not

observed in the inversion results using a long wavelength signal (Figs. 4-6A and 4-6B), or in the results from the AUV data (Fig. 4-4). Since short wavelength anomalies strongly reflect shallow sub-seafloor magnetization, these results imply that the locally high magnetization of the lava-hosted area reflects high magnetization of the basaltic lavas. Previous studies of oceanic basalt NRM intensities at spreading ridges proposed that zero-age basalts carry strong NRM (several tens A/m) and their intensity is drastically decreased to several A/m with age following low-temperature oxidation [e.g., *Gee and Kent*, 1994; *Johnson and Atwater*, 1977; *Johnson and Tivey*, 1995]. Moreover, the geomagnetic field intensity has doubled over past several tens of thousands of years [e.g., *Guyodo and Valet*, 1996], which constitutes a considerable signal that cannot be ignored. Forward models of near-seafloor magnetic data [*Schoute*n et al., 1999] demonstrated that observed character of the central anomaly magnetization high (known as CAMH) was successfully reproduced by the convolution of a lava deposition distribution with age-dependent lava magnetization function, which is the product of geomagnetic paleo-geomagnetic field intensity and low-temperature alteration. Therefore, the high magnetization observed on the western slope of the YR (line 1) appears to originate from relatively young basalt.

However, basaltic rock samples, collected and analyzed in this study, showed low values of NRM (~2 A/m). Because these samples were collected from the lava surface, I consider that the low NRM values are attributed to low-temperature oxidation affecting on the surface of lava [e.g. *Gee and Kent*, 1994; *Irving*, 1970; *Johnson and Atwater*, 1977]. Indeed, the high-temperature saturation magnetization measurements for these basaltic rock samples showed large differences between heating and cooling processes, suggesting that low-temperature oxidation of the rock samples has progressed to some extent. The difference between magnetization from the magnetic anomaly and from rock samples possibly reflects spatial differences in the oxidation degree within the lava-scale [Chapter 2]. The low-temperature oxidation process must be faster on the surface than in the interior of the lavas, resulting in weaker NRM of rock samples than magnetization from magnetic anomaly representing bulk magnetization of accumulated lava flows.

4-4-2. Evolution of magnetite during serpentinization

The investigated serpentinized peridotites from the Yokoniwa Rise covered a full range of serpentinization degrees and provided a complete dataset that characterizes the magnetic properties of variously altered ultramafic rocks. The presence of pure magnetite was confirmed by petrographical observations and the high- and low-temperature magnetic measurements. Magnetite grains were developed within veins, and these were created from primary minerals in the peridotites through serpentinization reaction processes. Since no magnetite grains occurred near the pyroxene grains, magnetite creation was related to alteration of olivine. The amount of magnetite increased with the progression of serpentinization, and it was developed as an assemblage of small SD grains (Figs. 4-12A and 4-12B). On the other hand, magnetite grains in slightly serpentinized peridotite were dominant in the MD state, which were possibly created through (i) a primary igneous process with olivine and pyroxene formation (Fig. 4-12C), and/or (ii) a high-temperature water rock reaction (Fig. 4-12D). Both processes with high-temperature conditions promote the growth of magnetite grains. The former possibility is supported by oxygen fugacity in the upper mantle, in which magnetite is stable in the wüstite–magnetite buffer [*Frost and McCammon*, 2008]. The latter is indicated by numerical models of chemical thermodynamics, which show that olivine is partially or entirely persistent at equilibrium and that only a small amount of magnetite should form during initial alterations at temperatures higher than 315°C [*McCollom and Bach*, 2009].

The variations of magnetite amounts, NRM intensities, and magnetic susceptibility with serpentinization degrees (Figs. 4-10B, 4-10C, and 4-10D) are suggestive of the following features. First, the abundance of magnetite in the Yokoniwa samples appears to vary nonlinearly with serpentinization degrees. A remarkable increase of magnetite amount occurs in samples with high degrees of serpentinization (>70%), thus indicating the production of magnetite in the later stage of serpentinization processes. Second, magnetic susceptibility increases drastically with the degree of serpentinization. Third, the NRM intensity also increases with the degree of serpentinization, which is caused by the increase of magnetite production. The scatter of NRM intensity at a particular serpentinization degree is controlled by many factors such as the size and shape of ferromagnetic minerals and the geomagnetic field strength at the timing of remanence

acquisition. The maximum value of the NRM intensity was 8 A/m for the sample with a serpentinization degree of 96%, thus indicating that the remanence as well as induced magnetization of highly serpentinized peridotite can contribute to magnetic anomalies.

A drastic increase in the amount of magnetite after the progression of 60−70% serpentinization was clearly observed in studied serpentinized peridotites taken from the Yokoniwa Rise in the CIR (<1 Myr old). Highly serpentinized peridotites with a large amount of magnetite were also reported from the Azores platform (18 to 35 Myr old) and the Kane Fracture Zone (<1 to 7 Myr old) at the Mid-Atlantic Ridge and the East Pacific Rise (<1 Myr old) [*Oufi et al*. 2002]. These natural samples support the nonlinear increase of magnetite through the serpentinization process. In contrast, hydrothermal experiments of synthetic olivine [*Malvoisin et al*., 2012] showed that magnetite amounts (calculated by saturation magnetization) increase linearly during serpentinization. The discrepancy between magnetite production of synthetic olivine and natural serpentinized peridotites can be possibly explained by the changes of silica activity and oxygen fugacity. *Miyoshi et al*. [2014] investigated the changes in mineralogical textures in the Iwanaidake ultramafic body and demonstrated that silica supply from orthopyroxene alteration can be a trigger for magnetite formation. The breakdown of iron-rich serpentine and brucite in the latter stage of the reaction, as proposed by *Bach et al*. [2006], *Beard et al*. [2009], and *Frost et al*. [2013] has essentially the same role as the silica supply. Thermodynamic modeling by *Frost et al*. [2013] pointed out the importance of the redox budget and demonstrated that the transition from brucite–serpentine to brucite–serpentine–magnetite assemblages is accompanied by an increase of the oxygen fugacity (water/rock ratio) with a minor change of silica activity. Since redox conditions should be different between natural (open) experiments and laboratory experiments (closed), such as those by *Malvoisin et al*. [2012], the difference in redox budget changes can be the responsible factor driving the discrepancy between the linear and nonlinear changes of magnetite creation during serpentinization.

The total amount of magnetite creation during serpentinization is also controlled by various factors such as temperature and primary rock compositions. Thermodynamic equilibrium models [*Klein et al*., 2013a] and natural evidence [*Klein et al*., 2013b] have demonstrated that serpentinized peridotite with abundant magnetite forms at temperatures higher than 200°C with the involvement of Fe-poor brucite. Moreover,

thermodynamic modeling by *Klein et al*. [2013a] predicted that pyroxenite does not produce magnetite. The Yokoniwa serpentinized peridotite of 6K1170R22 with abundant orthopyroxene showed a high degree of serpentinization (85%), but a small amount of magnetite (0.8 wt%), thus lending further credence to the role of orthopyroxene. As discussed above, orthopyroxene could play an important role in the nonlinear change of magnetite creation, however, excessive amounts of orthopyroxene control the total amount of magnetite creation. There may be other factors for magnetite formation process during serpentinization, but in any case the magnetization of serpentinized peridotite was strongly related to degree of serpentinization and was carried by magnetite grains created through serpentinization.

4-4-3. Processes causing strong magnetization zones

One of the most significant features observed in analyzed magnetic data was the clear association between the YHF and enhanced crustal magnetization, which was higher than the surrounding seafloor (Figs. 4-4, 4-5, and 4-6). Equivalent magnetization estimated by the AUV for the assumed layers of 100 m and > 200 m increased by approximately 30 A/m and 10 A/m at the YHF, respectively (Fig. 4-4). Absolute magnetization estimated from the HOV anomaly, which reflects the uniform magnetization of the uppermost sub-seafloor < 50 m, was ~8 A/m at the YHF (Fig. 4-5). Equivalent magnetization of the long-wavelength anomaly in the HOV data increased by 8 A/m at the YHF (Fig. 4-6). The magnetization within 100 m layer thickness (30 A/m) for explaining the AUV data is not consistent with the absolute magnetization (~8 A/m) from the HOV *SHINKAI 6500*. Therefore, shallow concentration of magnetization of 30 A/m overestimated the magnetic anomaly from the HOV *SHINKAI 6500*. Consequently, the AUV and HOV datasets imply that approximately 10 A/m of the magnetization for the > 200 m thickness layer represents reliable explanation for the magnetic anomaly highs in the YHF.

The rock magnetic properties showed that the highly serpentinized peridotite was sufficient to represent a reasonable source for the magnetic high at the YHF (Fig. 4-7 and 4-10). As discussed in the chapter 4-4-2, the NRM intensity of serpentinized peridotite increases with the degree of serpentinization as a result of the increase of magnetite production. The value of magnetization in serpentinized peridotites with a

serpentinization degree of 96% was up to 11 A/m, consistent with the high magnetization value of the YHF deduced from the magnetic anomaly observations. The measured Curie temperature (~580°C) and confirmed Verwey transition (90–120 K) in serpentinized peridotites showed that magnetite is the main magnetic carrier, while the wide range in Koenigsberger ratios (0.4–5.1) suggests the variation in grains size of magnetite. Saturation magnetization measurements showed that magnetite abundances are up to 5.5 wt% with grains occurring within veins in olivine mesh structures. These observations strongly suggest that serpentinized peridotites hosted magnetite formed due to a reaction with hydrothermal fluids, and appear to have acquired their chemical remanent magnetization during the progress of their growth.

As discussed in section 5.1, the highest absolute magnetization based on the short-wavelength anomaly was distributed in the lavas-hosted area, but basaltic lavas cannot be a source of the magnetization high around the YHF, because no lava flows were observed around the YHF. Even if there were an intruded body beneath the hydrothermal sulfide deposit, it is unlikely that the intruded body could carry a strong remanence (up to 10 A/m) with a spatial extent of a few hundred meters. Dike sections generally show low NRM intensity, and provide only minor contributions to marine magnetic anomalies [e.g. *Pariso and Johnson*, 1991; *Tivey*, 1996]. Besides, hydrothermal processes decrease the magnetization of lavas due to the alteration of the strongly magnetic titanomagnetite to less magnetic titanomaghemite and to nonmagnetic minerals [e.g., *Irving*, 1970; *Johnson and Atwater*, 1977].

Tivey [1994] and *Gee et al*. [2001] proposed that a combination of magnetic pyrrhotite and magnetite mineralization was responsible source for the magnetic anomaly at the Bent Hill massive sulfide in the Middle Valley, the JFR. There, samples of the Ocean Drilling Program (ODP) drill cores contained predominantly pyrite (90%), with 2–10% magnetite and smaller amounts of hematite, pyrrhotite and other sulfides [*Korner*, 1994]. In the YHF, sulfide samples show low magnetic susceptibility (<0.002 SI) and NRM intensity (< 0.1 A/m). Thermomagnetic curves show no evidence for the presence of pyrrhotite. Therefore, I concluded that sulfide mineralization does not contribute to crustal magnetization. Although systematic variation in the degree of oxidation with depth was not evident, we speculate that enhanced seawater or hydrothermal circulation may have led to oxidative conditions under which pyrrhotite cannot exist.

In summary, based on the results of this study, I propose that enhanced magnetization at the YHF results from an abundance of magnetite within the highly serpentinized peridotites. The accumulation of dead chimneys and low-temperature venting in the YHF implies a long-lived hydrothermal system that is significant enough to react with sub-seafloor ultramafic rocks.

4-5. Chapter Conclusions

Near-seafloor magnetic fields were obtained by using the AUV *r2D4* and the HOV *SHINKAI 6500*, and seafloor rock samples were collected by dredge hauling and the *SHINKAI 6500* in the area near the inactive YHF of the CIR. The integrated analysis of the magnetic anomaly and rock magnetic properties led to the following conclusions:

1. The inactive ultramafic-hosted YHF is associated with a strong magnetization intensity of ~10 A/m. Conversely, the surrounding seafloor does not exhibit such a magnetic signature.
2. Highly serpentinized peridotites have a well-developed serpentine mesh texture along with abundant magnetite. The grain size of the magnetite formed during serpentinization changes with the progression of the serpentinization reaction. The MD grains were formed through a primary igneous process and the initial stage of serpentinization under high-temperature conditions. The SP particles were also formed during the initial stage of serpentinization. The SD magnetite was formed during the later stage of serpentinization and occurs within the mesh structure as needle-like grains with strong magnetic interactions.
3. The highly serpentinized peridotites have higher magnetic susceptibility and NRM intensities than those in the basalts, dolerites, gabbros, and sulfides. The value of magnetization for the highly serpentinized peridotites, which is carried by the constituent magnetite, is sufficient for explaining the crustal magnetization intensity observed near the YHF. Therefore, I conclude that the strong magnetization intensity at the YHF reflects highly progressed serpentinization resulting from hydrothermal circulation and causing the formation of magnetite-rich serpentinized peridotite.

Near-seafloor magnetic field measurements and rock magnetic analysis have revealed the source of enhanced magnetization of the ultramafic-hosted YHF as that resulting from differing degrees of serpentinization. These observations highlight the importance of subsurface chemical processes in hydrothermal systems and in the geochemical budget of the oceanic lithosphere.

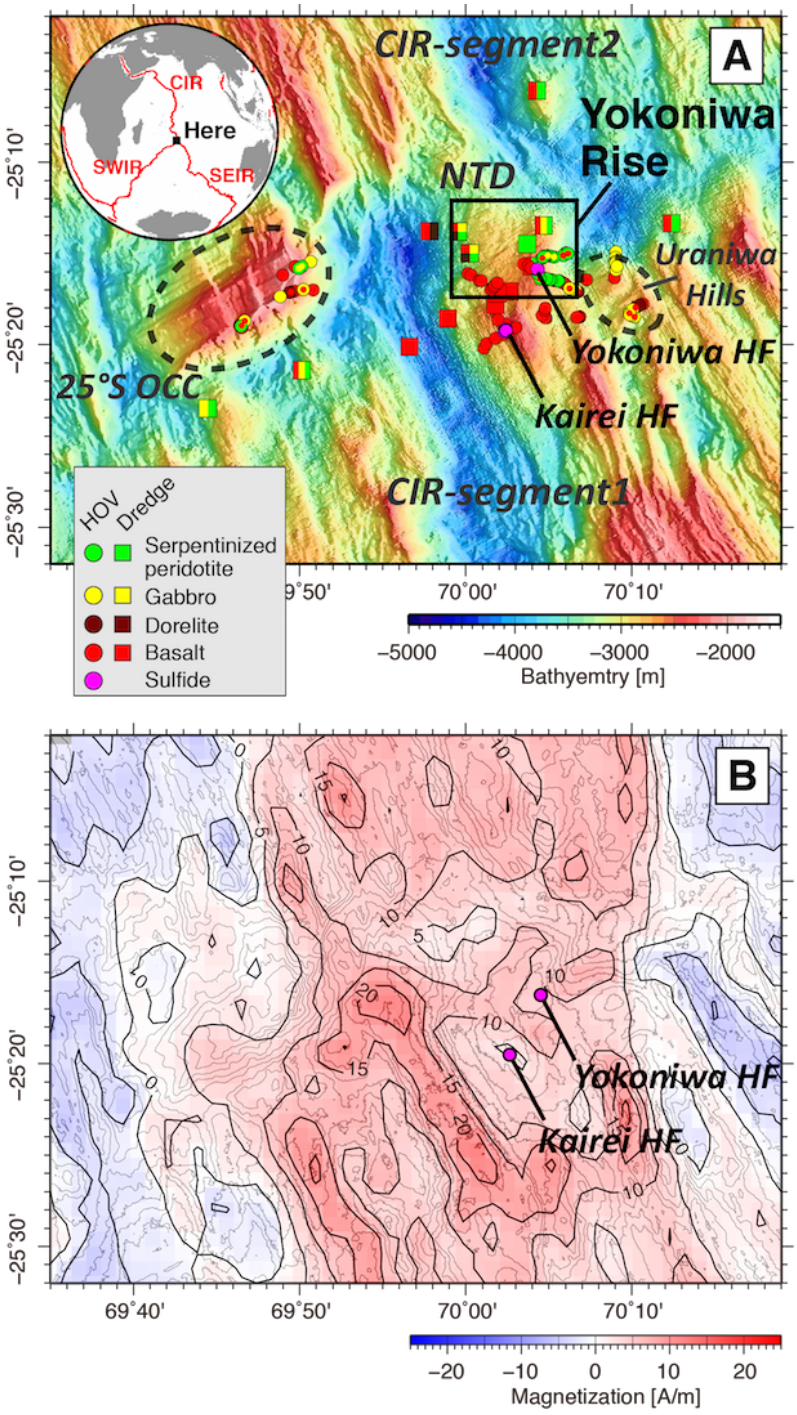

Figure 4-1. Seafloor bathymetry and magnetization in the Yokoniwa Rise region. Bathymetry (m; A) and magnetization (A/m; B) around the Yokoniwa Rise including the Yokoniwa Hydrothermal Field (HF; *Okino et al.*, 2015). Rock samples collected by submersible (circles) and dredge (squares) are shown as basalt (red), dolerite (brown), gabbro (yellow), serpentinized peridotite (green), and sulfide (purple). CIR = Central Indian Ridge, NTD = non-transform discontinuity, OCC = oceanic core complex.

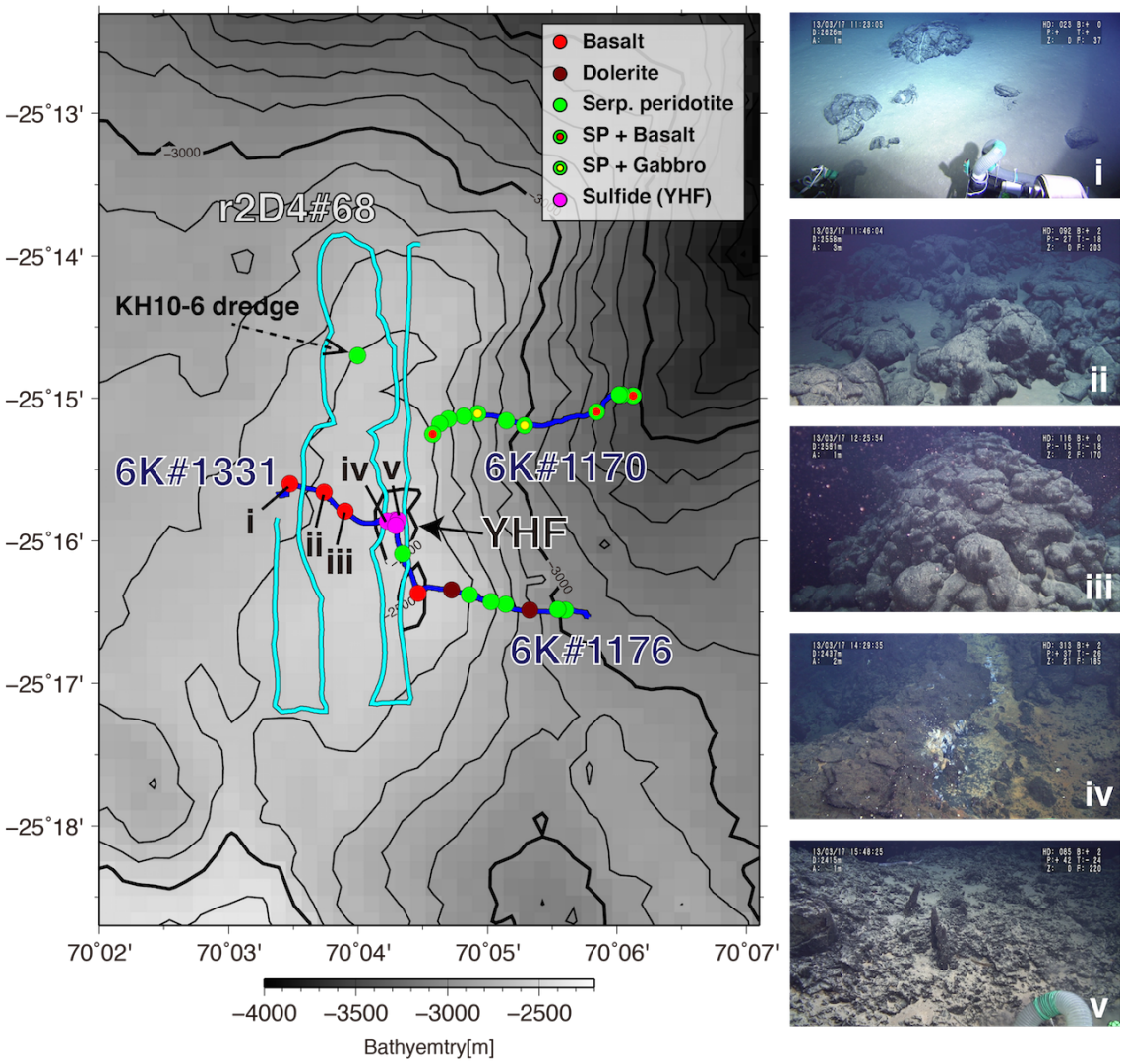

Figure 4-2. Magnetic survey tracks and collected sample locations.

Magnetic survey tracks and rock sample collection locations in the Yokoniwa hydrothermal fields (YHF), overlain on the regional bathymetry (m). Solid lines denote the AUV r2D4 survey (light blue) and the HOV *Shinkai6500* (blue). Circles denote basalt (red), dolerite (brown), gabbro (yellow), serpentinized peridotite (green), and sulfide (purple). The contour intervals are 100 m.

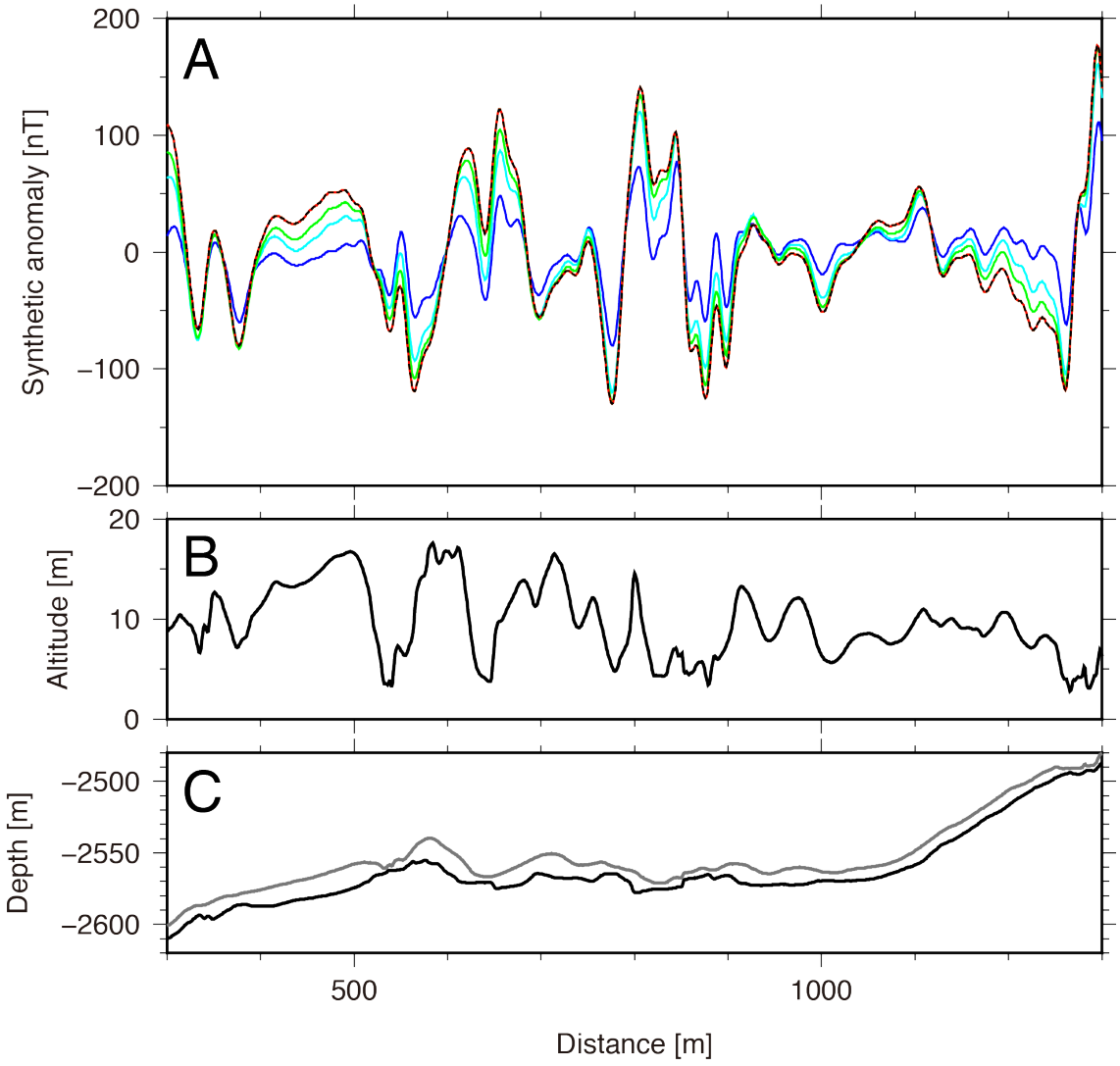

Figure 4-3. Synthetic downward magnetic anomalies assuming various thickness of layer source.

Synthetic downward magnetic anomaly (nT; A) calculated by 2D forward modeling along the track of dive 6K#1331 for dive altitudes of 0–20 m, assuming different magnetic source layer thicknesses: 10 m (blue line), 30 m (light blue line), 50 m (green line), 100 m (red line), and infinite (black broken line). Vehicle altitude (m; B) and vehicle depth (m; C) are shown along the same track, with seafloor topography defined by summation of vehicle altitude and depth.

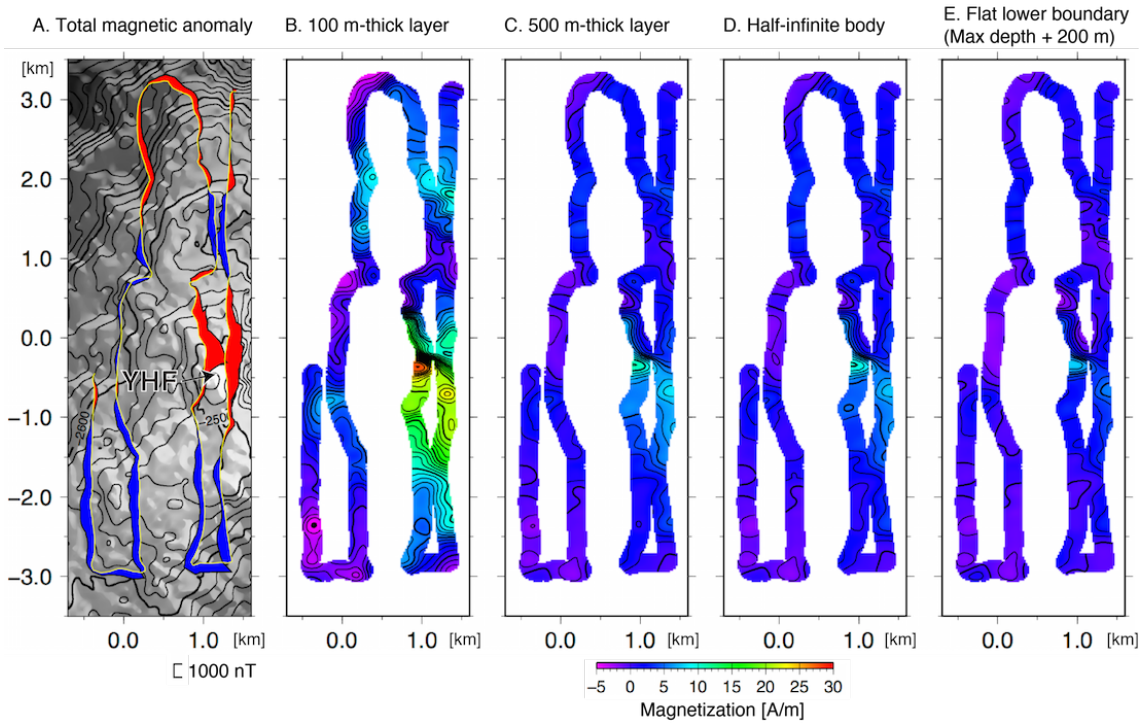

Figure 4-4. Total magnetic anomaly and equivalent magnetization distribution.

Total magnetic anomaly (nT; A) for track AUV *r2D4*, and the equivalent magnetization (A/m) distribution from the magnetic anomaly assuming a 100 m-thick layer (B), a 500 m-thick layer (C), half-infinite body (D), and a layer with flat lower boundary at maximum water depth plus 200 m (E). The inversion solution was estimated using the Akaike's Bayesian Information Criterion (ABIC) inversion technique developed by *Honsho et al*. (2012).

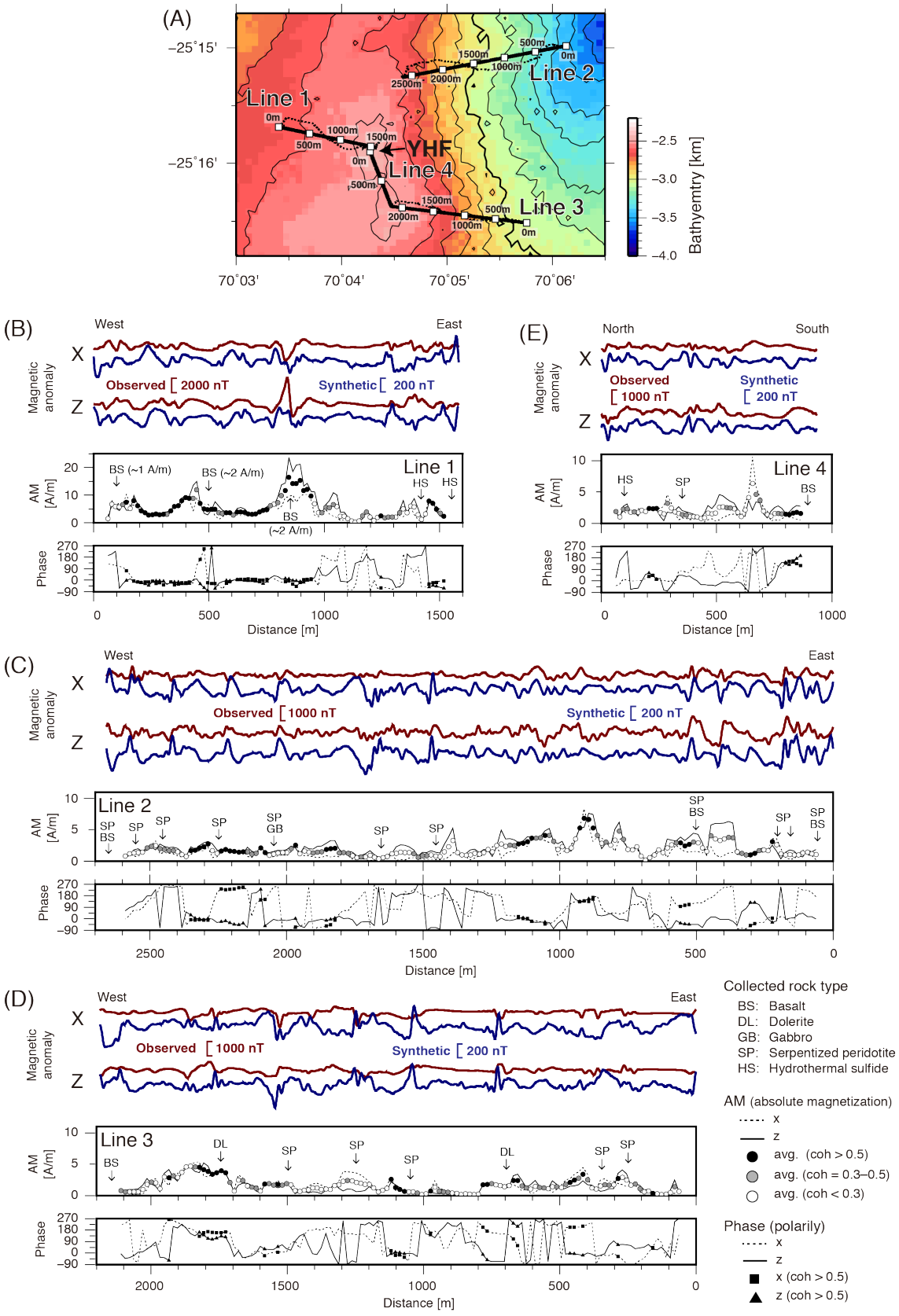

Figure 4-5. Forward solutions of short-wavelength anomalies from submersible.

(continued)

(A) Projected 2D tracks of the vehicle (solid lines) overlain on regional bathymetry (km), with the original vehicle tracks (broken line). The results of absolute magnetization (A/m), and phase calculated for each set of the segments from short-wavelength magnetic anomalies in lines 1, 2, 3, and 4 are shown in (B), (C), (D), and (E). For B–E, the top plots show horizontal (x) and vertical (z) components of both observed (red line) and synthetic (blue line) magnetic anomalies; the middle plots show the distribution of absolute magnetization averaged by the calculated ratio of the x (broken lines) and z (solid lines) components; the bottom plots show the distribution of phase of the x (broken lines) and z (solid lines) components. Reliable results, as confirmed by high coherency (> 0.5 in both x and z), are indicated by solid circles. Gray and open circles show results with middle (0.3–0.5) and low (< 0.3) coherency. Collected rock sample locations are shown together, including basalt (BS), dolerite (DL), gabbro (GB), serpentinized peridotite (SP), and hydrothermal sulfide (HS). Resultant phase values with high coherency (> 0.5) were shown as squares for x component and as triangles for z component.

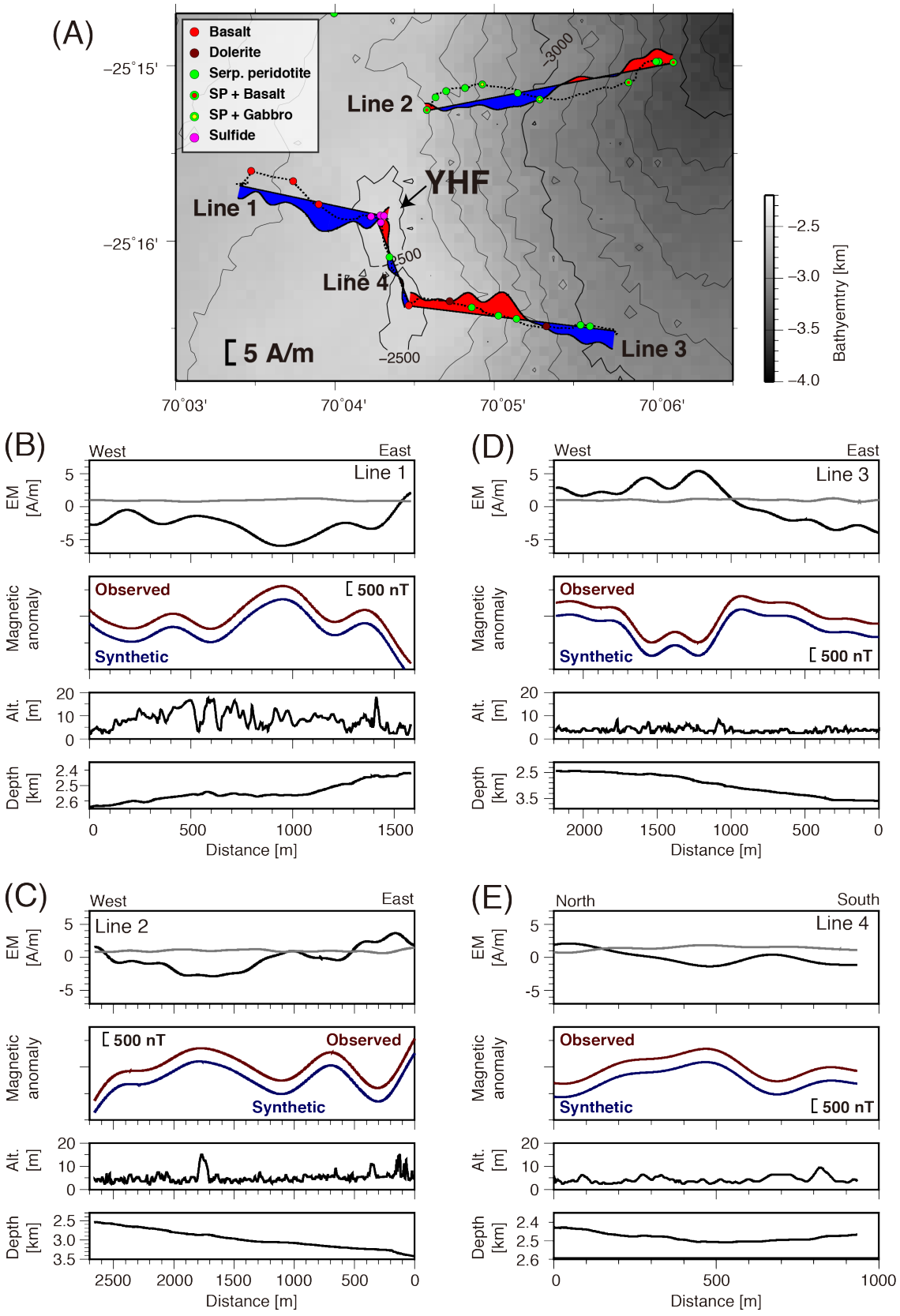

Figure 4-6. Inversion solutions of long-wavelength anomalies from submersible.

(continued)

(A) Equivalent magnetization (A/m) distribution along projected 2D tracks in map view (overlain on regional bathymetry; km). Dotted line with colored circles show the original HOV track and collected rock species. (B–E) Results of line 1–4, respectively, with the top plots showing obtained equivalent magnetization (A/m; black) derived from downward component, and the annihilator (grey). Middle plots show a comparison between the observed anomaly (red line) and the synthetic anomaly (blue line), reproduced from the obtained magnetization distribution and the real geometry between the vehicle and topography. The bottom two plots show altitude (m) and the depth of the vehicle (km).

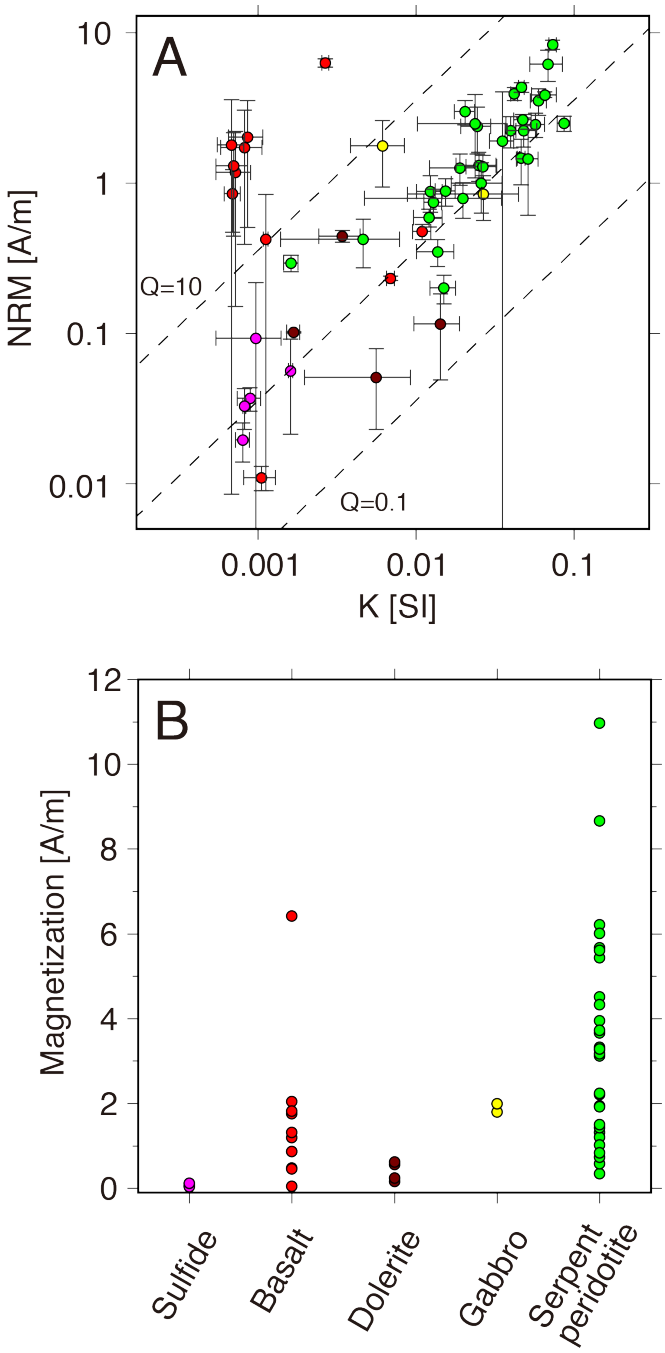

Figure 4-7. Results of rock magnetic properties for various host rock samples.

(A) Log-log plot of magnetic susceptibility (K; SI) and natural remanent magnetization (NRM; A/m) of host rocks collected from the Yokoniwa Rise. Broken lines show constant Q (Koenigsberger ratio), calculated for a magnetic field of 45000 nT. (B) Magnetization (A/m) estimated by the sum of NRM, with induced magnetization calculated for a magnetic field of 45000 nT. Rock samples include: sulfide (purple), basalt (red), dolerite (brown), gabbro (yellow), and serpentinized peridotite (green).

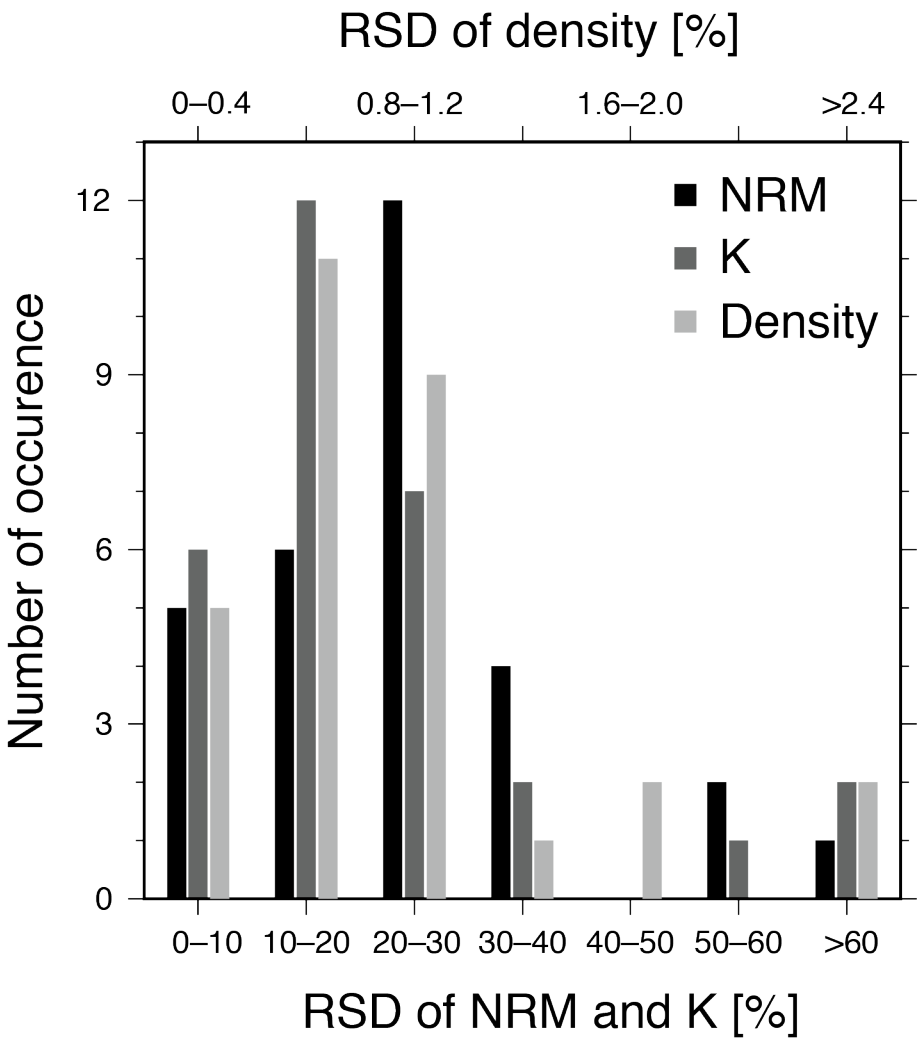

Figure 4-8. Heterogeneity of NRM, susceptibility, and grain density.

Relative standard deviation (RSD) of natural remanent magnetization (NRM) intensity, magnetic susceptibility (K), and density measured on four cubic subsamples (2 cm cubic) of each of the 30 serpentinized peridotite samples.

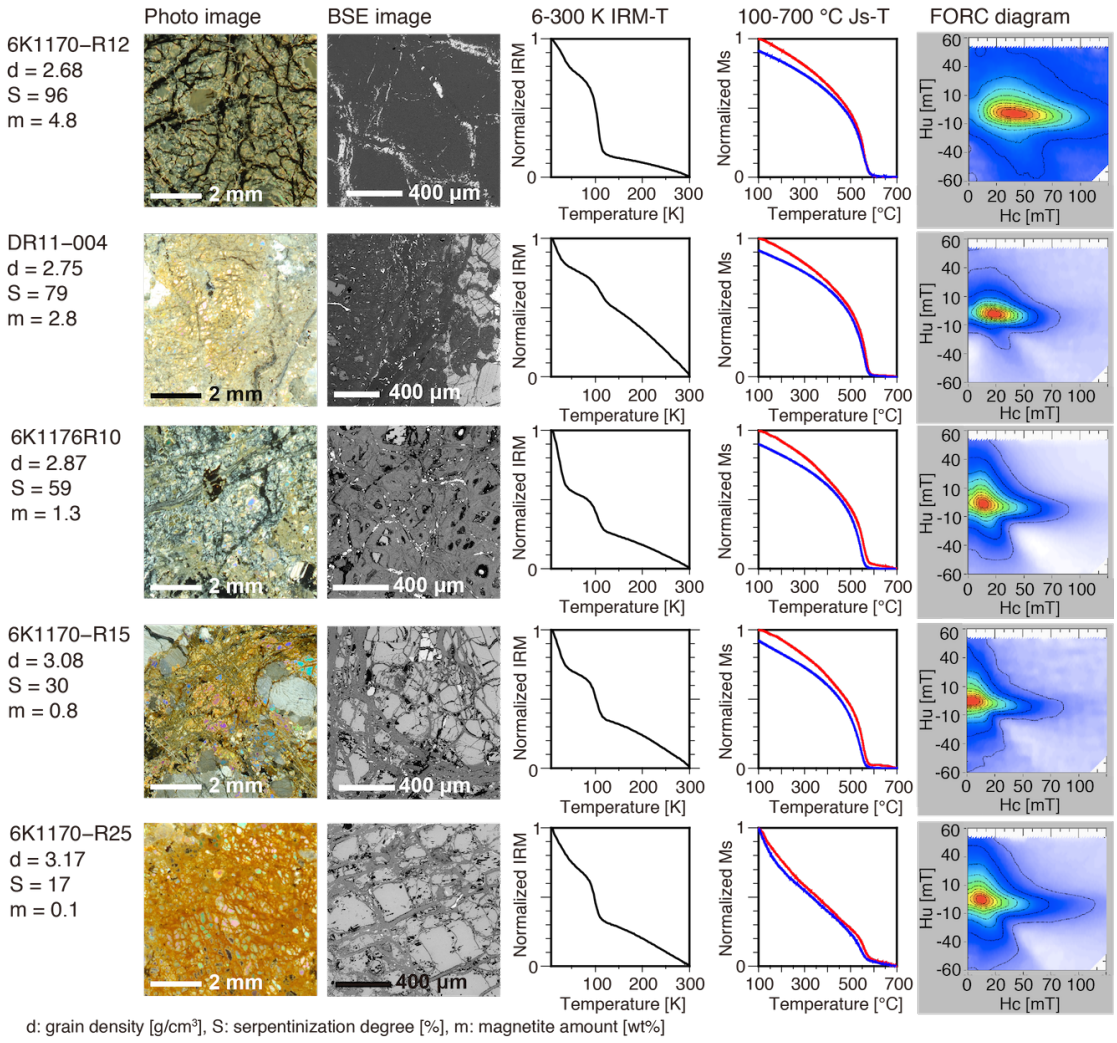

Figure 4-9. Petrography and magnetic properties for serpentinized peridotites with various serpentinization degrees.

Polarization images, back-scattered electron (BSE) images, isothermal remanent magnetization (IRM) demagnetization curves from 6 K to 300 K, warming (red) and cooling (blue) thermomagnetic curves from 100 to 700°C, and first-order reversal curve (FORC) diagrams of representative serpentinized peridotites. The serpentinization degree increases from the bottom to top panels.

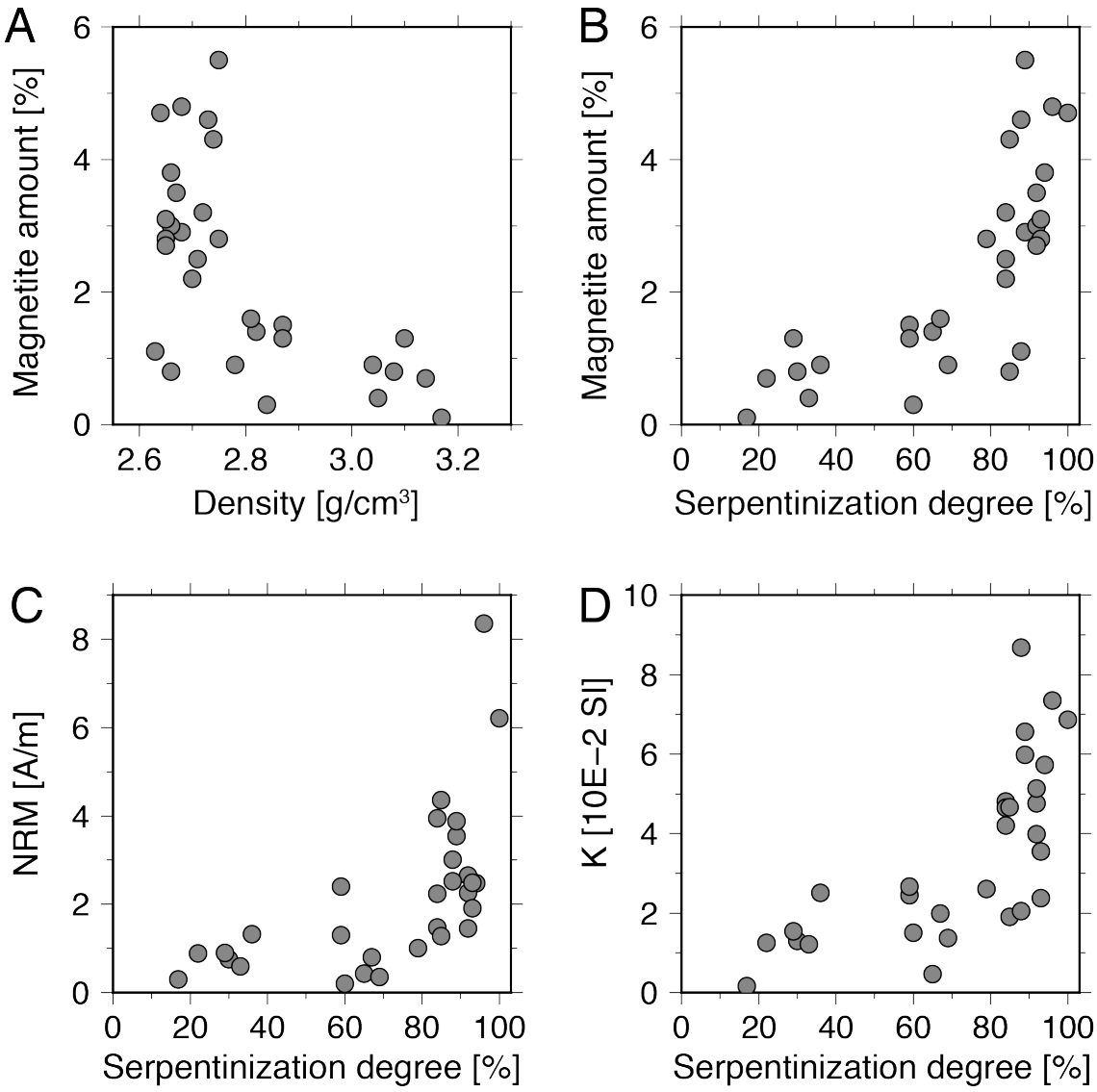

Figure 4-10. Bulk grain density serpentinization degree, and rock magnetic properties.

Relationships between (a) grain density and magnetite amount, (b) serpentinization degree and magnetite amount, (c) serpentinization degree and natural remanent magnetization (NRM) intensity, and (d) serpentinization degree and magnetic susceptibility.

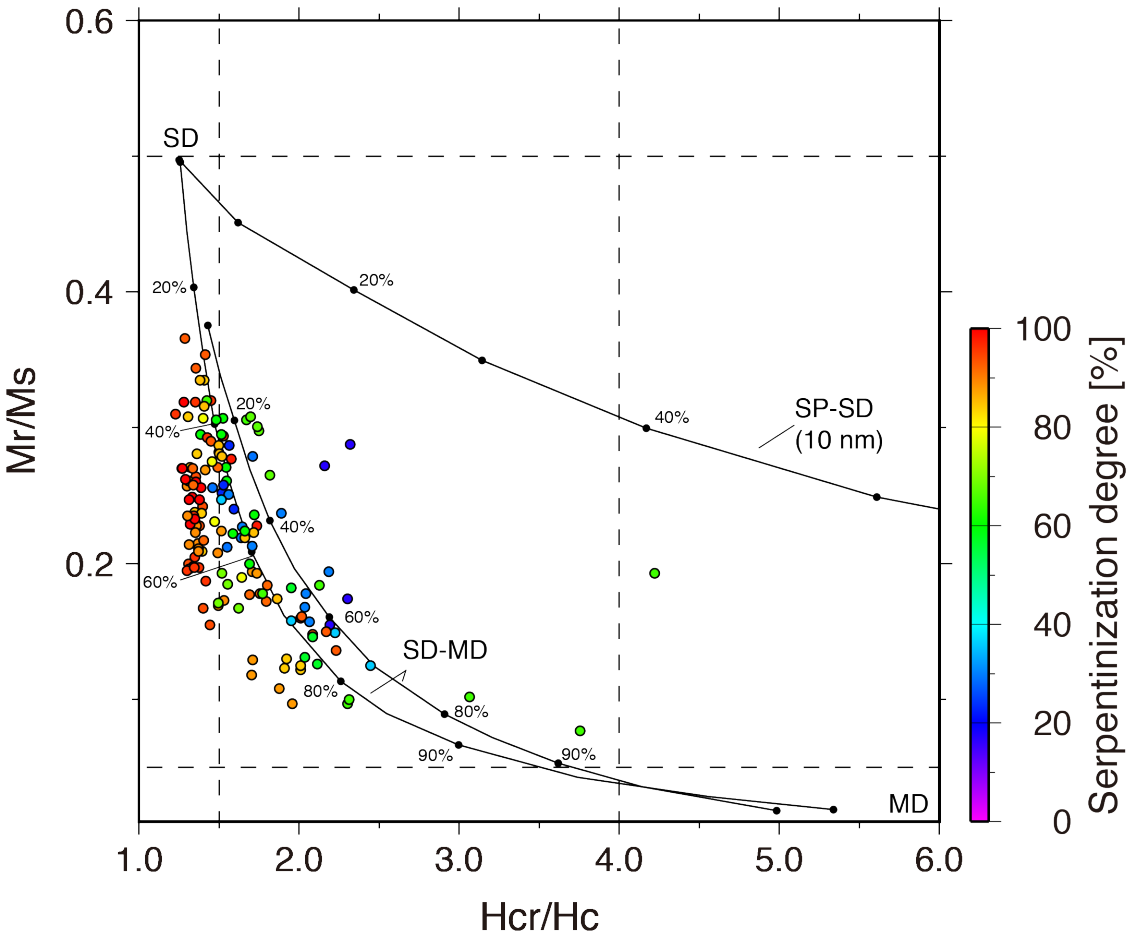

Figure 4-11. Day plot for serpentinized peridotites with serpentinization degrees of 17−100%.

Day plot [*Day et al*., 1977] for all 30 samples of serpentinized peridotites from the Yokoniwa Rise of the Central Indian Ridge. The solid lines show the theoretical mixing curves of SD–MD and SP–SD for magnetite [*Dunlop*, 2002]. SD, single-domain; MD, multi-domain; SP super-paramagnetic.

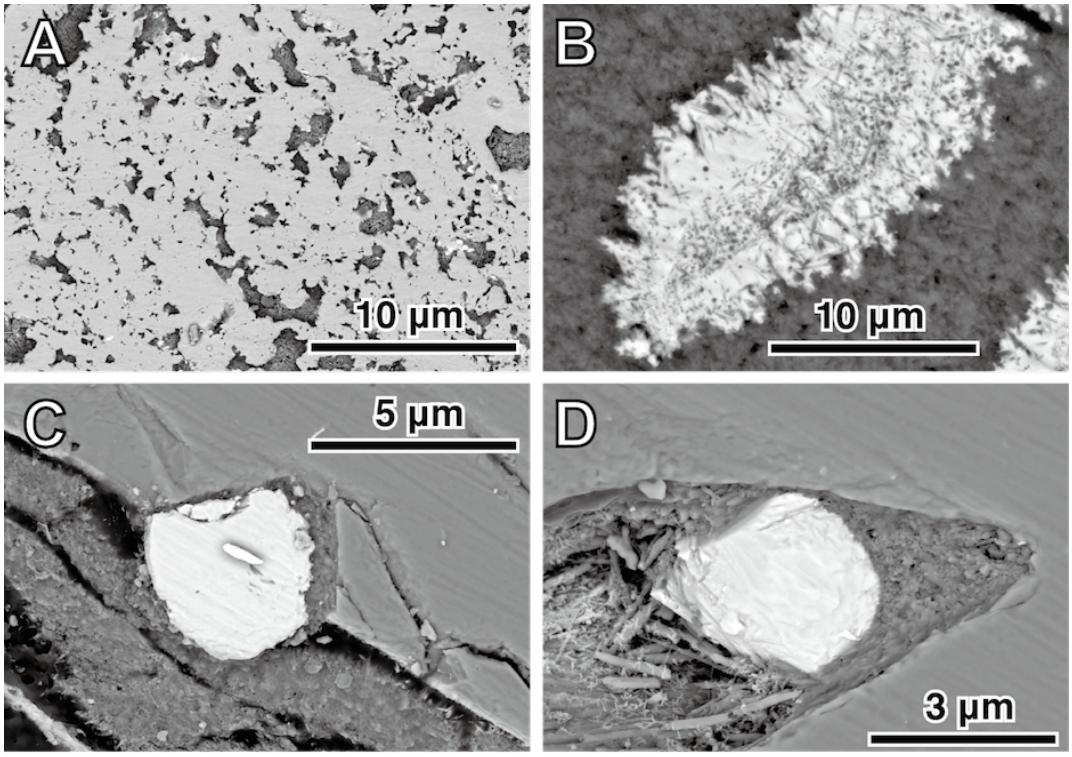

Figure 4-12. BSE-images of serpentinized peridotite.

Back-scattered electron (BSE) images of magnetite grains showing (a) concentration of magnetite grains in the 96% serpentinized peridotite (6K1170R12) with a magnetite amount of 4.8 wt% (b) assemblage of the needle-like grains in the 79% serpentinized peridotite (DR11-004) with a magnetite amount of 2.8 wt%, (c) primary creation along the primary mineral rim in the 17% serpentinized peridotite (6K1170-R25) with a magnetite amount of 0.1 wt%, and (d) development within cracks in the 17% serpentinized peridotite (6K1170-R25) with a magnetite amount of 0.1 wt%.

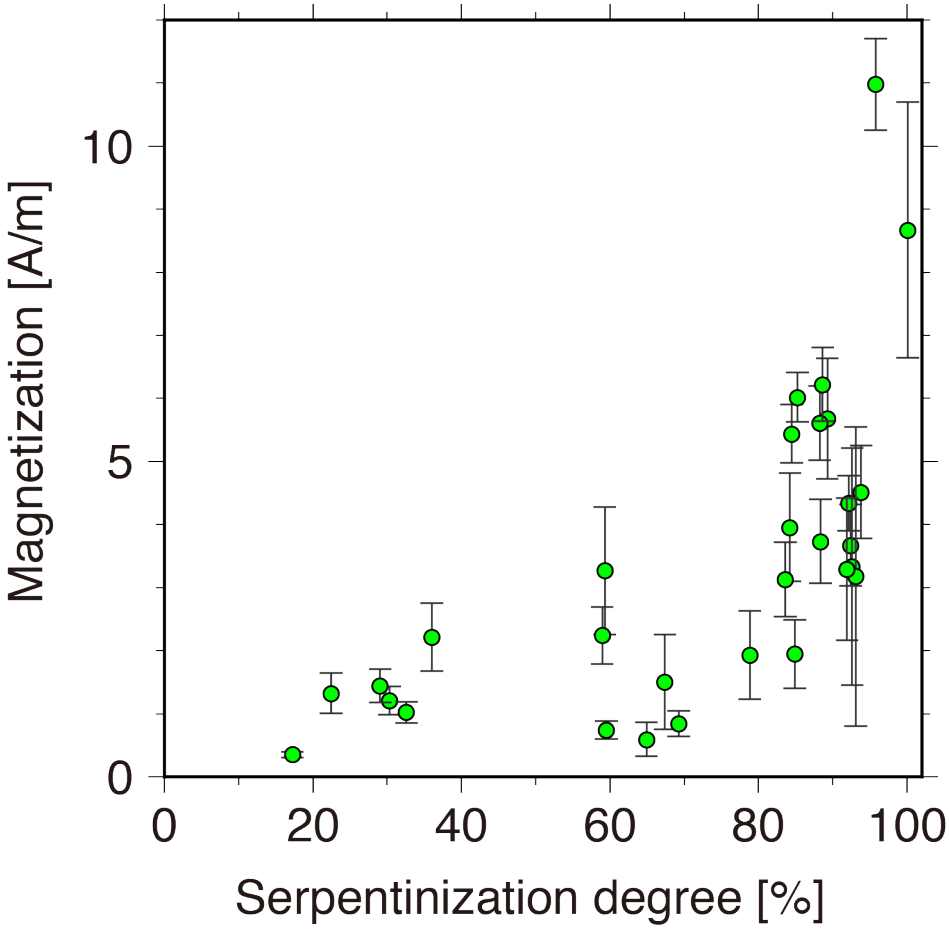

Figure 4-13. Magnetization and serpentinization degree of serpentinized peridotites.

Magnetization (A/m) and serpentinization degree (%) of 30 serpentinized peridotites. Magnetization was estimated by the sum of natural remanent magnetization (NRM) with induced magnetization calculated for a magnetic field of 45000 nT.

Table 4-1. Rock magnetic properties and density of seafloor rock samples from the Yokoniwa Rise, including serpentinized peridotite, sulfide, basalt, dolerite, and gabbro.

			ρ (g/cm^3)		NRM (A/m)		K (SI)			
Rock type	Sample name	N	mean	stdv	mean	stdv	mean	stdv	Q	S (%)
Serpentinized peridotite	6K#1170R01	4	2.66	0.01	2.47	0.45	0.0572	0.0081	1.2	94
	6K#1170R03	4	2.68	0.03	3.54	0.71	0.0598	0.0069	1.7	89
	6K#1170R04	4	2.72	0.01	3.94	0.38	0.0420	0.0022	2.6	84
	6K#1170R05	4	2.67	0.05	2.25	0.53	0.0398	0.0031	1.6	92
	6K#1170R08	4	2.87	0.01	2.39	0.82	0.0244	0.0053	2.7	59
	6K#1170R09	4	2.70	0.01	2.23	0.49	0.0480	0.0103	1.3	84
	6K#1170R12	4	2.68	0.02	8.35	0.58	0.0734	0.0039	3.2	96
	6K#1170R14	4	3.14	0.02	0.88	0.24	0.0124	0.0023	2.0	22
	6K#1170R15	4	3.08	0.02	0.75	0.16	0.0129	0.0017	1.6	30
	6K#1170R19	4	3.10	0.01	0.89	0.18	0.0154	0.0022	1.6	29
	6K#1170R20	4	2.66	0.02	2.64	0.22	0.0475	0.0060	1.6	92
	6K#1170R21	4	2.71	0.01	1.47	0.50	0.0464	0.0026	0.9	84
	6K#1170R22	4	2.66	0.02	1.27	0.30	0.0190	0.0069	1.9	85
	6K#1170R23	4	2.63	0.02	3.00	0.56	0.0205	0.0030	4.1	88
	6K#1170R25	4	3.17	0.03	0.29	0.04	0.0016	0.0002	5.1	17
	6K#1170R26	4	3.05	0.14	0.59	0.08	0.0121	0.0025	1.4	33
	6K#1170R27	4	3.04	0.05	1.32	0.29	0.0250	0.0071	1.5	36
	6K#1170R31	4	2.82	0.01	0.42	0.15	0.0046	0.0033	2.6	65
	6K#1176R01	4	2.65	0.02	2.48	1.40	0.0237	0.0135	2.9	93
	6K#1176R03	4	2.64	0.02	6.21	1.46	0.0686	0.0159	2.5	100
	6K#1176R04	4	2.73	0.02	2.51	0.29	0.0867	0.0084	0.8	88
	6K#1176R09	4	2.65	0.01	1.91	2.15	0.0354	0.0062	1.5	93
	6K#1176R10	4	2.87	0.03	1.29	0.24	0.0266	0.0059	1.4	59
	6K#1176R15	4	2.65	0.01	1.45	0.84	0.0513	0.0081	0.8	92
	6K#1176R21	2	2.75	0.03	3.87	0.17	0.0655	0.0116	1.7	89
	DR11-002	4	2.84	0.03	0.20	0.04	0.0150	0.0028	0.4	60
	DR11-003	4	2.81	0.13	0.80	0.21	0.0198	0.0151	1.1	67
	DR11-004	4	2.75	0.02	1.00	0.37	0.0260	0.0092	1.1	79
	DR11-008	4	2.78	0.04	0.35	0.07	0.0137	0.0037	0.7	69
	DR11-011	2	2.74	0.01	4.35	0.32	0.0466	0.0020	2.6	85
Sulfide	6K#1331R08	4	3.48	0.04	0.06	0.04	0.0016	0.0001	1.0	
	6K#1331R09	4	4.21	0.08	0.04	0.01	0.0009	0.0002	1.2	
	6K#1331R10	4	4.02	0.07	0.03	0.01	0.0008	0.0000	1.1	
	6K#1331R11	4	3.92	0.06	0.02	0.01	0.0008	0.0001	0.7	
	6K#1176R23	4	3.79	0.19	0.09	0.12	0.0010	0.0004	2.7	
Basalt	6K#1331R01	4	2.94	0.03	1.18	1.03	0.0007	0.0002	45.8	
	6K#1331R02	4	2.96	0.02	0.85	0.38	0.0007	0.0001	34.5	
	6K#1331R03	6	2.97	0.02	2.03	1.52	0.0009	0.0002	65.8	
	6K#1331R04	5	2.96	0.03	1.30	0.86	0.0007	0.0002	52.0	
	6K#1331R06	8	2.95	0.05	1.73	1.34	0.0008	0.0002	59.0	
	6K#1331R07	4	2.97	0.04	1.80	1.80	0.0007	0.0001	74.1	
	6K#1170R02	4	3.05	0.03	0.01	0.00	0.0011	0.0002	0.3	
	6K#1170R10	4	3.02	0.02	0.23	0.01	0.0069	0.0004	0.9	
	6K#1170R11	4	3.07	0.02	0.48	0.06	0.0110	0.0014	1.2	
	6k#1170R30	4	3.04	0.02	6.33	0.40	0.0027	0.0001	66.2	
	6K#1176R19	2	3.03	0.07	0.43	0.42	0.0011	0.0000	10.6	
Dolerite	6K#1176R05	4	2.96	0.01	0.44	0.04	0.0034	0.0010	3.6	
	6K#1176R07	4	2.92	0.00	0.10	0.00	0.0017	0.0002	1.7	
	6K#1176R17	4	3.05	0.02	0.05	0.03	0.0056	0.0036	0.3	
	6K#1176R18	4	3.05	0.03	0.12	0.07	0.0143	0.0046	0.2	
Gabbro	6K#1170R13	4	2.70	0.02	0.85	0.28	0.0268	0.0180	0.9	
	6K#1170R18	4	2.94	0.05	1.78	0.83	0.0061	0.0023	8.1	

Abbrevations are ρ, grain density; NRM, natural remanent magnetization; K, magnetic susceptibility; Q, Koenigsberger ratio; S, serpentinization degree.

Table 4-2. Detailed rock magnetic properties, density, and serpentinization degree of serpentinized peridotite samples.

Sample name	N_{CU}	Density (kg/m^3)	σ_{DEN} (kg/m^3)	NRM (A/m)	σ_{NRM} (A/m)	K (SI)	σ_K (SI)	Q	N_{CH}	W_{CHIP} (mg)	Ms (Am^2/kg)	σ_{Ms} (Am^2/kg)	Mgt (wt%)	Sc (%)	MDF (mT)	Latitude (°)	Longitude (°)	Depth (m)
6K#1170R01	4	2.66	0.01	2.5	0.45	0.057	0.008	1.2	6	808	3.50	2.84	3.8	94	16	-25.2497	70.10210	3420
6K#1170R03	4	2.68	0.03	3.5	0.71	0.060	0.007	1.7	5	613	2.68	0.48	2.9	89	22	-25.2497	70.10210	3420
6K#1170R04	4	2.72	0.01	3.9	0.38	0.042	0.002	2.6	4	696	2.90	1.23	3.2	84	29	-25.2496	70.10060	3315
6K#1170R05	4	2.67	0.05	2.2	0.53	0.040	0.003	1.6	4	576	3.21	0.76	3.5	92	18	-25.2496	70.10060	3315
6K#1170R08	4	2.87	0.01	2.4	0.82	0.024	0.005	2.7	7	1934	1.39	1.48	1.5	59	20	-25.2496	70.10030	3298
6K#1170R09	4	2.70	0.01	2.2	0.49	0.048	0.010	1.3	4	964	2.06	1.28	2.2	84	21	-25.2516	70.09740	3216
6K#1170R12	4	2.68	0.02	8.4	0.58	0.073	0.004	3.2	12	1257	4.41	2.74	4.8	96	25	-25.2532	70.08810	2987
6K#1170R14	4	3.14	0.02	0.9	0.24	0.012	0.002	2.0	4	1159	0.67	0.29	0.7	22	36	-25.2532	70.08810	2987
6K#1170R15	4	3.08	0.01	0.7	0.16	0.013	0.002	1.6	4	669	0.70	0.13	0.8	30	21	-25.2526	70.08580	2885
6K#1170R19	4	3.10	0.01	0.9	0.18	0.015	0.002	1.6	4	975	1.21	0.79	1.3	29	40	-25.2518	70.08210	2783
6K#1170R20	4	2.66	0.02	2.6	0.22	0.047	0.006	1.6	4	1068	2.78	0.81	3.0	92	13	-25.2518	70.08210	2783
6K#1170R21	4	2.71	0.01	1.5	0.50	0.046	0.003	0.9	4	728	2.31	0.34	2.5	84	18	-25.2521	70.08030	2700
6K#1170R22	4	2.66	0.02	1.3	0.30	0.019	0.007	1.9	5	819	0.78	0.51	0.8	85	24	-25.2521	70.08030	2700
6K#1170R23	4	2.63	0.02	3.0	0.56	0.021	0.003	4.1	4	553	1.00	0.11	1.1	88	37	-25.2521	70.08030	2700
6K#1170R25	4	3.17	0.03	0.3	0.04	0.002	0.000	5.1	4	1054	0.07	0.05	0.1	17	44	-25.2524	70.07830	2635
6K#1170R26	4	3.05	0.14	0.6	0.08	0.012	0.002	1.4	4	830	0.34	0.20	0.4	33	38	-25.2524	70.07830	2635
6K#1170R27	4	3.04	0.05	1.3	0.29	0.025	0.007	1.5	4	928	0.85	0.73	0.9	36	30	-25.2530	70.07720	2569
6K#1170R31	4	2.82	0.01	0.4	0.15	0.005	0.003	2.6	9	2258	1.31	1.23	1.4	65	47	-25.2542	70.07630	2539
6K#1176R01	4	2.65	0.02	2.5	1.40	0.024	0.013	2.9	4	870	2.57	1.35	2.8	93	56	-25.2748	70.09340	3031
6K#1176R03	4	2.64	0.02	6.2	1.46	0.069	0.016	2.5	10	1143	4.29	1.46	4.7	100	28	-25.2747	70.09240	2998
6K#1176R04	4	2.73	0.02	2.5	0.29	0.087	0.008	0.8	4	635	4.27	1.03	4.6	88	24	-25.2747	70.09240	2998
6K#1176R09	4	2.65	0.01	1.9	2.15	0.035	0.006	1.5	4	810	2.83	0.91	3.1	93	44	-25.2741	70.08570	2763
6K#1176R10	4	2.87	0.03	1.3	0.24	0.027	0.006	1.4	4	1050	1.24	0.82	1.3	59	31	-25.2738	70.08380	2657
6K#1176R15	4	2.65	0.01	1.5	0.84	0.051	0.008	0.8	4	735	2.44	0.39	2.7	92	34	-25.2730	70.08100	2530
6K#1176R21	2	2.75	0.03	3.9	0.17	0.066	0.012	1.7	4	714	5.03	0.89	5.5	89	19	-25.2682	70.07240	2491
DR11-002	4	2.84	0.03	0.2	0.04	0.015	0.003	0.4	4	1198	0.31	0.28	0.3	60	43	-25.2450	70.06660	2594
DR11-003	4	2.81	0.13	0.8	0.21	0.020	0.015	1.1	4	880	1.46	0.11	1.6	67	90	-25.2450	70.06660	2594
DR11-004	4	2.75	0.02	1.0	0.37	0.026	0.009	1.1	4	642	2.53	1.17	2.8	79	35	-25.2450	70.06660	2594
DR11-008	4	2.78	0.04	0.4	0.07	0.014	0.004	0.7	4	803	0.85	0.28	0.9	69	28	-25.2450	70.06660	2594
DR11-011	2	2.74	0.01	4.4	0.32	0.047	0.002	2.6	4	654	3.93	0.69	4.3	85	34	-25.2450	70.06660	2594

Abbreviations are N_{CU}, number of measured cubic subsamples ; σ_{DEN}, standard deviation of density; NRM, natural remanent magnetization; σ_{NRM}, standard deviation of natural remanent magnetization; K, magnetic susceptibility; σ_K, standard deviation of magnetic susceptibility; Q, Koenigsberger ratio; Js, saturation magnetization; N_{CH}, number of measured chip subsamples; W_{CHIP}, total weight of chip subsamples; Ms, saturation magnetization; σ_{Ms}, standard deviation of saturation magnetization; Mgt, magnetite amount; Sc, serpentinization degree; MDF, median destructive field.

Chapter 5

Discussion

5-1. Magnetic Signature of Volcanic Lava-hosted Hydrothermal Systems

The general correlation between reduced crustal magnetization and hydrothermal activity in basalt-hosted systems has been well documented in mid-ocean ridges (MORs); on the TAG site developed along the detachments faults of the northern Mid-Atlantic Ridge (MAR) [*Tivey et al*., 1993]; the Krasnov site within the axial volcanic ridge near the axial valley wall of the mid-MAR [*Szitkar et al*., 2014a]; the 4°48′S area within the axial rift on very fresh lavas in the southern MAR including the Comfortless Cove, Turtle Pits, and Red Lion sites [*German et al*., 2008; *Tivey and Dyment*, 2010]; the Endeavour Field developed within the axial rift valley of the Juan de Fuca Ridge (JFR) [*Tivey and Johnson*, 2002]; and a hydrothermal site on the southwestern Indian Ridge (SWIR) [*Zhu et al*., 2010]. In this study of hydrothermal fields of the southern Mariana Trough (SMT) [Chapter 2] and the Okinawa Trough [Chapter 3], it was clearly demonstrated that reduced magnetization zones associated with hydrothermal areas are accompanied by basalt to andesite-hosted systems in back-arc regions; at the Snail and Yamanaka sites along a back-arc spreading center, at the Archean site at the foot of an axial high; at the Pika and Urashima sites on an off-axis knoll; and at the Irabu site within a back-arc rift. Moreover, the rhyolite-hosted hydrothermal system of the Tarama site developed near the volcanic arc also shows a magnetic low at an active hydrothermal vent field [Chapter 3]. Although the mineral compositions of basalt, andesite, and rhyolite are different, as are the types and amounts of their magnetic minerals, the magnetic signature of andesite- to rhyolite-hosted arc–

back-arc hydrothermal systems is essentially the same as that of basalt-hosted MOR systems. Such zones of weak magnetization are observed in the hydrothermal fields of the SMT and Okinawa Trough, and in other arc–back-arc hydrothermal systems such as the basalt to andesite-hosted hydrothermal fields of the Palinuro volcano on the Aeolian volcanic arc [*Caratori-Tontini et al*., 2014; *Szitkar et al*., 2015], the Hakurei hydrothermal field hosted in andesite to dacite rocks on the Izu–Ogasawara back-arc rift zone [*Honsho et al*., 2013], and dacite to rhyodacite-hosted hydrothermal fields of the Brothers volcano on the Kermadec arc [*Caratori-Tontini et al*., 2012a, 2012b].

Four possible factors are considered for producing magnetic low related to hydrothermal activity: (i) alteration of magnetic mineral (titanomagnetite) within volcanic basement rock, (ii) accumulation of nonmagnetic hydrothermal deposits, (iii) thermal demagnetization, and (iv) self-reversal. It is considered that the primary process causing weak magnetization is alteration of the host rock with highly corrosive hydrothermal fluid, altering the magnetic mineral (titanomagnetite) that carries strong natural remanent magnetization (NRM) in volcanic rock to less magnetic or nonmagnetic mineral phases [e.g., *Hochstein and Soengkono*, 1997; *Irving*, 1970; *Johnson and Atwater*, 1977; *Johnson et al*., 1982; *Hall*, 1992; *Ade-Hall et al*., 1971; *Watkins and Paster*, 1971]. The presence of thick hydrothermal deposits increases the distance between the magnetic field measurements and the underlying magnetized basement rocks, resulting in an apparent magnetic low [*Szitkar et al*., 2014a]. Thermal demagnetization is also a possible source for reduced magnetization if the subsurface temperature beneath a vent site approaches the Curie temperature of the mineral carrying the magnetic signal, which is typically 150–200°C for titanomagnetite within mid-ocean ridge basalts (MORBs) [*Dunlop and Ozdemir*, 1997] as reported in an early magnetic study of *Wooldridge et al*. [1992]. However, demagnetized zones have been confirmed at both active and inactive, or low-temperature, vent sites of the SMT [Chapter 2], the Endeavour Field in the JFR [*Tivey and Johnson*, 2002], and the Krasnov site in the MAR [*Szitkar et al*., 2015]. These results suggest that hydrothermal alteration rather than elevated temperatures should be the primary mechanism for the crustal demagnetization. Furthermore, *Tivey et al*. [2014] demonstrated that discrete areas of reduced magnetization of the Endeavour Field in the JFR are associated with active and inactive hydrothermal vent deposits in addition to areas of high conductive heat flow [*Salmi et al*., 2014] and near-bottom water temperature anomalies [*Hearn et*

al., 2013]. In this area, downward continuation of the geothermal gradient from the conductive heat flow data [*Salmi et al*., 2014] suggests that the subsurface temperatures in the zones of reduced magnetization are not sufficiently elevated to thermally demagnetize the crust on the observed scale. Moreover, because arc and back-arc volcanic rocks with high Fe and low Ti contents had high Curie temperatures up to 480°C [Chapter 3], the contribution of thermal demagnetization is likely small in arc and back-arc hydrothermal systems. Another possibility for the magnetic low over hydrothermal fields is self-reversed chemical remanent magnetization (CRM), which has been discussed for the last 40 years [e.g., *Verhoogen*, 1956; *O'Reilly and Banerjee*, 1966]. Self-reversal could be produced during extreme low-temperature oxidation (maghemitization) of titanomagnetite by ionic reordering [e.g., *Dunlop and Ozdemir*, 1997]. Hydrothermal fields are generally under high-temperature conditions rather than those of extreme low-temperature; therefore, it is unlikely that the hosted volcanic rocks of hydrothermal systems become self-reversed. A recent study of oxidized basalts recovered at nine drilling sites in the Pacific Ocean indicated that very high oxidation states (z >0.9) and relatively high Ti contents (x > 0.6) are needed to produce natural self-reversed components and that self-reversed magnetizations is not a general feature of the magnetization carried by oceanic basalt [*Doubrovine and Tarduno*, 2006].

In summary, observations of near-seafloor high-resolution magnetic signatures in various tectonic settings have clearly demonstrated that lava-hosted hydrothermal sites with wide ranges of hosted volcanic rock types such as basalt–rhyolite yield a common magnetic signature: a magnetic anomaly reflecting a zone of weak or null magnetization. Crustal magnetization is considerably affected by hydrothermal fluid circulation, particularly in the focused discharge zones where high-temperature buoyant fluids ascend to the seafloor surface. The origin of magnetic lows is mainly the alteration of titanomagnetite within volcanic rocks and secondary accumulation of nonmagnetic hydrothermal deposits. This signature is generally common even if the type of basement rock differ from basalt to rhyolite.

5-2. Magnetic Evolution at Ultramafic-hosted Hydrothermal Systems

In contrast to the magnetic low at lava-hosted hydrothermally discharge zones, enhanced magnetic anomalies and crustal magnetization of approximately 10 A/m were observed at an extinct site of the ultramafic-hosted Yokoniwa hydrothermal field (YHF) in the Central Indian ridge (CIR) [Chapter 4]. Rock magnetic analysis for the host rock surrounding the YHF indicated that this positive magnetization resulted from an abundance of magnetite within highly serpentinized peridotites [Chapter 4]. A sample with serpentinization degree of 96% was shown to have a NRM value of 8.4 A/m and magnetic susceptibility of 0.073 SI equivalent to induced magnetization of 2.3 A/m under 40,000 nT geomagnetic field intensity [Chapter 4]. A highly serpentinized body can be formed through long-lived hydrothermal circulation that is significant enough to react with sub-seafloor ultramafic rocks.

Enhanced magnetization in ultramafic-hosted hydrothermal fields has also been reported at the Rainbow and Ashadze-1 sites of the MAR [*Szitkar et al.*, 2014b; *Nakase*, 2002; *Tivey and Dyment et al*., 2010]. Furthermore, strong magnetization associated with hydrothermal sites has been observed at the sediment-hosted Bent Hill massive sulfide (BHMS) on the JFR [*Tivey*, 1994; *Gee et al*., 2001].

The BHMS is an inactive massive sulfide mound located within the Middle Valley that has been buried by 200 m to more than 1000 m of turbiditic and hemipelagic sediments derived from the adjacent continental margin during the Pleistocene sea level low stand. The BHMS is one of the most prominent modern Besshi-type deposits, which are related to the interaction of seawater with hot oceanic crust and often to the subsequent reaction of these fluids with organic-rich sediments [*Davis et al*., 1987]. The Ocean Drilling Program (ODP) legs 139 and 169 clarified that BHMS deposits were produced by high-temperature fluids at 350–400°C [*Goodfellow and Peter*, 1994; *Peter et al*., 1994], and that a significant volume of the deposit was likely formed 200–140 ka [*Mottl et al*., 1994]. A deep-tow magnetic survey conducted at an altitude of 50–100 m reported a strong magnetization with 5 A/m for a uniformly magnetized body (Fig. 1-12) [*Gee et al*., 2001]. A comparison of the data from the submersible *Alvin* survey 5 m above the seafloor [*Tivey*, 1994] and drill core samples [*Korner*, 1994] revealed that the upper portion of the sulfide mound must have a significantly higher

magnetization of 10% magnetite + pyrrhotite than that at deeper levels. Moreover, their ratio of saturation remanence to saturation magnetization of 0.01–0.15 suggests that the magnetite within the sulfide mound occurs primarily as coarse, multi-domain (MD) grains [*Korner*, 1994]. These results suggest that the magnetization may be adequately modeled as entirely induced magnetization rather than remanence in the BHMS.

The Rainbow and Ashadze-1 sites are both high-temperature active vents with fluid temperatures >300°C [*Fouquet et al*., 2010]. The magnetization intensity from magnetic anomalies increases ~30 A/m at the Rainbow site (Fig. 1-13) [*Szitkar et al*., 2014b], which is significantly larger than that observed at the YHF (~10 A/m). In contrast, the magnetization intensity at the Ashadze-1 (~4 A/m) is smaller than that at the YHF (Fig. 1-14) [*Szitkar et al*., 2014b]. No rock samples were collected from the Ashdze-1 site. *Tivey and Dyment et al*. [2010] proposed that the magnetization high at the Rainbow site reflects the presence of a magnetic iron sulfide (pyrrhotite). *Szitkar et al.* [2014b] interpreted the high magnetization zone to reflect strongly magnetized magnetite in the stockwork created during the serpentinization of ultramafic rocks. At the Rainbow site, the maximum values for magnetization of serpentinized peridotite samples in the stockwork zone are <13 A/m, as calculated by using magnetic susceptibility of 0.007 SI and NRM intensity of 12 A/m [*Szitkar et al*., 2014b]. The main magnetic bearer is magnetite, according to the Curie temperature of ~580°C [*Szitkar et al*., 2014b]. However, this magnetization value does not sufficiently explain the magnetization intensity of ~30 A/m estimated from the observed magnetic anomaly [*Szitkar et al*., 2014b]. As discussed by *Tivey and Dyment et al*. [2010], the presence of the strongly magnetized magnetic iron sulfides (pyrrhotite) are considered to be part of the source of the magnetic anomaly at the Rainbow site. The abundant H_2 content of ~16 mM resulting from the serpentinization process created a more reducing environment, which may have protected the pyrrhotite from oxidation [*Charlou et al*., 2010]. One noteworthy feature is that the highest magnetization intensity of the serpentinized peridotite from the Rainbow site (~13 A/m) is consistent with the highest value for the Yokoniwa sample (~11 A/m). This result implies that magnetization of ~10–15 A/m is the contribution of magnetite-rich serpentinized peridotite.

On the basis of the differences in magnetization intensity among the YHF, Rainbow, and Ashadze sites, I propose a three-stage model for magnetic mineral formation in ultramafic-hosted hydrothermal fields (Fig. 5-1). During the initial stage of

an ultramafic-hosted hydrothermal system, magnetite forms with serpentine and H_2 thorough hydrothermal alteration of peridotites. Strongly magnetized pyrrhotite creation also occurs through sulfide mineralization under reductive conditions, according to the presence of pyrrhotite confirmed at several hydrothermal fields [*Fouquet et al*., 2010]. I consider the Ashadze-1 site to be within this stage of development (Stage 1 in Fig. 5-1). The hydrothermal alteration in the Ashadze-1 site has not progressed; thus, the magnetite and pyrrhotite concentrations remain low, resulting in a low magnetization intensity of ~4 A/m. Once the serpentinization reaction has progressed by ~60%–70%, the amount of magnetite creation increases dramatically [e.g. *Oufi et al*., 2002; Chapter 4], which strengthens the magnetization. Pyrrhotite creation continues as long as the H_2 content of the hydrothermal fluids continues to create a reducing environment [e.g., *Bach et al.*, 2004]. Moreover, hot and reduced hydrothermal fluids enable the magnetite and pyrrhotite to maintain stability without low-temperature oxidation by reacting with cold seawater. I consider the Rainbow site (~30 A/m) to be in this stage of development (Stage 2 in Fig. 5-1). Once the reaction of ultramafic rocks ceases, H_2 is no longer formed in the system, and conditions become oxidative. This allows pyrrhotites to convert into nonmagnetic iron sulfide or oxide, reducing their magnetization considerably. I consider the YHF (~10 A/m) to be in this stage of development (Stage 3 in Fig. 5-1). The magnetization intensity of the YHF implies that the ultramafic bodies were completely serpentinized and that sulfide mineralization did not contribute to the magnetic anomaly. That is, strongly magnetized iron sulfides such as pyrrhotite do not exist in this area.

It should be noted that the amount of magnetite creation is known to be controlled by various factors such as temperature and primary rock composition. Natural samples [*Klein et al*., 2009, 2013b] and thermodynamic equilibrium models [*Klein et al*., 2013a] have demonstrated that serpentinized peridotite with abundant magnetite forms at temperatures higher than 200°C with the involvement of Fe-poor brucite. Although serpentinization of olivine-dominated lithology results in the formation of serpentine, brucite, and magnetite, that of orthopyroxene-dominated lithology results in the formation of serpentine and talc with little magnetite [*Klein et al*., 2013a]. These factors affecting the progress of serpentinization were not considered in this model because alteration conditions of the Yokoniwa peridotites are unknown. In addition, the formation and weathering conditions of magnetic sulfide minerals, as well as their

relationship with magnetite creation during serpentinization, have not been fully understood. Pyrrhotite can be transformed into magnetite as well as pyrite. However, my simplified conceptual evolutionary model can be used to effectively explain the observations. To confirm this preferred three-stage model for magnetic mineral formation in ultramafic-hosted hydrothermal systems and to develop a more comprehensive model, the contribution of pyrrhotite to crustal magnetization needs to be determined by future investigation based on drilled sub-seafloor samples.

5-3. Location and Spatial Scale of Seafloor Hydrothermal Systems

Hydrothermal processes involve complex interplay between the dynamics of heat supply and the evolution of crustal permeability to allow seawater to access the source. Therefore, the location and spatial scale of a hydrothermal system are controlled by the tectonic background of each vent field. For hydrothermal systems of mid-ocean ridges, early study of *Francheteau and Ballard* [1983] proposed a magmatic budget hypothesis such that hydrothermal activity increases with the magmatic budget. Global verification using 11 ridge sections totaling >6000 km showed good correlation between either the site frequency or hydrothermal plume incidence and the magmatic budget estimated from the crustal thickness [*Baker and German*, 2004]. This insight suggests that variability in magma or in the heat supply is the primary control for the distribution of seafloor hydrothermal fields, with permeability as a secondary control. Permeability likely becomes more important as the spreading rate decreases, where deep faults develop and mine deep heat of the upper mantle, gabbro intrusions, and serpentinization. Permeability may also play a key role in calderas and rift faults, particularly at volcanic arcs such as Izu–Bonin and Kermadec. The spatial scale of the magnetic contrast and duration time of seafloor hydrothermal systems of various tectonic settings are summarized in Table 5-1 and are discussed in the following subsections.

Fast-spreading ridges

Many hydrothermal vent systems are located in neo-volcanic zones of the fast-spreading East Pacific Rise (EPR), where about half of the known black smoker vents occur [e.g., *Hannington et al*., 2005]. Active vent fields of the EPR consist of small low-lying mounds (<10 m in diameter) with individual structures of a few meters, formed by the coalescence of smaller chimneys (Fig. 1-4) [e.g., *Haymon and Kastner*, 1981]. These systems are controlled by the heat and fluid flow associated with high-temperature black smoker vents, which are driven mainly by shallow dike-like intrusions. The high rate of heat removal by individual black smokers ensures that venting associated with shallow diking events on fast-spreading ridges is relatively short lived [e.g., *Lowell et al*., 1995]. *German and Lin* [2004] proposed a simple

conceptual model in which ridge extension is achieved via episodic diking of several meters in maximum width, in which the repeat period at any given location is about 50 years, followed by heat removal in three stages; (i) instantaneous generation of event plumes (−5% of total heat available); (ii) an evolving period of about five years of relatively fast heat discharge (−20%); (iii) and a decadal quiescent period (−75%). The first well-documented volcanic eruption at a hydrothermal vent site was observed in 1991 at the EPR 9°N, and eruptions are believed to occur at intervals of tens of years to cycles lasting 100–1,000 years [*Haymon et al*., 1991, 1993]. Such frequent eruptions can disrupt the flow of hydrothermal fluids and bury sulfide deposits that are localized along the eruptive fissures. As a result, the vent complexes at fast-spreading ridges tend to be small, and the deposits are rapidly displaced from their heat sources by the high spreading rates. This process has been confirmed by isotopic dating, which indicates that hydrothermal discharge at individual black smokers lasts only 10–100 years [e.g., *Kadko et al*., 1985; *Stakes and Moore*, 1991; *Koski et al*., 1994].

Detachment-fault-controlled slow-spreading ridges

The TAG site, a well-investigated basalt-hosted hydrothermal site located at the slow-spreading center of the MAR [e.g., *Rona et al*., 1986], is known to be significantly larger and longer-lived than equivalent systems at fast-spreading ridges (Fig. 1-4). This site occurs at the edge of the median valley on ~100 ka crust [*Tivey et al*., 1993] ~4 km east of the neo-volcanic ridge in an area of intense ridge-parallel faults. High-resolution sonar and photographic data have revealed that the localization of TAG hydrothermal activity is strongly controlled by permeable conduits at the intersections of actively developing faults [*Kleinrock and Humphris*, 1996]. High-resolution bathymetric data [*White et al*., 1998; *Roman and Singh*, 2007; *Pontbriand and Sohn*, 2014] have revealed a donut-shaped, 50 m-high hydrothermal deposit composed of two superimposed mounds. The largest mound is ~200 m in diameter, whereas the second mound is only ~100 m diameter and corresponds to the currently active hydrothermal area marked by numerous black smokers. The first magnetic study of this area was conducted by using the *Alvin* submersible at a maximum altitude of 20 m [*Tivey et al*., 1993]. That study revealed a reduction in crustal magnetization beneath the active sulfide mound. At 10–15 A/m, its intensity is smaller than that in the surrounding area, and it extends across

~200 m (Fig. 1-6). The TAG is one of only three sites drilled by the ODP or the Integrated Ocean Drilling program (IODP). The lithological data from drilling data [*Humphris et al*., 1996; *Herzig et al*., 1998] indicates that the hydrothermal deposit ranges in thickness from 0 m at the edges of the mound to 60 m beneath the active black smoker area, and that the stockwork zone including sulfide veins within altered basalt is restricted to a central zone of 80 m in diameter beneath the mound. Magnetic modeling considering these drilling data [*Szitkar and Dyment*, 2015] have revealed that the non-magnetic hydrothermal deposit material accounts for one-third of the negative magnetic anomaly observed by the *Alvin* (~20 m in altitude); thus, the remaining part requires a deeper demagnetized source. Radiometric dating data of hydrothermal deposits show that the TAG has persisted intermittently for 140,000 years [*Lalou et al*., 1995; *Humphris and Cann*, 2000]. These results indicate that both the giant hydrothermal deposit (~60 m thickness and ~200 m diameter) and the hydrothermally altered basement rock (80 m diameter) have been formed for more than 10^5 years under the controls of both detachment faults and deeper heat sources. Moreover, the formation of these bodies reduced the crustal magnetization, represented by a 10–15 A/m magnetic low across an area ~200 m diameter, as shown in the inverted crustal magnetization distribution.

Ultramafic exposure

A different class of hydrothermal systems is hosted in ultramafic rock. Ultramafic-hosted hydrothermal systems have been discovered only on slow- and ultraslow-spreading ridges, where peridotite outcrops are common. Several vent fields, such as the Rainbow [*German et al*., 1996], Ashadze [*Cherkashov et al*., 2008], and Yokoniwa sites [Chapter 4] occur in non-transform offsets, where the mafic crust is thin or patchy and large-scale normal faulting or detachment faulting is common. A detachment fault system is also important for controlling ultramafic-hosted hydrothermal systems, as well as larger and longer-lived system hosted in basaltic rock such as the TAG. *McCaig et al*. [2007] presented a model (Fig. 1-5) that explains fault-controlled hydrothermal systems in terms of different stages in the development of detachment faults. In their model, hydrothermal circulation near detachment faults evolves from basalt-hosted (TAG type) to footwall ultramafic-hosted (Rainbow type),

to low-temperature ultramafic-hosted (Lost City type) systems. The key features of their model are the intrusion of gabbro bodies below the detachment to provide a heat source for circulation and the focusing of fluid flow into the detachment fault to allow venting from the neo-volcanic axis. In an ultramafic-hosted system, the magnetization contrast is directly related to the hydrothermal alteration zone of stockwork because magnetic minerals such as magnetite and pyrrhotite are created by hydrothermal fluid reaction with ultramafic rock [Chapter 5-2]. The mapping of near-seafloor magnetic anomalies in the Rainbow, Ashadze [*Szitkar et al.*, 2014b; *Nakase*, 2002; *Tivey and Dyment et al*., 2010], and Yokoniwa [Chapter 4] hydrothermal sites has revealed the enhanced magnetization. The magnetic data reveal that the horizontal spatial scale of the high-magnetization zone is 200 m wide in the Rainbow site (Fig. 1-13) and 100 m wide in the Ashadze site (Fig. 1-14); the data were collected at 10 m and 20 m, respectively [*Szitkar et al*., 2014b]. In the Yokoniwa site, no gridded detailed magnetic data were acquired just above the seafloor, although AUV data at an altitude of 100 m showed a concentration of high magnetization zones a few hundred meters in width [Chapter 4]. Because the spatial scale of enhanced magnetization zones at these ultramafic-hosted sites is equivalent to that of the reduced magnetization zone at the TAG, it is considered that hydrothermal systems hosted in ultramafic rock might be large and long-lived systems similar to the TAG. The oldest hydrothermal deposits dated at the active Rainbow field yielded a U/Th age of 23±1.5 ka [*Kuznetsov et al.,* 2006], which is similar to the ^{14}C age of ~25 ka reported for the low-temperature fossil Clamstone site [*Lartaud et al.,* 2010].

Back-arc spreading region

Back-arc basins also include submarine hydrothermal systems similar to those observed at MORs, and their heat source is associated with arc–back-arc volcanism. The five active hydrothermal fields hosted in basalt–andesite are located in the intraoceanic back-arc spreading region of the SMT [Chapter 2]. The spatial extent of the low magnetization zone is regarded as a trace of hydrothermal activity that differs depending on the tectonic setting of the site [Chapter 2]. In contrast to long-lived and giant hydrothermal sites reported in slow- and ultraslow-spreading environments controlled by low-angle detachment faults, the hydrothermal systems in the SMT are

not associated with large fault systems cutting into the deeper crust and uppermost mantle, as suggested by the bathymetry and the very low seismicity [*Sato et al*., 2015b]. On the basis of the magnetization distribution derived from submersible magnetic data, I conclude that the off-axis hydrothermal vent sites are larger than those in on-axis sites, reflecting the longevity of the hydrothermal activity. The Snail and Yamanaka on-axis sites, at ~30 m in diameter, are located in a neo-volcanic zone and were likely controlled by dike intrusions over decadal timescales similar to those of the hydrothermal systems in the fast-spreading region [e.g., *German and Lin*, 2004]. In contrast, the Archean, Pika, and Urashima off-axis sites, at ~100 m in diameter, were controlled by off-axis magmatic activity over thousands of years, which produced a larger hydrothermal flux and longer duration of hydrothermal circulation [Chapter 2]. Radiometric dating of the sulfide deposits showed maximum ages of ~3500 years at the Archean site and ~9000 years at the Pika and Urashima sites [*Takamasa et al*., 2013; *Ishibashi et al*., 2015], suggesting the presence of relatively long-lived hydrothermal activity. The Archean site is actually located at the eastern foot of an axial high. *Sohn and Sims* [2005] proposed that bending stresses play a key role in triggering volcanism on the flanks of fast-spreading ridges with axial high morphologies by simultaneously opening tensile cracks near the surface and increasing the pore pressure of melt bodies trapped in the lower crust. A similar bending stress–crack-related type of volcanism may have provided the relatively longer heat source driving the Archean hydrothermal field. The longevity of the Pika and Urashima sites is likely related to giant off-axis volcanism that formed the seamount on which they are located. *Sato et al*. [2015b] mapped an upward convex high-velocity structure that suggests a trace of volcanic activity beneath the knoll. They inferred that off-axis volcanism once existed in that area to form the knoll and that intruded magma body was cooled, causing the boundary between layers 2 and 3 to form a convex shape upward. The seismicity near this off-axis volcano was very low during the observation period of three months, suggesting that volcanism might have ceased. The off-axis seamount represents a localized anomalous area with a high magmatic budget with the ability to drive several successive hydrothermal systems at the same place for a long time. The spatial scale of the reduced magnetization of Archean, Pika, and Urashima off-axis sites, at ~100 m in diameter, is not larger than that of the TAG, at ~200 m in diameter, possibly reflecting that smaller amounts of hydrothermal deposits formed during a period of ~10^4 years. This period is

shorter than the ~10^5 years determined for the TAG formation. The core samples obtained by benthic multi-coring clarified that a hydrothermal deposit with a sulfide chimney accumulated with minimum thickness of 4 m [*Nakamura et al*., 2015]. However, the lower boundary of the hydrothermal deposit and the extent of the stockwork remain unclear and require further exploration such as ODP and IODP deep drilling.

Calderas on volcanic arc and back-arc

Large hydrothermal venting fields related to arc volcanism have been discovered within giant summit calderas (several kilometers in diameter) along the Izu–Ogasawara island arc, the Tonga–Kermadec arc, and the Okinawa Trough. Hydrothermal vents are generally localized along the caldera walls or on the post caldera domes in these regions [e.g., *Fiske et al*., 2001]. Caldera faulting can provide a necessary structural control for focusing hydrothermal fluid. The post caldera lava domes also indicate the presence of a shallow magma reservoir, which can drive hydrothermal activity. The Myojin knoll near the volcanic front of the Izu–Ogasawara arc hosts extensive patches of hydrothermally altered pumiceous sediment, scattered outcrops of sulfide and barite, and breccia containing stockwork material along the caldera wall and on a 500-m high volcanic cone at the caldera center [*Iizasa et al*., 1999]. The caldera rim, 520–880 m below sea level, is about 7 km in diameter, and its floor is 4 km × 3 km at depths of 1350–1400 m; the caldera's collapse is approximately 18 km^3. The largest hydrothermal venting area, known as the Sunrise deposit, occupies an area of ~400 m in diameter with height of ~30 m [*Iizasa et al*., 1999]. The Hakurei hydrothermal field is located on another Izu–Ogasawara arc volcano, known as the Bayonnaise knoll, which is situated on the eastern boundary fault of the rift zone and has a summit caldera with ~3 km diameter. This field exists near the intersection of a caldera boundary fault and an inferred N–S-trending normal fault in the back-arc rift zone. A large number of active and inactive sulfide chimneys on sulfide mounds extend over an area of ~500 m × ~700 m [*Iizasa et al*., 2004]. A near-seafloor magnetic study for the Bayonnaise knoll was conducted by using the AUV *URASHIMA* at a general altitude of 80 m [*Honsho et al*., 2013]. In that study, it was reported that a low magnetization distribution associated with the Hakurei hydrothermal deposit extends mainly across an area of ~500 m × ~300 m (Fig. 1-10).

The correlation between the elongated direction of the magnetization low and the caldera wall strike strongly suggest that the up-flow zone is restricted by the caldera fault structure. *Honsho et al*. [2013] also pointed out that the hydrothermal deposit area, which runs uphill at the caldera wall, apparently extends beyond the low magnetization zone and over the high magnetization zone. It is implied that hydrothermal fluid rising from the deeper part through the alteration zone was transported laterally along many fissures and fractures in the caldera wall. The Brother volcano of the Tonga–Kermadec arc hosts large hydrothermal deposits within the summit caldera up to 3.5 km in diameter and 450 m deep. Active black smoker vents and massive sulfide deposits occur on the NW caldera wall, and lower temperature venting and apparent magmatic degassing occur on a 350 m-high dacitic volcanic cone on the caldera floor [*de Ronde et al*., 2001; 2005]. A near-seafloor magnetic study using AUVs *ABE* and *Sentry* (at an altitude of ~50 m) revealed that each hydrothermal field at the Brother volcano is marked by reduced magnetization (Fig. 1-11) [*Caratori-Tontini et al*., 2012]. In the hydrothermal field of the NW caldera wall, the very low magnetization extending across an area of 1 km × 0.5 km is consistent with area of focused venting that includes black smoker chimneys and numerous dead spires, which is at least 1200 years old [*de Ronde et al*., 2005]. The cone hydrothermal site is considered to be much younger than the NW caldera site, and contains no massive sulfides or black smoker chimneys [*de Ronde et al*., 2011]. In contrast to the NW caldera site, diffuse venting has been observed atop both on the main and satellite cones, which have been interpreted as a nascent magmatic-hydrothermal system. The cone site also has low crustal magnetization, although its intensity is higher that that at the NW caldera site [*Caratori-Tontini et al*., 2012]. *Caratori-Tontini et al*. [2012] considered that the diffuse venting at the cone site simply had insufficient time to alter a large volume of rock compared with the focused venting at the NW caldera site. A large hydrothermal field of the Okinawa Trough, known as Hakurei site, is developed within the Izena Hole, which is also referred to as the Izena Cauldron [*Ishibashi et al*., 2015]. This field is situated along the SW continuation of a chain of Quaternary volcanoes of the Ryukyu arc [*Shinjo et al*., 1999] and on the eastern end of the Aguni rift graben segment [*Halbach et al*., 1989]. The Izena Hole is a rectangular-shaped depression of about 6 km × 3 km. Hydrothermal activity including vigorous high temperature fluid venting associated with >10 m chimney structures has been observed over an area of exceeding 500 m. The electron

spin resonance (ESR) dating of barite crystals has revealed ages up to 16,000 years for the inactive chimneys [*Fujiwara et al*., 2015]. These hydrothermal fields on the Myojin, Bayonnaise, Brother volcanoes and on the Izena Hole are all related to the caldera structure and arc volcanism, and are large compared with the lateral scale of hydrothermal alteration and deposits found at MORs, which are typically a few hundreds of meter or less [e.g. *Tivey and Dyment*, 2010]. The spatial scale of these seafloor hydrothermal fields is similar to onland Kuroko deposits formed in the Hokuroku Basin, Japan, such as the Doyashiki and Matsumine-Shakanai in Hanaoka area and Motoyama-Uchinotai in Kosaka area [e.g., *Tanahashi et al*., 2008]

Similar hydrothermal fields associated with caldera structures have been confirmed in the Irabu-East, but are situated on the axial area of the back-arc rift of the southern Okinawa Trough [Chapter 3]. The unique signature of this knoll is a small caldera diameter of up to 500 m, which is significantly smaller than the summit caldera of the Myojin, Bayonnaise, and Brother volcanoes and the Izena Hole, which are >3 km in diameter. This difference was likely caused by the size differences of the magma chamber between back-arc and arc volcanisms. A near-seafloor magnetic study for the Irabu knolls was conducted by using the AUV *URASHIMA* at a general altitude of 100 m [Chapter 3]. I reported that the low magnetization zone is located on the foot and wall of the south caldera of the Irabu-East, which is consistent with the loci of focused venting and hydrothermal deposits. This case of a low magnetization zone situated along a caldera rim with hydrothermal deposits is similar to that in other fields of the Bayonnaise (Hakurei site) and Brother knolls, as previously mentioned. The caldera faults likely enhanced the crustal permeability, creating a pathway of hydrothermal fluid even in the relatively small summit caldera with ~500 m in diameter as well as in giant calderas with several kilometers in diameter. In the south caldera rim of the Irabu-East, the area with magnetization intensity is less than 12 A/m, which corresponds to a confirmed hydrothermal deposit extending across an area of 200 m × 300 m. The horizontal spatial scale of this low magnetization zone is less than half that of the caldera rim sites on the Bayonnaise and the Brother knolls. The hydrothermal site of the Irabu-East south is considered to be significantly younger than the sites on the Bayonnaise and the Brother knolls because the massive sulfide deposit, as observed at the Hakurei site on the Bayonnaise knoll and at the NW caldera site on the Brother knoll, was not observed at the Irabu site. The collected lava flow samples from the Irabu

knolls show significantly lower degree of maghemitization, suggesting that the lava is very fresh with no low-temperature oxidation [Chapter 3]. The Irabu-East site overall can be interpreted as a nascent hydrothermal system controlled by caldera faults. It is implied that the smaller spatial scale of low magnetization zone than that on the Bayonnaise and Brother knolls reflects a smaller extent of hydrothermal deposits with less volume. The potential for hydrothermal fluid resulting in hydrothermal deposits is also significantly smaller because of the poor magma budget. The volume of the caldera and volcano body of the Irabu-East is two to three times smaller than that of the Bayonnaise and Brother knolls. The reduced magnetization zone clarified by this study is still sufficient for covering an unobserved area; thus, the distribution of hydrothermal deposits and active chimneys of the Irabu-East possibly is likely to be wider. It is noteworthy that the magnetization intensity is clearly reduced at the Irabu-East, Bayonnaise, and Brother caldera sites. These observations imply that focused hydrothermal fluid immediately decreased the crustal magnetization. Moreover, the horizontal scale of the magnetic low associated with hydrothermal processes at the Irabu-East is equal to or larger than that at MORs such as the TAG [e.g. *Tivey and Dyment*, 2010], even though the Irabu-East site is a young hydrothermal system. It is considered that permeability structure may play an important role in the formation of a larger demagnetized hydrothermal fluid pathway in the caldera-controlled system. Further systematic surveys of heat flow measurements are needed to determine the permeability structure or style of hydrothermal circulation in the caldera-related hydrothermal system.

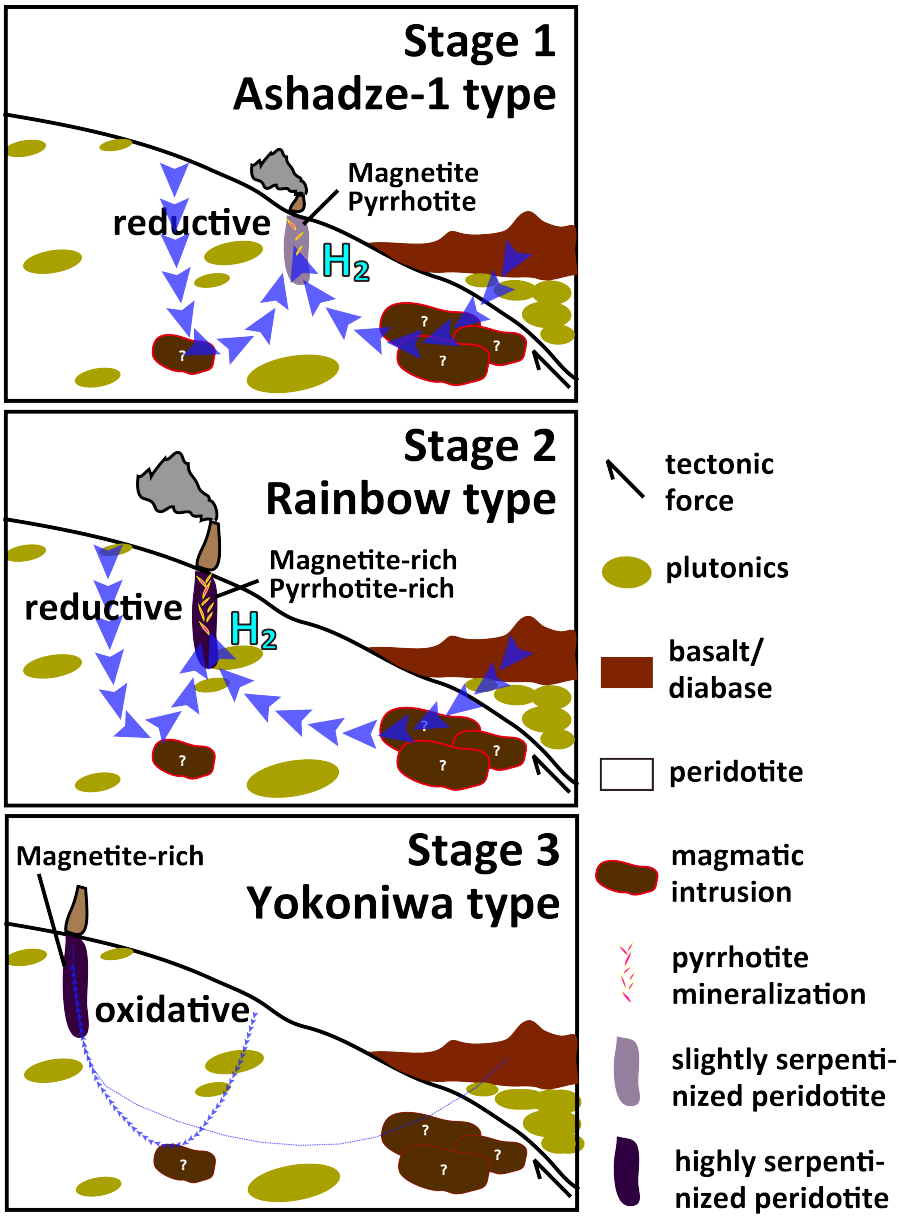

Figure 5-1. Model of magnetic mineral formation in ultramafic-hosted hydrothermal systems.

Model showing the three-stage formation history of magnetic minerals in ultramafic-hosted hydrothermal systems. Stage 1: some magnetized magnetite and pyrrhotite form thorough serpentinization and sulfide mineralization under reductive conditions, Stage 2: large quantity of magnetized magnetite and pyrrhotite are accumulated thorough serpentinization and sulfide mineralization under reductive conditions, Stage 3: only magnetized magnetite remains as main magnetic source under oxidative condition after serpentinization of host rock.

Table 5-1. Summary of horizontally spatial scale of magnetic contrast and duration time of seafloor hydrothermal systems in various tectonic setting.

Tectonic setting	Duration time	Spatial scale of magnetic contrast	Examples	Reference
Neo-volcanic zone	10^1-10^3 yr	$<10^3$ m^2	Snail, Yamanaka, (EPRs)	1
Foot of axial high	~10^3-10^4 yr	~10^4 m^2	Archean	1
Off-axis volcano	~10^3-10^4 yr	~10^4 m^2	Pika, Urashima	1
Detachment fault	>10^5 yr	>10^4 m^2	TAG	2, 3, 4
Non-transform offset	~10^5 yr	>10^4 m^2	Yokoniawa, Rainbow, Ashadze-1	3, 5, 6, 7
Summit caldera	~10^3-10^4 yr	10^5-10^6 m^2	Irabu, Hakure, Brothers	8, 9, 10

1: *This study* (Chapter 2), 2: *Tivey et al*., 1993, 3: *Tivey and Dyment*, 2010, 4: *Szitkar and Dyment*, 2014, 5: *This study* (Chapter 3), 6: *Szitkar et al*., 2014b, 7: *Nakase*, 2002, 8: *This study* (Chapter 4), 9: *Honsho et al*., 2013, 10: *Caratori-Tontini et al*., 2012.

Chapter 6

Conclusions

On the basis of the near-seafloor magnetic anomaly surveys and rock magnetic analyses in the present study, the following generalizations and conclusions are drawn concerning the magnetic response of hydrothermal systems in various tectonic settings:

1. Low magnetization zones were detected in on- and off-axis back-arc spreading center in the Mariana Trough and arc–back-arc volcanoes in the Okinawa Trough. These observations suggest that volcanic lava-hosted hydrothermal fields in various tectonic settings, including volcanic arcs and back-arc regions as well as previously studied MORs, yield a common magnetic signature: a magnetic anomaly reflecting a zone of weak or null magnetization. The crustal magnetization is considerably affected by hydrothermal fluid circulation, particularly in the focused discharge zones where high-temperature buoyant fluid ascends to the seafloor surface. The origin of magnetic lows is primarily alteration of titanomagnetite within volcanic rocks with a secondary mechanism of nonmagnetic hydrothermal deposit accumulation. This signature is generally common even if the type of basement rock differs from basalt to rhyolite.
2. Ultramafic-hosted hydrothermal system of the Yokoniwa field developed in a non-transform offset massif of the slow-spreading Central Indian Ridge is characterized by enhanced magnetization. Rock magnetic analyses reveal that this enhanced magnetization is due to abundant magnetite in highly serpentinized peridotite. Compared with similar ultramafic-hosted hydrothermal fields of the Rainbow and Ashadze-1 sites along the Mid-Atlantic Ridge, the following three-stage model for magnetic mineral formation in ultramafic-hosted

hydrothermal fields is proposed in the present study. During the initial stage of an ultramafic-hosted hydrothermal system, magnetite forms with serpentine and H_2 thorough hydrothermal alteration of peridotites. Strongly magnetized pyrrhotite is also created through sulfide mineralization under reductive conditions. This stage occurs at the Ashadze-1 site. Once the serpentinization reaction has progressed, the amount of magnetite creation increases dramatically, strengthening the magnetization. Pyrrhotite creation continues as long as the H_2 content of the hydrothermal fluids continues to create a reducing environment in this developing stage, such as that occurring at the Rainbow site. Hot and reduced hydrothermal fluids enable the magnetite and pyrrhotite to maintain stability with no low-temperature oxidation. Finally, once the reaction of ultramafic rocks ceases, H_2 is no longer formed in the system, and the conditions become oxidative. This allows the pyrrhotites to convert into nonmagnetic iron sulfide or oxide, reducing their magnetization considerably, such as that occurring at the Yokoniwa site.

3. Hydrothermal processes involve complex interplay between the dynamics of heat supply and the evolution of crustal permeability to allow seawater to access the source. As a result, the locations and spatial scales of hydrothermal systems are controlled by the tectonic background of each vent field. The results show that the horizontal extent of magnetic anomalies and its amplitude can be good indicator of scale of hydrothermal systems. Near-seafloor magnetic surveys in the Mariana Trough reveal that the Archean, Pika, and Urashima sites in the off-axis area are larger than the Snail and Yamanaka sites located in the axial area. Comparison with radiometric dating results of hydrothermal deposits suggests that the difference of the spatial scales reflects the longevity of the hydrothermal activity. On-axis sites located in a neo-volcanic zone are likely controlled by dike intrusions over decadal timescales, whereas off-axis sites are controlled by off-axis magmatic activity over thousands of years. Near-seafloor magnetic surveys of back-arc volcano with summit caldera (Irabu knoll) also demonstrate that the low magnetization zone extends across several hundred meters along the caldera rim. Compared with similar hydrothermal fields (Hakurei and Brothers) situated in active arc volcanoes with summit calderas, it is clarified that caldera-fault-controlled hydrothermal systems have horizontal spatial scale equal to or larger than those of detachment-controlled large hydrothermal fields at slow-spreading ridges. It is implied that the

permeability structure and style of hydrothermal circulation may play important roles in the formation of the larger demagnetized hydrothermal fluid pathways in caldera-controlled systems.

Although active hydrothermal sites are usually found by detecting their chemical and physical plumes in the water column, there is no such simple way to detect inactive hydrothermal systems. However, inactive sites are much better targets for seafloor mineral exploration because they do not host fragile ecosystems and are not affected by high thermal gradients. A major finding of this research is that the presence of hydrothermal sulfides and the oxidation, transformation, and/or creation of magnetic minerals at hydrothermal sites in various tectonic settings produce specific magnetic signatures that can be used to detect and characterize both active and inactive hydrothermal sites. Near-seafloor magnetic surveys using ROVs or AUVs can therefore be an important component of deep-sea exploration of hydrothermal systems.

Acknowledgements

I first would like to express my sincere gratitude to my supervisor, *Kyoko Okino* for providing this precious study opportunity to me as a PhD student at the University of Tokyo. She also provided many opportunities for me to meet many domestic and foreign researchers, which helped my research to have a wide scope.

I also express my deepest appreciation to my advisor *Chie Honsho* for invaluable discussion and comments, particularly concerning the methodology of this research. She encouraged and helped my work from the initial processing of data to the publication of articles. The various discussions about the magnetic anomalies are essentially for this work and will be the basis of my future studies.

I am very grateful to my advisor *Toshitsugu Yamazaki* for his elaborated guidance, considerable encouragement, and discussion that enable the great achievement of my research and made my research unforgettable. He provided many comments related to rock magnetic research.

I spent five years in the Department of the Ocean Floor Geoscience (OFGS), Atmosphere and Ocean Research Institute (AORI), University of Tokyo. I would like to thank all people in the OFGS as well as my advisors for offering advice throughout my studies, including *Juichiro Ashi*, *Hidekazu Tokuyama*, *Shuro Yoshikawa, Jin-Oh Park*, *Asuka Yamaguchi*, *Hironori Otsuka*, *Arata Kioka*, *Hodaka Kawahata*, *Yusuke Yokoyama*, *Toshihiro Yoshimura*, *Akiko Omura*, *Kazuya Naito*, *Kanehara Tomiko*, *Chieko Komatsu*, and *Akiko Mochizuki*. In particular, I am deeply grateful to *Chiori Tamura* for her technical support of magnetometer handling.

I would like to thank *Jerome Dyment* at the Institut de Physique du Globe de Paris for his advice and discussion during my two-month visit there. I also thank many researchers and friends I met during my visit, particularly *Florent Szitkar* for his kind support in developing the new analytical technique.

My heartfelt appreciation goes to *Masako Tominaga* at Michigan State University, whose encouragement and suggestions regarding my English ability are of inestimable

value. She provided the opportunity for me to stay in Michigan for three months and to hone my English skills by participating in graduate student classes and daily discussions.

I am grateful to many researchers for their offering sound advice in the meetings, workshops, research cruises, and geological field trips, including *Nobukazu Seama*, *Yoshifumi Nogi*, *Taichi Sato*, *Hiroshi Sato*, *Yasuhiko Ohara*, *Naoto Ishikawa*, *Miho Asada*, *Kentaro Nakamura, Tatsuo Nozaki, Hidenori Kumagai, Tetsuo Matsuno, Takuroh Noguchi, Toshiya Fujiwara, Keiichi Tadokoro, Koukichi Iizasa*, *Osamu Ishizuka*, *Tamaki Ura*, *Michinari Sunamura*, *Kazuo Nakahigashi*, *Shiki Machida, Sumio Miyashita*, *Yoshiko Adachi*, *Shusaku Yamazaki*, *Satoru Haraguchi*, *Susumu Umino*, *Katsuyoshi Michibayashi*, *Takafumi Kasaya*, *Junichiro Ishibashi*, *Hidetoshi Shibuya*, *Hirokuni Oda*, *Masao Ohno*, *Kazuto Kodama*, *Tomoaki Morishita*, *Natsue Abe*, and all others that cannot be mentioned here owing to space concerns. In particular, I learned measurement techniques for rock magnetism from *Yuhji Yamamoto* and *Nobutatsu Mochizuki* during my visit to the Center for Advance Marine Core Research, Kochi University, and to Kumamoto University.

I am greatly indebted to the crew of R/Vs *Yokosuka*, *Hakuho-maru*, *Oshoro-maru*, and *Shinsei-maru* and to the support teams of the HOV *SHINKAI 6500* and AUV *URASHIMA* for their professional support during cruises.

I have been financially supported by the Japan Society for the Promotion of Science (JSPS). The Department of Earth and Planetary Science, University of Tokyo, provided the opportunity for me to stay at the Institut de Physique du Globe de Paris with the financial support of the Institutional Program for Young Researcher Overseas Visits of the JSPS.

Finally I would like to extend my indebtedness to my family and friends for their support, understanding, and warm encouragement throughout my study.

Bibliography

Ade-Hall, J., F. Aumento, P. J. C. Ryall, R. E. Gerstein, J. Brooke, and D. L. McKeown (1973), The Mid-Atlantic Ridge Near 45 °N. XXI. Magnetic Results from Basalt Drill Cores from the Median Valley, *Can. J. Earth Sci.*, *10*(5), 679–696, doi:10.1139/e73-068.

Ade-Hall, J. M., H. C. Palmer, and T. P. Hubbard (1971), The Magnetic and Opaque Petrological Response of Basalts to Regional Hydrothermal Alteration, *Geophys. J. R. Astron. Soc.*, *24*(2), 137–174, doi:10.1111/j.1365-246X.1971.tb02171.x.

Alt, J. C. (1995), Subseafloor processes in mid-ocean ridge hydrothennal systems, in *Seafloor Hydrothermal Systems: Physical, Chemical, Biological, and Geological Interactions*, vol. 91, pp. 85–114, AGU, Washington, DC.

Amante, C., and B. W. Eakins (2009), ETOPO1 1 Arc-Minute Global Relief Model: Procedures, Data Sources and Analysis., *NOAA Tech. Memo. NESDIS NGDC-24*, 19 pp.

Andreani, M., J. Escartin, A. Delacour, B. Ildefonse, M. Godard, J. Dyment, A. E. Fallick, and Y. Fouquet (2014), Tectonic structure, lithology, and hydrothermal signature of the Rainbow massif (Mid-Atlantic Ridge 36°14′N), *Geochemistry, Geophys. Geosystems*, *15*(9), 3543–3571, doi:10.1002/2014GC005269.

Asada, M., A. Deschamps, T. Fujiwara, and Y. Nakamura (2007), Submarine lava flow emplacement and faulting in the axial valley of two morphologically distinct spreading segments of the Mariana back-arc basin from Wadatsumi side-scan sonar images, *Geochemistry, Geophys. Geosystems*, *8*(4), Q04001, doi:10.1029/2006GC001418.

Bach, W., C. J. Garrido, H. Paulick, J. Harvey, and M. Rosner (2004), Seawater-peridotite interactions: First insights from ODP Leg 209, MAR 15°N, *Geochemistry, Geophys. Geosystems*, *5*(9), Q09F26, doi:10.1029/2004GC000744.

Bach, W., H. Paulick, C. J. Garrido, B. Ildefonse, W. P. Meurer, and S. E. Humphris (2006), Unraveling the sequence of serpentinization reactions: petrography, mineral chemistry, and petrophysics of serpentinites from MAR 15°N (ODP Leg 209, Site 1274), *Geophys. Res. Lett.*, *33*(13), L13306, doi:10.1029/2006GL025681.

Baker, E. T., and C. R. German (2004), On the Global Distribution of Hydrothermal Vent Fields, in *Mid-Ocean Ridges*, pp. 245–266, American Geophysical Union.

Barker, A. K., L. A. Coogan, and K. M. Gillis (2010), Insights into the behaviour of sulphur in mid-ocean ridge axial hydrothermal systems from the composition of the sheeted dyke complex at Pito Deep, *Chem. Geol.*, *275*(1–2), 105–115, doi:http://dx.doi.org/10.1016/j.chemgeo.2010.05.003.

Barrie, C. T., and M. D. Hannington (1999), Classification of Volcanic-Associated Massive Sulfide Deposits Based on Host-Rock Composition, *Rev. Econ. Geol.*, *8*, 1–11.

Beard, J. S., B. R. Frost, P. Fryer, A. McCaig, R. Searle, B. Ildefonse, P. Zinin, and S. K. Sharma (2009), Onset and Progression of Serpentinization and Magnetite Formation in Olivine-rich Troctolite from IODP Hole U1309D, *J. Petrol.* , *50* (3), 387–403, doi:10.1093/petrology/egp004.

Becker, N. C., P. Fryer, and G. F. Moore (2010), Malaguana-Gadao Ridge: Identification and implications of a magma chamber reflector in the southern Mariana Trough, *Geochemistry, Geophys. Geosystems*, *11*(4), Q04X13, doi:10.1029/2009GC002719.

Bhattacharyya, B. (1964), Magnetic anomalies due to prism-shaped bodies with arbitrary polarization, *GEOPHYSICS*, *29*(4), 517–531, doi:10.1190/1.1439386.

Bina, M. M., and B. Henry (1990), Magnetic properties, opaque mineralogy and magnetic anisotropies of serpentinized peridotites from ODP Hole 670A near the Mid-Atlantic Ridge, *Phys. Earth Planet. Inter.*, *65*(1–2), 88–103, doi:10.1016/0031-9201(90)90078-C.

Boström, K., M. N. A. Peterson, O. Joensuu, and D. E. Fisher (1969), Aluminum-poor ferromanganoan sediments on active oceanic ridges, *J. Geophys. Res.*, *74*(12), 3261–3270, doi:10.1029/JB074i012p03261.

Briais, A. (1995), Structural analysis of the segmentation of the Central Indian Ridge between 20°30′S and 25°30′S (Rodriguez Triple Junction), *Mar. Geophys. Res.*, *17*(5), 431–467, doi:10.1007/BF01371787.

Bullard, E. C., A. E. Maxwell, and R. Revelle (1956), *Advances in Geophysics Volume 3*, Advances in Geophysics, Elsevier.

Cannat, M. (1993), Emplacement of mantle rocks in the seafloor at mid-ocean ridges, *J. Geophys. Res. Solid Earth*, *98*(B3), 4163–4172, doi:10.1029/92JB02221.

Cannat, M. et al. (1995), Thin crust, ultramafic exposures, and rugged faulting patterns at the Mid-Atlantic Ridge (22°–24°N), *Geol.* , *23* (1), 49–52, doi:10.1130/0091-7613(1995)023<0049:TCUEAR>2.3.CO;2.

Caratori-Tontini, F., B. Davy, C. E. J. De Ronde, R. W. Embley, M. Leybourne, and M. A. Tivey (2012), Crustal Magnetization of Brothers Volcano, New Zealand, Measured by Autonomous Underwater Vehicles: Geophysical Expression of a Submarine Hydrothermal System, *Econ. Geol.*, *107*(8), 1571–1581, doi:10.2113/econgeo.107.8.1571.

Caratori-Tontini, F., G. Bortoluzzi, C. Carmisciano, L. Cocchi, C. E. J. de Ronde, M. Ligi, and F. Muccini (2014), Near-Bottom Magnetic Signatures of Submarine Hydrothermal Systems at Marsili and Palinuro Volcanoes, Southern Tyrrhenian Sea, Italy, *Econ. Geol.*, *109*(8), 2119–2128, doi:10.2113/econgeo.109.8.2119.

Caratori-Tontini, F., C. E. J. de Ronde, D. Yoerger, J. Kinsey, and M. Tivey (2012), 3-D focused inversion of near-seafloor magnetic data with application to the Brothers volcano hydrothermal system, Southern Pacific Ocean, New Zealand, *J. Geophys. Res. Solid Earth*, *117*(B10), B10102, doi:10.1029/2012JB009349.

Carbotte, S. M., J. P. Canales, M. R. Nedimović, H. Carton, and J. C. Mutter (2012), Recent seismic studies at the East Pacific Rise 8°20'–10°10'N and Endeavour Segment: Insights into mid-ocean ridge hydrothermal and magmatic processes., *Oceanography*, *25*((1)), 100–112, doi:org/10.5670/oceanog.2012.08.

Charlou, J. L., J. P. Donval, C. Konn, H. OndréAs, Y. Fouquet, P. Jean-Baptiste, and E. Fourré (2010), High production and fluxes of H2 and CH4 and evidence of abiotic hydrocarbon synthesis by serpentinization in ultramafic-hosted hydrothermal systems on the Mid-Atlantic Ridge, in *Diversity Of Hydrothermal Systems On Slow Spreading Ocean Ridges*, pp. 265–296, American Geophysical Union.

Cherkashov, G., V. Bel'tenev, V. Ivanov, L. Lazareva, M. Samovarov, V. Shilov, T. Stepanova, G. P. Glasby, and V. Kuznetsov (2008), Two New Hydrothermal Fields at the Mid-Atlantic Ridge, *Mar. Georesources Geotechnol.*, *26*(4), 308–316, doi:10.1080/10641190802400708.

Connelly, D. P. et al. (2012), Hydrothermal vent fields and chemosynthetic biota on the world's deepest seafloor spreading centre, *Nat Commun*, *3*, 620.

Corliss, J. B. et al. (1979), Submarine Thermal Springs on the Galápagos Rift, *Science (80-.).*, *203*(4385), 1073–1083, doi:10.1126/science.203.4385.1073.

Von Damm, K. L. (1995), Controls on the chemistry and temporal variability of seafloor hydrothermal fluids, in *Seafloor Hydrothermal Systems: Physical, Chemical, Biological, and Geological Interactions*, vol. 91, pp. 222–247, AGU, Washington, DC.

Davis, E. E., W. D. Goodfellow, B. D. Bornhold, J. Adshead, B. Blaise, H. Villinger, and G. M. Le Cheminant (1987), Massive sulfides in a sedimented rift valley, northern Juan de Fuca Ridge, *Earth Planet. Sci. Lett.*, *82*(1-2), 49–61, doi:10.1016/0012-821X(87)90106-3.

Day, R., M. Fuller, and V. A. Schmidt (1977), Hysteresis properties of titanomagnetites: Grain-size and compositional dependence, *Phys. Earth Planet. Inter.*, *13*(4), 260–267, doi:10.1016/0031-9201(77)90108-X.

Delaney, J. R., V. Robigou, R. E. McDuff, and M. K. Tivey (1992), Geology of a vigorous hydrothermal system on the Endeavour Segment, Juan de Fuca Ridge, *J. Geophys. Res.*, *97*(B13), 19663, doi:10.1029/92JB00174.

deMartin, B. J., R. A. Sohn, J. Pablo Canales, and S. E. Humphris (2007), Kinematics and geometry of active detachment faulting beneath the Trans-Atlantic Geotraverse (TAG) hydrothermal field on the Mid-Atlantic Ridge, *Geol.* , *35* (8), 711–714, doi:10.1130/G23718A.1.

DeMets, C., R. G. Gordon, and D. F. Argus (2010), Geologically current plate motions, *Geophys. J. Int.*, *181*(1), 1–80.

Deschamps, A., and T. Fujiwara (2003), Asymmetric accretion along the slow-spreading Mariana Ridge, *Geochem. Geophys. Geosyst.*, *4*(10), 8622, doi:10.1029/2003GC000537.

Dick, H. J. B. (1989), Abyssal peridotites, very slow spreading ridges and ocean ridge magmatism, *Geol. Soc. London, Spec. Publ.* , *42* (1), 71–105, doi:10.1144/GSL.SP.1989.042.01.06.

Doubrovine, P. V, and J. A. Tarduno (2006), Alteration and self-reversal in oceanic basalts, *J. Geophys. Res.*, *111*(B12), B12S30, doi:10.1029/2006JB004468.

Dunlop, D. J. (2002), Theory and application of the Day plot (Mrs/Ms versus Hcr/Hc) 1. Theoretical curves and tests using titanomagnetite data, *J. Geophys. Res.*, *107*(B3), 2056, doi:10.1029/2001JB000486.

Dunlop, D. J., and O. Ozdemir (1997), *Rock Magnetism - Fundamentals and frontiers*, Cambridge University Press.

Dunlop, D. J., and O. Ozdemir (2007), Magnetizations in Rocks and Minerals, in *Geomagnetism, Treatise on Geophysics*, pp. 277–336.

Dyment, J., J. Arkani-Hamed, and A. Ghods (1997), Contribution of serpentinized ultramafics to marine magnetic anomalies at slow and intermediate spreading centres: insights from the shape of the anomalies, *Geophys. J. Int.*, *129*(3), 691–701, doi:10.1111/j.1365-246X.1997.tb04504.x.

Dyment, J., K. Tamaki, H. Horen, Y. Fouquet, K. Nakase, M. Yamamoto, M. Ravilly, and M. Kitazawa (2005), A Positive Magnetic Anomaly at Rainbow Hydrothermal Site in Ultramafic Environment, in *American Geophysical Union, Fall Meeting 2005, abstract #OS21C-08*.

Dyment, J., Y. Choi, M. Hamoudi, V. Lesur, and E. Thebault (2015), Global equivalent magnetization of the oceanic lithosphere, *Earth Planet. Sci. Lett.*, *430*, 54–65, doi:http://dx.doi.org/10.1016/j.epsl.2015.08.002.

Elderfield, H., and A. Schultz (1996), Mid-ocean ridge hydrothermal fluxes and the chemical composition of the ocean, *Annu. Rev. Earth Planet. Sci.*, *24*(1), 191–224, doi:10.1146/annurev.earth.24.1.191.

Escartin, J., D. K. Smith, J. Cann, H. Schouten, C. H. Langmuir, and S. Escrig (2008), Central role of detachment faults in accretion of slow-spreading oceanic lithosphere, *Nature*, *455*(7214), 790–794, doi:10.1038/nature07333.

Escartín, J., G. Hirth, and B. Evans (1997), Effects of serpentinization on the lithospheric strength and the style of normal faulting at slow-spreading ridges, *Earth Planet. Sci. Lett.*, *151*(3–4), 181–189, doi:http://dx.doi.org/10.1016/S0012-821X(97)81847-X.

Ferré, E. C., S. A. Friedman, F. Martín-Hernández, J. M. Feinberg, J. A. Conder, and D. A. Ionov (2013), The magnetism of mantle xenoliths and potential implications for sub-Moho magnetic sources, *Geophys. Res. Lett.*, *40*(1), 105–110, doi:10.1029/2012GL054100.

Fiske, R. S., J. Naka, K. Iizasa, M. Yuasa, and A. Klaus (2001), Submarine silicic caldera at the front of the Izu-Bonin arc, Japan: Voluminous seafloor eruptions of rhyolite pumice, *Geol. Soc. Am. Bull.* , *113* (7), 813–824, doi:10.1130/0016-7606(2001)113<0813:SSCATF>2.0.CO;2.

Fouquet, Y., U. von Stackelberg, J. L. Charlou, J. Erzinger, P. M. Herzig, R. Muehe, and M. Wiedicke (1993), Metallogenesis in back-arc environments; the Lau Basin example, *Econ. Geol.* , *88* (8), 2154–2181, doi:10.2113/gsecongeo.88.8.2154.

Fouquet, Y., H. Ondreas, J.-L. Charlou, J.-P. Donval, J. Radford-Knoery, I. Costa, N. Lourenco, T. M. K., and M. K. Tivey (1995), Atlantic lava lakes and hot vents, *Nature*, *377*(6546), 201.

Fouquet, Y. et al. (2010), Geodiversity of hydrothermal processes along the Mid-Atlantic Ridge and ultramafic-hosted mineralization: A new type of oceanic Cu-Zn-Co-Au volcanogenic massive sulfide deposit, in *Diversity of Hydrothermal Systems on Slow Spreading Ocean Ridges*, vol. 188, pp. 321–367, AGU, Washington, DC.

Francheteau, J., and R. D. Ballard (1983), The East Pacific Rise near 21°N, 13°N and 20°S: inferences for along-strike variability of axial processes of the Mid-Ocean Ridge, *Earth Planet. Sci. Lett.*, *64*(1), 93–116, doi:10.1016/0012-821X(83)90055-9.

Frost, B. R., K. A. Evans, S. M. Swapp, J. S. Beard, and F. E. Mothersole (2013), The process of serpentinization in dunite from New Caledonia, *Lithos*, *178*(0), 24–39, doi:http://dx.doi.org/10.1016/j.lithos.2013.02.002.

Frost, D. J., and C. A. McCammon (2008), The Redox State of Earth's Mantle, *Annu. Rev. Earth Planet. Sci.*, *36*(1), 389–420, doi:10.1146/annurev.earth.36.031207.124322.

Früh-Green, G. L., D. S. Kelley, S. M. Bernasconi, J. A. Karson, K. A. Ludwig, D. A. Butterfield, C. Boschi, and G. Proskurowski (2003), 30,000 Years of Hydrothermal Activity at the Lost City Vent Field, *Sci.* , *301* (5632), 495–498, doi:10.1126/science.1085582.

Fujiwara, T., and H. Fujimoto (1998), Seafloor geomagnetic vector anomaly of the intersection of the Mid-Atlantic Ridge and the Kane Transform Fault: Implications for magnetization of the oceanic crust, *J. Geophys. Res. Solid Earth*, *103*(B12), 30335–30349, doi:10.1029/1998JB900015.

Fujiwara, T., S. Toyoda, A. Uchida, J. Ishibashi, S. Nakai, and A. Takamasa (2015), ESR Dating of Barite in Sea-Floor Hydrothermal Sulfide Deposits in the Okinawa Trough, in *Subseafloor Biosphere Linked to Hydrothermal Systems SE - 29*, edited by J. Ishibashi, K. Okino, and M. Sunamura, pp. 369–386, Springer Japan.

Gamo, T. et al. (2001), Chemical characteristics of newly discovered black smoker fluids and associated hydrothermal plumes at the Rodriguez Triple Junction, Central Indian Ridge, *Earth Planet. Sci. Lett.*, *193*(3–4), 371–379, doi:http://dx.doi.org/10.1016/S0012-821X(01)00511-8.

Gee, J., and D. V Kent (1994), Variations in layer 2A thickness and the origin of the central anomaly magnetic high, *Geophys. Res. Lett.*, *21*(4), 297–300, doi:10.1029/93GL03422.

Gee, J., and D. V Kent (1997), Magnetization of axial lavas from the southern East Pacific Rise (14°-23°S): Geochemical controls on magnetic properties, *J. Geophys. Res.*, *102*(B11), 24873–24886, doi:10.1029/97JB02544.

Gee, J. S., and D. V Kent (2007), Source of Oceanic Magnetic Anomalies and the Geomagnetic Polarity Timescale, in *Geomagnetism, Treatise on Geophysics*, pp. 455–507.

Gee, J. S., S. C. Cande, J. A. Hildebrand, K. Donnelly, and R. L. Parker (2000), Geomagnetic intensity variations over the past 780 kyr obtained from near-seafloor magnetic anomalies, *Nature*, *408*(6814), 827–832.

Gee, J. S., S. C. Webb, J. Ridgway, H. Staudigel, and M. A. Zumberge (2001), A deep tow magnetic survey of Middle Valley, Juan de Fuca Ridge, *Geochemistry, Geophys. Geosystems*, *2*(11), 1059, doi:10.1029/2001GC000170.

German, C. ., and L. . Parson (1998), Distributions of hydrothermal activity along the Mid-Atlantic Ridge: interplay of magmatic and tectonic controls, *Earth Planet. Sci. Lett.*, *160*(3-4), 327–341, doi:10.1016/S0012-821X(98)00093-4.

German, C. R., and J. Lin (2004), The Thermal Structure of the Oceanic Crust, Ridge-Spreading and Hydrothermal Circulation: How Well do we Understand

their Inter-Connections?, in *Mid-Ocean Ridges*, pp. 1–18, American Geophysical Union.

German, C. R., G. P. Klinkhammer, and M. D. Rudnicki (1996), The Rainbow Hydrothermal Plume, 36°15′N, MAR, *Geophys. Res. Lett.*, *23*(21), 2979–2982, doi:10.1029/96GL02883.

German, C. R. et al. (2008), Hydrothermal activity on the southern Mid-Atlantic Ridge: Tectonically- and volcanically-controlled venting at 4–5°S, *Earth Planet. Sci. Lett.*, *273*(3–4), 332–344, doi:http://dx.doi.org/10.1016/j.epsl.2008.06.048.

Gillis, K. M., and P. T. Robinson (1988), Distribution of alteration zones in the upper oceanic crust, *Geol.* , *16* (3), 262–266, doi:10.1130/0091-7613(1988)016<0262:DOAZIT>2.3.CO;2.

Gillis, K. M., and P. T. Robinson (1990), Patterns and processes of alteration in the lavas and dykes of the Troodos Ophiolite, Cyprus, *J. Geophys. Res. Solid Earth*, *95*(B13), 21523–21548, doi:10.1029/JB095iB13p21523.

Goodfellow, W. D., and J. M. Peter (1994), GEOCHEMISTRY OF HYDROTHERMALLY ALTERED SEDIMENT, MIDDLE VALLEY, *Proc. Ocean Drill. Program, Sci. Results*, *139*, 207–289.

Granot, R., J. Dyment, and Y. Gallet (2012), Geomagnetic field variability during the Cretaceous Normal Superchron, *Nat. Geosci*, *5*(3), 220–223.

Guyodo, Y., and J. P. Valet (1999), Global changes in intensity of the Earth's magnetic field during the past 800 kyr, *Nature*, *399*(6733), 249–252.

Halbach, P. et al. (1989), Probable modern analogue of Kuroko-type massive sulphide deposits in the Okinawa Trough back-arc basin, *Nature*, *338*(6215), 496–499.

Hall, J. M. (1992), Interaction of submarine volcanic and high-temperature hydrothermal activity proposed for the formation of the Agrokipia, volcanic massive sulfide deposits of Cyprus, *Can. J. Earth Sci.*, *29*(9), 1928–1936, doi:10.1139/e92-150.

Hannington, M., J. Jamieson, T. Monecke, S. Petersen, and S. Beaulieu (2011), The abundance of seafloor massive sulfide deposits, *Geol.* , *39* (12), 1155–1158, doi:10.1130/G32468.1.

Hannington, M. D., I. R. Jonasson, P. M. Herzig, and S. Petersen (1995), Physical and chemical processes of seafloor mineralization at mid-ocean ridges, in *Seafloor*

Hydrothermal Systems: Physical, Chemical, Biological, and Geological Interactions, vol. 91, pp. 115–157, AGU, Washington, DC.

Hannington, M. D., C. E. J. de Ronde, and S. Petersen (2005), Sea-Floor Tectonics and Submarine Hydrothermal Systems, *Econ. Geol.*, *100th Anni*, 111–141.

Haymon, R. M., and M. Kastner (1981), Hot spring deposits on the East Pacific Rise at 21°N: preliminary description of mineralogy and genesis, *Earth Planet. Sci. Lett.*, *53*(3), 363–381, doi:10.1016/0012-821X(81)90041-8.

Haymon, R. M., D. J. Fornari, M. H. Edwards, S. Carbotte, D. Wright, and K. C. Macdonald (1991), Hydrothermal vent distribution along the East Pacific Rise crest (9°09′–54′N) and its relationship to magmatic and tectonic processes on fast-spreading mid-ocean ridges, *Earth Planet. Sci. Lett.*, *104*(2-4), 513–534, doi:10.1016/0012-821X(91)90226-8.

Haymon, R. M. et al. (1993), Volcanic eruption of the mid-ocean ridge along the East Pacific Rise crest at 9°45–52′N: Direct submersible observations of seafloor phenomena associated with an eruption event in April, 1991, *Earth Planet. Sci. Lett.*, *119*(1-2), 85–101, doi:10.1016/0012-821X(93)90008-W.

Hearn, C. K., K. L. Homola, and H. P. Johnson (2013), Surficial permeability of the axial valley seafloor: Endeavour Segment, Juan de Fuca Ridge, *Geochemistry, Geophys. Geosystems*, *14*(9), 3409–3424, doi:10.1002/ggge.20209.

Herzig, P. M., S. E. Humphris, D. J. Miller, and R. A. Zierenberg (1998), No Title, *Proc. Ocean Drill. Program, Sci. results*, *158*, doi:10.2973/odp.proc.sr.158.1998.

Hochstein, M. P., and S. Soengkono (1997), Magnetic anomalies associated with high temperature 779 reservoirs in the Taupo volcanic zone (New Zealand), *Geothermics*, *26*(1), 1–24.

Hofmann, A. W. (1988), Chemical differentiation of the Earth: the relationship between mantle, continental crust, and oceanic crust, *Earth Planet. Sci. Lett.*, *90*(3), 297–314, doi:10.1016/0012-821X(88)90132-X.

Honsho, C. (1999), Magnetic structure of the Mid-Atlantic ridge 21°40′N segment: an approach from near-bottom magnetic measurements onboard a submersible.

Honsho, C., K. Tamaki, and H. Fujimoto (1996), Three-dimensional magnetic and gravity studies of the Rodriguez Triple Junction in the Indian Ocean, *J. Geophys. Res.*, *101*(B7), 15837–15848, doi:10.1029/96JB00644.

Honsho, C., J. Dyment, K. Tamaki, M. Ravilly, H. Horen, and P. Gente (2009), Magnetic structure of a slow spreading ridge segment: Insights from near-bottom magnetic measurements on board a submersible, *J. Geophys. Res.*, *114*(B5), B05101, doi:10.1029/2008JB005915.

Honsho, C., T. Ura, and K. Tamaki (2012), The inversion of deep-sea magnetic anomalies using Akaike's Bayesian information criterion, *J. Geophys. Res.*, *117*(B1), B01105, doi:10.1029/2011JB008611.

Honsho, C., T. Ura, and K. Kim (2013), Deep-sea magnetic vector anomalies over the Hakurei hydrothermal field and the Bayonnaise knoll caldera, Izu-Ogasawara arc, Japan, *J. Geophys. Res. Solid Earth*, *118*(10), 5147–5164, doi:10.1002/jgrb.50382.

Hsu, H.-W. et al. (2015), Ongoing hydrothermal activities within Enceladus, *Nature*, *519*(7542), 207–210.

Humphris, S. E., and J. R. Cann (2000), Constraints on the energy and chemical balances of the modern TAG and ancient Cyprus seafloor sulfide deposits, *J. Geophys. Res.*, *105*(B12), 28477, doi:10.1029/2000JB900289.

Humphris, S. E., and T. M. McCollom (1998), The Cauldron Beneath the Seafloor: Percolating Through Volcanic Subsurface Rocks, Seawater is Chemically Transformed into Hydrothermal Fluid, *Oceanus*, *41*(2).

Humphris, S. E., P. M. Herzig, D. J. Miller, and E. Al. (1996), No Title, *Proc. Ocean Drill. Program, Initial reports*, *158*, doi:10.2973/odp.proc.ir.158.1996.

Hunt, C. P., B. M. Moskowitz, and S. K. Banerjee (1995), Magnetic Properties of Rocks and Minerals, in *Rock Physics & Phase Relations*, pp. 189–204, American Geophysical Union.

Hussenoeder, S. A., M. A. Tivey, and H. Schouten (1995), Direct inversion of potential fields from an uneven track with application to the Mid‐Atlantic Ridge, *Geophys. Res. Lett.*, *22*(23), 3131–3134, doi:10.1029/95GL03326.

Hussong, D. M., and S. Uyeda (1982), Tectonic processes and the history of the Mariana Arc: A synthesis of the results of deep-sea drilling project Leg 60, *Initial Rep. Deep Sea Drill. Proj.*, *60*, 909–929.

Iizasa, K. et al. (1999), A Kuroko-Type Polymetallic Sulfide Deposit in a Submarine Silicic Caldera, *Sci.* , *283* (5404), 975–977, doi:10.1126/science.283.5404.975.

International Association of Geomagnetism and Aeronomy, W. G. V.-M. P. members et al. (2010), International Geomagnetic Reference Field: the eleventh generation, *Geophys. J. Int.*, *183*(3), 1216–1230, doi:10.1111/j.1365-246X.2010.04804.x.

Irving, E. (1970), The Mid-Atlantic Ridge at 45° N. XIV. Oxidation and magnetic properties of basalt; review and discussion, *Can. J. Earth Sci.*, *7*(6), 1528–1538, doi:10.1139/e70-144.

Isezaki, N. (1986), A new shipboard three‐component magnetometer, *GEOPHYSICS*, *51*(10), 1992–1998, doi:10.1190/1.1442054.

Ishibashi, J., and T. Urabe (1995), Hydrothermal activity related to arc-backarc magmatism in the western Pacific, in *Backarc Basins: Tectonics and Magmatism*, edited by B.Taylor, pp. 451–495.

Ishibashi, J. et al. (2004), Geochemistry of Hydrothermal Fluids in South Mariana Backarc Spreading Center, in *American Geophysical Union, Fall Meeting 2004, abstract #V44A-05*.

Ishibashi, J. et al. (2015), Dating of hydrothermal mineralizatoin in active hydrothermal fields in the Southern Mariana Trough, in *Subseafloor Biosphere Linked to Global Hydrothermal Systems; TAIGA Concept*, edited by J.-I. Ishibashi, K. Okino, and M. Sunamura.

Jannasch, H. W., and M. J. Mottl (1985), Geomicrobiology of Deep-Sea Hydrothermal Vents, *Sci.* , *229* (4715), 717–725, doi:10.1126/science.229.4715.717.

Johnson, H. P., and T. Atwater (1977), Magnetic study of basalts from the Mid-Atlantic Ridge, lat 37°N, *Geol. Soc. Am. Bull.*, *88*(5), 637–647, doi:10.1130/0016-7606(1977)88<637:MSOBFT>2.0.CO;2.

Johnson, H. P., and R. T. Merrill (1972), Magnetic and Mineralogical Changes Associated with Low-Temperature Oxidation of Magnetite, *J. Geophys. Res.*, *77*(2), 334–341, doi:10.1029/JB077i002p00334.

Johnson, H. P., and R. T. Merrill (1973), Low-Temperature Oxidation of a Titanomagnetite and the Implications for Paleomagnetism, *J. Geophys. Res.*, *78*(23), 4938–4949, doi:10.1029/JB078i023p04938.

Johnson, H. P., and M. A. Tivey (1995), Magnetic properties of zero‐age oceanic crust; A new submarine lava flow on the Juan de Fuca Ridge, *Geophys. Res. Lett.*, *22*(2), 175–178, doi:10.1029/94GL02053.

Johnson, H. P., J. L. Karsten, F. J. Vine, G. C. Smith, and G. Schonharting (1982), Low-level magnetic survey over a massive sulfide ore body in the Troodos ophiolite complex, Cyprus, *Mar. Technol. Soc. J.*, *16*(3), 76–80.

Kadko, D., R. Koski, M. Tatsumoto, and R. Bouse (1985), An estimate of hydrothermal fluid residence times and vent chimney growth rates based on210Pb/Pb ratios and mineralogic studies of sulfides dredged from the Juan de Fuca Ridge, *Earth Planet. Sci. Lett.*, *76*(1-2), 35–44, doi:10.1016/0012-821X(85)90146-3.

Kakegawa, T., M. Utsumi, and K. Marumo (2008), Geochemistry of Sulfide Chimneys and Basement Pillow Lavas at the Southern Mariana Trough (12.55°N–12.58°N), *Resour. Geol.*, *58*(3), 249–266.

Karson, J., and J. Brown (1988), Geologic setting of the Snake Pit hydrothermal site: An active vent field on the Mid-Atlantic Ridge, *Mar. Geophys. Res.*, *10*(1-2), 91–107, doi:10.1007/BF02424662.

Kelley, D. S. et al. (2001), An off-axis hydrothermal vent field near the Mid-Atlantic Ridge at 30[deg] N, *Nature*, *412*(6843), 145–149.

Kelley, D. S. et al. (2005), A Serpentinite-Hosted Ecosystem: The Lost City Hydrothermal Field, *Sci.* , *307* (5714), 1428–1434, doi:10.1126/science.1102556.

Kent, D. V, and J. Gee (1996), Magnetic alteration of zero-age oceanic basalt, *Geology*, *24*(8), 703–706, doi:10.1130/0091-7613(1996)024<0703:MAOZAO>2.3.CO;2.

Kitada, K., N. Seama, T. Yamazaki, Y. Nogi, and K. Suyehiro (2006), Distinct regional differences in crustal thickness along the axis of the Mariana Trough, inferred from gravity anomalies, *Geochemistry, Geophys. Geosystems*, *7*(4), Q04011, doi:10.1029/2005GC001119.

Klein, F., W. Bach, and T. M. McCollom (2013a), Compositional controls on hydrogen generation during serpentinization of ultramafic rocks, *Lithos*, *178*(0), 55–69, doi:10.1016/j.lithos.2013.03.008.

Klein, F., W. Bach, S. E. Humphris, W.-A. Kahl, N. Jöns, B. Moskowitz, and T. S. Berquó (2013b), Magnetite in seafloor serpentinite—Some like it hot, *Geol.* , doi:10.1130/G35068.1.

Kleinrock, M. C., and S. E. Humphris (1996), Structural control on sea-floor hydrothermal activity at the TAG active mound, *Nature*, *382*(6587), 149–153.

Klingelhoefer, F., C.-S. Lee, J.-Y. Lin, and J.-C. Sibuet (2009), Structure of the southernmost Okinawa Trough from reflection and wide-angle seismic data, *Tectonophysics*, *466*(3-4), 281–288, doi:10.1016/j.tecto.2007.11.031.

Korenaga, J. (1995), Comprehensive analysis of marine magnetic vector anomalies, *J. Geophys. Res.*, *100*(B1), 365–378, doi:10.1029/94JB02596.

Korner, U. (1994), Rock magnetic properties of hydrothermally formed iron sulfides from Middle Valley, Juan de Fuca ridge, *Proc. Ocean Drill. Program, Sci. Results*, *139*, 535–542.

Koschinsky, A., D. Garbe-Schönberg, S. Sander, K. Schmidt, H.-H. Gennerich, and H. Strauss (2008), Hydrothermal venting at pressure-temperature conditions above the critical point of seawater, 5°S on the Mid-Atlantic Ridge, *Geol.* , *36* (8), 615–618, doi:10.1130/G24726A.1.

Koski, R. A., I. R. Jonasson, D. C. Kadko, V. K. Smith, and F. L. Wong (1994), Compositions, growth mechanisms, and temporal relations of hydrothermal sulfide-sulfate-silica chimneys at the northern Cleft segment, Juan de Fuca Ridge, *J. Geophys. Res.*, *99*(B3), 4813, doi:10.1029/93JB02871.

Kumagai, H. et al. (2008), Geological background of the Kairei and Edmond hydrothermal fields along the Central Indian Ridge: Implications of their vent fluids' distinct chemistry, *Geofluids*, *8*(4), 239–251, doi:10.1111/j.1468-8123.2008.00223.x.

Kuznetsov, V., G. Cherkashev, A. Lein, V. Sshilov, F. Maksimov, K. Arslanov, T. Stepanova, N. Baranova, S. Chernov, and D. Tarasenko (2006), 230Th/U DATING OF MASSIVE SULFIDES FROM THE LOGATCHEV AND RAINBOW HYDROTHERMAL FIELDS, *J. Methods Appl. Absol. Chronol.*, *25*, 51–55.

Lalou, C., J.-L. Reyss, E. Brichet, P. A. Rona, and G. Thompson (1995), Hydrothermal activity on a 10 5 -year scale at a slow-spreading ridge, TAG hydrothermal field, Mid-Atlantic Ridge 26°N, *J. Geophys. Res.*, *100*(B9), 17855, doi:10.1029/95JB01858.

Lartaud, F. et al. (2010), Fossil clams from a serpentinite-hosted sedimented vent field near the active smoker complex Rainbow, MAR, 36°13′N: Insight into the biogeography of vent fauna, *Geochemistry, Geophys. Geosystems*, *11*(8), n/a–n/a, doi:10.1029/2010GC003079.

Lister, C. R. B. (1970), Measurement of in Situ Sediment Conductivity by means of a Bullard-type Probe, *Geophys. J. Int.* , *19* (5), 521–532, doi:10.1111/j.1365-246X.1970.tb00157.x.

Lister, C. R. B. (1972), On the Thermal Balance of a Mid-Ocean Ridge, *Geophys. J. Int.* , *26* (5), 515–535, doi:10.1111/j.1365-246X.1972.tb05766.x.

Lowell, R. P., and M. DuBose (2005), Hydrothermal systems on Europa, *Geophys. Res. Lett.*, *32*(5), L05202, doi:10.1029/2005GL022375.

Lowell, R. P., P. A. Rona, and R. P. Von Herzen (1995), Seafloor hydrothermal systems, *J. Geophys. Res. Solid Earth*, *100*(B1), 327–352, doi:10.1029/94JB02222.

Ludwig, K. A., C.-C. Shen, D. S. Kelley, H. Cheng, and R. L. Edwards (2011), U–Th systematics and 230Th ages of carbonate chimneys at the Lost City Hydrothermal Field, *Geochim. Cosmochim. Acta*, *75*(7), 1869–1888, doi:http://dx.doi.org/10.1016/j.gca.2011.01.008.

Macdonald, K. C., S. P. Miller, S. P. Huestis, and F. N. Spiess (1980), Three-dimesional modeling of a magnetic reversal boundary from inversion of deep-tow memasurements, *J. Geophys. Res.*, *85*(B7), 3670–3680, doi:10.1029/JB085iB07p03670.

Maffione, M., A. Morris, O. Plümper, and D. J. J. van Hinsbergen (2014), Magnetic properties of variably serpentinized peridotites and their implication for the evolution of oceanic core complexes, *Geochemistry, Geophys. Geosystems*, n/a–n/a, doi:10.1002/2013GC004993.

Malvoisin, B., J. Carlut, and F. Brunet (2012), Serpentinization of oceanic peridotites: 1. A high-sensitivity method to monitor magnetite production in hydrothermal experiments, *J. Geophys. Res. Solid Earth*, *117*(B1), B01104, doi:10.1029/2011JB008612.

Marques, A. F. A., F. Barriga, V. Chavagnac, and Y. Fouquet (2006), Mineralogy, geochemistry, and Nd isotope composition of the Rainbow hydrothermal field, Mid-Atlantic Ridge, *Miner. Depos.*, *41*(1), 52–67, doi:10.1007/s00126-005-0040-8.

Marshall, M., and A. Cox (1971), Magnetism of Pillow Basalts and Their Petrology, *Geol. Soc. Am. Bull.*, *82*(3), 537–552, doi:10.1130/0016-7606(1971)82[537:MOPBAT]2.0.CO;2.

Martínez, F., P. Fryer, and N. Becker (2000), Geophysical characteristics of the southern Mariana Trough, 11°50′N–13°40′N, *J. Geophys. Res. Solid Earth*, *105*(B7), 16591–16607, doi:10.1029/2000JB900117.

McCaig, A. M., R. A. Cliff, J. Escartin, A. E. Fallick, and C. J. MacLeod (2007), Oceanic detachment faults focus very large volumes of black smoker fluids, *Geol.* , *35* (10), 935–938, doi:10.1130/G23657A.1.

McCollom, T. M., and W. Bach (2009), Thermodynamic constraints on hydrogen generation during serpentinization of ultramafic rocks, *Geochim. Cosmochim. Acta*, *73*(3), 856–875, doi:http://dx.doi.org/10.1016/j.gca.2008.10.032.

McKenzie, D., and C. Bowin (1976), The relationship between bathymetry and gravity in the Atlantic Ocean, *J. Geophys. Res.*, *81*(11), 1903–1915, doi:10.1029/JB081i011p01903.

Melchert, B. et al. (2008), First evidence for high-temperature off-axis venting of deep crustal/mantle heat: The Nibelungen hydrothermal field, southern Mid-Atlantic Ridge, *Earth Planet. Sci. Lett.*, *275*(1–2), 61–69, doi:http://dx.doi.org/10.1016/j.epsl.2008.08.010.

Mendel, V., D. Sauter, P. Patriat, and M. Munschy (2000), Relationship of the Central Indian Ridge segmentation with the evolution of the Rodrigues Triple Junction for the past 8 Myr, *J. Geophys. Res. Solid Earth*, *105*(B7), 16563–16575, doi:10.1029/2000JB900098.

Michael, P. J. et al. (2003), Magmatic and amagmatic seafloor generation at the ultraslow-spreading Gakkel ridge, Arctic Ocean, *Nature*, *423*(6943), 956–961.

Miller, D. J., and N. I. Christensen (1997), Seismic velocities of lower crustal and upper mantle rocks from the slow-spreading Mid-Atlantic Ridge, south of the Kane Fracture Transform Zone (MARK)., in *Karson, J.A., Cannat, M., Miller, D.J., and Elthon, D. (Eds.), Proc. ODP, Sci. Results, 153: College Station, TX (Ocean Drilling Program)*, pp. 437–454.

Mitchell, N., J. Escartin, and S. Allerton (1998), Detachmentfaultsatmid- ocean ridges garner interest, *Eos Trans. AGU*, *79*(127).

Miyoshi, A., T. Kogiso, N. Ishikawa, and K. Mibe (2014), Role of silica for the progress of serpentinization reactions: Constraints from successive changes in mineralogical textures of serpentinites from Iwanaidake ultramafic body, Japan, *Am. Mineral.* , *99* (5-6), 1035–1044, doi:10.2138/am.2014.4748.

Mochizuki, N., N. Yoshifumi, M. Asada, S. Yoshikawa, and K. Okino (2012), Decay of natural remanent magnetization of oceanic basalt on the back-arc spreading axis of the southern Mariana, in *American Geophysical Union, Fall Meeting 2012; T43D-2705*.

Morishita, T., K. Hara, K. Nakamura, T. Sawaguchi, A. Tamura, S. Arai, K. Okino, K. Takai, and H. Kumagai (2009), Igneous, Alteration and Exhumation Processes Recorded in Abyssal Peridotites and Related Fault Rocks from an Oceanic Core Complex along the Central Indian Ridge, *J. Petrol.* , doi:10.1093/petrology/egp025.

Morishita, T., K. Nakamura, T. Shibuya, H. Kumagai, T. Sato, K. Okino, H. Sato, R. Nauchi, K. Hara, and R. Takamaru (2015), Petrology of Peridotites and Related Gabbroic Rocks Around the Kairei Hydrothermal Field in the Central Indian Ridge, in *Subseafloor Biosphere Linked to Hydrothermal Systems SE - 14*, edited by J. Ishibashi, K. Okino, and M. Sunamura, pp. 177–193, Springer Japan.

Moss, R., and S. D. Scott (2001), GEOCHEMISTRY AND MINERALOGY OF GOLD-RICH HYDROTHERMAL PRECIPITATES FROM THE EASTERN MANUS BASIN, PAPUA NEW GUINEA, *Can. Mineral.* , *39* (4), 957–978, doi:10.2113/gscanmin.39.4.957.

Mottl, M. J., C. G. Wheat, and J. Boulegue (1994), TIMING OF ORE DEPOSITION AND SILL INTRUSION AT SITE 856: EVIDENCE FROM STRATIGRAPHY, ALTERATION, AND SEDIMENT PORE-WATER COMPOSITION, *Proc. Ocean Drill. Program, Sci. Results*, *139*, 679–693.

Munschy, M., and R. Schlich (1989), The Rodriguez Triple Junction (Indian Ocean): Structure and evolution for the past one million years, *Mar. Geophys. Res.*, *11*(1), 1–14, doi:10.1007/BF00286244.

Nakamura, K., and K. Takai (2014), Theoretical constraints of physical and chemical properties of hydrothermal fluids on variations in chemolithotrophic microbial communities in seafloor hydrothermal systems, *Prog. Earth Planet. Sci.*, *1*(1), 5, doi:10.1186/2197-4284-1-5.

Nakamura, K., and K. Takai (2015), Indian Ocean Hydrothermal Systems: Seafloor Hydrothermal Activities, Physical and Chemical Characteristics of Hydrothermal Fluids, and Vent-Associated Biological Communities, in *Subseafloor Biosphere*

Linked to Hydrothermal Systems SE - 12, edited by J. Ishibashi, K. Okino, and M. Sunamura, pp. 147–161, Springer Japan.

Nakamura, K., T. Morishita, W. Bach, F. Klein, K. Hara, K. Okino, K. Takai, and H. Kumagai (2009), Serpentinized troctolites exposed near the Kairei Hydrothermal Field, Central Indian Ridge: Insights into the origin of the Kairei hydrothermal fluid supporting a unique microbial ecosystem, *Earth Planet. Sci. Lett.*, *280*(1–4), 128–136, doi:http://dx.doi.org/10.1016/j.epsl.2009.01.024.

Nakamura, K., T. Toki, N. Mochizuki, M. Asada, J. Ishibashi, Y. Nogi, S. Yoshikawa, J. Miyazaki, and K. Okino (2013), Discovery of a new hydrothermal vent based on an underwater, high-resolution geophysical survey, *Deep Sea Res. Part I Oceanogr. Res. Pap.*, *74*April, 1–10, doi:10.1016/j.dsr.2012.12.003.

Nakase, K. (2002), Magnetic structure of the Rainbow hydrothermal field at the Mid-Atlantic Ridge 36°14′N obtained from near-bottom geomagnetic measurements, Universtity of Tokyo.

Nazarova, K. (1994), Serpentinized peridotites as a possible source for oceanic magnetic anomalies, *Mar. Geophys. Res.*, *16*(6), 455–462 LA – English, doi:10.1007/BF01270519.

Newsom, H. E. (1980), Hydrothermal alteration of impact melt sheets with implications for Mars, *Icarus*, *44*(1), 207–216, doi:http://dx.doi.org/10.1016/0019-1035(80)90066-4.

Nishimura, S., M. Hashimoto, and M. Ando (2004), A rigid block rotation model for the GPS derived velocity field along the Ryukyu arc, *Phys. Earth Planet. Inter.*, *142*(3–4), 185–203, doi:http://dx.doi.org/10.1016/j.pepi.2003.12.014.

Nogi, Y., N. Mochizuki, K. Okino, and M. Asada (2011), Near-bottom magnetic surveys around hydrothermal sites in the southern Mariana Trough, in *American Geophysical Union, Fall Meeting 2011, abstract #GP41A-0993*.

NT09-10-leg2 cruise report (2009), http://www.godac.jamstec.go.jp/darwin/cruise/natsushima/NT09-10_leg2/j.

NT10-06-leg2 cruise report (2010), http://www.godac.jamstec.go.jp/darwin/cruise/natsushima/NT10-06_leg2/j.

NT11-17 cruise report (2011), http://www.godac.jamstec.go.jp/darwin/cruise/natsushima/NT11-17/j.

NT11-18 cruise report (2011), http://www.godac.jamstec.go.jp/darwin/cruise/natsushima/NT11-18/j.

NT11-20 cruise summary (2011), http://www.godac.jamstec.go.jp/darwin/cruise/natsushima/NT11-20/j.

NT13-25 cruise report (2013), http://www.godac.jamstec.go.jp/darwin/cruise/natsushima/NT13-25/j.

O'Reilly, W., and S. K. Banerjee (1966), Oxidation of Titanomagnetites and Self-Reversal, *Nature*, *211*(5044), 26–28.

Ohara, Y. et al. (2012), A serpentinite-hosted ecosystem in the Southern Mariana Forearc, *Proc. Natl. Acad. Sci.* , doi:10.1073/pnas.1112005109.

Okino, K., Y. Ohara, S. Kasuga, and Y. Kato (1999), The Philippine Sea: New survey results reveal the structure and the history of the marginal basins, *Geophys. Res. Lett.*, *26*(15), 2287–2290, doi:10.1029/1999GL900537.

Okino, K., K. Nakamura, and H. Sato (2015), Tectonic Background of Four Hydrothermal Fields Along the Central Indian Ridge, in *Subseafloor Biosphere Linked to Hydrothermal Systems SE - 11*, edited by J. Ishibashi, K. Okino, and M. Sunamura, pp. 133–146, Springer Japan.

Oufi, O., M. Cannat, and H. Horen (2002), Magnetic properties of variably serpentinized abyssal peridotites, *J. Geophys. Res. Solid Earth*, *107*(B5), EPM 3–1–EPM 3–19, doi:10.1029/2001JB000549.

Özdemir, Ö., D. J. Dunlop, and B. M. Moskowitz (1993), The effect of oxidation on the Verwey transition in magnetite, *Geophys. Res. Lett.*, *20*(16), 1671–1674, doi:10.1029/93GL01483.

Pariso, J. E., and H. P. Johnson (1991), Alteration processes at Deep Sea Drilling Project/Ocean Drilling Program Hole 504B at the Costa Rica Rift: Implications for magnetization of oceanic crust, *J. Geophys. Res. Solid Earth*, *96*(B7), 11703–11722, doi:10.1029/91JB00872.

Parker, R. L., and S. P. Huestis (1974), The Inversion of Magnetic Anomalies in the Presence of Topography, *J. Geophys. Res.*, *79*(11), 1587–1593, doi:10.1029/JB079i011p01587.

Pedersen, R. B., H. T. Rapp, I. H. Thorseth, M. D. Lilley, F. J. A. S. Barriga, T. Baumberger, K. Flesland, R. Fonseca, G. L. Fruh-Green, and S. L. Jorgensen

(2010), Discovery of a black smoker vent field and vent fauna at the Arctic Mid-Ocean Ridge, *Nat Commun*, *1*, 126.

Peter, J. M. (1994), FLUID INCLUSION PETROGRAPHY AND MICROTHERMOMETRY OF THE MIDDLE VALLEY HYDROTHERMAL SYSTEM, NORTHERN JUAN DE FUCA RIDGE, *Proc. Ocean Drill. Program, Sci. Results*, *139*, 411–428.

Pontbriand, C. W., and R. A. Sohn (2014), Microearthquake evidence for reaction-driven cracking within the Trans-Atlantic Geotraverse active hydrothermal deposit, *J. Geophys. Res. Solid Earth*, *119*(2), 822–839, doi:10.1002/2013JB010110.

Pouliquen, G., Y. Gallet, P. Patriat, J. Dyment, and C. Tamura (2001), A geomagnetic record over the last 3.5 million years from deep-tow magnetic anomaly profiles across the Central Indian Ridge, *J. Geophys. Res. Solid Earth*, *106*(B6), 10941–10960, doi:10.1029/2000JB900442.

Ravilly, M., H. Horen, M. Perrin, J. Dyment, P. Gente, and H. Guillou (2001), NRM intensity of altered oceanic basalts across the MAR (21°N, 0–1.5 Ma): a record of geomagnetic palaeointensity variations?, *Geophys. J. Int.*, *145*(2), 401–422.

Richards, H. G., J. R. Cann, and J. Jensenius (1989), Mineralogical zonation and metasomatism of the alteration pipes of Cyprus sulfide deposits, *Econ. Geol.* , *84* (1), 91–115, doi:10.2113/gsecongeo.84.1.91.

Roberts, A. P., C. R. Pike, and K. L. Verosub (2000), First-order reversal curve diagrams: A new tool for characterizing the magnetic properties of natural samples, *J. Geophys. Res. Solid Earth*, *105*(B12), 28461–28475, doi:10.1029/2000JB900326.

Roman, C., and H. Singh (2007), A Self-Consistent Bathymetric Mapping Algorithm, *J. F. Robot.*, *24*(1-2), 23–50, doi:10.1002/rob.20164.

Rona, P. A. (1978), Magnetic signatures of hydrothermal alteration and volcanogenic mineral deposits in oceanic crust, *J. Volcanol. Geotherm. Res.*, *3*(1–2), 219–225, doi:http://dx.doi.org/10.1016/0377-0273(78)90010-0.

Rona, P. A. (2008), The changing vision of marine minerals, *Ore Geol. Rev.*, *33*(3–4), 618–666, doi:http://dx.doi.org/10.1016/j.oregeorev.2007.03.006.

Rona, P. A., G. Klinkhammer, T. A. Nelsen, J. H. Trefry, and H. Elderfield (1986), Black smokers, massive sulphides and vent biota at the Mid-Atlantic Ridge, *Nature*, *321*(6065), 33–37.

De Ronde, C. E. J., E. T. Baker, G. J. Massoth, J. E. Lupton, I. C. Wright, R. A. Feely, and R. R. Greene (2001), Intra-oceanic subduction-related hydrothermal venting, Kermadec volcanic arc, New Zealand, *Earth Planet. Sci. Lett.*, *193*(3-4), 359–369, doi:10.1016/S0012-821X(01)00534-9.

De Ronde, C. E. J. et al. (2005), Evolution of a Submarine Magmatic-Hydrothermal System: Brothers Volcano, Southern Kermadec Arc, New Zealand, *Econ. Geol.* , *100* (6), 1097–1133, doi:10.2113/gsecongeo.100.6.1097.

Ryall, P. J. C., and J. M. Ade-Hall (1975), Radial Variation of Magnetic Properties in Submarine Pillow Basalt, *Can. J. Earth Sci.*, *12*(12), 1959–1969, doi:10.1139/e75-174.

Sager, W. W., C. J. Weiss, M. A. Tivey, and H. P. Johnson (1998), Geomagnetic polarity reversal model of deep‐tow profiles from the Pacific Jurassic Quiet Zone, *J. Geophys. Res.*, *103*(B3), 5269–5286, doi:10.1029/ 97JB03404.

Salmi, M. S., H. P. Johnson, M. A. Tivey, and M. Hutnak (2014), Quantitative estimate of heat flow from a mid-ocean ridge axial valley, Raven field, Juan de Fuca Ridge: Observations and inferences, *J. Geophys. Res. Solid Earth*, *119*(9), 6841–6854, doi:10.1002/2014JB011086.

Sato, H., K. Nakamura, H. Kumagai, R. Senda, T. Morishita, A. Tamura, and S. Arai (2015a), Petrology and Geochemistry of Mid-Ocean Ridge Basalts from the Southern Central Indian Ridge, in *Subseafloor Biosphere Linked to Hydrothermal Systems SE - 13*, edited by J. Ishibashi, K. Okino, and M. Sunamura, pp. 163–175, Springer Japan.

Sato, T., K. Okino, and H. Kumagai (2009), Magnetic structure of an oceanic core complex at the southernmost Central Indian Ridge: Analysis of shipboard and deep-sea three-component magnetometer data, *Geochemistry, Geophys. Geosystems*, *10*(6), Q06003, doi:10.1029/2008GC002267.

Sato, T., M. Mizuno, T. Takata, T. Yamada, T. Isse, K. Mochizuki, M. Shinohara, and N. Seama (2015b), Seismic structure and seismicity in the Southern Mariana Trough and their relation to hydrothermal activity, in *Subseafloor Biosphere*

Linked to Global Hydrothermal Systems; TAIGA Concept, edited by J. Ishibashi, K. Okino, and M. Sunamura.

Sayanagi, K., A. Oshida, M. Watanabe, and K. Tamaki (1994), New Self-Contained Deep-Towed Proton Magnetometer System, *J. Geomagn. Geoelectr.*, *46*(8), 631–642, doi:10.5636/jgg.46.631.

Schouten, H., M. A. Tivey, D. J. Fornari, and J. R. Cochran (1999), Central anomaly magnetization high: constraints on the volcanic construction and architecture of seismic layer 2A at a fast-spreading mid-ocean ridge, the EPR at 9°30′–50′N, *Earth Planet. Sci. Lett.*, *169*(1–2), 37–50, doi:10.1016/S0012-821X(99)00063-1.

Schroeder, T., B. John, and B. R. Frost (2002), Geologic implications of seawater circulation through peridotite exposed at slow-spreading mid-ocean ridges, *Geol.* , *30* (4), 367–370, doi:10.1130/0091-7613(2002)030<0367:GIOSCT>2.0.CO;2.

Scott, R. B., P. A. Rona, B. A. Mcgregor, and M. R. Scott (1974), The TAG hydrothermal field, *Nature*, *251*(5473), 301–302.

Seama, N., Y. Nogi, and N. Isezaki (1993), A New Method For Precise Determination of the Position and Strike of Magnetic Boundaries Using Vector Data of the Geomagnetic Anomaly Field, *Geophys. J. Int.*, *113*(1), 155–164.

Seama, N., H. Sato, Y. Nogi, and K. Okino (2015), The mantle dynamics, the crustal formation, and the hydrothermal activity of the Southern Mariana Trough back-arc Basin, in *Subseafloor Biosphere Linked to Global Hydrothermal Systems; TAIGA Concept*, edited by J.-I. Ishibashi, K. Okino, and M. Sunamura.

Seno, T., and S. Maruyama (1984), Paleogeographic reconstruction and origin of the Philippine Sea, *Tectonophysics*, *102*(1–4), 53–84, doi:http://dx.doi.org/10.1016/0040-1951(84)90008-8.

Seyfried, W. E. (1987), Experimental and Theoretical Constraints on Hydrothermal Alteration Processes at Mid-Ocean Ridges, *Annu. Rev. Earth Planet. Sci.*, *15*(1), 317–335, doi:10.1146/annurev.ea.15.050187.001533.

Seyfried, W. E., M. E. Berndt, and J. S. Seewald (1988), Hydrothermal alteration processes at mid-ocean ridges: constraints from diabase alteration experiments, hot-spring fluids and composition of the oceanic crust, *Can. Mineral.*, *26*(3), 787–804.

Shinjo, R., S.-L. Chung, Y. Kato, and M. Kimura (1999), Geochemical and Sr-Nd isotopic characteristics of volcanic rocks from the Okinawa Trough and Ryukyu Arc: Implications for the evolution of a young, intracontinental back arc basin, *J. Geophys. Res.*, *104*(B5), 10591, doi:10.1029/1999JB900040.

Sibuet, J.-C. et al. (1987), Back Arc Extension in the Okinawa Trough, *J. Geophys. Res. Solid Earth*, *92*(B13), 14041–14063, doi:10.1029/JB092iB13p14041.

Singh, S. C., W. C. Crawford, H. Carton, T. Seher, V. Combier, M. Cannat, J. Pablo Canales, D. Dusunur, J. Escartin, and J. Miguel Miranda (2006), Discovery of a magma chamber and faults beneath a Mid-Atlantic Ridge hydrothermal field, *Nature*, *442*(7106), 1029–1032.

Sinton, J. M., and R. S. Detrick (1992), Mid-ocean ridge magma chambers, *J. Geophys. Res.*, *97*(B1), 197, doi:10.1029/91JB02508.

Sohn, R. A., and K. W. W. Sims (2005), Bending as a mechanism for triggering off-axis volcanism on the East Pacific Rise, *Geol.* , *33* (2), 93–96, doi:10.1130/G21116.1 .

Spiess, F.N., Macdonald, K.C., Atwater, T., Ballard, R., Carranza, A., Cordoba, D., Cox, C., Diaz-Garcia, V., Francheteau, J., Guerrero, J., Hawkins, J., Haymon, R., Hessler, R., Juteau, T., Kastner, M., Larson, R., Luyendyk, B., MacDougall, D., Miller, S, C. (1980), Hot springs and geophysical experiments on the East Pacific Rise., *Science (80-.).*, *207*, 1421–1433.

Stakes, D., and W. S. Moore (1991), Evolution of hydrothermal activity on the Juan de Fuca Ridge: Observations, mineral ages, and Ra isotope ratios, *J. Geophys. Res.*, *96*(B13), 21739, doi:10.1029/91JB02038.

Stein, C. A., and S. Stein (1992), A model for the global variation in oceanic depth and heat flow with lithospheric age, *Nature*, *359*(123-129), doi:10.1038/359123a0.

Stein, C. A., and S. Stein (1994), Constraints on hydrothermal heat flux through the oceanic lithosphere from global heat flow, *J. Geophys. Res.*, *99*(B2), 3081–3095, doi:10.1029/93JB02222.

Stern, R. J., M. J. Fouch, and S. L. Klemperer (2003), An overview of the Izu-Bonin-Mariana subduction factory, in *Inside the Subduction Factory*, vol. 138, pp. 175–222, AGU, Washington, DC.

Szitkar, F., and J. Dyment (2014), Near-seafloor magnetics reveal tectonic rotation and deep structure at the TAG (Trans-Atlantic Geotraverse) hydrothermal site (Mid-Atlantic Ridge, 26°N), *Geol.* , doi:10.1130/G36086.1.

Szitkar, F., J. Dyment, Y. Fouquet, C. Honsho, and H. Horen (2014a), The magnetic signature of ultramafic-hosted hydrothermal sites, *Geology*, *42*(8), 715–718, doi:10.1130/G35729.1.

Szitkar, F., J. Dyment, Y. Choi, and Y. Fouquet (2014b), What causes low magnetization at basalt-hosted hydrothermal sites? Insights from inactive site Krasnov (MAR 16°38′N), *Geochemistry, Geophys. Geosystems*, *15*(4), 1441–1451, doi:10.1002/2014GC005284.

Szitkar, F., S. Petersen, F. Caratori-Tontini, and L. Cocchi (2015), High-resolution magnetics reveal the deep structure of a volcanic-arc-related basalt-hosted hydrothermal site (Palinuro, Tyrrhenian Sea), *Geochemistry, Geophys. Geosystems*, *16*(6), 1950–1961, doi:10.1002/2015GC005769.

Takai, K., T. Gamo, U. Tsunogai, N. Nakayama, H. Hirayama, K. Nealson, and K. Horikoshi (2004), Geochemical and microbiological evidence for a hydrogen-based, hyperthermophilic subsurface lithoautotrophic microbial ecosystem (HyperSLiME) beneath an active deep-sea hydrothermal field, *Extremophiles*, *8*(4), 269–282, doi:10.1007/s00792-004-0386-3.

Takai, K., K. Nakamura, K. Suzuki, F. Inagaki, K. H. Nealson, and H. Kumagai (2006), Ultramafics-Hydrothermalism-Hydrogenesis-HyperSLiME (UltraH3) linkage: a key insight into early microbial ecosystem in the Archean deep-sea hydrothermal systems, *Paleontol. Res.*, *10*(4), 269–282, doi:10.2517/prpsj.10.269.

Takamasa, A., S. Nakai, F. Sato, S. Toyoda, D. Banerjee, and J. Ishibashi (2013), U–Th radioactive disequilibrium and ESR dating of a barite-containing sulfide crust from South Mariana Trough, *Quat. Geochronol.*, *15*, 38–46, doi:10.1016/j.quageo.2012.12.002.

Talwani, M., and J. R. Heirtzler (1964), Computation of magnetic anomalies caused by two-dimensional structures of arbitrary shape, in *Computers in the Mineral Industries*, edited by G. A. Parks, pp. 464– 480.

Tanahashi, M., K. Fujioka, and S. Machida (2008), Myojin Rift, Izu–Bonin Arc as the Modern Analog of Hokuroku Basin, Northeast Japan: Geotectonic Significance of the New Hydrothermal Deposit in the Back-Arc Rift, *Resour. Geol.*, *58*(3), 301–312, doi:10.1111/j.1751-3928.2008.00063.x.

Tivey, M. A. (1994), Fine-scale magnetic anomaly field over the southern Juan de Fuca Ridge: Axial magnetization low and implications for crustal structure, *J. Geophys. Res.*, *99*(B3), 4833–4855, doi:10.1029/93JB02110.

Tivey, M. A. (1996), Vertical magnetic structure of ocean crust determined from near-bottom magnetic field measurements, *J. Geophys. Res.*, *101*(B9), 20275–20296, doi:10.1029/96JB01307.

Tivey, M. A., and J. Dyment (2010), The magnetic signature of hydrothermal systems in slow spreading environments, in *Diversity of Hydrothermal Systems on Slow Spreading Ocean Ridges*, vol. 188, pp. 43–66, AGU, Washington, DC.

Tivey, M. A., and H. P. Johnson (1993), Variations in oceanic crustal structure and implications for the fine-scale magnetic anomaly signal, *Geophys. Res. Lett.*, *20*(17), 1879–1882, doi:10.1029/93GL01485.

Tivey, M. A., and H. P. Johnson (2002), Crustal magnetization reveals subsurface structure of Juan de Fuca Ridge hydrothermal vent fields, *Geology*, *30*(11), 979–982.

Tivey, M. A., P. A. Rona, and H. Schouten (1993), Reduced crustal magnetization beneath the active sulfide mound, TAG hydrothermal field, Mid-Atlantic Ridge at 26°N, *Earth Planet. Sci. Lett.*, *115*(1–4), 101–115, doi:http://dx.doi.org/10.1016/0012-821X(93)90216-V.

Tivey, M. A., P. A. Rona, and M. C. Kleinrock (1996), Reduced crustal magnetization beneath Relict Hydrothermal Mounds: TAG Hydrothermal Field, Mid-Atlantic Ridge, 26°N, *Geophys. Res. Lett.*, *23*(23), 3511–3514, doi:10.1029/96GL02082.

Tivey, M. A., H. P. Johnson, A. Bradley, and D. Yoerger (1998), Thickness of a submarine lava flow determined from near-bottom magnetic field mapping by autonomous underwater vehicle, *Geophys. Res. Lett.*, *25*(6), 805–808, doi:10.1029/98GL00442.

Tivey, M. A., H. Schouten, and M. C. Kleinrock (2003), A near-bottom magnetic survey of the Mid-Atlantic Ridge axis at 26°N: Implications for the tectonic evolution of the TAG segment, *J. Geophys. Res.*, *108*(B5), 2277, doi:10.1029/2002JB001967.

Tivey, M. A., W. W. Sager, S.-M. Lee, and M. Tominaga (2006), Origin of the Pacific Jurassic quiet zone, *Geology*, *34*(9), 789–792, doi:10.1130/G22894.1.

Tivey, M. A., H. P. Johnson, M. S. Salmi, and M. Hutnak (2014), High-resolution near-bottom vector magnetic anomalies over Raven Hydrothermal Field, Endeavour Segment, Juan de Fuca Ridge, *J. Geophys. Res. Solid Earth*, *119*(10), 2014JB011223, doi:10.1002/2014JB011223.

Tivey, M. K. (2007), Generation of Seafloor Hydrothermal Vent Fluids and Associated Mineral Deposits, *Oceanography*, *20*(1), 50–65.

Tivey, M. K., and J. R. Delaney (1986), Growth of large sulfide structures on the endeavour segment of the Juan de Fuca ridge, *Earth Planet. Sci. Lett.*, *77*(3–4), 303–317, doi:http://dx.doi.org/10.1016/0012-821X(86)90142-1.

Toft, P. B., J. Arkani-Hamed, and S. E. Haggerty (1990), The effects of serpentinization on density and magnetic susceptibility: a petrophysical model, *Phys. Earth Planet. Inter.*, *65*(1–2), 137–157, doi:http://dx.doi.org/10.1016/0031-9201(90)90082-9.

Urabe, T., J. Ishibashi, A. Maruyama, K. Marumo, N. Seama, and M. Utsumi (2004), Discovery and drilling of on- and off-axis hydrothermal sites in backarc spreading center of southern Mariana Trough, Western Pacific, in *American Geophysical Union, Fall Meeting 2004, abstract #V44A-03*.

Verhoogen, J. (1956), Ionic ordering and self-reversal of magnetization in impure magnetites, *J. Geophys. Res.*, *61*(2), 201–209, doi:10.1029/JZ061i002p00201.

Walls, C. C., and J. M. Hall (1998), Interpretation of aeromagnetic anomalies in terms of hydrothermal alteration in Cretaceous normal polarity superchron extrusives of the Troodos, Cyprus, ophiolite, *J. Geophys. Res. Solid Earth*, *103*(B12), 30311–30321, doi:10.1029/98JB02846.

Watkins, N. D., and T. P. Paster (1971), The Magnetic Properties of Igneous Rocks from the Ocean Floor, *Philos. Trans. R. Soc. London A Math. Phys. Eng. Sci.*, *268*(1192), 507–550.

Watts, A. B. (1978), An analysis of isostasy in the world's oceans 1. Hawaiian-Emperor Seamount Chain, *J. Geophys. Res. Solid Earth*, *83*(B12), 5989–6004, doi:10.1029/JB083iB12p05989.

Wessel, P., and W. H. F. Smith (1998), New, improved version of generic mapping tools released, *Eos, Trans. Am. Geophys. Union*, *79*(47), 579, doi:10.1029/98EO00426.

Wheat, C. G., and M. J. Mottl (2000), Composition of pore and spring waters from Baby Bare: global implications of geochemical fluxes from a ridge flank

hydrothermal system, *Geochim. Cosmochim. Acta*, *64*(4), 629–642, doi:10.1016/S0016-7037(99)00347-6.

Wheat, C. G., P. Fryer, S. Hulme, N. Becker, A. Curtis, and C. Moyer (2003), Hydrothermal Venting in the Southern Most Portion of the Mariana Backarc Spreading Center at 12.57 Degrees N, in *American Geophysical Union, Fall Meeting 2003, abstract #T32A-0920*.

White, S., S. Humphris, and M. Kleinrock (1998), New Observations on the Distribution of Past and Present Hydrothermal Activity in the TAG Area of the Mid-Atlantic Ridge (26°08′ N), *Mar. Geophys. Res.*, *20*(1), 41–56, doi:10.1023/A:1004376229719.

White, W. M., and E. M. Klein (2014), Composition of the Oceanic Crust, in *The Crust, Treatise on Geochemistry (Second Edition)*, pp. 457–496.

Wolfe, C. J., G. M. Purdy, D. R. Toomey, and S. C. Solomon (1995), Microearthquake characteristics and crustal velocity structure at 29°N on the Mid-Atlantic Ridge: The architecture of a slow spreading segment, *J. Geophys. Res.*, *100*(B12), 24449, doi:10.1029/95JB02399.

Wooldridge, A. L., S. E. Haggerty, P. A. Rona, and C. G. A. Harrison (1990), Magnetic properties and opaque mineralogy of rocks from selected seafloor hydrothermal sites at oceanic ridges, *J. Geophys. Res. Solid Earth*, *95*(B8), 12351–12374, doi:10.1029/JB095iB08p12351.

Wooldridge, A. L., C. G. A. Harrison, M. A. Tivey, P. A. Rona, and H. Schoutens (1992), Magnetic Modeling Near Selected Areas of Hydrothermal Activity on the Mid-Atlantic and Gorda Ridges, *J. Geophys. Res.*, *97*(B7), 10911–10926, doi:10.1029/92JB00605.

Yamanaka, T. et al. (2015), The Tarama Knoll: Geochemical and Biological Profiles of Hydrothermal Activity BT, in *Subseafloor Biosphere Linked to Global Hydrothermal Systems; TAIGA Concept*, edited by J.-I. Ishibashi, K. Okino, and M. Sunamura.

Yamamoto, M., N. Seama, and N. Isezaki (2005), Geomagnetic paleointensity over 1.2 Ma from deep-tow vector magnetic data across the East Pacific Rise, *Earth, Planets Sp.*, *57*(5), 465–470, doi:10.1186/BF03351835.

Yamazaki, T., N. Seama, K. Okino, K. Kitada, M. Joshima, H. Oda, and J. Naka (2003), Spreading process of the northern Mariana Trough: Rifting-spreading transition at 22°N, *Geochemistry, Geophys. Geosystems*, *4*(9), n/a–n/a, doi:10.1029/2002GC000492.

YK05-09-leg2 cruise report (2005), http://www.godac.jamstec.go.jp/darwin/cruise/yokosuka/YK05-09_leg2/j.

YK12-05 cruise report (2012), http://www.godac.jamstec.go.jp/darwin/cruise/yokosuka/YK12-05/j.

Yoshikawa, S., K. Okino, and M. Asada (2012), Geomorphological variations at hydrothermal sites in the southern Mariana Trough: Relationship between hydrothermal activity and topographic characteristics, *Mar. Geol.*, *303–306*(0), 172–182, doi:http://dx.doi.org/10.1016/j.margeo.2012.02.013.

Zhao, X., D. Heslop, and A. P. Roberts (2015), A protocol for variable-resolution first-order reversal curve measurements, *Geochemistry, Geophys. Geosystems*, *16*(5), 1364–1377, doi:10.1002/2014GC005680.

Zhou, W., R. Van der Voo, and D. R. Peacor (1997), Single-domain and superparamagnetic titanomagnetite with variable Ti content in young ocean-floor basalts: No evidence for rapid alteration, *Earth Planet. Sci. Lett.*, *150*(3–4), 353–362, doi:http://dx.doi.org/10.1016/S0012-821X(97)00099-X.

Zhou, W., R. Van der Voo, D. R. Peacor, D. Wang, and Y. Zhang (2001), Low-temperature oxidation in MORB of titanomagnetite to titanomaghemite: A gradual process with implications for marine magnetic anomaly amplitudes, *J. Geophys. Res.*, *106*(B4), 6409–6421, doi:10.1029/2000JB900447.

Zhu, J., J. Lin, Y. J. Chen, C. Tao, C. R. German, D. R. Yoerger, and M. A. Tivey (2010), A reduced crustal magnetization zone near the first observed active hydrothermal vent field on the Southwest Indian Ridge, *Geophys. Res. Lett.*, *37*(18), L18303, doi:10.1029/2010GL043542.